A STUDY OF POSSIBLE FAILURE MECHANISMS

FOR MINING-INDUCED SEISMICITY IN SASKATCHEWAN

by

Mushfique Ahmed

A Thesis
Submitted to the Faculty of Graduate Studies
in Partial Fulfilment of the Requirement
for the Degree of

Doctor of Philosophy

Department of Civil Engineering
University of Manitoba
Winnipeg, Manitoba

July, 1990

A STUDY OF POSSIBLE FAILURE MECHANISMS

FOR MINING-INDUCED SEISMICITY IN SASKATCHEWAN

BY

MUSHFIQUE AHMED

A thesis submitted to the Faculty of Graduate Studies of
the University of Manitoba in partial fulfillment of the requirements
of the degree of

DOCTOR OF PHILOSOPHY

© 1990

ABSTRACT

A number of earthquakes have been recorded in recent years in the strata above Saskatchewan potash mines. These are widely understood to be mining-induced and to have been generated in the carbonate Dawson Bay Formation that lies above the immediate roof of the mine which is a thin salt layer. A rock mechanics study of possible mechanisms for this seismicity was undertaken. Analytical modelling as well as experimental investigations and numerical analyses were performed.

A theory for the elastic beam on elastic supports, based on the differential equation of the elastic line was developed, and was adopted as the analytical model for simulating the response of the Dawson Bay Formation to potash mining. This model was employed to examine the potential for failure along bedding planes as a source of seismicity in the Dawson Bay Formation. The results obtained show that, although failure along the bedding plane of the Dawson Bay Formation is capable of generating microseismicity, the larger events could not be attributed to this mechanism.

In an experimental study, the Dawson Bay Formation was simulated by a thick rock beam loaded to ultimate failure in a specially designed testing frame which provided longitudinal constraint. The experimental results established that failure of a thick rock beam involves three distinct fracture events : (a) vertical midspan cracking and development of a linear arch, (b) diagonal cracking, and (c) failure of remnant rock bridges. The first two events release a small amount of energy, while the ultimate failure occurs violently. Numerical analyses, using both finite difference and finite element models, validated these experimental findings. The finite difference analysis simulated the initiation of the diagonal cracking in a beam test. But, the discrete crack propagation FEM successfully replicated the three-stage failure mechanism of a

typical beam test.

It is proposed that failure of a Dawson Bay linear arch under the "dead weight" of the overburden is a possible causal explanation of some of the larger seismic events. Calculations indicate that the theoretical upper limit for an earthquake magnitude generated by a full scale rupture of intact Dawson Bay linear arch is about 2.7, which is in the order that has been recorded for the larger events in the Saskatchewan potash mines.

ACKNOWLEDGEMENT

TABLE OF CONTENTS

LIST OF FIGURES

LIST OF TABLES

CHAPTER 1

INTRODUCTION

1.1 BACKGROUND AND PERSPECTIVE

Potash deposits, limited to a few producing countries in the world, are the main source of potash consumed in the fertilizer and other chemical industries. The richest deposits of potash in the world are located at a depth of nearly 1 km beneath the farmlands of Saskatchewan, Canada. Canada is also the leading producer of potash in the Western World. The Potash industry has been an important contributor to the Western Canadian economy by providing long-term investment for a large amount of capital and, in the process, creating jobs.

Potash was discovered in Saskatchewan in the early 1940's and was brought to production in the 1960's. The Saskatchewan potash deposits are renowned for their richness, thickness, flatness, continuity and extent. The advantages of these positive factors are, however, offset to some extent by the depth of the deposits, the presence of water-bearing formations in the overburden and their remoteness from the major potash markets.

There are eight operating conventional mines in Saskatchewan. Five of these mines are located in the Saskatoon area, while the remaining three are in southeast Saskatchewan. Although the long term outlook for potash is regarded as bright, the potash industry is highly competitive. Continuous research and development carried out by the industry to maintain production as well as safety enable the Saskatchewan mines to be among the lowest unit cost potash producers in the world.

1

1.2 CHALLENGES FACING THE POTASH INDUSTRY

IN SASKATCHEWAN

In the early years of mining, the most important problem was room stability and convergence. Unique methods were eventually devised in this regard; still more are being evaluated. Although the potash mining operations in Saskatchewan are among the most mechanized in the world, the overall extraction ratio (35 to 40 percent) still remains relatively low. The primary reason for this low extraction ratio is the perceived risk of flooding arising from the presence of overlying aquifers should the extraction ratio be increased.

One of the most difficult tasks has been the sinking of shafts due to the presence of several water-bearing formations. The most difficult unit to penetrate is the Blairmore Formation, which is 62 to 152 meters thick, and is composed of unconsolidated sand, silt, mudstone and shale. This formation is at a depth of approximately 365 meters, having water pressures as high as 5500 kPa. Other water-bearing formations, e.g., Dawson Bay Formation, are known to contain water at pressures of 7500 kPa or higher. Freezing the ground or grouting has been the most successful method of penetrating the water-bearing zones.

As mining continues, progressive accumulation of waste salt and brine on surface causes another challenge for the potash industry, namely, the long-term environmental problem. Initially, subsidence over potash mines was thought unlikely to be transmitted as far as the ground surface, which is approximately 1 km above. It was believed that the gradual collapse of the mining galleries would be taken up by the salt and the unconsolidated sand in the Cretaceous strata above. Recent measurements at the surface, however, show that several inches of subsidence have actually taken place. The subsidence profile is characterized by a very shallow region extending several km outside the primary trough. While the maximum possible subsidence could be 120 cm, the current consensus is that subsidence will be about 30 cm (Dunn, 1975).

Geological anomalies, such as channels, salt-horses with leached zones, and collapse features have resulted in loss of production. The last two have been found to cause ingress of water into the mine openings (Molavi,1987).

Although the presence of a high percentage of carnallite, which is weaker than sylvite, within or above the mining horizon does not cause immediate collapse, it can cause major failures in the long term, thereby creating avenues for water inflow.

In more recent years, a new rock mechanics problem has surfaced as the area of mining increased, namely, mining-induced seismicity. These seismic events indicate sudden rupture or fracture of rock relatively close to the mine working, a phenomenon which could also allow water ingress into the mines.

1.3 PURPOSE OF THE THESIS

Geophysical investigations by mining companies and university researchers have established beyond reasonable doubt that seismicity recorded above operating potash mines in Saskatchewan is (a) mining-induced and (b) associated with the Dawson Bay Formation, which lies slightly above the mining horizon. By earthquake standards, the magnitude of even the largest events recorded to date (3.6 on the Richter Scale) is relatively minor. Nonetheless, if these events indicate, as they surely must do, sudden rupture or fracture of rock relatively close to the mine workings, that is reason enough to warrant further study. Moreover, the associated fracturing could also provide cracks for water ingress.

In order to assess the practical significance of these seismic events to mining, one has to understand their mechanism(s) and the factors controlling their occurrence. With this objective, the writer decided to undertake a rock mechanics study, the first of its kind, of mini-

ng-induced seismicity in the Saskatchewan potash mines.

1.4 OBJECTIVES

In this study, the writer has considered two possible causal explanations of seismicity in the Dawson Bay Formation. These are :

(a) Slip along bedding planes,

(b) Ultimate failure of a linear arch.

The objectives of this study were to examine the plausibility and scope of these hypotheses. To this end, for (a), the writer developed analytical models (see Chapter 6), in which the Dawson Bay Formation was idealized as an elastic beam resting on elastic abutments. The other hypothesis involved laboratory experiments, in which the linear arch was simulated by a rock beam loaded to ultimate failure in a specially designed testing frame.

1.5 LAYOUT OF THESIS

Chapter 2 reviews the regional geology and lithology of the Saskatchewan potash mining districts. It discusses the difficulties associated with evaluating material properties. The procedures for obtaining the virgin in-situ stress, so essential to any meaningful rock mechanics analysis, are discussed. Finally geological anomalies, which can be detrimental to mining operations, are described.

Chapter 3 reviews the mining methods employed in Saskatchewan potash mining and briefly discusses the continuing process of the evolution of mining methods.

Chapter 4 describes mining-induced seismicity of the area in the context of natural seismicity of the region, and reviews the two conceptual models proposed to date by other researchers for the failure mechanism generating the induced seismicity. Also, the concept of Critical energy release rate as predictor of induced-seismicity in bedded deposits is discussed.

Chapter 5 explains the rock mechanics approach undertaken in this study.

Chapter 6 discusses the development of a new analytical model for an elastic beam on an elastic support. Both thin and thick beam formulations are presented.

Chapter 7 examines the potential for bedding plane slip as a source mechanism of seismicity in the Dawson Bay Formation. Results obtained from the analytical model (Chapter 6) were derived for two bounding conditions. These are : (a) slip along a frictionless surface representing the condition of the Dawson Bay Formation containing bitumen laminae, and (b) maximum horizontal shear stress representing the situation of a homogeneous Dawson Bay Formation with a perfectly cemented bedding plane.

In Chapter 8 the experimental work on longitudinally constrained beams is described. From the results of these experiments, a number of failure mechanisms have been identified. Implications of these experimental findings for induced seismicity are drawn.

Chapter 9 deals with the numerical modelling —— both finite difference and finite element (discrete crack propagation). The principal objective of these numerical analyses has been to gain greater understanding of the failure mechanisms which were observed in the beam testing (Chapter 8).

The penultimate Chapter 10 presents the summary of the study —— analytical as well as experimental and numerical —— regarding possible mechanisms for mining-induced seismicity above Saskatchewan potash mines, along with the corroborative field evidence. Also, a direction for future work is given.

Finally, Chapter 11 concludes on the entire study.

CHAPTER 2

ENGINEERING GEOLOGY

2.1 REGIONAL GEOLOGY

The potash deposits in Saskatchewan occur within a thick sequence of rocks known as the Prairie Evaporite Formation (Fig. 2.1). These salts were laid down in a depositional basin, referred to as the Elk Point Basin, that extended over a thousand miles from northernmost Alberta southeastwards into North Dakota (Fig. 2.2).

The Prairie Evaporite beds rest conformably upon carbonate rocks of the Winnipegosis Formation and are overlain disconformably by carbonates, evaporites and mudstones of the Dawson Bay Formation.

2.2 PRAIRIE EVAPORITE FORMATION

The sediments of the Prairie Evaporite Formation are predominantly salt with minor amounts of anhydrite and potash. Potash occurs in the upper part of the formation in four levels known as potash "members". In ascending order, these are: Esterhazy, White Bear, Belle Plain, and Patience Lake Members. All the mines in the Saskatoon area work the Patience Lake member, while the mines in the southeast produce from the Esterhazy Member.

The mineralogy of the Saskatchewan potash deposits is simple: only halite,

SOCONY SOHIO
HATFIELD 11-14
L.S.D.14-11-28-22W2
K.B. 1718

	FORMATION	CYCLE	SYSTEM
DAVIDSON EVAPORITE	LOWER SOURIS RIVER (DAVIDSON MEMBER)	CYCLE THREE	
1ST RED BEDS			
HUBBARD EVAP.	DAWSON BAY	CYCLE TWO	
2ND RED BEDS			
POTASH	PRAIRIE EVAPORITE		MIDDLE DEVONIAN
		CYCLE ONE (ELK POINT GROUP)	
	WINNIPEGOSIS		
3RD RED BEDS	ASHERN		
			SILURIAN

▦ SALTS ▤ CARBONATES ■ SHALES

0   100 m

Vertical Scale
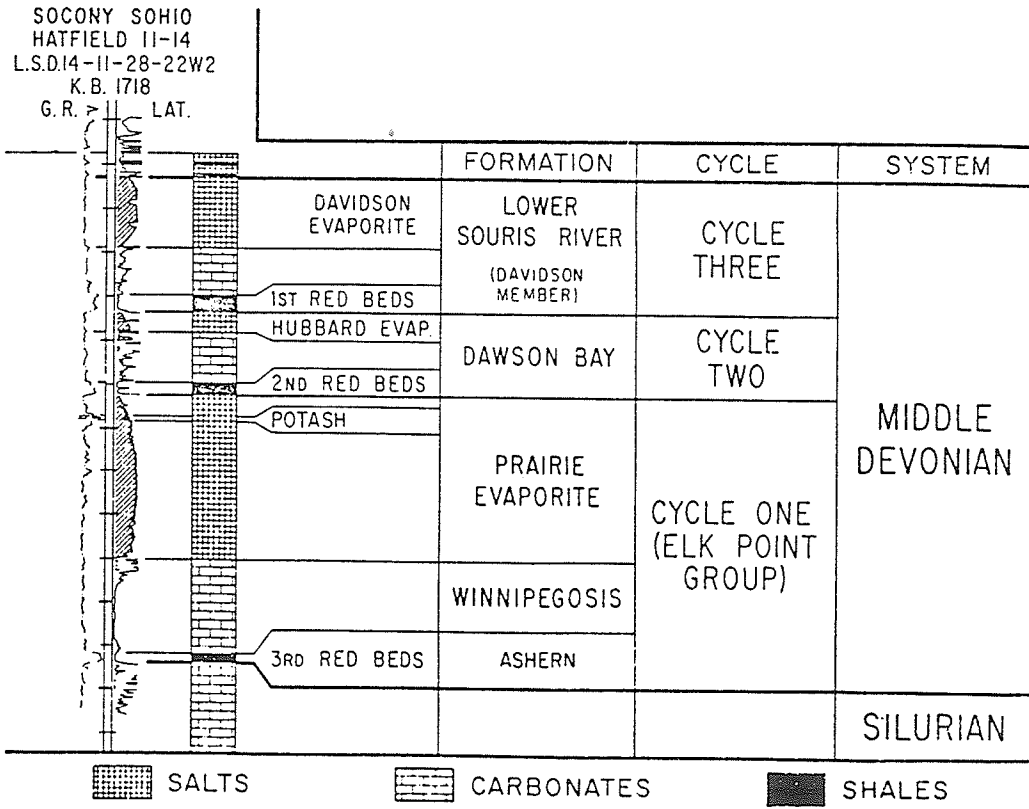
Fig. 2.1   Columnar section showing Middle Devonian Evaporite cycles in Saskatchewan (after Lane, 1959).
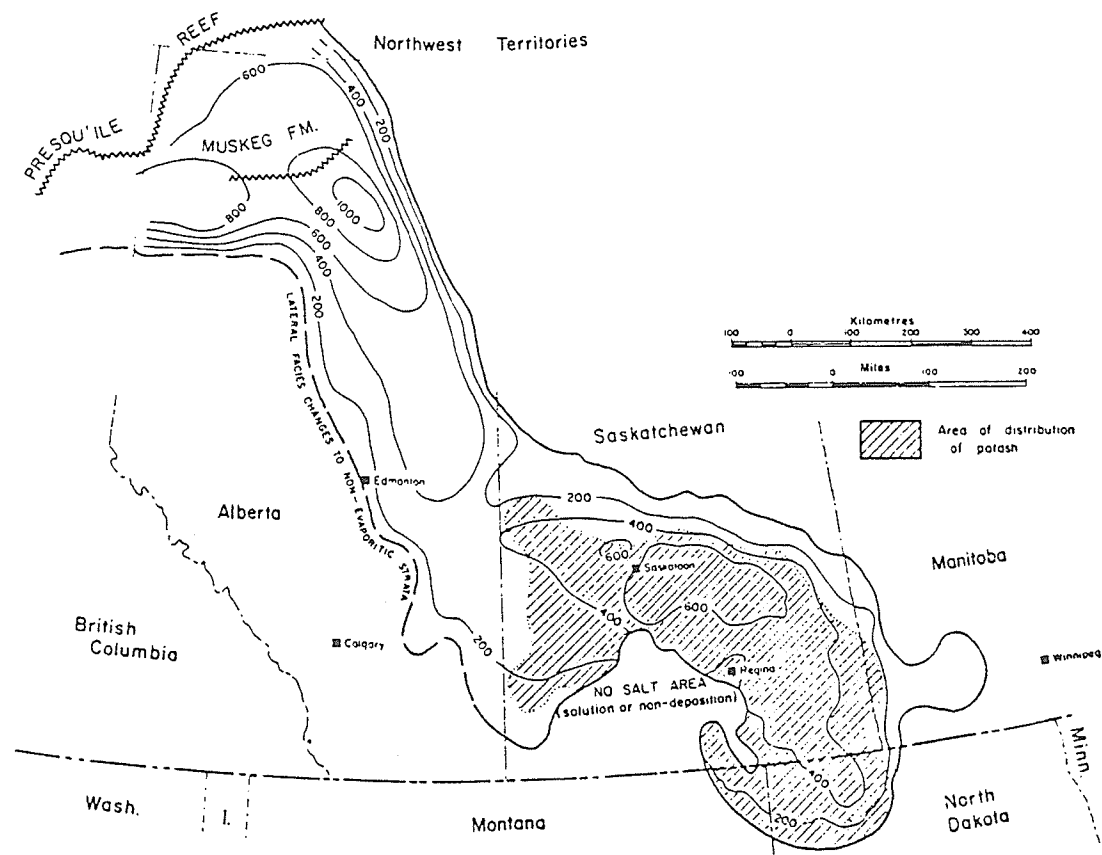
Fig. 2.2 Isopach map of the Prairie Evaporite in the Elk Point Basin (after Holter,1969).

sylvite, and carnallite are present with minor amounts of clay. Sylvite is the desired mineral, as it is almost pure KCl. In the southeastern potash mines, which produce from the Esterhazy Member, certain areas are rich in carnallite. Carnallite occurs either with sylvite and halite in the potash beds, in veins between sylvite and halite crystals, or as pods of pure carnallite. The carnallite zones are known to extend vertically above and below the ore body in the southeastern potash mines.

2.3 DAWSON BAY FORMATION

The Dawson Bay Formation extends from eastern Alberta to western Manitoba, where it outcrops (Fig. 2.3). In southeast Saskatchewan, the Dawson Bay Formation is believed to be generally wet. All potash mines in the Saskatoon region are situated in areas of "dry" Dawson Bay, but some are not far from water-bearing Dawson Bay beds.

This Formation consists of four members. These are, in ascending order: Second Red Bed, Burr Member, Neely Member, and Hubbard Evaporite Member (Fig.2.4).

The Second Red Bed follows, with a minor disconformity, the salts of the Prairie Evaporite Formation. It lies slightly above the mining horizon, e.g., in Saskatoon area approximately 10 m above the potash seam. It is composed of a dolomitic mudstone which is red at the base, grading into brown, and then grey at the top. This, 3 to 6 meter thick, mudstone is commonly heavily fractured, having slickensides (RQD < 100%).

The Burr Member rests with an unconformity on the Second Red Bed. This member is almost 20 m thick and consists entirely of very fine grained dolomite, dolomitic microcrystalline, bioturbated limestone, and a calcic limestone containing hard grounds. Fractures, which are relatively infrequent in this rock, are found to be sub-vertical and generally filled

Outcrop of Dawson Bay Formation (after Bannatyne, 1975)

Subsurface extent of Dawson Bay Formation (after Grayston et al., 1964); northern erosional edge after Paterson, 1975, and Fuzesy, 1980.
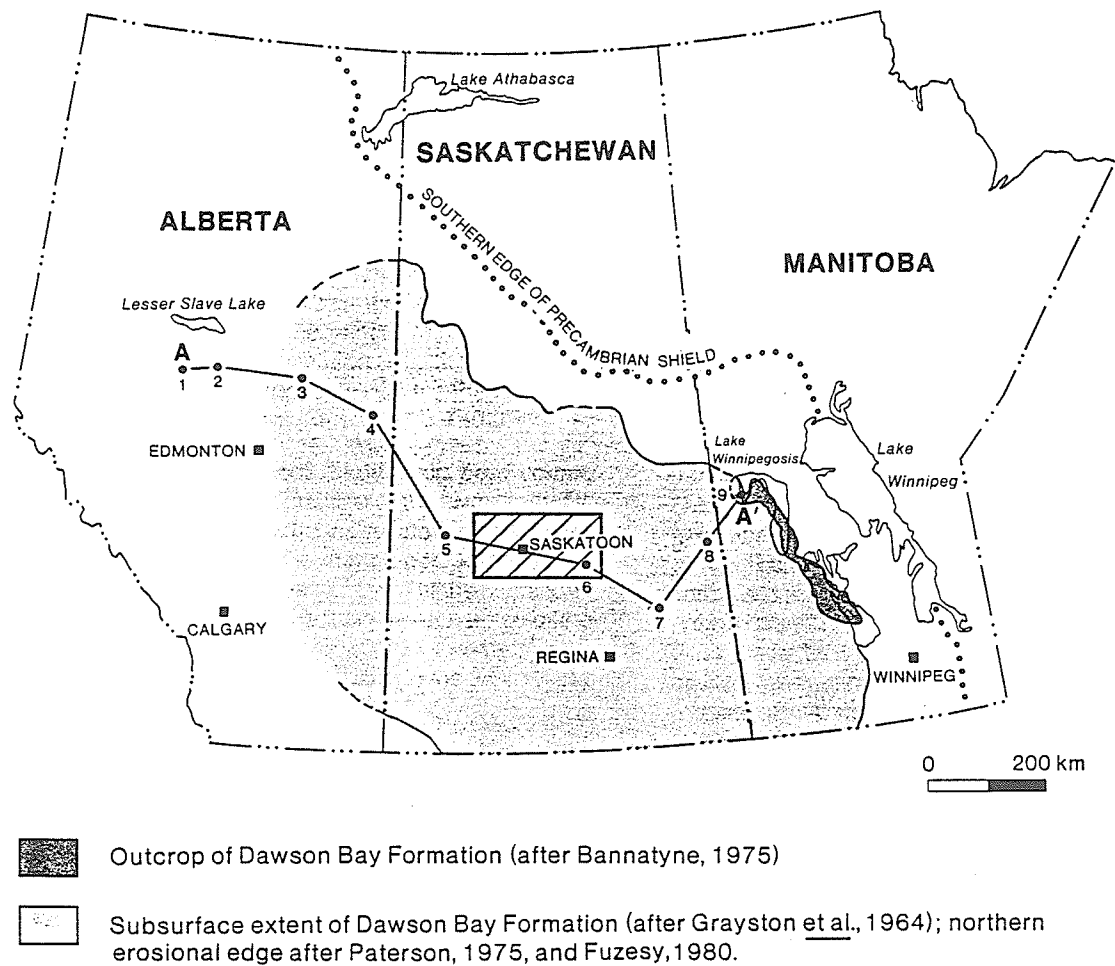
Fig. 2.3 Location, outcrop and subcrop map of the Dawson Bay Formation.
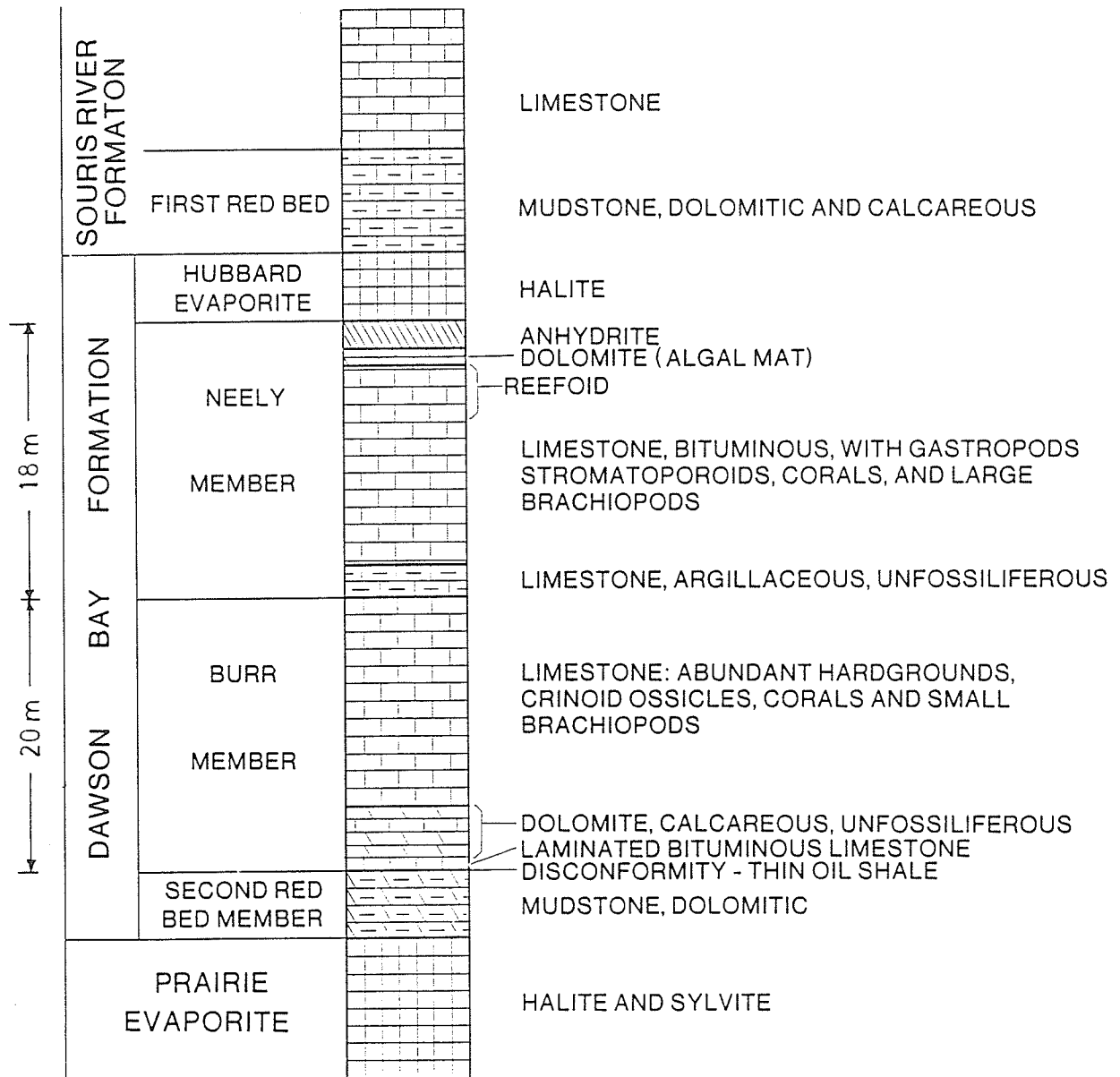
Fig. 2.4 Stratigraphic sequence of the Dawson Bay Formation (after Dunn, 1982).

11

with calcite. For all practical purposes, the RQD of this member is 100%.

The Neely Member lies disconformably upon the Burr Member. Its thickness ranges from 15 to 18 meters. It is composed predominantly of massive limestone. The upper sections are highly fossiliferous with intermittent bitumen laminae. Although some core of the upper part show relative weakness along bitumen laminae and fossil contacts, the RQD of this member is virtually 100%.

The Hubbard Evaporite Member is the uppermost unit of the Dawson Bay Formation. This halite bed is of variable thickness up to 14 m.

The Second Red Bed and Hubbard Evaporite Members are composed of low strength materials which are unlikely to generate significant seismic events. Therefore, it is almost certain that mining-induced seismicity is restricted to the Burr and Neely Members.

The above description of Dawson Bay Formation is based on Kroll (1987) where selected core samples from the Central Canada Potash and Lanigan mines, and the Subsurface Geological Laboratory, Regina were examined. The Dawson Bay Formation, however, is not uniform. For example, at K—1 mine, it is found to be fractured and "rotten" (Stimpson, personal communication).

2.4 GEOLOGICAL ANOMALIES

A sequence of ore which has been locally disturbed and is devoid of potash is frequently referred in the literature by the term "salt horse". The salt horses are of three distinct categories: (a) channels, (b) leached zones, and (c) collapse features.

U-shaped or irregular, channel-like features have been observed in the Saskatchewan mines. Some of them are filled with Dawson Bay type material. Geologists belie-

ve that these channels were created on the surface of the Prairie Evaporite Formation by rivers, prior to the deposition of Red Bed sediments.

In a leached zone sylvite is absent or partially removed. The leached zones are believed to have been created in depressions on a surface of regular sedimentation sequence due to lowering of the local water table, or due to the accumulation of water unsaturated in sylvite, but saturated in halite.

Recemented and recrystallized breccias of sylvite, halite, fragmented clay, and Dawson Bay sediments from above are known as collapse structures. Presence of Dawson Bay material in these features indicate that post-Prairie Evaporite solution events caused the upper strata to collapse into the ore zone.

2.5 VIRGIN STRESS

Theoretically, at a subsurface point, vertical total normal stress,

$$\sigma_z = \gamma z$$

where γ is the unit weight of the rock mass and z is the depth below the ground surface. Assuming a plane strain condition and linear elastic behaviour of the rock mass, the horizontal principal stress σ_x, is

$$\sigma_x = \{\nu/(1-\nu)\}\sigma_z$$

where, ν is the Poisson's ratio of the rock mass.

In reality, the state of stress in a rock mass can vary spatially due to both the presence of geologic structural features, such as folding, faults and variation in material properties, as well as the tectonic history of the region. For instance, in Canada's Pre-Cambrian Shield, at a depth of several hundred meters the horizontal principal stresses are 2-3 times larger than the vertical

principal stress.

Saskatchewan potash mining areas, however, are relatively free from significant geologic structural features,as well as any tectonic activity, both presently and in the past. It, therefore, seems likely that the theoretically computed stresses are close to the ones that actually exist in the Dawson Bay Formation. Owing to the time-dependent mechanical properties of evaporites, it is likely that virgin stresses in the potash ore zone are hydrostatic. However, in order to obtain more reliable estimates of the state of virgin in situ stress, it is essential to conduct field measurements.

2.6 MATERIAL PROPERTIES

Rock masses are complex materials, and are generally heterogeneous and anisotropic. Depending on rock type, stress and temperature, their behaviour can range from brittle on one hand to ductile on the other.

Standard laboratory testing, performed by several researchers (e.g., Kroll, 1987) on samples from various strata from the Saskatchewan potash mining region, show wide variations in material properties. These wide variations caused by inherent heterogeneities in the rock mass (which necessitate a large number of samples to provide a representative mean value), the biases in the data base (e.g., a weak core may not survive preparation procedures), and, above all, the limited access to the non-evaporite strata, make the evaluation of material properties difficult. These problems are particularly acute in the case of the Dawson Bay Formation as there are no accessible excavations in that Formation. Further, core drilling upwards into the Dawson Bay Formation from mine openings has frequently been prevented because of the concern about mine flooding. Under these circumstances, a composite of laboratory data where

available and assumed values based on the experience and judgement is the best that can be achieved. One such tabulation (Table 2.1) has been given by Sepehr(1988).

Formation Category	Young's Modulus (E) (MPa)	Poisson's Ratio	Density (MKg/m³)	Cohesion & Residual (MPa)	Friction Angle & Residual (Deg.)	Tensile Strength T_o (MPa)	Uniaxial Yield B_y (MPa)	Hardening Parameter H'	Uniaxial Peak B_p (MPa)	Softening Parameter S'	Creep Parameters A (MPa^{-m} S^{-n})	m	n
Limestone Statistical Average (test data)	35,000	0.25	0.28×10^{-2}	23 & 10	46 & 46	10	98	46667	104	-26000	N.R	N.R.	N.R.
Bedding Plane Best Judgement	10,000	0.3	0.2×10^{-2}	10&0.01	32 & 27	0.1	N.R.*	N.R.	N.R.	N.R.	N.R.	N.R.	N.R.
Second Red Bed Best Judgement	10,000	0.3	0.2×10^{-2}	0.1&0.01	38 & 30	0.5	0.5	600	0.5	-100	N.R.	N.R.	N.R.
Joints Best Judgement	650	0.4	0.0	0.1&0.01	40 & 28	0.01	N.R.	N.R.	N.R.	N.R.	N.R.	N.R.	N.R.
Potash Statistical Average (test data)	3,500	0.3	0.2×10^{-2}	N.R.	N.R.	N.R.	N.R.	N.R.	N.R.	N.R.	3.78×10^{-8}	2.64	0.38

*N.R. - NOT REQUIRED

Table 2.1 Material properties for various strata from the Saskatchewan potash mines (after Sepehr, 1988).

CHAPTER 3

MINING METHODS

3.1 INTRODUCTION

In this chapter, only a brief account of the development of the mining methods in Saskatchewan will be presented. A detailed treatment can be found in Molavi (1987). All potash mines in Saskatchewan, with the exception of Rocanville, which is one of the latest to go into production, started their underground workings with a conventional room and pillar method. This method was adopted from New Mexico and West German potash mines, in which the pillars had either square or rectangular configuration.

However, very early in mining, safety and problems of low productivity led the potash producers of Saskatchewan to seek alternative methods. They found that the old system was not applicable to their particular setting. The principal reasons for the eventual abandonment of this system were the greater mining depths, thin saltback, and the presence of clay seams within and above the ore body.

3.2 MINING METHODS

Theoretical principles of mine design based on laboratory testing of elastic material, including photo-elastic experiments, postulate vertical stress peaks near the walls and

horizontal stress peaks near the roof and the floor of underground opening. Connecting these peaks tangentially results in a "stress envelope" around the mine opening (Baar, 1971). According to Serata (1968), creep would be restricted to the interior of such theoretical stress envelopes. Outside, the rock would remain elastic and would provide for stable conditions. This concept, known as stress relief theory, states that wider rooms generate a larger stress envelope around the opening, consequently creating a greater stress relieved zone in the roof and the floor of the opening. This situation pertains if the ground is competent and there are no planes of weakness above and below. Originally, this concept was applied in the Saskatchewan potash mines. Fig. 3.1 shows that an increased in room size would create a larger stress envelope and hence a larger relaxed zone in the vicinity of the opening, yielding improved conditions in the roof and floor.

One step beyond this is the time-control technique which, as the name signifies, requires sequential excavation of parallel openings. This technique utilizes small yielding pillars to improve strata control. These pillars in the mined panels are meant to yield and over a period of time, transfer their load to the adjacent stiffer, or abutment pillars. In one application of this method, two openings are created at some distance apart to form their own stress envelopes with a strain hardened pillar in between. After a certain period of time, a third room is excavated through the strain hardened ground. Once the inner opening has been created the yield pillars fail, forming a larger stress envelope and thus generating a stable central entry (Fig. 3.2). This method is used in sequential cutting of three, four and five entry system. Generally, in successful use of this technique, the outside entries are cut first, yield pillars are left in between, and finally the middle entry, or entries, are excavated (Fig. 3.3). The transfer of load from yield pillars, with crushing and shedding of their load, causes the outside entries, which are no longer in use, to collapse. This technique is not recommended for mines with upper strata containing water.
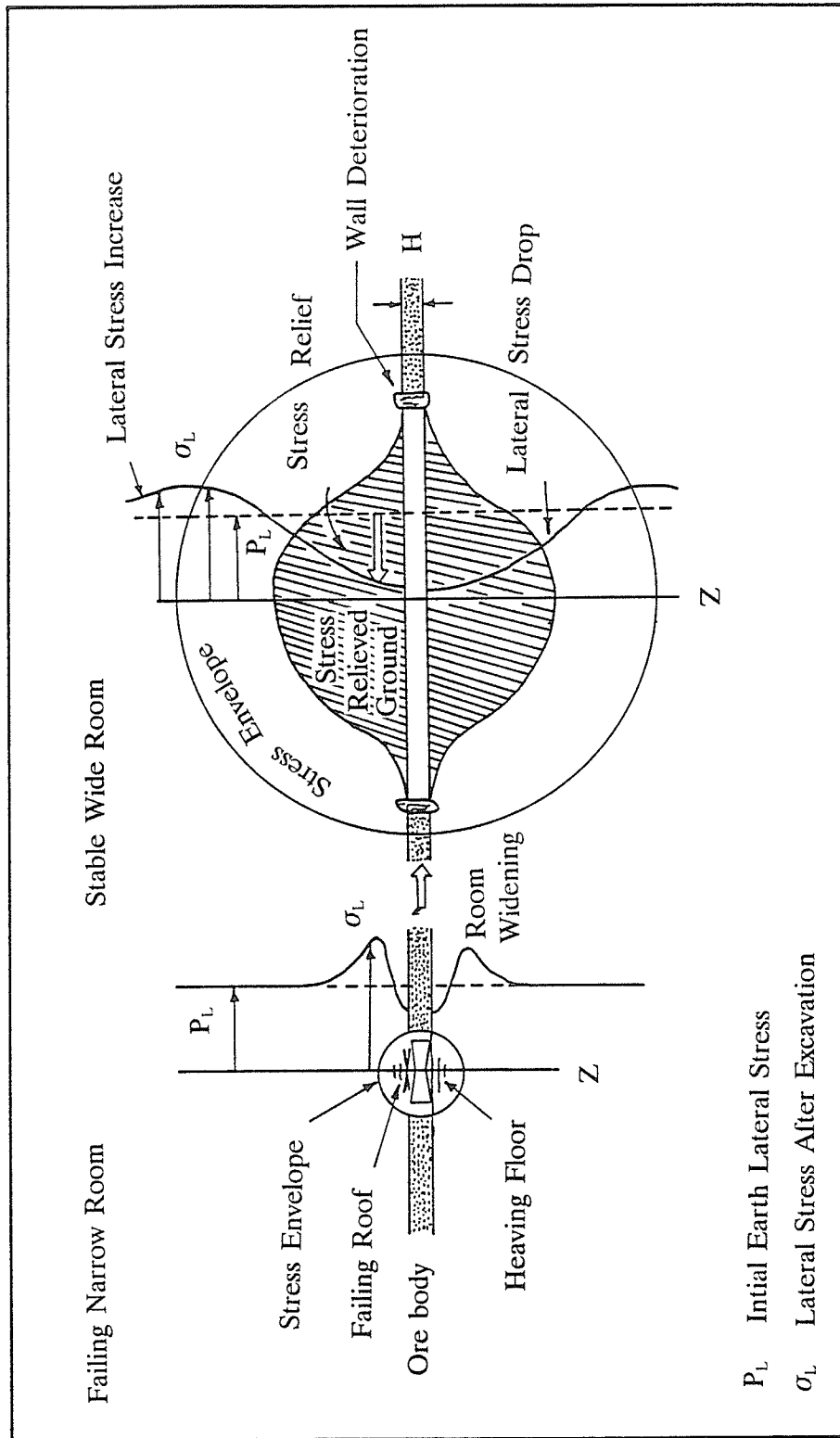
Fig. 3.1 Formation of larger stress envelope helps stabilize failing mine openings (after Serata, 1982).

P_L Intial Earth Lateral Stress

σ_L Lateral Stress After Excavation

19

σ_v : Vertical Stress

σ_L : Lateral Stress

σ_o : Initial Lateral Stress

σ_1 : Lateral Stress After Initial Step

σ_2 : Lateral Stress After Final Step

Stress-Relieved Zone

Failing Yield Pillar

Secondary Stress Envelope
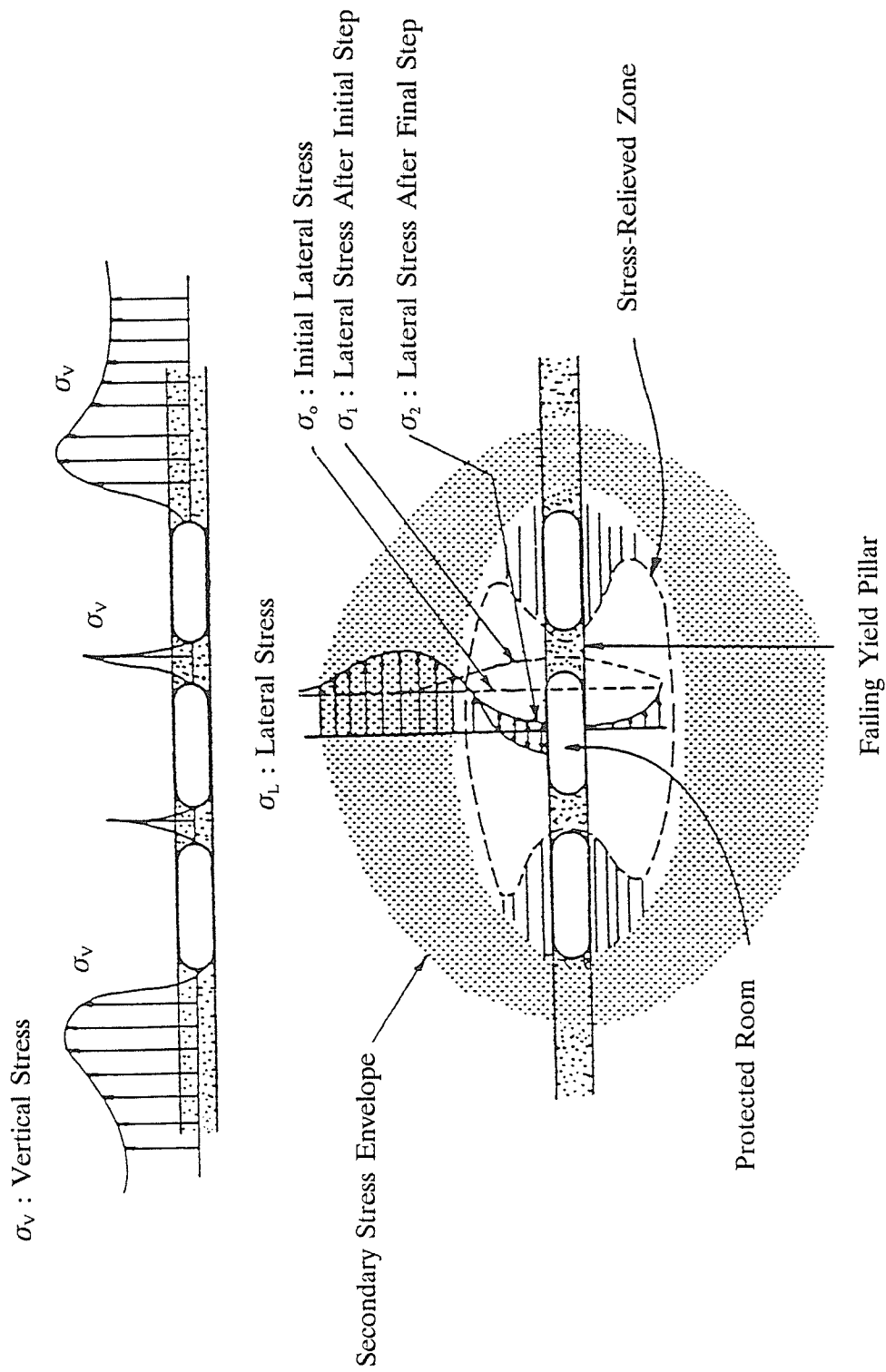
Protected Room

Fig. 3.2 Formation of secondary stress envelope after excavation of the middle protected room (after Serata, 1982).

All room widths = 30' [9.1m]

All yield pillar widths = 20' [6.1m]
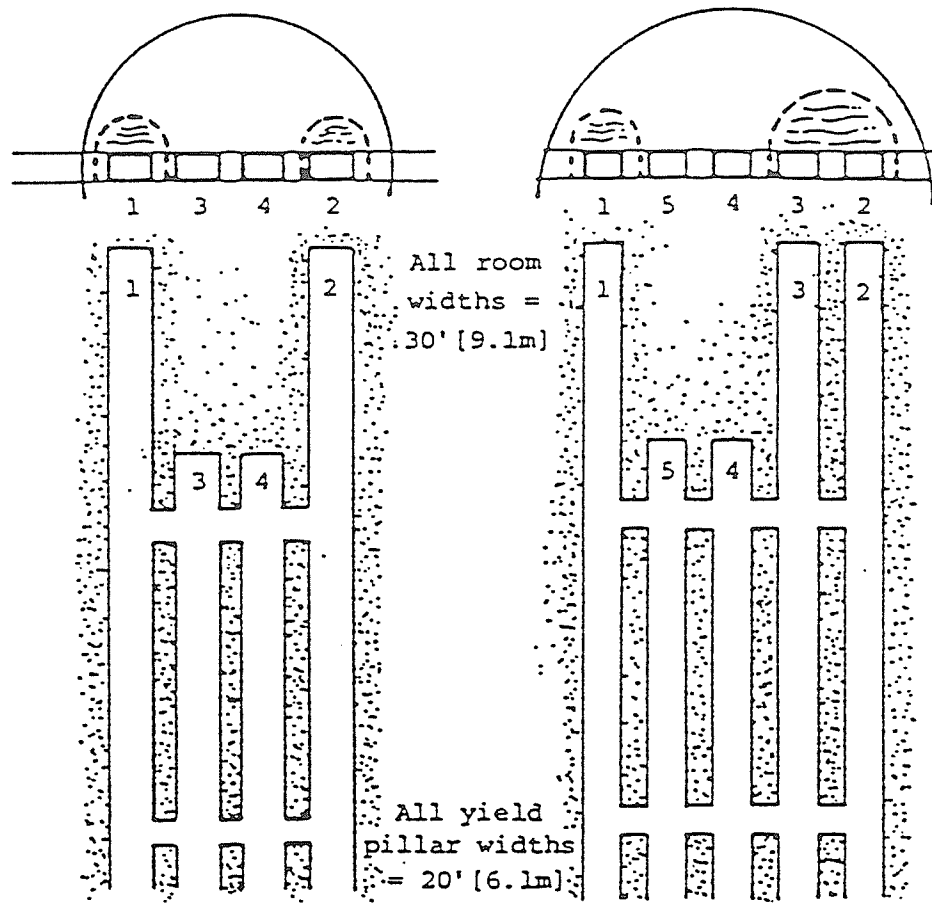
Fig. 3.3   Two protected rooms provided by four and five room entry system, Time-control Technique (after Serata, 1982).

21

Another application of the time-control approach is in bi-level mining for the recovery of two seams, though presently, it is in an experimental stage.

The principal advantages of the time-control technique over the conventional room and pillar method are more stable backs, more time for installation of conveyor belts, shops and alternative means of exit, less floor heave, less cleaning up of loose slabs, unrestricted ventilation passages, and increased mine life. Additionally, increased extraction results from bi-level mining.

Today, out of eight operating mines in Saskatchewan, the conventional room and pillar method is used by none. Three of the five operating Saskatoon mines employ time-control technique using a chevron pattern (Fig.3.4). A fourth Saskatoon mine, Cominco Fertilizers Ltd., uses a variation of the stress relief method —— the parallel room technique (Fig.3.5). This technique requires excavation of several rooms separated by yield pillars. It generates an advancing, increasingly larger stress envelope to provide protection for the latest room being excavated at the expense of the deterioration of the earlier ones. The limiting factor is unfavourable ground in the roof. The remaining mines produce using a long room and pillar method. Though the basic principle of stress-relief is utilized here, the openings are not designed to collapse intentionally as in the case of time-control. This technique is better suited for the case where the Dawson Bay Formation is wet.

The mining methods employed in the Saskatchewan potash mines are the results of years of patient trial-and-error. New methods, e.g., bi-level mining, are being experimented with. This is a continuing process as new methods are being sought to increase extraction and safety.
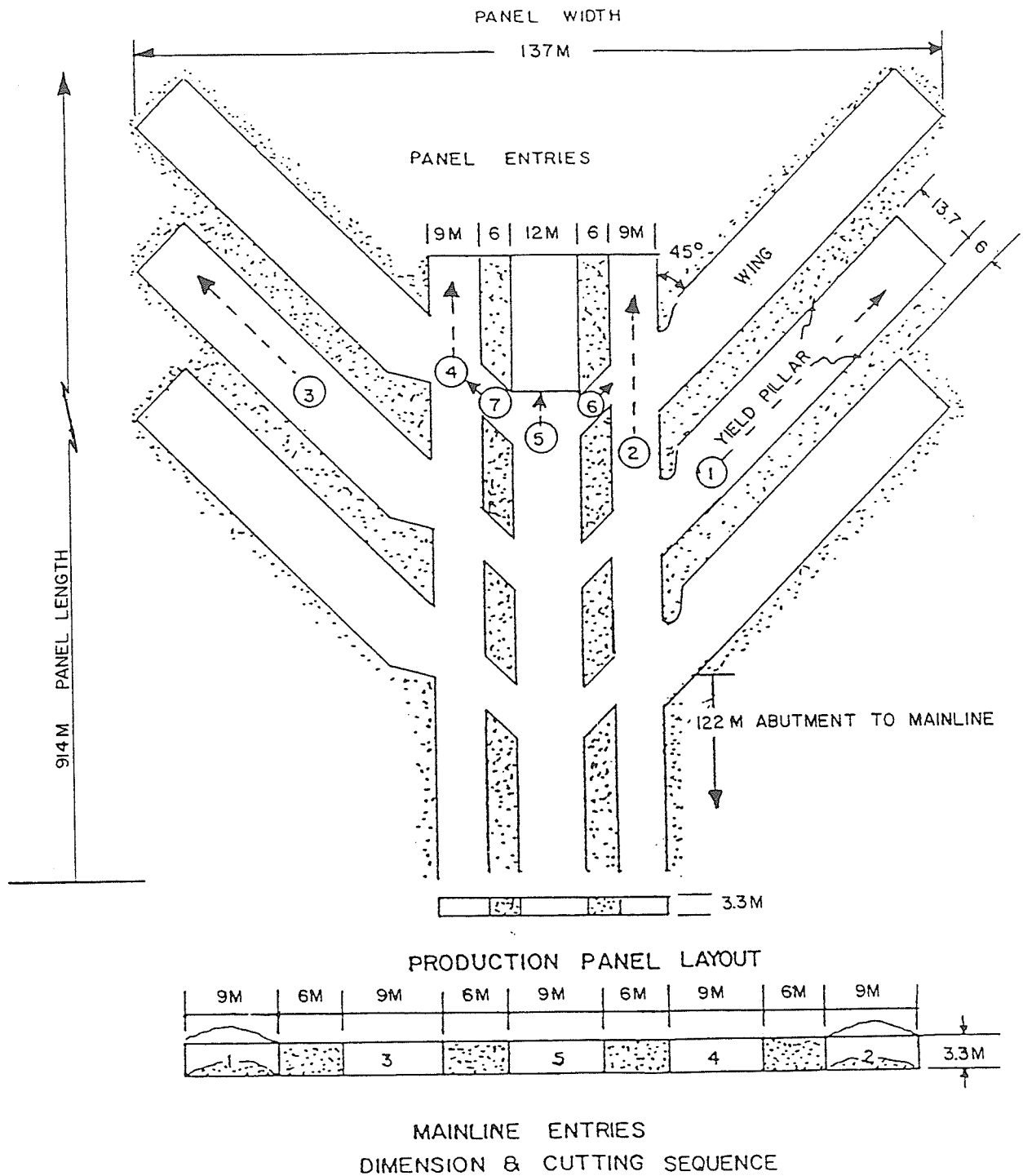
Fig. 3.4 Present chevron pattern at PCS Cory mine (after Molavi, 1987).

Secondary Envelope

Stress Relieved Ground

Initial Stress Envelope   Yield Pillars   Final Protected Room
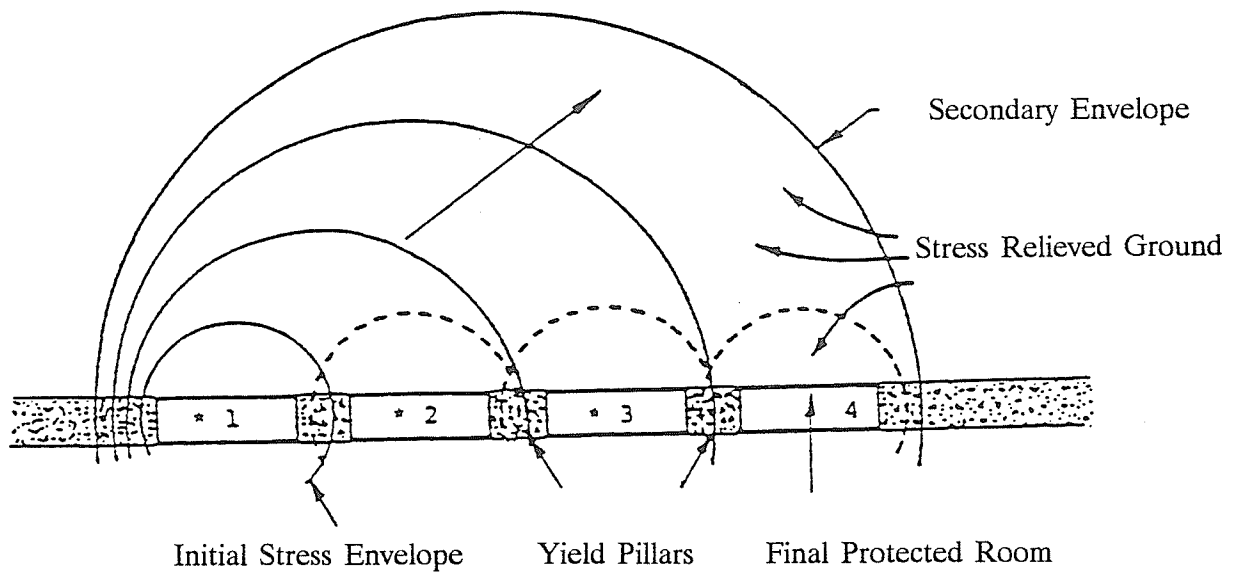
Fig. 3.5 Application of Parallel-Room Technique (after Serata, 1982).

3.3 CONVERGENCE OF OPENINGS

As discussed in the previous section, according to the theoretical principles of mine design, creep would be restricted to the rock inside the stress envelope. Outside the stress envelope the rock would remain in an elastic state. This design method states that the mine opening reaches a stable condition with the total convergence approaching the ultimate value beyond which no further closure is possible (Serata, 1968).

Strain-hardening of salt and potash observed in laboratory tests, which lead to the assertion of a stable condition with maximum possible closure, has not been validated by in situ data. Salt and potash are not affected by strain-hardening, as was demonstrated by in situ tests using a sealed borehole section to create differential stress (Baar, 1971). Also, strain-hardening of the sample in the laboratory due to rapid loading makes the determination of the limits of elastic behaviour of salt and potash very difficult. According to Baar (1971), the true elastic limits of virgin salt and potash is less than 1 MPa, which is one order less than the reported laboratory value.

The virgin stress field in the potash mining areas is assumed to be hydrostatic, the stresses being determined by the dead weight of the overburden. As a mine opening is created, the original stresses perpendicular to the opening surfaces are lowered to atmospheric pressure. The salt and potash, as a result, begin to creep into the opening, tending to re-establish a local hydrostatic stress condition.

In a mine, at the surface of a new excavation, where stresses are removed in one direction, stress relief creep starts. As a result, the stresses in the two other mutually perpendicular directions are lowered, and consequently a partial stress relieved zone in the next layer of rock behind the surface is created. This establishes a chain-reaction affecting rocks at greater distances by stress relief creep into the opening.

In theory, it is possible to support the total overburden by stable pillars, which have been designed so that no horizontal creep occurs in the centre of pillars. Although, vertical creep above and below the opening allows horizontal creep in corresponding areas above and below the pillars, it has no direct influence on overburden support.

However, the large extent of creep zones in actual pillars makes the design of stable pillars elusive unless the extraction ratios were reduced far below the economic limit (Baar,1971). A uniform stress gradient characterizes the horizontal dimension of the creep zone. Near-hydrostatic local stresses increase from near zero at the walls to high values outside the creep zone at the centre of the pillar where the vertical stress depends on local overburden loads. In practice, creep zones overlap in pillars rendering the horizontal creep a function of the load on the pillars. The resulting constant pillar loads lead to constant creep rates. This would cause constant vertical closure rate as observed in the IMC mines (Figs. 3.6 and 3.7). An important rock mechanics consequence of this phenomenon is the deflection of the brittle dolomites and limestones of the Dawson Bay Formation just above the salt and potash in the form of continuously increasing subsidence.
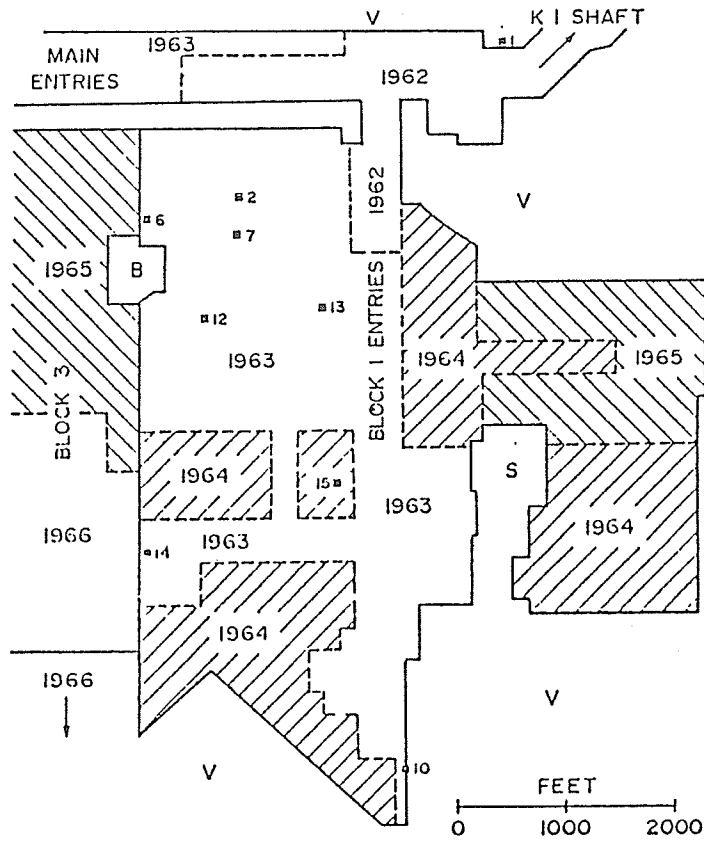
Fig. 3.6 Mining sequence and location of closure measuring sites in blocks 1 and 3, K–1 mine, IMC. Numbers of measuring site correspond to creep curves in Fig. 3.7. V = virgin stress, S = salt horses, and B = bore hole pillar (after Baar, 1971).
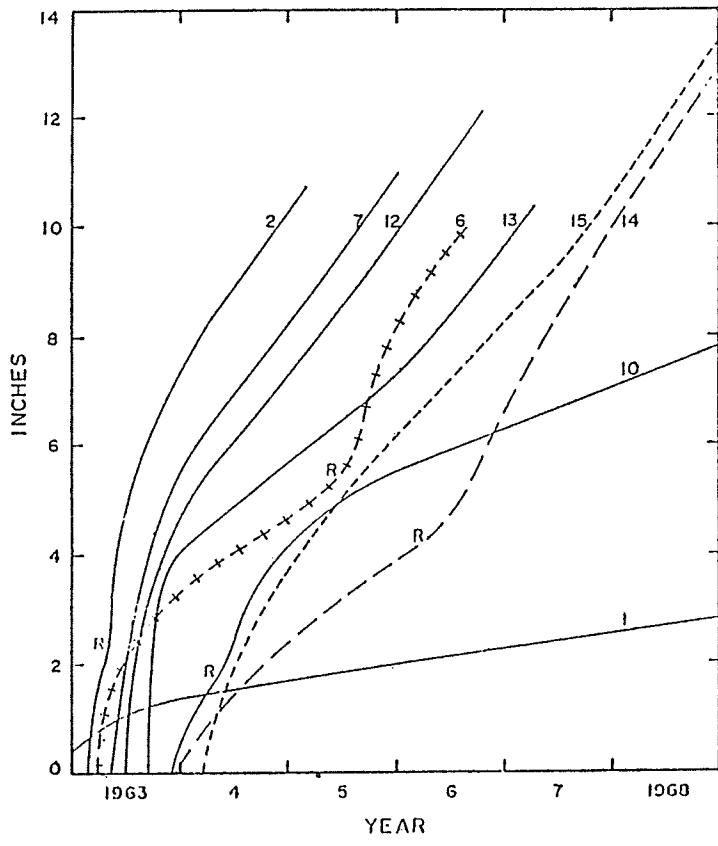
Fig. 3.7 Vertical closure of rooms in relation to the development of the mined-our area
shown in Fig. 3.6. Creep curves identified with the same numbers for the
respective locations shown in Fig. 3.6. R = rilief creep terminated at the
respective mine. Begin of pillar re-loading indicated by increasing creep rates
(after Baar, 1971).

CHAPTER 4

MINING-INDUCED SEISMICITY

4.1 HISTORY OF MINING-INDUCED SEISMICITY

Southern Saskatchewan is a region of low level natural seismicity. Since 1968, a number of earthquakes have been located instrumentally, with the largest event having magnitude 3.7 on the Richter Scale. On the record, however, the largest known event, a magnitude 5.5 on the Richter Scale, was felt in this region. This event was not located instrumentally; its epicentre, shown on Fig. 4.1, represents the approximate location.

These natural earthquakes have been distributed in two zones. One is part of a larger zone extending into northeast Montana (Fig. 4.1), while the other is approximately along the northern limit of the Prairie Evaporite Formation, north and east of the Saskatchewan-Esterhazy region (Figs. 2.2 and 4.1). Both those zones are outside the potash mining districts.

Since 1976, earthquakes have also been detected in the potash mining districts of Saskatchewan. Twenty three events of magnitude greater than 2.3 have been identified over or very close to mined areas. Geophysical investigations by mining companies and university researchers (e.g. Horner, 1983; Gendzwill, 1983) have established beyond reasonable doubt that these events are (a) mining-induced, and (b) are associated with a 30 - 40 m thick sequence of limestones and dolomites approximately 30 m above the potash workings, which forms the intermediate roof of the mine excavations (Fig. 2.1).

Five of the nine conventional mines (eight operating and one abandoned) in the
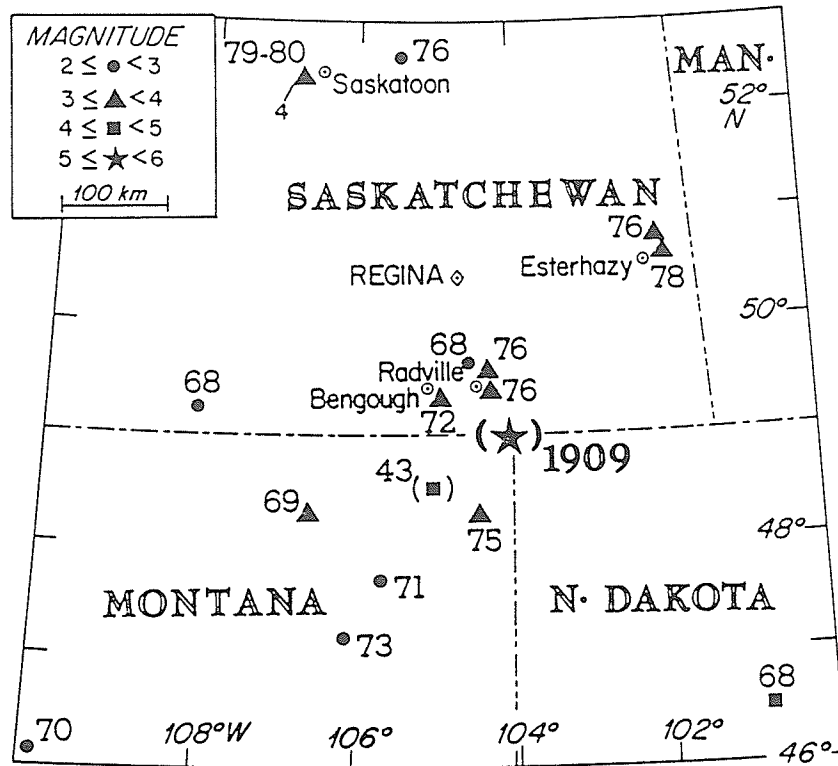
Fig. 4.1 Known seismicity in southern Saskatchewan and adjacent areas in the north-central United States. The largest of the four events near Saskatoon is plotted. The year of occurrence for each event is also indicated (after Gendzwill et al., 1982).

province have generated seismic events large enough to have been felt on surface. These include the PCS Cory mine 10 km west of Saskatoon, PCA's mine (flooded in 1986 and subsequently abandoned), 15 km east of Saskatoon, the CCP mine at Colonsay, 60 km east of Saskatoon, and the K-1 and K-2 mines of IMC, Esterhazy about 400 km southeast of Saskatoon. The largest earthquake recorded to date was of magnitude 3.6 on the Richter Scale at the K-2 mine in 1984. Isoseismal maps of four PCS, Cory mine events are shown in Fig. 4.2. These maps clearly show that the intensity of major events increases towards the mined out panels. The more numerous microseismic events (magnitude < 0 on the Richter Scale) are also found to cluster over the panels that are being actively mined (Fig. 4.3). Focal mechanism diagrams of the February 29 and March 18, 1980 events (Fig. 4.4) suggest a dip-slip motion downward towards the side of the opening at source.

For all these events there has been are no noticeable immediate damage in the mines. Although, some of the events generated noise, movements of air and some falls of loose rocks in the mine, no lasting damage was observed. There have been no reports of rockbursting. In two of the mines water inflows have taken place some time after a significant event, but a causal connection has not yet been found.

Two conceptual models for the failure mechanism generating the seismicity have been proposed to date —— vertical shearing and bedding plane slip —— primarily based on interpretation of seismological data, but corroborative evidence of either mechanism is lacking. In the first model, Gendzwill et al. (1982) assumed the roof of the mine opening behaved as a built-in beam. Accordingly, they pointed out that maximum bending moment and shear stress developed near the extremities. Finally, they proposed that these would lead to vertical shearing as shown in Fig. 4.5.

The recorded spectra of the seismic events have lower frequencies than those reported for rockbursts elsewhere. It has been suggested that the lower frequencies are due to

31
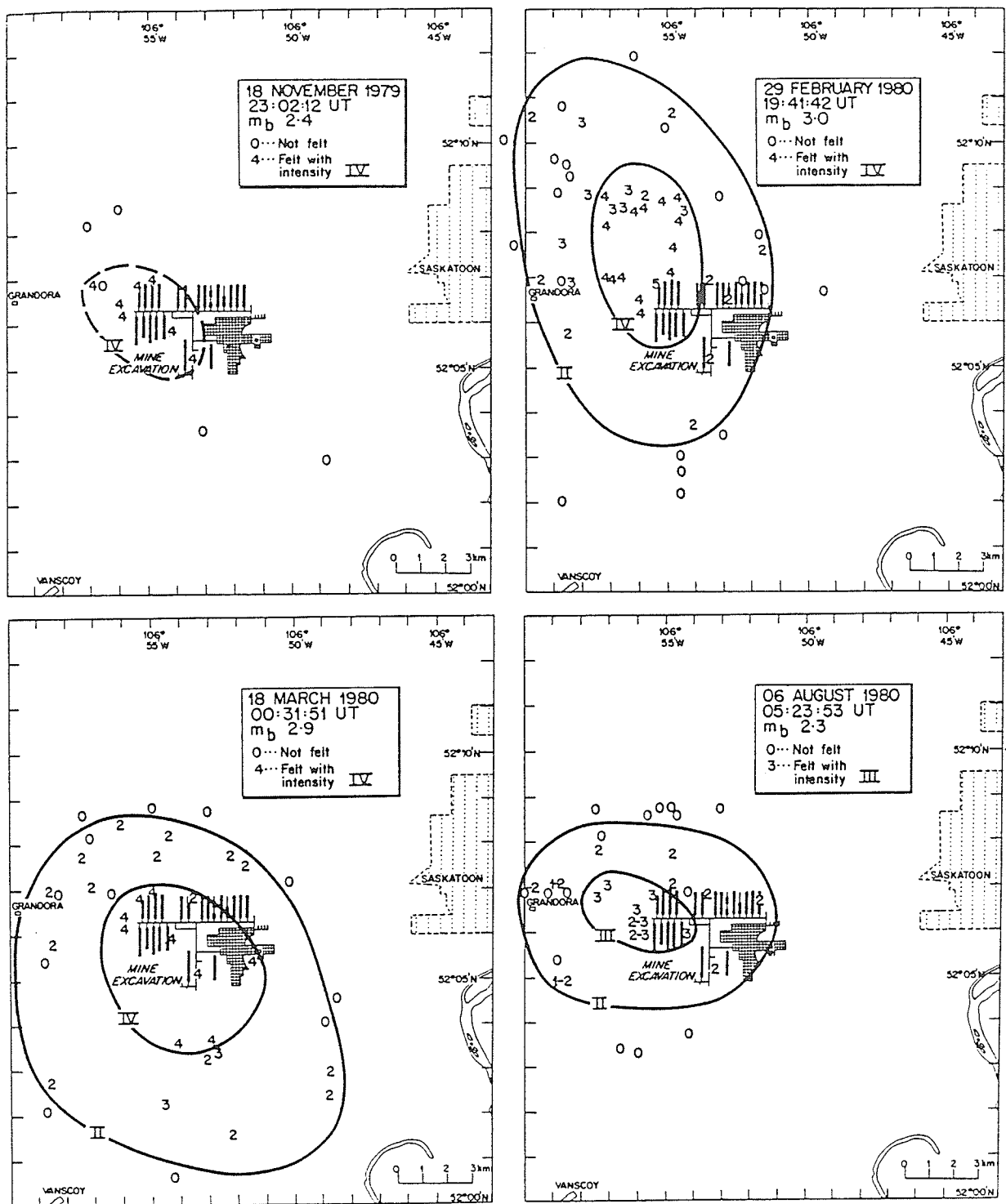
Fig. 4.2 Isoseismal Maps of Earthquakes at Cory Mine (after Gendzwill et al., 1982).
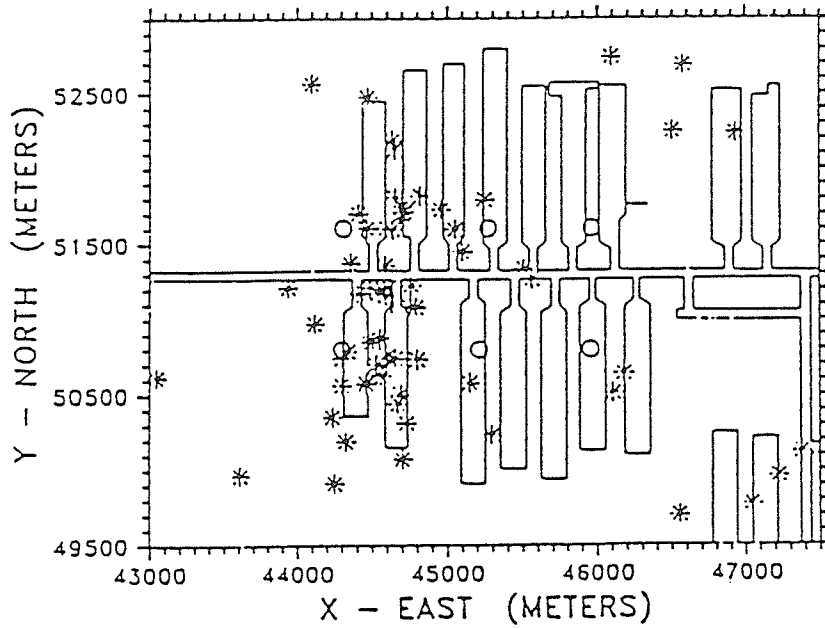
Fig. 4.3 Microearthquake locations at Cory Mine (after Gendzwill et al., 1982).
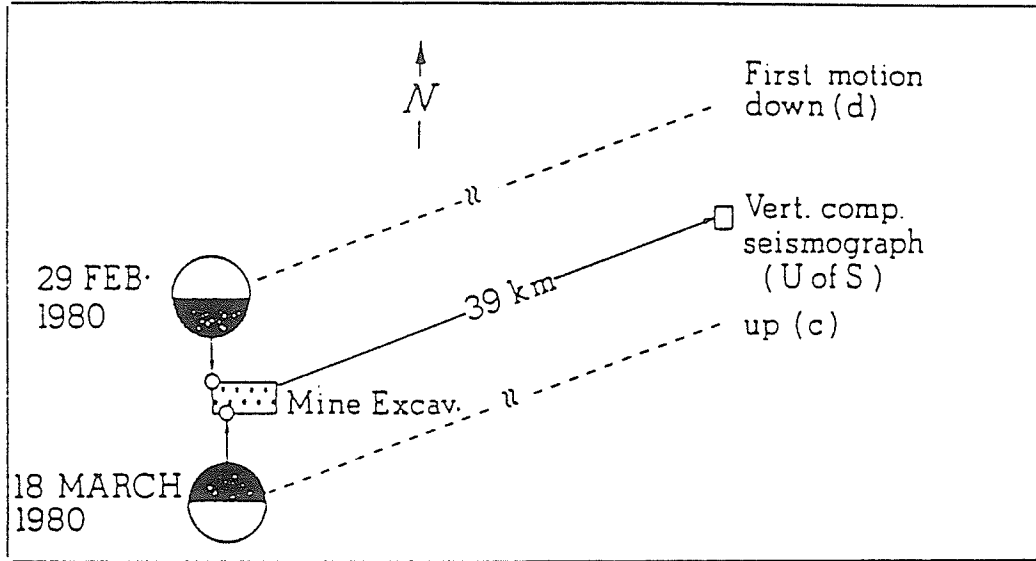
Fig. 4.4 Schematic diagram showing relative locations of mines excavation and the University of Saskatchewan seismograph. Epecentres of 29 February and 18 March earthquakes are represented by small open circles. Associated equal-area lower hemisphere projections of assumed normal fault focal mechanisms are shown by large circles. Shaded area correspond to relative downward motion at source; c stands for compression, d for dilation (after Gendzwill et al., 1982).
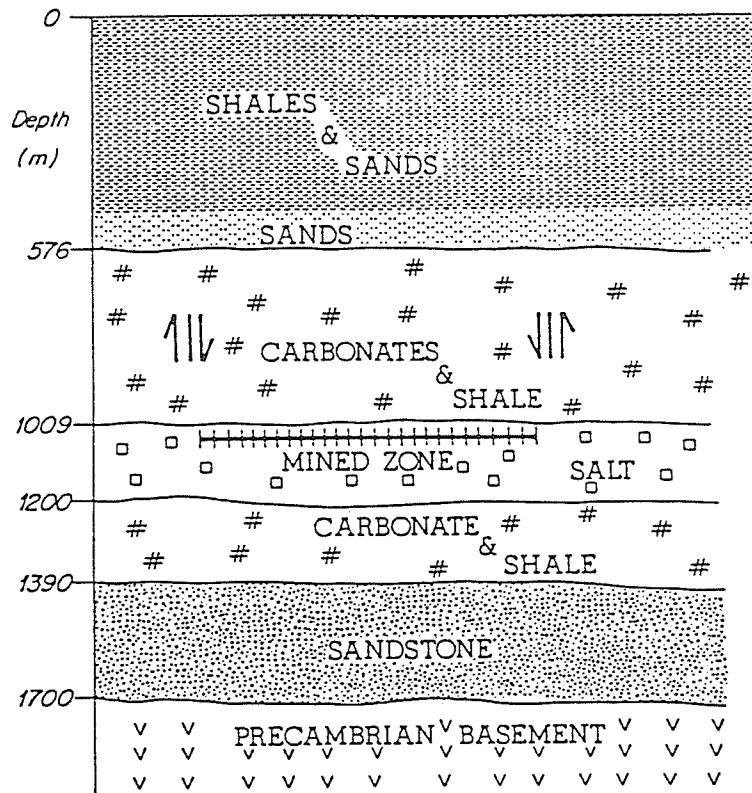
Fig. 4.5 Generalized geologic section in the Cory mine area showing the position of the mine opening and normal dip-slip faulting aroung the periphery of the excavation in areas of high shear stress (after Gendzwill et al., 1982).

either band limiting by the recording system or to absorption by the rock, or both. Gendzwill and Prugger (1987), however, emphasized the fact that the frequency data used for comparison were from "hard" rock mines. They assumed that the failure mechanism in Saskatchewan potash mines is different from rockbursts in "hard" rock mines. Consequently, the second mechanism proposed is failure along the bedding surface induced by flexural strain (Fig. 4.6) with "failure" occurring over almost the entire mining panel. It should be noted that the postulated relative motion contradicts that established by Gendzwill et al. (1982) using their focal mechanism diagram.

4.2 THE PHENOMENON OF SEISMICITY

In this Section, the phenomenon of seismicity is briefly discussed and it is shown that the magnitude of strain energy in the rock mass and the rate at which it is released are major factors in determining the occurrence and magnitude of seismic events, whether natural or man-made.

A seismic event is the manifestation of a disturbance of a state of unstable equilibrium. In the case of unstable equilibrium, energy is extracted from a system when it is slightly disturbed, as opposed to the stable equilibrium situation, where energy must be provided to sustain displacement. In Fig. 4.7(a), the hanging slab will eventually come to rest in its original vertical position if it is subjected to tilting. On the other hand, the slab in Fig. 4.7(b) will topple and kinetic energy will be developed if there is the slightest disturbance. In the case of a seismic event the associated seismic energy is extracted from the rock mass. The source of seismic energy is the strain energy stored in the rock mass surrounding the centre of the event.

Ortlepp (1983) used a simple mechanical model to explain seismicity resulting
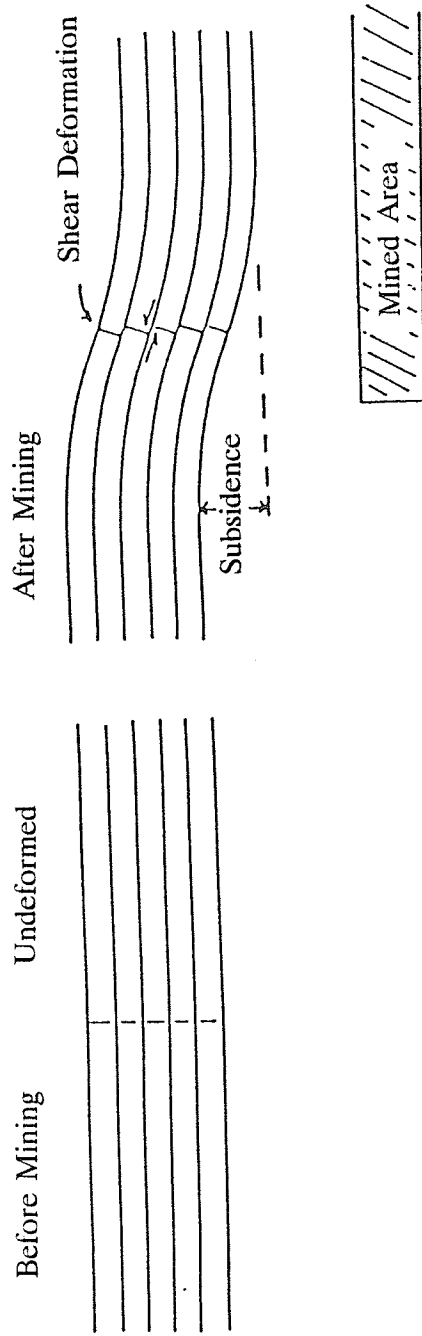
Fig. 4.6 Conceptual model for mechanism of potash mine earthquakes (after Gendzwill and Prugger, 1987).
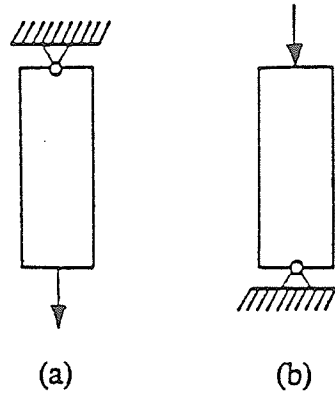
Fig. 4.7 Simple examples of (a) stable and (b) unstable equilibria.
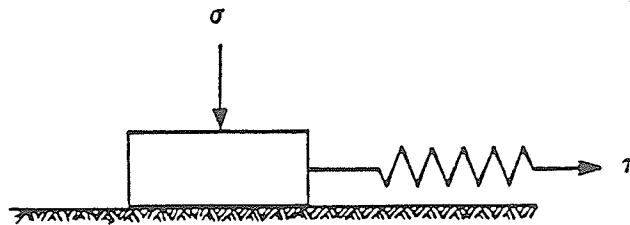
Fig. 4.8 Quasi-static transition from stable equilibrium to unstable acceleration.

from slip along an existing fracture or fault. A block is placed on a rough surface (Fig. 4.8) with a normal force, and a tangential force, applied through an elastic spring. The system maintains stable equilibrium as long as inequality (4.1) is satisfied.

$$F = \tau - \mu_s\sigma < 0 \qquad\qquad (4.1)$$

where μ_s is the static coefficient of friction. As long as the inequality (4.1) holds, τ can be increased gradually without moving the block. However, at the instant of $\tau = \mu_s\sigma$, the system will become unstable. At this point, at the slightest attempt to increase τ further, the block will slip. As soon as the block moves, the smaller, dynamic coefficient of friction, μ_d becomes operative. Consequently, the block will be accelerated by a force of initial value $(\mu_s - \mu_d)\sigma$. The block gathers kinetic energy during this acceleration. Additionally, heat energy, created by movement against the frictional force $\mu_d\sigma$, is dissipated. Here, clearly the strain energy stored in the spring during the gradual increase of τ from zero to $\mu_s\sigma$ is the source of the kinetic and heat energy.

A seismic event initiated by shear failure in the rock mass or slip along a geological weakness is quite analogous to this mechanical model. From this analogy, one can arrive at two important conclusions : (a) if any point in the rock mass is close to unstable equilibrium, an instability, in the form of a seismic event, will be initiated by the slightest change in stress, and (b) the strain energy stored in the rock mass around the region where an event is initiated is the source of the kinetic energy imparted to the rock particles in the course of propagating the seismic event. This strain energy is mostly due to strain induced by mining; a minor part is of geological origin.

4.3 ENERGY CHANGE DUE TO MINING

In this Section, a fundamental principle relating to energy change due to mining, namely the concept of Critical strain energy release rate with respect to span, will be discussed, and its application to the problem of excavating in bedded deposits developed. It is assumed that the Dawson Bay Formation is a homogeneous, isotropic, constant thickness stratum and that an opening is mined beneath it (Fig. 4.9). During excavation, the surface tractions on the beam boundaries change from their initial (upper, P_{ui} and lower, P_{li}) unmined state to the final mined state (upper, P_{uf} and lower, P_{lf}) as the beam deflects (Fig. 4.10). If the opening is created instantaneously the pre-mining surface tractions will drop to zero along the lower surface and the beam will vibrate before coming to rest. During this dynamic phase, stresses in the beam also oscillate and at times exceed the static values. The excess energy, manifested as kinetic energy in the system, is transferred into elastic waves and heat and, if dynamic stresses are sufficiently high, by the creation of new surface area by rock fracturing.

If the surface tractions on the lower surface of the beam are reduced gradually , e.g., support is provided during deflection, then work is done against the support and the amount of energy released is reduced.

As well as energy release there is also energy storage around an opening. For a linear elastic body it can be shown that this stored strain energy is equal to the released energy. The expressions for the energy release and strain energy stored by a beam which is suddenly undermined are derived fully in Appendix — IV. Large excavations are, however, not made i-nstantaneously, so what is of greater interest is the energy release for the next increment in span.

Derivation for energy release rates with respect to span have been derived for circular, spherical and elliptical openings in isotropic, homogeneous rock (Brady and Brown, 1985) but not for a rectangular elastic roof beam. In Appendix — IV the strain energy and

40
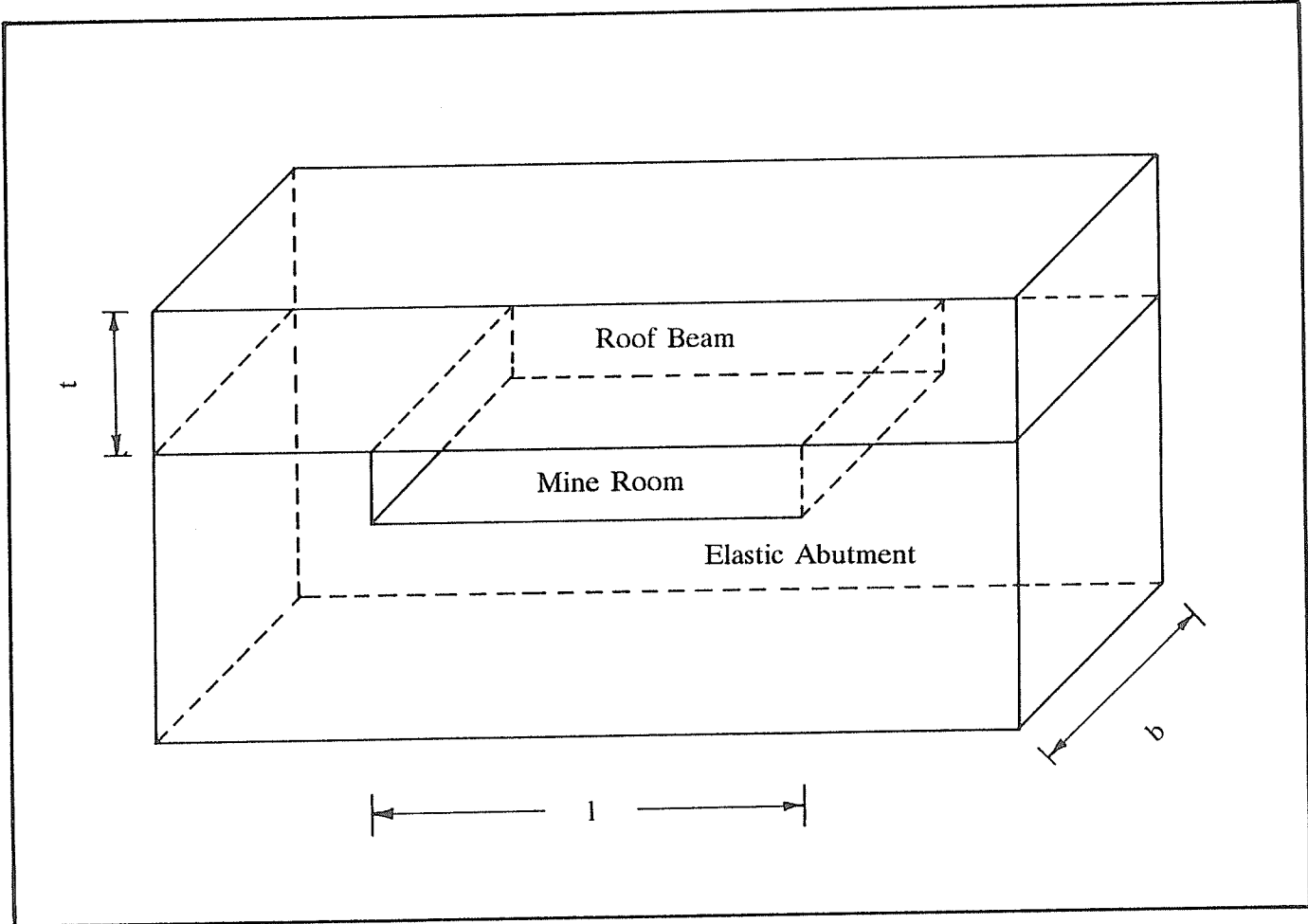
Fig. 4.9 Basic geometry of a mine opening.

$P_{ui} > 0$

Before Mining

dx

x

$P_{li} > 0$

y

$P_{uf} >= 0$

After Mining

dx

x

$P_{lf} = 0$

y
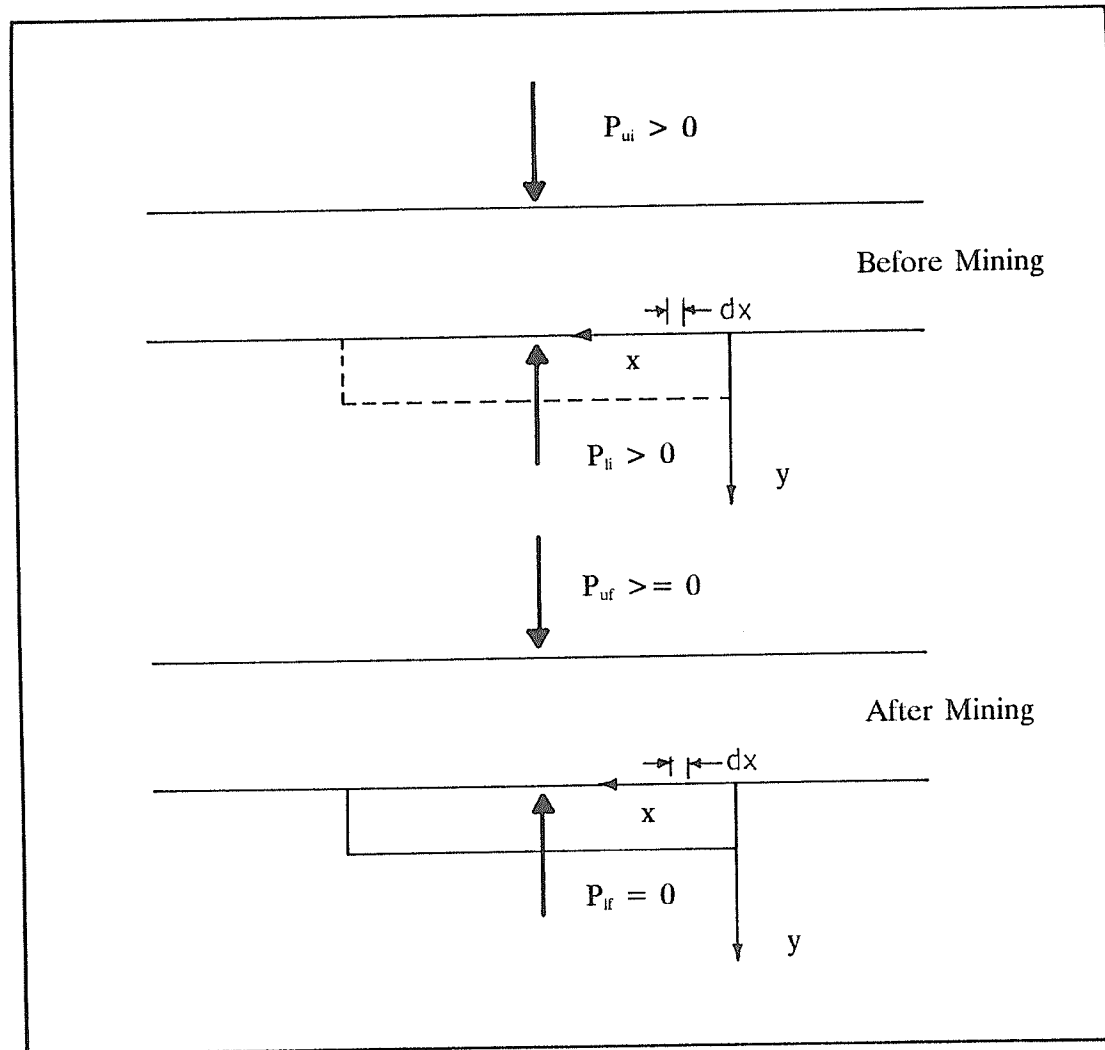
Fig. 4.10 External loading pre- and post-mining.

energy release rates are derived for the case of rectangular elastic slab representing the undermined Dawson Bay Formation.

The concept of energy release rate has been applied as a measure of potentiality of mining-induced seismicity, particularly in South Africa where it is used as a tool in mining layout design for deep level gold mines. Fig. 4.11 illustrates relationship between computed energy release rate and the severity of rock bursts in the form of damaging bursts per 1000 cu.m. of mining advance. This figure represents South African experience from longwall mining in very strong quartzites.

Fig. 4.12 shows plots of energy release rate vs. span for a 50 m long room. The excavation height (3 m) used is typical of Saskatchewan mining practice. The excavation depth used in this analysis was 1000 m, while the unit weight of rock was 0.027 MN/m^3. The elastic moduli and poisson's ratios of the Dawson Bay rock beam and potash abutment were 35 GPa and 0.25, and 2.5 GPa and 0.3 respectively.

As briefly describe in 4.2, rock has a capacity to absorb strain energy up to a certain critical rate, beyond which violent failure is likely. From Fig. 4.12, it can be inferred that violent failure in the Dawson Bay Formation will occur with limited warning because of the very strong sensitivity of energy release rate to increase in mining span.

In order to predict seismicity from the calculated energy release rate, it is necessary to have a knowledge of the corresponding critical value established for a given mining regime, as has been done in for deep level gold mining in South Africa. No work has been c-arried out to determine such limits for the Saskatchewan potash mines. This study represents the first attempt to employ energy concepts to the problem of mining-induced seismicity in Saskatchewan.

However, for interest, one can apply the critical energy release rate for South Africa gold mining to the Saskatchewan situation. One must be careful not to draw too close a
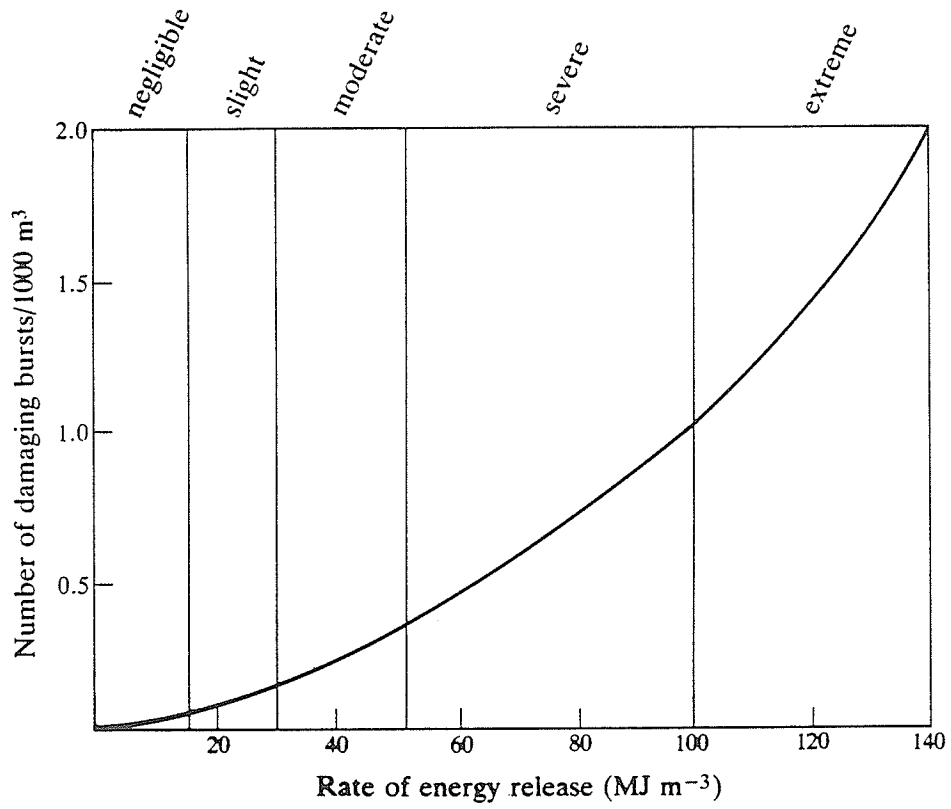
Fig. 4.11 Relationship between the frequency of rockbursts and energy release rate in longwalll mining of gold reefs (after Cook, 1978).
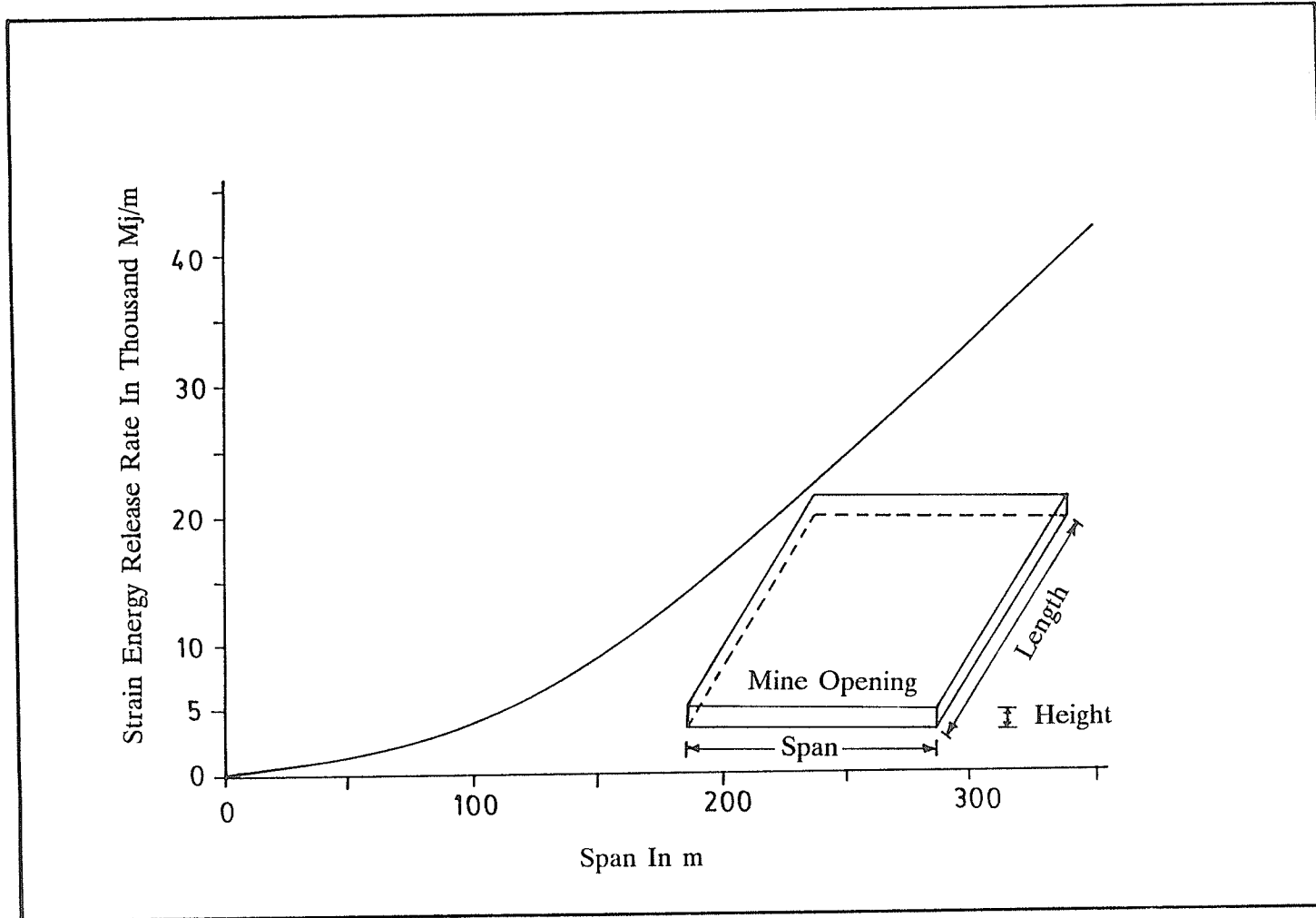
Fig. 4.12 Strain energy storage rate as a function of span for a panel length of 50m.

comparison between these two cases because the ground conditions and mining methods are different, but it is interesting to note a seismic severity of "negligible to slight" corresponding to the energy release rate estimated for the Dawson Bay Formation from the new theory. The actual comparison are below :

From Fig. 4.12, for a single span of 50 m, strain energy release rate per unit span increase for the whole excavation height of 3 m and a excavation length of 50 m E_{50}, is

$$E_{50} = 1450 \text{ MJ/m}$$

Therefore, for the same geometry of the opening, strain energy release rate per unit span per unit length per unit excavation height E_s, is

$$E_s = 10 \text{ MJ/m}^3$$

Putting the above value on the abscissa of Fig. 4.11, one finds the number of damaging burst of $0.1/1000 \text{ m}^3$ or, negligible on the ordinate.

For a typical panel length of 1200 m, span of 50 m and height of 3 m, the volume of excavated rock V, is

$$V = 150000 \text{ m}^3$$

Using this volume the number of rockbursts per panel N, is

$$N = (0.1 * 150000)/1000 = 15$$

This number representing a seismic severity of negligible to slight appears to match that observed in the Saskatchewan potash mining district.

CHAPTER 5

ROCK MECHANICS APPROACH

The subject of rock mechanics, as applied to mining engineering practice, is a study of the performance of rock structures generated by mining activity. Together with soil mechanics, it belongs to a broader discipline called geomechanics. Although both subjects share some basic principles, contrary to a tendency to regard their relationship otherwise, there are key issues which clearly distinguish rock mechanics from soil mechanics. While the failure process in intact rock involves fracture mechanisms such as crack generation and growth in a pseudo-continuum, failure of an element in soil does not affect the mechanical integrity of individual grains. Soils have relatively low elastic moduli, and are subject to relatively low states of stress in their operating engineering environment. The opposite is generally true for rock. The material permeability of soils is relatively high compared with intact rock. In most rock formations, fluid flow occurs through cracks, fissures and channels, whereas in soils, fluid movement involves pore space networks.

Rock mechanics constitutes the conceptual base for the understanding, prediction, and control of rock behaviour during mining activity.

Under the action of mining-induced forces, the adjacent country rock moves towards the mined opening. The surface forces acting through the induced displacements result in an increase of strain energy in the rock mass. The strain energy is stored locally, in zones of increased stress concentration. Rock displacement of engineering consequence may involve such processes as slip, fracture of intact rock, or unstable failure in the system. The last process is expressed physically as a sudden release of stored potential energy in the form of a seismic event.

47

Popular existing models for the rock mechanics analysis of mine excavations include :

(a) Theory of openings in an infinite elastic medium,

(b) Elastic beam theory,

(c) Linear arching theory, and

(d) Numerical solutions.

The theory for an opening in an infinite elastic medium, through analytical or photo-elastic studies, can be useful in identifying those zones around the excavation where the stress concentrations are the highest, as well as assessing the effect of changing opening shape on the distribution of stresses around the excavation. This theory, however, assumes the rock mass to be a homogeneous body, and is hence not very suitable for stratified sedimentary rock masses.

The elastic beam theory is most relevant to the bedded roof problem. With the creation of an underground opening, the roof of the excavation resembles a beam until tensile cracking of the lower fibres at the midspan occurs. This theory is valid up to this point. What transpires after the advent of the midspan crack is beyond description by beam theory. However, for horizontal strata, the development of a flat or linear arch has been postulated by various authors. An idealization of a linear arch is shown in Fig. 5.1, where vertical load is being carried by horizontal thrust developed due to arching action. It has been shown by Sepehr and Stimpson (1988) that a linear arch can also develop even if the rock layer has vertical cross-joints. Linear arching can occur even in a very fractured rock (Sterling, 1977). There exists ample physical evidence of such linear arches in underground excavations as well (e.g. Sterling, 1977). Thus, it appears that the theory of linear arching is the best approach for modelling a bedded excavation roof.

Superimposed Load (If Any)

Central
Compression Zone

Arch Thrust

Lever Arm

Vertical Shear

Horizontal Thrust

Self Weight Of Blocks

Abutment Compression Zone
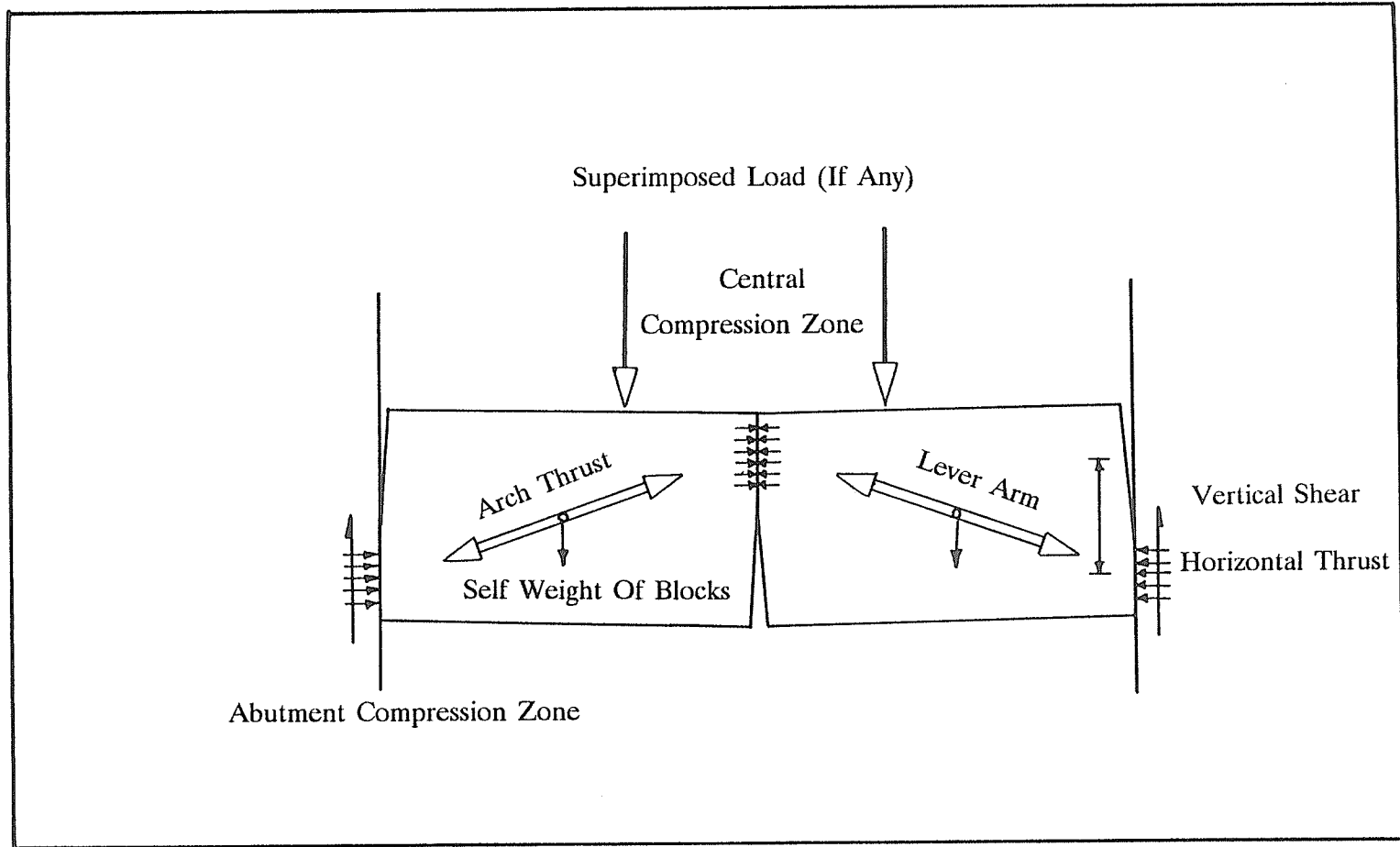
Fig. 5.1 Idealization of linear arch .

Previous research of the linear arch has mostly concentrated on matching the theory to the behaviour of model beams in the linear range below ultimate load. Sterling (1977) was the first to study linear arching action at and beyond ultimate load. However, the purpose of Sterling's work was to formulate a design equation using an ultimate load approach to the strength of the linear arch.

The provision of fairly simple idealized models, such as beam theory and linear arch theory, does not preclude the use of sophisticated numerical techniques for mining excavations. However, the use of numerical models in most rock mechanics problems involving mining is still supplementary to experience. Even if the expertise to carry out the sophisticated rock modelling numerical program is available, the sketchy knowledge-base of the material properties and geometry of the rock mass does not permit one to take full advantage of this powerful analytical tool. The inherent variability of material properties and geometry of the rock mass, in most cases, makes it difficult, and not to mention, expensive, to obtain the detailed data needed as input in the numerical model.

In the present study, the writer considered two possible causal explanations of seismicity in the Dawson Bay Formation. These are: (a) Failure along bedding planes and (b) Ultimate failure of a linear arch. To examine the plausibility and scope of (a), a new analytical rock mechanics model based on elastic beam theory were developed. The other hypothesis involved laboratory experiments, in which the linear arch was modelled by a rock beam loaded to ultimate failure in a specially designed testing frame. Finally, numerical analysis was also employed to corroborate the experimental results.

CHAPTER 6

ANALYTICAL MODEL

6.1 INTRODUCTION

The objective of this part of the research was to develop an analytical model for studying the response of the Dawson Bay Formation to potash mining beneath. This model was employed to examine the potential for failure along bedding planes as a source of seismicity in the Dawson Bay Formation as it deflects in response to potash extraction. Owing to the load transference due to the excavation opening, a non-uniform loading for this problem is assumed. Fig. 6.1 shows a widely accepted conception of distribution of vertical stress around an opening. Here, stress rapidly increases from a very low value at the wall of the opening to a peak at the end of the yield zone flanking the wall, and then reduces gradually towards the overburden stress. Hence, for analytical purposes the Dawson Bay Formation was modelled as a beam resting on a deformable abutment "clamped" by these abutment normal stresses, and an elastic solution was sought.

The theory for an elastic beam resting on elastic supports, based on the differential equation of the elastic line has been derived by Stephansson (1971). Both thin beam (span/thickness ratio > 5) and thick beam (span/thickness ratio between 2 and 5) formulations were presented in that paper. However, as Sheorey (1972) pointed out, a similar thin beam formulation by Alder (1961) and thick beam formulations by Tincelin and Sinou (1960) and Hofer and Menzel (1963) have been attempted .
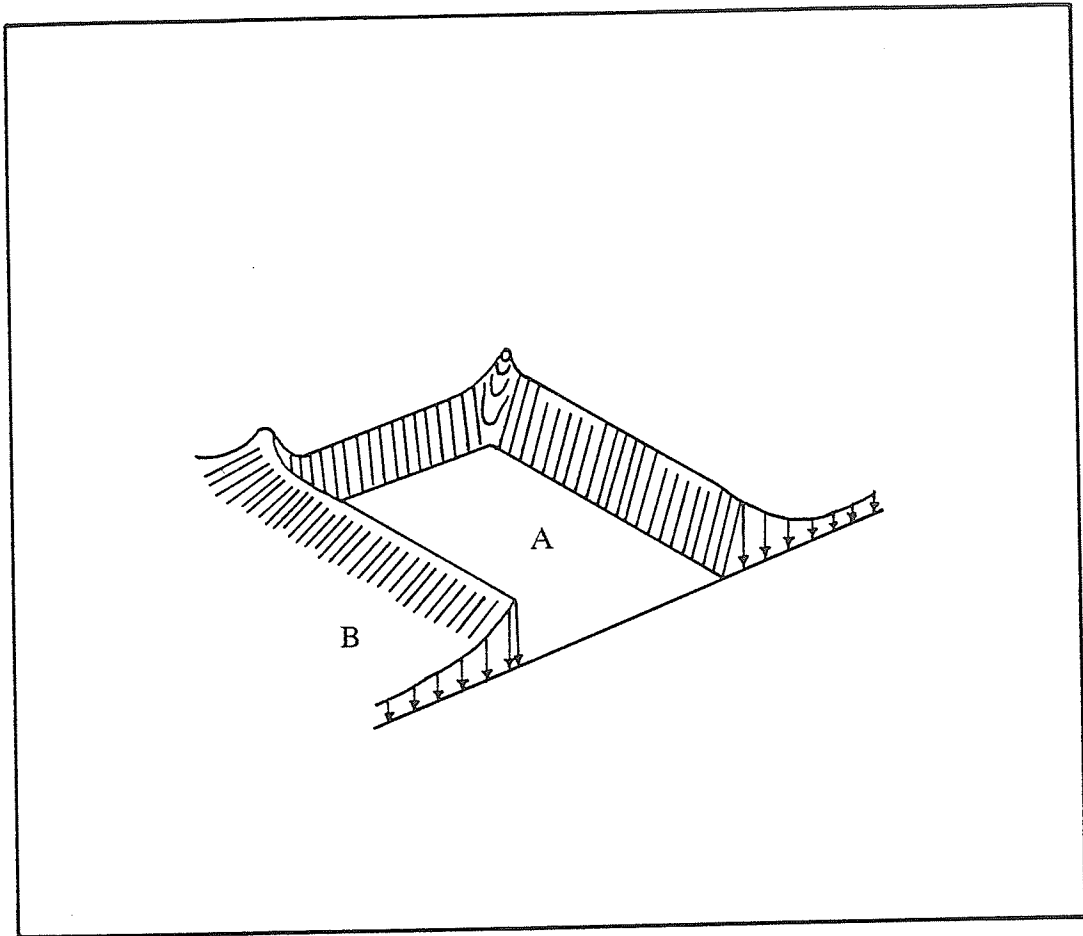
Fig. 6.1 Vertical normal stress redistribution around mining panel (A —— mining panel; B —— flanking abutment stress).

In all these cases, a uniformly distributed load was used. Moreover, there was a crucial error in deriving the above thick beam equation (first recognized by Sheorey, 1972), rendering it incorrect.

In this study, a theory for the elastic beam on elastic supports, based on the differential equation of the elastic line has been derived for a general variable load, and has been adopted as the analytical model for simulating the response of the Dawson Bay Formation to potash mining. Both thin beam and thick beam formulations have been derived. Consideration of two different elastic moduli for the beam has been made. The complete derivation is included in Appendix – I.

6.2 NEW FORMULATION FOR ELASTIC BEAM/SUPPORT PROBLEM

For the model, the horizontally bedded Dawson Bay Formation above the potash mining horizon, deemed the source of mining induced seismicity, is assumed to act as an elastic beam supported on elastic abutments of potash, with frictionless surfaces of contact between the abutments and the bottom layer of the beam (Fig. 6.2). With the creation of a rectangular opening, a new vertical normal stress distribution on the abutment results. For this analytical model, the vertical normal stress distribution has been defined as a general analytical expression that takes into account the load transfer due to the creation of the opening as well as the yielding close to the wall of the opening (Fig. 6.3). Finally, computer programs in BASIC were written to implement this model. A listings of the programs is presented in Appendix – II.
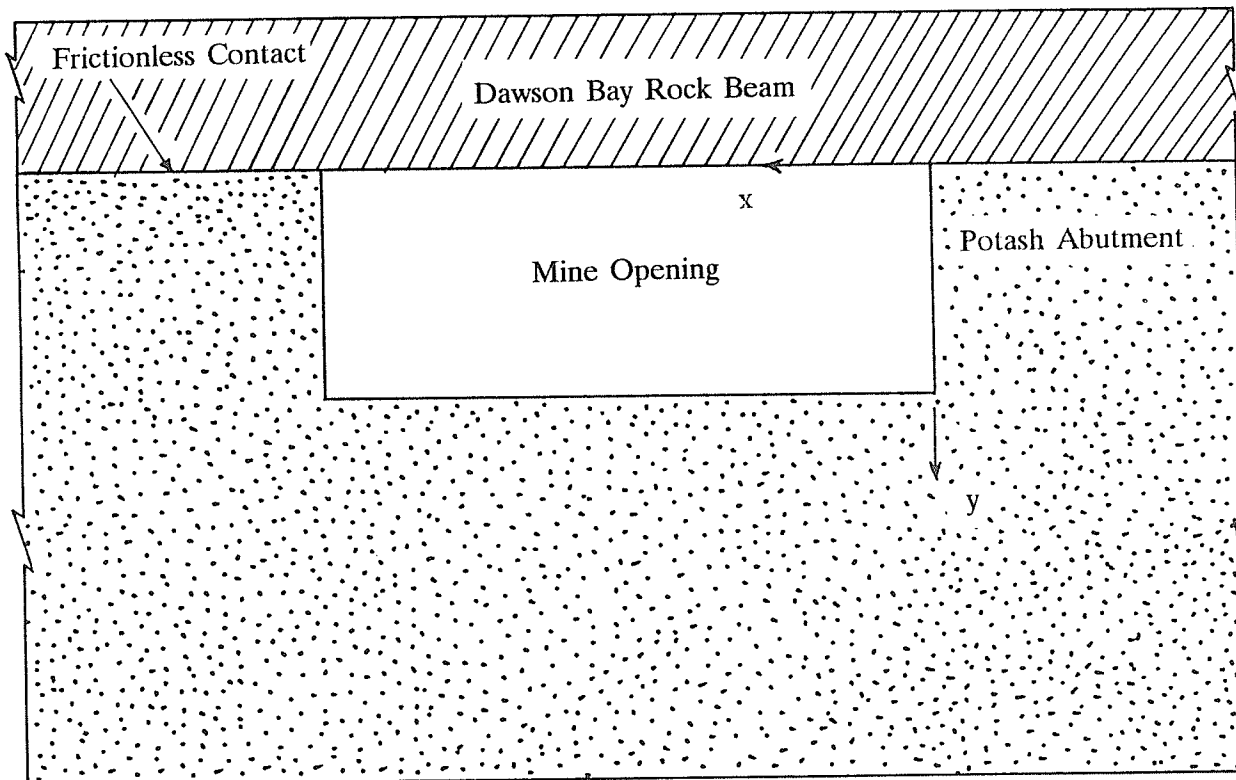
Fig. 6.2 Idealization of potash mine excavation.
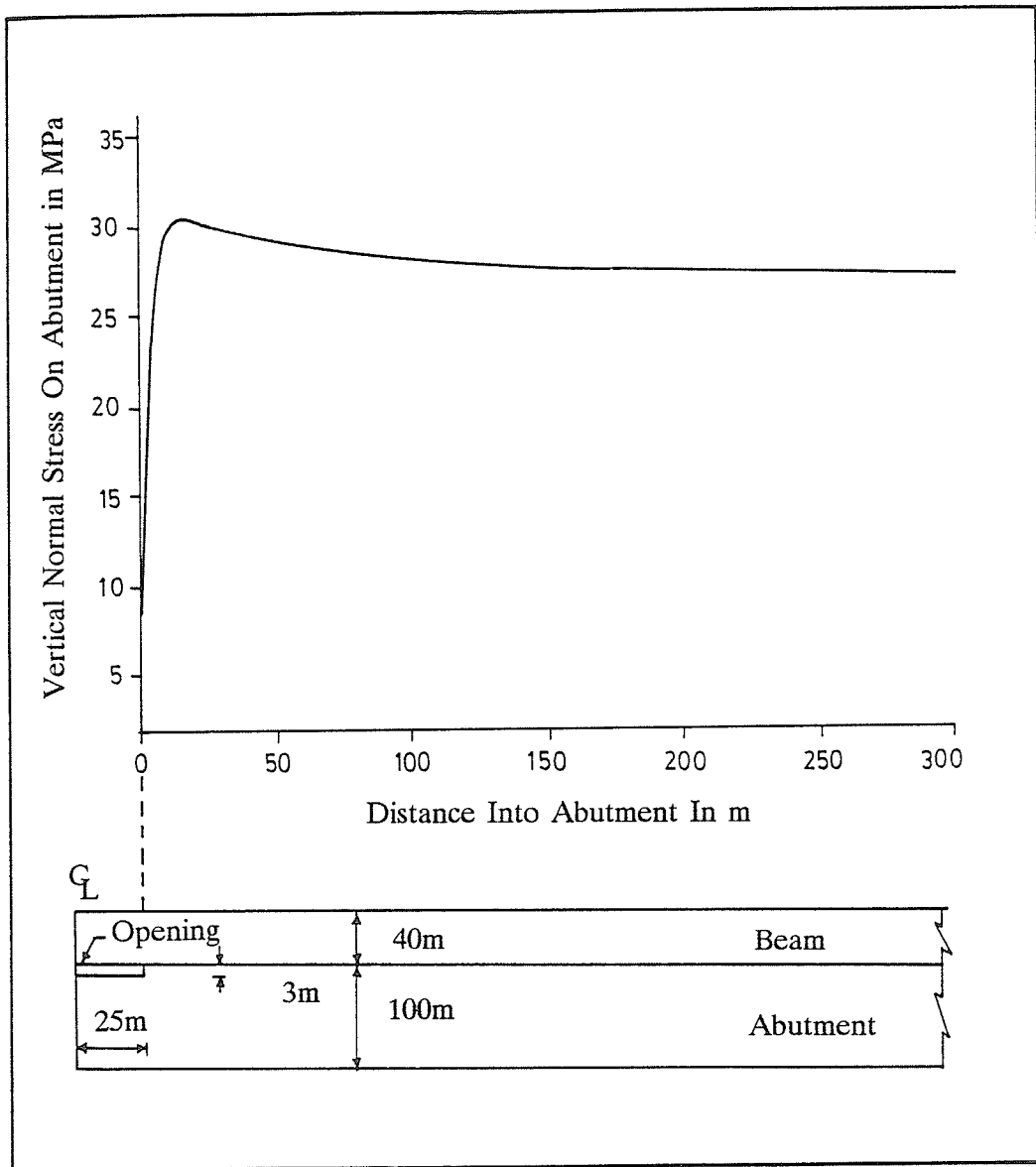
Fig. 6.3 Vertical normal stress on abutment vs. distance into abutment for elastic beam on elastic abutment (not to scale).

6.2.1 CLAMPING LOAD OVER ABUTMENT

In this section, the equation representing the vertical stress distribution over the abutment after mining of a rectangular opening, is derived. The distribution of stress due to an opening may be given by (Fig. 6.4) :

$$Y_c = P + Ce^{\lambda_c x} \qquad (-\infty \leq x \leq 0) \qquad (6.1)$$

where,

P = load on beam over the opening.

C and λ_c are constants.

@ x = 0,

$$Y_c = PY_m \qquad (6.2)$$

where,

Y_m = maximum stress concentration

The expression for Y_m appropriate for the case of potash mines of Saskatchewan, is given in Appendix − III.

From Eqns. (6.1) and (6.2) :

$$PY_m = P + C$$

Therefore,

$$C = P (Y_m - 1) \qquad (6.3)$$

Another fuction (Fig. 6.5), which compensates for the effects of yielding, has been defined by the following equation :

$$Y_s = (S_v - P) - Se^{\lambda_s x} \qquad (-\infty \leq x \leq 0) \qquad (6.4)$$

$$Y_c = P + Ce^{\lambda_c x}$$
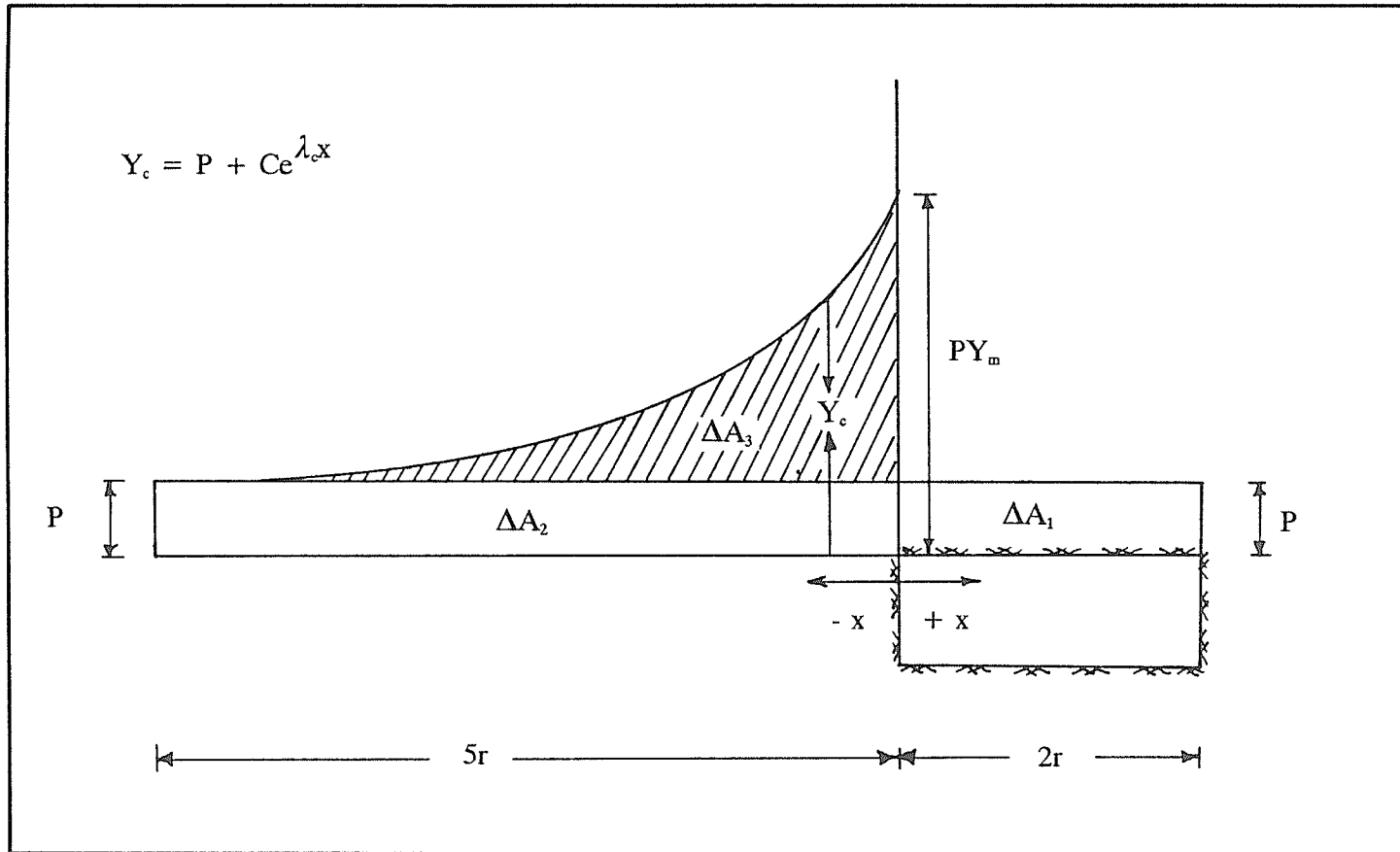
Fig. 6.4   Normal stress over abutment (no yielding).
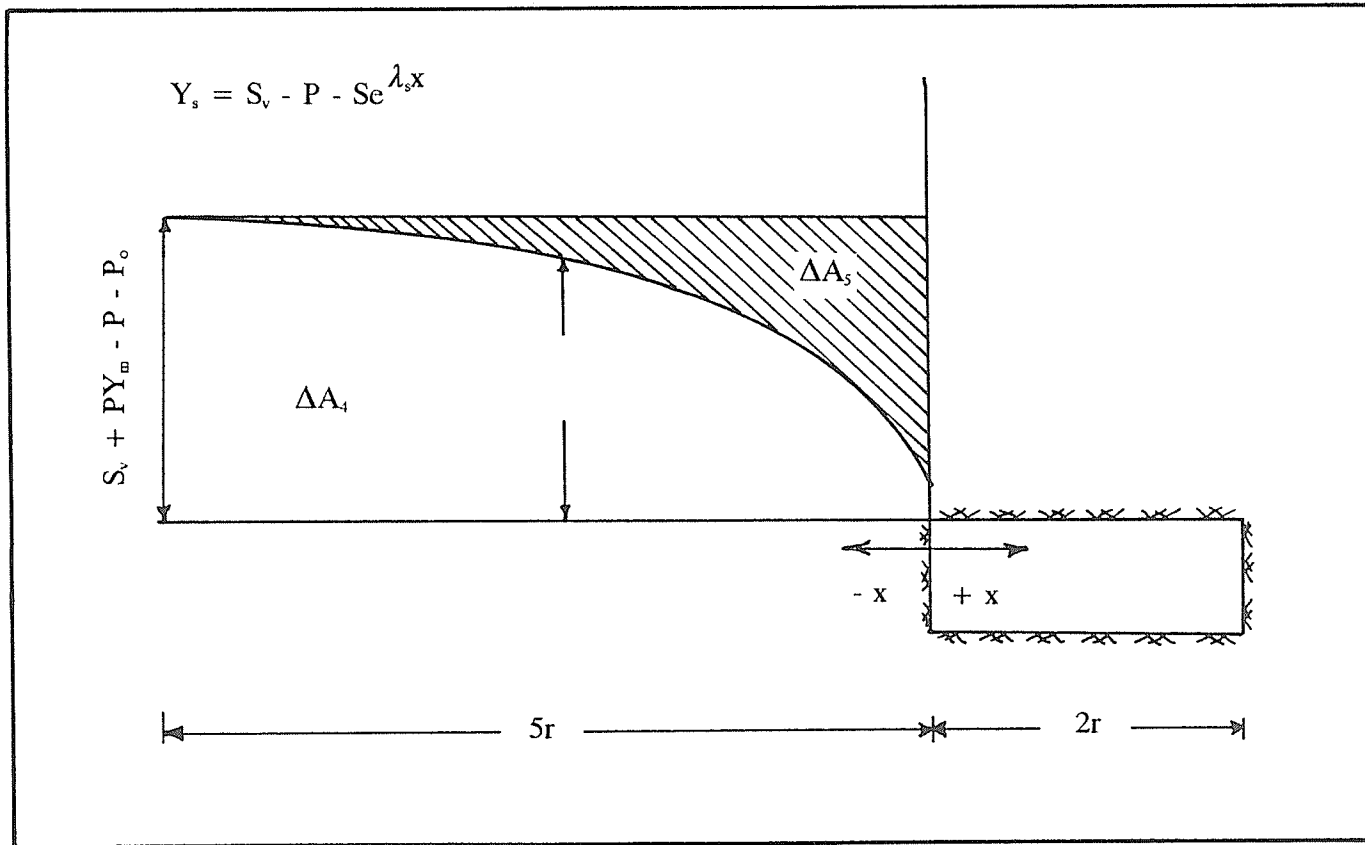
$$Y_s = S_v - P - Se^{\lambda_s x}$$

Fig. 6.5   Assumed yielding function.

Let,

@ $x = 0$,

$$Y_s = -PY_m + P_o \qquad (6.5)$$

where,

S_v = overburden load

P_o = load @ $x = 0$

From eqns. (6.4) and (6.5) :

$$-PY_m + P_o = S_v - P - S$$

$$\text{or,} \quad S = S_v + PY_m - P - P_o \qquad (6.6)$$

Let,

@ $x = -L_s$,

$$Y_s = -PY_m + M_sS_v \qquad (6.7)$$

where,

$$0 < M_s < 1$$

From eqns. (6.6) and (6.7), @ $x = -L_s$:

$$Y_s = M_sS_v + S_v - P - S - P_o \qquad (6.8)$$

From eqn. (6.4), @ $x = -L_s$:

$$Y_s = S_v - P - Se^{-\lambda_s L_s} \qquad (6.9)$$

From eqns. (6.8) and (6.9) :

$$Se^{-\lambda_s L_s} = S + P_o - M_sS_v$$

$$\text{or,} \quad \lambda_s = \ln \left(\frac{S}{S + P_o - M_sS_v} \right) \qquad (6.10)$$

It is widely accepted that the effect of an opening will become negligible at a distance greater than five times its radius.

Therefore, from Fig. 6.4 :

$$\Delta A_3 \approx \int_{-5r}^{0} (P + Ce^{\lambda_c x})dx \; - \Delta A_2$$

$$\approx C/\lambda_c \tag{6.11}$$

Also, from Fig. 6.4,

$$\Delta A_1 = 2Pr \tag{6.12}$$

And from Fig. 6.5 :

$$\Delta A_5 \quad \approx (S_v + PY_m - P - P_o)*5r - \int_{-5r}^{0} (S_v - P - Se^{\lambda_s x})dx$$

$$\text{or,} \quad \Delta A_5 \approx 5PY_m r - 5P_o Pr + S/\lambda_s \tag{6.13}$$

The total redistributed load must be equal to the total virgin load which existed before the creation of the opening. Hence, from Figs. 6.4 and 6.5 :

$$(\Delta A_2 + \Delta A_3) + \Delta A_4 = (0.5*\Delta A_1 + \Delta A_2) + (\Delta A_4 + \Delta A_5)$$

$$\text{or,} \quad \Delta A_3 = 0.5*\Delta A_1 + \Delta A_5 \tag{6.14}$$

Now, from eqns. (6.11), (6.12), (6.13) and (6.14) :

$$C/\lambda_c \approx Pr + 5PY_m r - 5P_o r + S/\lambda_s$$

Therefore,

$$\lambda_c \approx \frac{C\lambda_c}{5PY_m r\lambda_s + Pr\lambda_s + S - 5P_o\lambda_s} \tag{6.15}$$

Now, from eqns. (6.1) and (6.4), the distribution of clamping load Y_1 can be found as follows :

$$Y_1 = Y_c + Y_s$$

$$= S_v - Se^{\lambda_s x} + Ce^{\lambda_c x} \tag{6.16}$$

60

In the following sections solutions are derived for the differential equation of both thin and thick beams resting on deformable abutments, with abutment vertical stress distribution or " clamping load " as defined in eqn. (6.16).

6.2.2 THIN BEAM

The differential equation of a thin beam over a deformable abutment (Fig. 6.2) for the defined clamping load (eqn. 6.16) :

$$K \frac{d^4y}{dx^4} + C_u y = S_v - Se^{\lambda_s x} + Ce^{\lambda_c x}$$

or, $$\frac{d^4y}{dx^4} + \alpha^4 y = \frac{S_v}{C_u} - Se^{\lambda_s x} + Ce^{\lambda_c x}$$ (6.17)

where,

$$K = \frac{EI}{1 - \nu^2}$$

$$I = \frac{D^3}{12}$$

D = thickness of beam

E = elastic modulus of beam

ν = Poisson's ratio of beam

$$\alpha = (\frac{C_u}{4k})^{1/4}$$

$$C_u = \frac{E_a}{D_a(1 - \nu_a^2)}$$

E_a = elastic modulus of abutment

D_a = thickness of abutment

61

ν_a = Poisson's ratio of abutment

From eqn. (6.17) :

Complementary function = $(A_1 Sin\alpha x + B_1 Cos\alpha x)e^{\alpha x} + C_1 Sin\alpha x$

$+ D_1 Cos\alpha x)e^{-\alpha x}$

Particular integral = $\dfrac{S_v}{C_u} + Ae^{\lambda_s x} + Be^{\lambda_c x}$

where,

$$A = -\dfrac{S}{K\lambda_s^4 + C_u}$$

$$B = \dfrac{C}{K\lambda_c^4 + C_u}$$

$\therefore y = (A_1 Sin\alpha x + B_1 Cos\alpha x)e_{\alpha x} + (C_1 Sin\alpha x + D_1 Cos\alpha x)e^{-\alpha x}$

$$+ \dfrac{S_v}{C_u} + Ae^{\lambda_s x} + Be^{\lambda_c x} \tag{6.18}$$

But, as $x \to \infty$, $y = \dfrac{S_v}{C_u}$

Hence, $y = A_1 Sin\alpha x e^{\alpha x} + B_1 Cos\alpha x e^{\alpha x} + \dfrac{S_v}{C_u} + Ae^{\lambda_s x} + Be^{\lambda_c x}$ (6.19)

The differential equation for a thin beam over the opening is as follows :

$$K\dfrac{d^4 y}{dx^4} = P \tag{6.20}$$

Let, $y = \dfrac{Px^4}{24K} + L_1 x^3 + N_1 x^2 + tan\phi_1 + y_1$ (6.21)

Successively differentiating eqns. (6.19) and (6.21), and equating @ $x = 0$, the integration constants of eqn. (6.21) have been found :

$$y_1 = B_1 + \dfrac{S_v}{C_u} + A + B \tag{6.22}$$

$$tan\phi_1 = \alpha(A_1 + B_1) + \lambda_s A + \lambda_c B \tag{6.23}$$

62

$$N_1 = \frac{1}{2} (2\alpha^2 A_1 + \lambda_s^2 A + \lambda_c^2 B) \tag{6.24}$$

$$L_1 = \frac{1}{6} [2\alpha^3 (A_1 - B_1) + \lambda_s^3 A + \lambda_c^3 B)] \tag{6.25}$$

From eqns. (6.22) and (6.23) :

$$A_1 = \frac{1}{\alpha} [\tan\phi_1 - \alpha (y_1 - \frac{S_v}{C_u}) + A(\alpha - \lambda_s) + B(\alpha - \lambda_c) \tag{6.26}$$

$$B_1 = y_1 - \frac{S_v}{C_u} - A - B \tag{6.27}$$

But, shearing force,

$$T = -K \frac{d^3y}{dx^3} \tag{6.28}$$

Successively differentiating eqn. (6.21) and equating with eqn. (6.28) @ x = 0 :

$$T = - 6KL_1 \tag{6.29}$$

Again, @ x = 0,

$$T = \frac{Pl}{2} + T_c \tag{6.30}$$

where,

l = beam span

T_c = contribution by variable load over the abutment

Inspecting eqn. (6.12) :

$$T_c = - K(\lambda_s^3 A + \lambda_c^3 B) \tag{6.31}$$

Therefore, from eqns. (6.29), (6.30) and (6.31) :

$$\frac{Pl}{2} = - K\alpha^3 (A_1 - B_1) \tag{6.32}$$

Substituting the values of A_1 and B_1 from eqns. (6.22) and (6.23) in eqn. (6.31) :

$$\tan\phi_1 = 2\alpha (y_1 - \frac{Sv}{C_u} - A - B) + \lambda_s A + \lambda_c B - \frac{Pl}{4K\alpha^2} \tag{6.33}$$

It is known that, @ $x = l/2$, $\dfrac{dx}{dy} = 0$ (6.34)

Differentiating eqn. (6.21) and equating with eqn. (6.33) @

$x = l/2$:

$$y_1 = \frac{Pl\alpha_3\beta_1}{C_u} + \frac{S_v}{C_u} + A(1 - \beta_2) + B(1 - \beta_3)$$ (6.35)

where,

$$\beta_1 = \frac{l^2/6 + 1/\alpha + 1/\alpha^2}{\alpha l + 2}$$

$$\beta_2 = \frac{\lambda_s + l\lambda_s^2/2 + l^2\lambda_s^3/8}{\alpha^2 l + 2\alpha}$$

$$\beta_3 = \frac{\lambda_c + l\lambda_c^2/2 + l^2\lambda_c^3/8}{\alpha^2 l + 2\alpha}$$

Having derived all the constants, the deflection over the opening as well as the abutment can be obtained using eqns. (6.19) and (6.21). However, these equations include the deformation of the abutment, S_v/C_u, which was present before the opening was created. Hence, to obtain the deflection due to the creation of the opening the term S_v/C_u has to be subtracted from the right-hand side of eqns. (6.19) and (6.21). The equations to calculate deflection, horizontal shear stress and outermost fibre stress for both the beam above the opening ($l/2 \geq x \geq 0$) as well as over the abutment ($-\infty \geq x \geq 0$) are given below :

Over opening :

$$\text{Deflection} = \frac{Px^4}{24K} + L_1x^3 + N_1x^2 + \tan\phi_1 + y_1 - \frac{S_v}{C_u}$$ (6.36)

$$\text{Maximum horizontal shear stress} = -\frac{3K}{2D}\left(\frac{Px}{K} + 6L_1\right)$$ (6.37)

$$\text{Outermost fibre stress} = \pm\frac{KD}{2I}\left(\frac{Px^2}{2K} + 6L_1x + 2N_1\right)$$ (6.38)

Over the abutment :

$$\text{Deflection} = A_1 Sin\alpha xe^{\alpha x} + B_1 Cos\alpha xe^{\alpha x} + Ae^{\lambda_s X} + Be^{\lambda_c X} \qquad (6.39)$$

$$\text{Maximum horizontal shear stress} = -\frac{3K}{2D}[2\alpha^3(A_1 - B_1)Cos\alpha xe^{\alpha x}$$

$$-2\alpha^3(A_1 + B_1)Sin\alpha xe^{\alpha x} + \lambda_s^3 Ae^{\lambda_s X} + \lambda_c^3 Be^{\lambda_c X}] \qquad (6.40)$$

$$\text{Outermost fibre stress} = \pm \frac{KD}{2I}(2\alpha^2 A_1 Cos\alpha xe^{\alpha x} - 2\alpha^2 B_1 Sin\alpha xe^{\alpha x}$$

$$+ \lambda_s^2 Ae^{\lambda_s X} + \lambda_c^2 Be^{\lambda_c X}) \qquad (6.41)$$

6.2.3 THICK BEAM

In thin beam, the deformation due to built-up shear stress is negligible. For a thick beam, however, the influence of shear stress can no longer be disregarded, and the deformation curve is regarded as the sum of the curvature due to bending moment and that due to shear.

For a small element of thick beam (Fig. 6.6),

$$\text{Shear stress, } \tau_{xy} = \frac{3T}{3D}(1 - \frac{d^2}{z^2}) \qquad (6.42)$$

where,

d = distance from the neutral axis

z = distance between the neutral axis and outer boundary

$$\text{Shear modulus, } G = \frac{E}{2(1 + \nu)} \qquad (6.43)$$

$$(S_v - Se^{\lambda_s x} + Ce^{\lambda_c x})dx$$

T

M

M + dM

T + dT
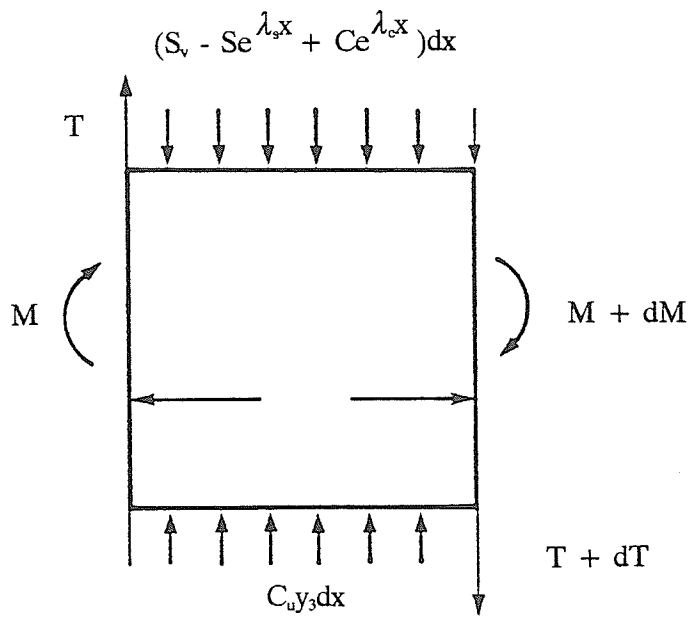
$C_u y_3 dx$

Fig. 6.6 Forces exerted on a small element of a thick beam.

From Fig. 6.6, summation of vertical forces :

$$T - (T + dT) + C_u y_3 dx - (S_v - Se^{\lambda_s x} + Ce^{\lambda_c x})dx = 0$$

where,

y_3 = deflection of lowest fibre of thick beam over

abutment

= deflection of thin beam over abutment

$$= A_1 Sin\alpha x e^{\alpha x} + B_1 Cos\alpha x e^{\alpha x} + \frac{S_v}{C_u} + Ae^{\lambda_s x} + Be^{\lambda_c x}$$

Therefore, $\dfrac{dT}{dx} = C_u y_3 - (S_v - Se^{\lambda_s x} - Ce^{\lambda_c x})$ (6.44)

From eqns. (6.42) and (6.43), the shearimg strain γ, is

$$\gamma = \frac{3T(1 + \nu)}{2DE} \left(1 - \frac{d^2}{z^2}\right)$$ (6.45)

Therefore, the slope of the deflection curve due to shear,

$$\frac{dy_4}{dx} = \frac{3T(1 + \nu)}{2DE} \left(1 - \frac{d_2}{z^2}\right)$$ (6.46)

where,

y_4 = deflection due to shear

Hence, the curvature produce by shear is

$$\frac{d^2 y_4}{dx^2} = \frac{3(1 + \nu)}{2DE} \left(1 - \frac{d^2}{z^2}\right)[C_u y_3 - (S_v - Se^{\lambda_s x} + Ce^{\lambda_c x})]$$ (6.47)

If y is the total deflection, then the total curvature is

$$\frac{d^2 y}{dx^2} = \frac{d^2 y_3}{dx^2} + \frac{d^2 y_4}{dx^2}$$ (6.48)

$$\therefore y = y_3 + y_4$$

$$= (A_1 + \frac{aC_uB_1}{2\alpha^2})Sin\alpha xe^{\alpha x} + (B_1 - \frac{aC_uA_1}{2\alpha^2})Cos\alpha xe^{\alpha x}$$

$$+(A_1 + \frac{aC_uA}{\lambda_s^2} + \frac{aS}{\lambda_s^2})e^{\lambda_s x} + (B + \frac{aC_uB}{\lambda_c^2} - \frac{aC}{\lambda_c^2})e^{\lambda_c x}$$

$$+ \frac{S_v}{C_u} \tag{6.49}$$

where,

$$a = \frac{3(1 + \nu)}{2DE}(1 - \frac{d^2}{z^2})$$

Hence, above the abutment the deflection can be obtained using eqn. (6.49).

To calculate the deflection over the opening, eqn. (6.36) has to be used after redefining y_1, $\tan\phi_1$, N_1 and L_1 accordingly (Appendix – I).

Unlike thin beam theory, though more accurate , the thick beam formulation can only be used to calculate deflection for a particular fiber. In thick beam formulation the deflection is a function of shear stress, which varies from fibre to fibre, as well (6.49). Hence, in order to obtain the deflection one has to define the position of the point by its distance from the neutral axis.

6.2.4 RELATIVE SLIP

Two elastic beam of equal thickness and elastic properties laid one over the other will deflect equally under load. For smalll deflections, the shear displacement, i.e., slip along the interface (Fig. 6.7) is given by :
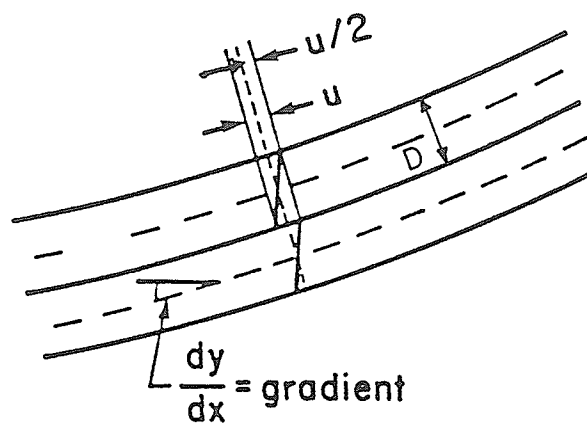
Fig. 6.7 Slip between two beams of equal thickness and properties.

$$\frac{u}{2} = D \frac{dy}{dx} \qquad (6.50)$$

where,

y = vertical displacement

The relative slip, δ, between the bedding planes is

given by

$$\delta = \delta_1 - \delta_2 \qquad (6.51)$$

where,

δ_1 = slip of the upper beam along the interface

δ_2 = slip of the lower beam along the interface

From Fig.(6.7) and eqn. (6.50) :

$$\delta_1 = D \frac{dy}{dx}$$

$$\delta_2 = - D \frac{dy}{dx}$$

Hence eqn. (6.51) reduces to

$$\delta = 2D \frac{dy}{dy} \qquad (6.52)$$

The relative slip over opening and over the abutment were derived. These are given

in the eqns. (6.53), (6.54) and (6.55) below :

Over opening:

$$\delta = D(\frac{Px^3}{6K} + 3L_1x^2 + 2N_1x + \tan\phi_1) \qquad (6.53)$$

Over the abutment :

Thin beam :

$$\delta = D[\alpha(A_1 + B_1)Cos\alpha xe^{\alpha x} + \alpha(A_1 - B_1)Sin\alpha xe^{\alpha x}$$

$$+ \lambda_s Ae^{\lambda_s x} + \lambda_c Be^{\lambda_c x}] \qquad (6.54)$$

70

Thick beam :

$$\delta = D \left[\left\{ \alpha(A_1 - B_1) + \frac{aC_u(A_1 - B_1)}{2\alpha} \right\} Sin\alpha x e^{\alpha x} \right.$$

$$+ \left\{ \alpha(A_1 - B_1) - \frac{aC_u(A_1 - B_1)}{2\alpha} \right\} Cos\alpha x e^{\alpha x}$$

$$+ (\lambda_s A + \frac{aC_u A}{\lambda_s} + \frac{aS}{\lambda_s}) e^{\lambda_s}$$

$$+ (\lambda_c B + \frac{aC_u B}{\lambda_c} + \frac{aC}{\lambda_c}) e^{\lambda_c x} \tag{6.55}$$

6.2.5 EFFECT OF DIFFERENCE IN YOUNG'S MODULUS IN COMPRESSION AND TENSION

For some rocks, it is probable that the compressive Young's modulus, E_C, is greater than tensile Young's modulus, E_T. However, classical the formulation of the deflection of a beam allows only the use of one Young's modulus, i.e., E_C, and E_T is assumed equal to E_C. This assumption results in decreased deflection and increased stresses compared to the case where $E_C > E_T$. To obtain the true deflection in the deformation analysis of a rock beam one should use the average modulus, E_{av}, which is given by the following eqn. (6.56) after Jaeger and Cook (1978) :

$$E_{av} = \frac{4E_C E_T}{(\sqrt{E_T} + \sqrt{E_T})^2} \tag{6.56}$$

Fig. 6.8(a) shows a beam of rectangular cross section having two elastic moduli, E_C and E_T. This beam is equivalent to the transformed beam [(Fig. 6.8(b)] with uniform Young's modulus E_T, but an increased width b'.

From Fig. 6.8, the relationship between the elastic moduli and sections are :

71
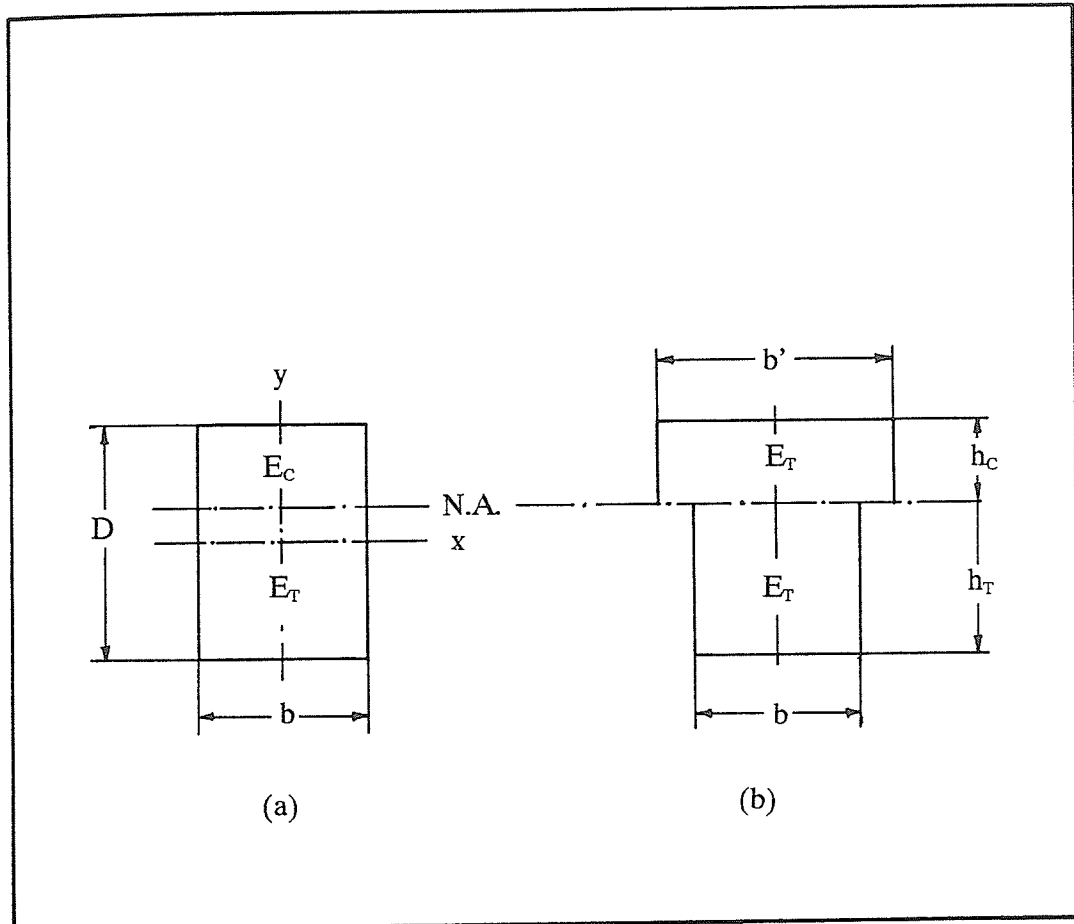
Fig. 6.8 (a) A beam of rectangular cross section with Young's modulus in compression, E_C, greater than in tension, E_T. (b) The transformed section of the beam (after Jaeger and Cook, 1976).

$$b/b' = E_C/E_T = (h_T/h_C)^2 \tag{6.57}$$

$$\therefore \quad h_C = h_T(E_T/E_C)^{1/2} \tag{6.58}$$

From Fig. 6.8, beam thickness D, is

$$D = h_T + h_C \tag{6.59}$$

From eqns. (6.58) and (6.59) :

$$h_T = D \left(\frac{\sqrt{E_C}}{\sqrt{E_C} + \sqrt{E_T}} \right) \tag{6.60}$$

And,

$$h_C = D \left(\frac{\sqrt{E_T}}{\sqrt{E_C} + \sqrt{E_T}} \right) \tag{6.61}$$

Now, to obtain the true stresses the following equations are necessary :

Horizontal tensile stress σ'_x is

$$\sigma'_x = \sigma_x \frac{D}{2h_T} \tag{6.62}$$

where,

σ_x = uncorrected tensile stress

Horizontal compressive stress σ'_{x1}, is

$$\sigma'_{x1} = \sigma_{x1} \frac{D}{2h_C} \tag{6.63}$$

6.2.6 EFFECT OF VERTICAL, DISCONTINUOUS JOINTING IN THE DAWSON BAY FORMATION BEAM ON ROCK MASS DEFORMABILITY IN TENSION AND COMPRESSION

Vertical, discontinuous jointing in the Dawson Bay Formation is known to occur. A model is proposed below for estimating the influence of this jointing on the

73

moduli of deformation in tension and compression. In the following analysis (Stimpson and Ahmed, 1987), it is proposed that the joints act as long, narrow, elliptical cracks that, prior to mining, are essentially closed under the action of the virgin lateral stresses and/or by crystallization of carbonate minerals and halite. However, as the limestone beam deflects in response to undermining, compressive and tensile stresses will be induced. For areas under increased compression the effective Young's modulus will be the same as that of the intact rock since it is assumed that the joints are closed. This assumption makes the analysis a bounding or "worst" case, since there is likely some additional capacity for joint closure under the action of increased compressive stresses above the virgin levels. Sections of the rock beam that experience reducing compressive stresses and, in some areas eventually go into tension, will respond under conditions of a lower Young's modulus as the narrow closed elliptical cracks open up. For this model the Young's moduli for compressive unloading and for tensile loading (E_T) are smaller than the Young's modulus for compressive loading (E_C). Also, E_T of the rock mass (E_{Trm}) will be smaller than E_T of the intact rock (E_{Tir}). A model is proposed below for determining the ratio E_{Tir}/E_{Trm}.

Jaeger and Cook (1970) derive an equation for the Young's modulus of a plate, E_T, length l, width b, and thickness t, containing a single elliptical crack parallel to the side b and acted upon by a tensile stress parallel to the length l (Fig. 6.9). They show that the effective Young's modulus of this plate in tension, E_T, is given by :

$$E_T = E / (1 + 2\pi c^2/bl$$

or, $\qquad E/E_T = 1 + 2\pi c^2/bl$ $\hfill$ (6.64)

where,

E = intact modulus in tension (uncracked rock)

c = half crack length

74
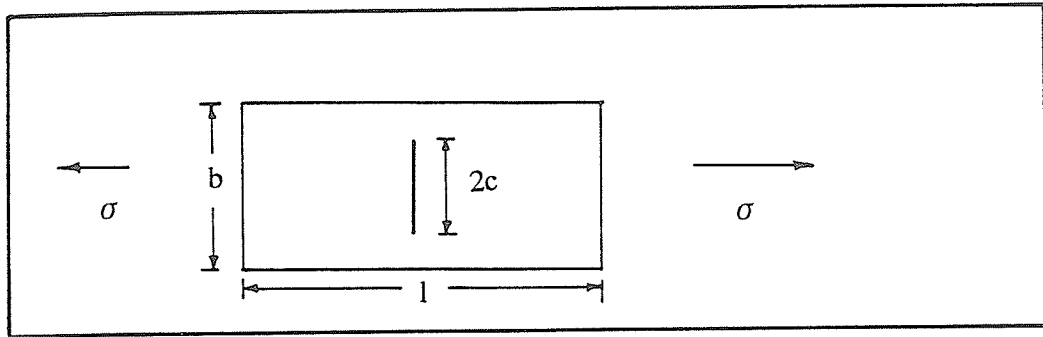
Fig. 6.9 Plate under tension containing a single narrow, elliptical crack .
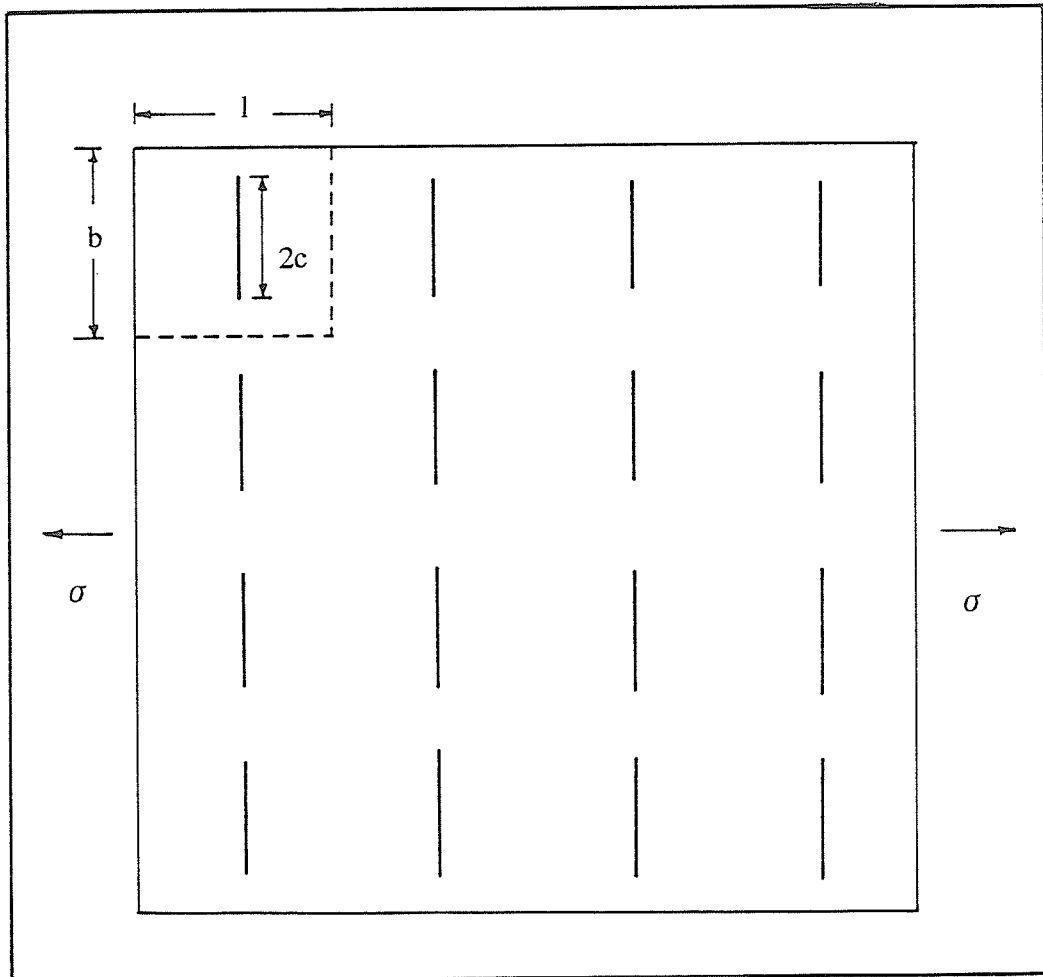
Fig. 6.10 Idealized rock mass with uniform joint pattern normal to tensile loading (after Stimpson and Ahmed, 1987).

This model was developed for the study of the effect of microcracking on rock moduli, but for the purposes of this study it is assumed that the narrow elliptical cracks represent macro-joints.

Fig. 6.10 shows an idealized model of a rock mass with a uniform joint pattern comprising joints of length 2c, with spacing normal and parallel to the direction of jointing of l and b, respectively. This rock mass may be divided into a series of blocks, side b, length l, unit thickness, each one containing a single crack (Fig. 6.9). For each such subzone eqn. (6.64) applies and it can further be shown that the modulus of the entire rock block (Fig. 6.10) is the same as the modulus of each subzone.

For the jointed rock mass $E = E_{Tir}$ and $E_T = E_{Trm}$ and therefore, from eqn. (6.64)

$$E_{Tir}/E_{Trm} = 1 + 2\pi c^2/bl \qquad (6.65)$$

Clearly, E_{Tir}/E_{Trm} is dependent upon the joint pattern, namely, the value b, l and c. These are not known with any certainty for the Dawson Bay Formation, but for the purpose of illustration, b = 200 cm, l = 400 cm and c = 50 cm, were assumed. Then, from eqn. (6.65), $E_{Tir}/E_{Trm} = 1.2$ (case 1). Again, for a 50% reduction in b and l (closer joint spacing) and a 50% increase in c (longer joints), $E_{Tir}/E_{Trm} = 4.1$ (case 2). An illustration of sensitivity of E_{Tir}/E_{Trm} to b, l, c is shown in Fig. 6.11.

Kroll's (1987) tests on intact rock gave a mean of E_C/E_T of the Dawson Bay limestone of 1.59. If the effect of jointing of case 1 is now added, the ratio of Young's modulus for compression to that for tension of the rock mass is :

$$E_{Crm}/E_{Trm} = 1.59 * 1.2 = 1.9$$

The above effect of vertical, discontinuous joints was incorporated in the computer programs (Appendix – II), which were employed to calculate the defomation of beam.
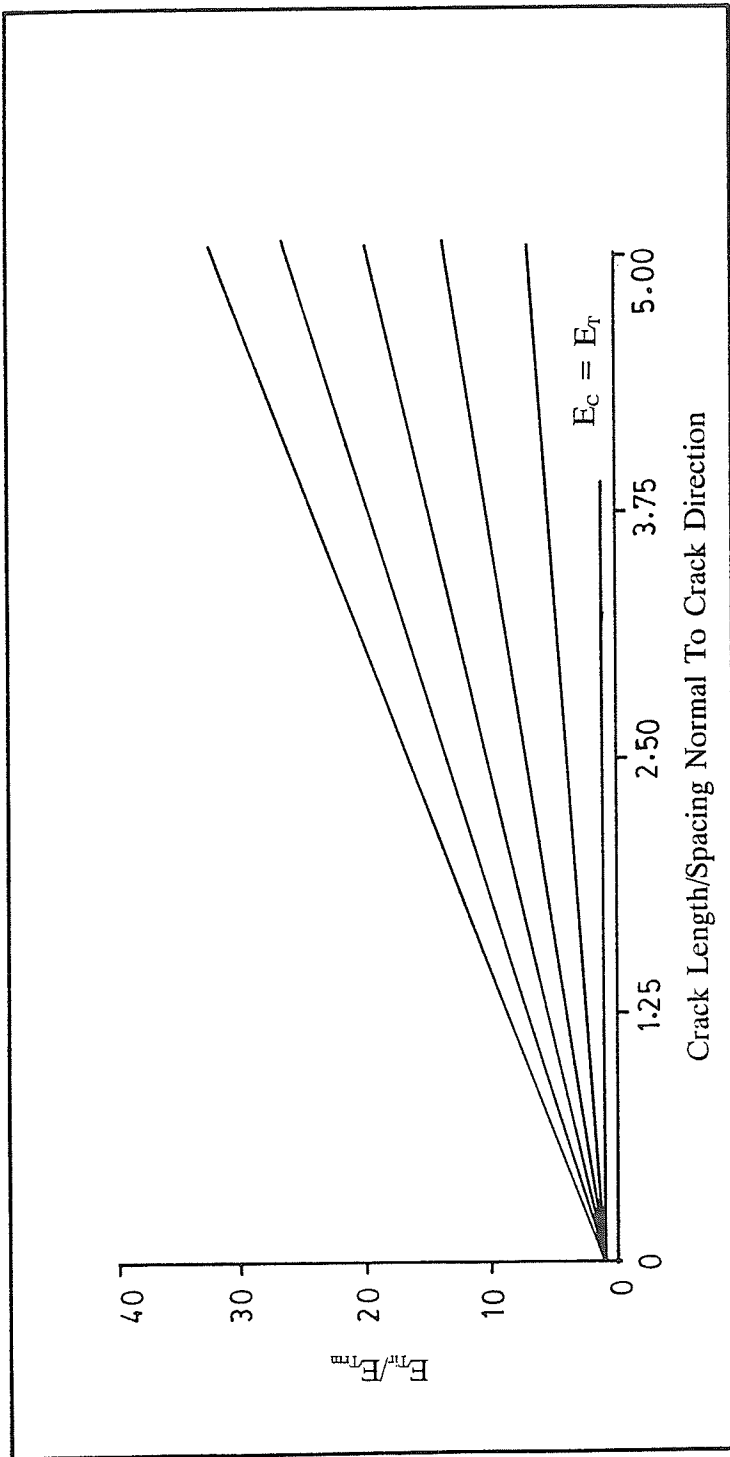
Fig. 6.11 Graph showing E_{Trl}/E_{Trm} vs. c/l for various c/b ratio (after Stimpson and Ahmed, 1987).

CHAPTER 7

BEDDING PLANE FAILURE

7.1 INTRODUCTION

In the last Chapter new formulations for a beam resting on deformable abutments under a non-uniform abutment "clamping load" were derived. In this chapter the new theory is applied to the problem of a beam with (a) a frictionless and (b) a perfectly cemented centroidal horizontal plane.

Planes of physical separation along bedding surfaces within the Dawson Bay Formation occur in less massive sequences. For example, weak layers of bitumen/mudstone have been logged in the core. However, movement along these planes of weakness in response to mining seems unlikely to lead to significant seismicity because of their characteristic low shear strengths as well as the anticipated small drop in shear resistance from peak to ultimate strength with shear displacement.

Since the volume of core drilled in the Dawson Bay Formation is minute in comparison to the total extent of the Formation, one cannot exclude the occurrence of uncemented or cemented bedding plane surfaces in this brittle limestone. Zones of recrystallization are common throughout the dolomitic limestone. Consequently, using the analytical model developed in Chapter 6, two bounding conditions have been examined : (a) relative slip along a frictionless bedding surface along the mid-plane of the Dawson Bay rock beam, and (b) shear stress along a perfectly cemented bedding plane, also at mid-surface. The

first condition idealizes the Dawson Bay Formation as separated at the middle by a layer having zero shear strength. The second situation, on the other hand, correspond to a homogeneous Dawson Bay beam. Actual bedding planes will, of course, be neither frictionless nor perfectly cemented, i.e., the cementing material will likely be weaker than the intact rock on either side. Therefore, the magnitudes of slip and horizontal shear stress predicted by the model will be higher than the "real" values.

The model employed allows one to use a realistic vertical normal stress that "clamps" the Dawson Bay rock beam on to the abutment. Fig. 6.3 shows that the vertical normal stress distribution on the abutment used in the analysis of bedding plane failure for a mining depth of 1000 m using a rock of unit weight of 0.027 MN/m^3. This distribution curve was simulated from the general analytical expression developed in Chapter 6 (eqn. 6.12). The vertical normal stress distribution on the abutment takes into account the load transfer due to the creation of the opening, as well as the yielding close to the wall of opening.

7.2 BEDDING PLANE SLIP

Fig. 7.1(c) illustrates two equal thickness beams separated by a frictionless interface representing a Dawson Bay Formation with a plane of weakness at mid-thickness. The term relative slip means combined slip of both upper and lower beams along the interface (see Section 6.2.4).

Plots of the extent and magnitude of relative slip according to thick beam and thin beam theories derived in Chapter 6 are shown in Figs. 7.1(a) and 7.1(b) respectively. The mining depth in this case is 1000 m, while the elastic moduli and Poisson's ratio of Dawson Bay rock beam and Potash abutment are 35GPa and 0.25, and 2.5 GPa and 0.3 respectively. In both

79
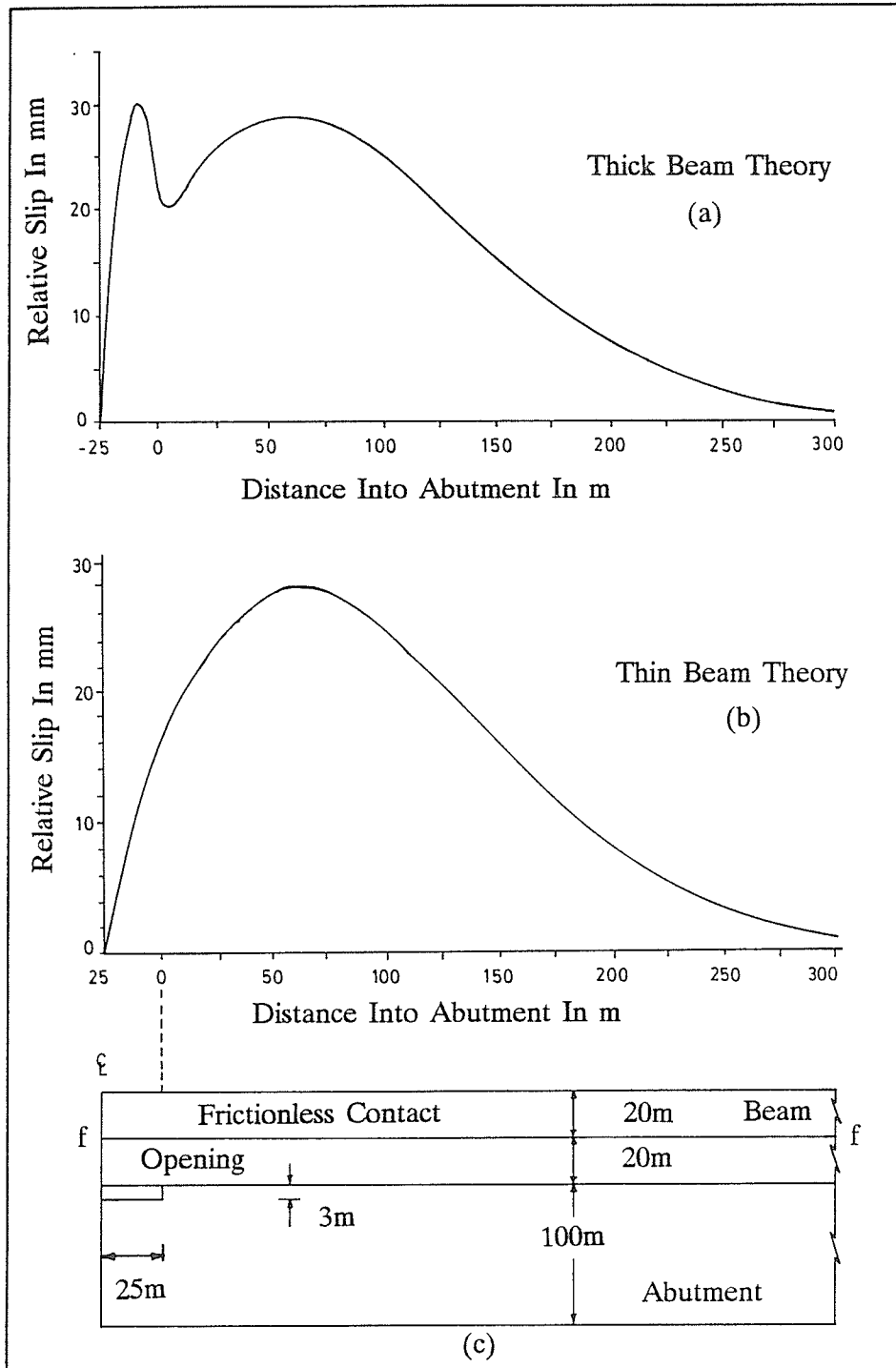
Fig. 7.1   Relative slip along frictionless interface ff vs.distance into abutment for two equal thickness beams on elastic abutment (not to scale).

the cases, the highest slip is just about 30 mm. The small difference between the results of the two theories comes from the extra slip contributed by the shear stress in the thick beam model, which is very small in this case. In both analyses, one point of maximum relative slip is reached over the abutment at a lateral distance of approximately 60 m. This result is of some interest because classical beam theory in rock mechanics has never examined the behaviour of the beam over an abutment.

7.3 MAXIMUM HORIZONTAL SHEAR STRESS

The lower half of Fig. 7.2 depicts a perfectly cemented surface, cc, i.e., an imaginary plane dividing a beam into two halves of equal thickness. This condition corresponds to a situation of a homogeneous Dawson Bay Formation or one with a perfectly cemented bedding plane at mid-point.

The upper half of Fig. 7.2 shows the extent and magnitude of the maximum horizontal shear stress, i.e., horizontal shear stress along the perfectly cemented surface for a mining depth of 1000 m. The elastic moduli and Poisson's ratios used are the same as in the case of bedding plane slip (see Section 7.2). The shear stress in this case is just about 3.5 Mpa which occurs at the wall of the opening. This value, however, is far below the shear strength of Dawson Bay Limestone, which is approximately 40 MPa (Gendzwill, 1984).

7.4 SUMMARY AND CONCLUSIONS

According to the analytical model, a 40 m thick Dawson Bay rock beam

81
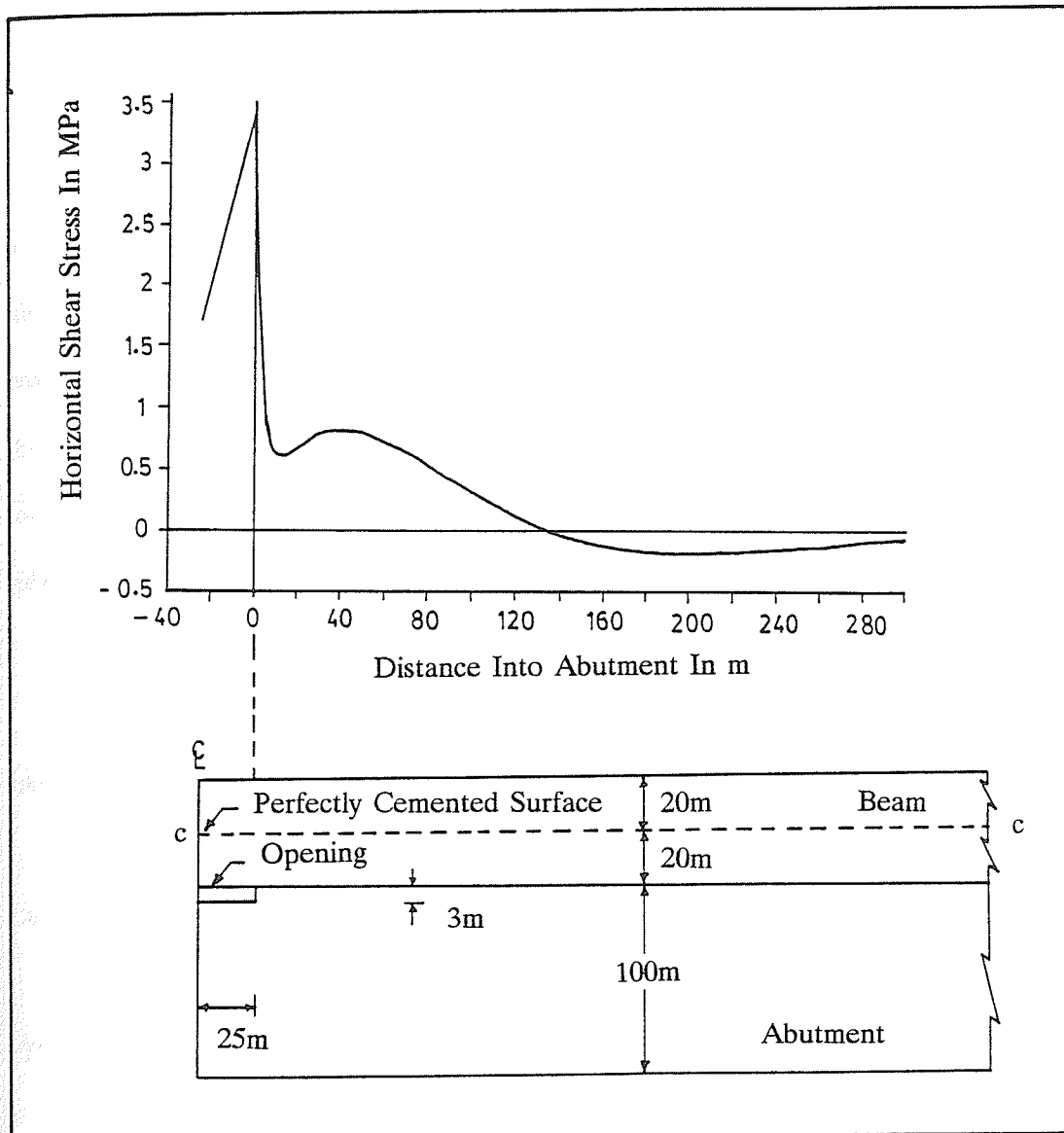
Fig. 7.2 Horizontal shear stress along perfectly cemented horizontal central plane cc vs. distance into abutment for elastic beam on elastic abutment (not to scale).

above an opening of 50 m span, develops relative slip and horizontal shear stresses along a mid-point bedding plane as shown in Figs. 7.1 and 7.2. These two distributions represent two bounding conditions and provide peak values of just over 30 mm relative slip and 3 Mpa horizontal shear stress respectively. In the case of a "real"bedding plane, the magnitudes would be smaller. Also, it should be noted that the analysis assumes a best-estimate of the of vertical "clamping" stress, in the absence of real data.

It is concluded from this model that failure along bedding planes in the rock beam cannot be completely excluded as a possible mechanism for seismicity. However, it is also noted that the zones of highest slip and horizontal shear stress are not extensive, i.e., they affect a small volume of the rock mass, and therefore it is considered unlikely that the larger seismic events can be attributed to this mechanism. Tentative calculations suggests that this mechanism is capable of generating only microseismicity. The sample calculations for the extreme case where bedding plane slip would occur, after full shear stress has been mobilized, instantly are given below :

From Fig. 7.2, the average shear stress τ_a, is

$$\tau_a = 1 \text{ MPa}$$

Also, the dimension effected along the span s, is

$$s = 300 \text{ m}$$

Assuming a mining advance of 1 m per step, the area effected at each step of advance A, is

$$A = s * 1 = 300 \text{ m}^2$$

Therefore, total shear force T, is

$$T = \tau_a * A = 300 \text{ MN}$$

The shear modulus of the Dawson Bay Formation G, is

$$G = 14 \text{ GPa (Sepehr, 1988)}$$

Hence, average shear strain along the slip plane γ, is

$$\gamma = \tau_a/G = 0.7*10^{-4}$$

And, in the event of failure, the displacement δ, is

$$\delta = \gamma * s = 0.021 \text{ m}$$

Therefore, the released energy E, is

$$E = \delta * T = 6.3 \text{ MJ}$$

Seismic efficiency, i.e., the percentage of seismic energy release has been found to be in the order of 1% (Cook, 1963)

Accordingly, Seismic Energy, E_s, is

$$E_s = 0.063 \text{ MJ}$$

From the relationship between local magnitude (i.e., Richter Magnitude) M_L and seismically radiated energy (expressed in MJ) by Richter (1958) :

$$\log(E_s) = 1.5 M_L - 1.2$$

or, $M_L = 0.$

CHAPTER 8

PHYSICAL MODELLING OF THE DAWSON BAY ROCK BEAM

8.1 INTRODUCTION

The research described in the previous Chapters of this thesis has been of an analytical nature. It was apparent at an early stage that, in the absence of access to in situ observation of mining-induced fractures in the Dawson Bay Formation and because of the limitation of the analytical methods derived earlier, any understanding of the fracturing process would require physical modelling in the laboratory. This chapter describes laboratory experiments in which longitudinally constrained rock beams were loaded to ultimate failure in a specially designed testing frame and their results.

8.2 DESIGN OF TESTING FRAME

In this study, the Dawson Bay Formation was simulated by a thick rock beam (span/depth : < 5) loaded to ultimate failure in a specially designed testing frame. Instead of the simple knife edge type of support, end plates were employed to constrain the beam, and permit the development of longitudinal thrust and a realistic arching action.

The testing frame was based after Sterling (1977) with modifications to suit the specific requirements of this study. The final design is illustrated in Figs. 8.1 and 8.2. In this
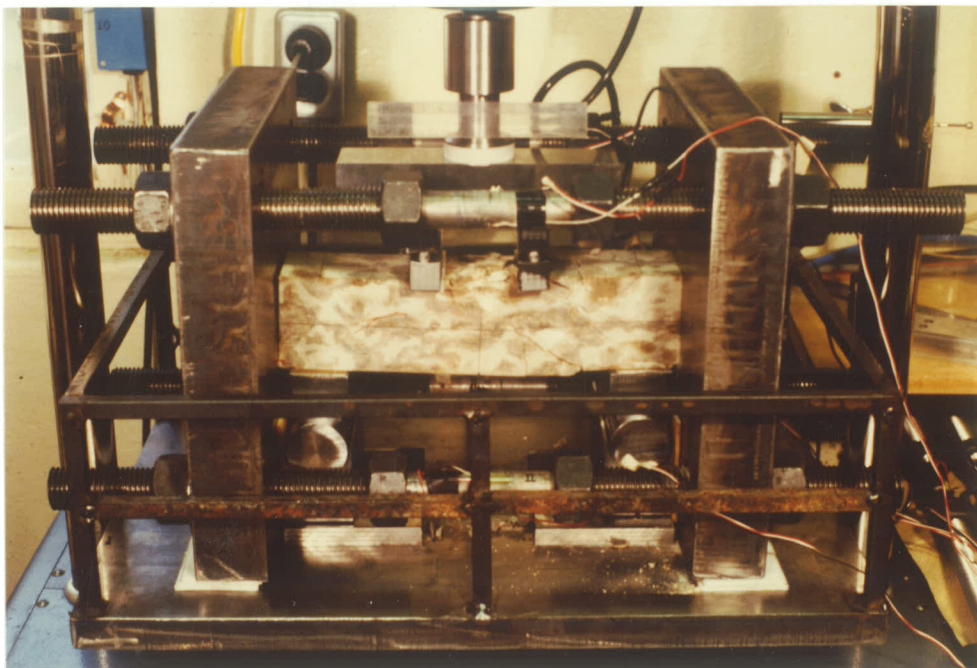
Fig. 8.1 Photograph of the beam testing frame.

a = Flexible Vertical Support

b = End Plate

c = Hard Board Place

d = Flexible Loading Strip

e = Constraining Bar

f = Rock specimen

g = Base of Frame
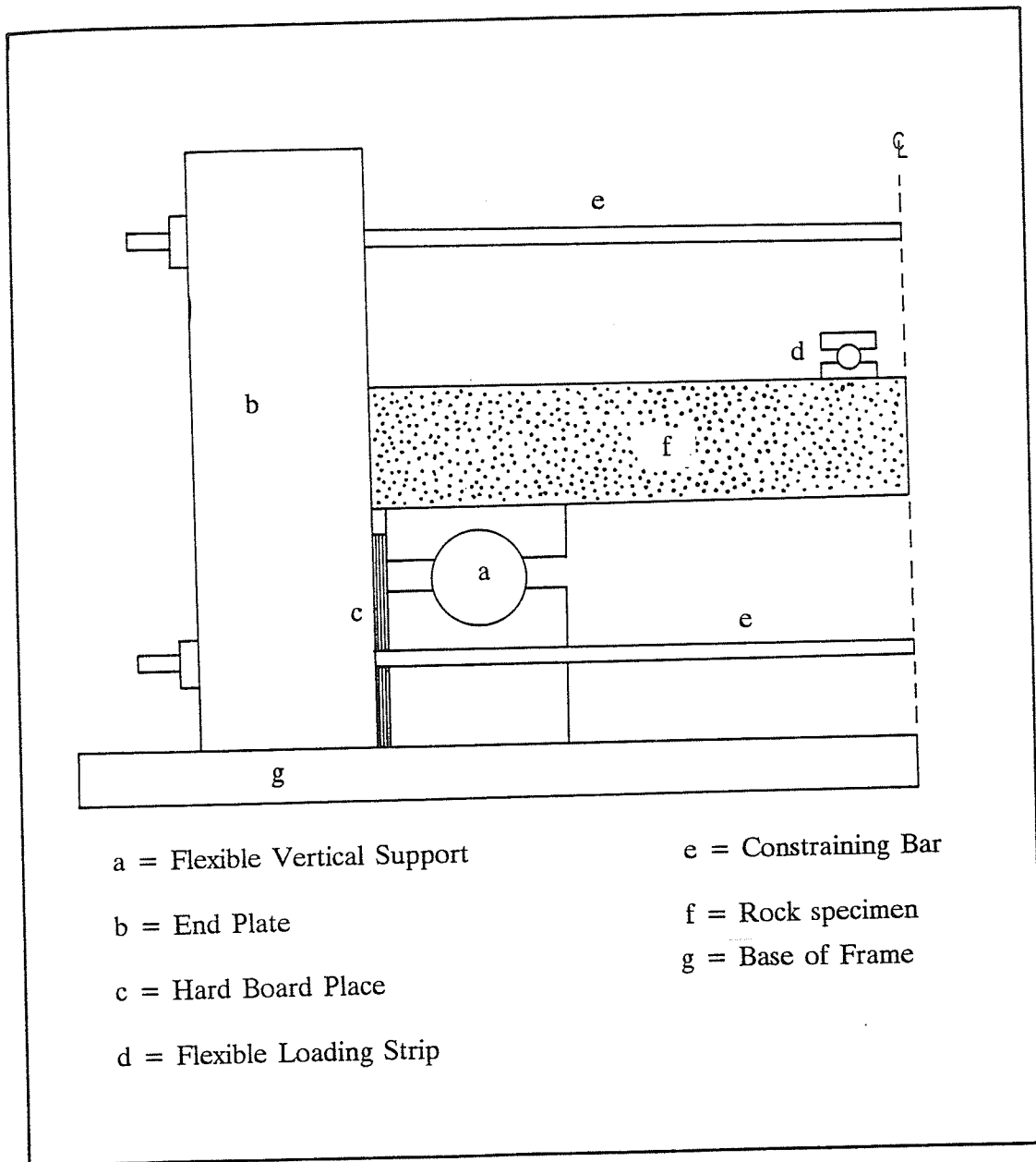
Fig. 8.2 Schematic diagram of one half of the testing frame left of the symmetry line (not to scale).

device, rock beams on vertical supports, constrained between two end plates, were vertically loaded by a displacement rate-controlled machine. For lower loads (Peak load range 8 kn to 100 kN), a 100 kN, gear-driven machine (Manufacturer : Engineering Laboratory Limited) was used. In the case of higher loads, a hydraulic machine —— a Baldwin Universal Testing System (Manufacturer : SATEC System Inc.) —— was used. Details of the testing frame are given in the following sections.

8.2.1 LOAD APPLICATION

One point, two point, and four point loading systems were used in these experiments. The small space between the end plates of the testing frame would not allow the use of more than the four point load spreading system. Rollers were used between the upper and lower components of the loading strips in order to reduce the lateral forces that would otherwise have been induced on the beam as it accommodated the end rotation during deflection. Moreover, teflon pieces and grease were used at the contact points to reduce friction. This flexible load spreading system allowed an even bearing of load along the beam width.

8.2.2 END PLATES

To minimize the bending distortion of the end plates which could effect the shape of the contact area with the beam when under load, the plates were made of 50 mm thick steel. Other dimensions of the plates were 30 cm X 30 cm. These dimensions were determined on the basis of a) available space between the testing machine columns, b) sufficient clearance between

the rock beam and the restraining bars, c) enough room to install LVDT's to measure beam deflection, and d) general access.

8.2.3 RESTRAINING BARS

In order to measure the longitudinal thrust produced by the arching action, four threaded rods were used to constrain the beam (Figs. 8.1 and 8.2). They could also be used to apply prestress on the rock beam by tightening all four of the nuts. Two sizes of restraining bar were chosen for these experiments —— 3.18 cm diam. threaded bars with tensile stress area of 7.95 cm^2 and 2.54 cm diam. threaded bars with tensile stress area of 5 cm^2. Whereas the larger size provides more abutment stiffness, the smaller is more sensitive to the change in load. To allow for the placement of strain gauges to measure the longitudinal thrust on the restraining bars, the centre section (10 cm) of each bar was turned down on a lathe to form a smooth contact surface. A quarter bridge configuration of strain gauges was used to register the output from each bar. Dummy gauges were employed in this configuration to eliminate the strain that might be induced as result of bending the restraining bars.

8.2.4 BEAM SUPPORTS

A pair of 10 cm long and 5 cm wide supports were used. Flexible vertical supports (Fig. 38) in the form of rollers were employed in order to reduce the lateral forces that would otherwise have been induced as the beam accommodated the end rotation during deflection. These flexible supports provided an even bearing of load along the beam width. Teflon pieces

and grease were used at the contact points to reduce friction.

8.2.5 BASE PLATE

The base plate is simply a reaction plate for the end loads passing through the beam supports and served as the base of the testing frame, with the remainder of the frame resting on it. The thickness of this plate was 2.54 cm, in order to minimize distortion due to bending. The other dimensions of the base plate, selected on the basis of the dimensions of the testing machine, were 56 cm in length and 38 cm in width.

8.3 LOAD AND DISPLACEMENT MEASUREMENTS

Two load cells were used for different load ranges to measure the vertical load applied by the gear-driven, 100 kN testing machine on the constrained rock beam : (a) 88 kN (Manufacturer : Transducer Inc., Model C92-20K-10P3) and (b) 220 kN (Manufacturer : Transducer Inc., Model C92-50K-10P3).

Precision electrical resistance strain gauges (Manufacturer : Micro Measurement Group Inc., Gauge Type CEA - 06 - 500UW - 350 and Gauge length 12 mm) were used with a quarter bridge configuration to measure the longitudinal thrust in the restraining bars. Strain Gauges (Manufacturer : Micro Measurement Group, Inc., Gauge Type CEA - 06 - 125UT - 120 and Gauge length 5 mm, and Gauge Type CEA -06 - 500UW - 350 and Gauge length 12 mm) were also used in some tests to measure the strains on the rock beam under load, where they were applied at the desired points of the front and back surfaces of the rock beams. From these

basic measurements the induced stresses were determined using the Young's modulus of the beam.

The restraining bars were calibrated for load/microstrain output of the strain gauges on a Baldwin Universal Testing System. The calibration data is recorded in Appendix — V.

A pair of LVDT's was employed to measure the rock beam deflection. These transducers were calibrated for displacement/millivolt output using a micrometer. They were used to measure the maximum vertical displacement of the beam, and were placed on the topside of the beam in the vicinity of the midspan.

The support plate, i.e., the base of the testing frame, was centred and screwed on to the lower platen of the testing machine using a shallow groove, cut on the underside of the plate, as a guide.

In this study, simultaneous recording of beam deflection, applied vertical load, and longitudinal thrust developed in the restraining bars, as well as the stresses developed on the rock beam under load were required. This was made possible by connecting the LVDT's, load cell, and strain gauges on the restraining bars and the rock beam strain gauges to a data acquisition system, which comprised an HP3421A DATA ACQUISITION/CONTROL UNIT, hooked up with a HP75C microcomputer.

8.4 TEST PROCEDURES

The basic procedures followed for all the beam tests were as follows :

Step 1 : Restraining bars were fitted into four holes on each of the end plates. The end plates were moved to a distance apart which was just greater than the length of the beam to be loaded, and the nuts of the restraining bars were brought up snug.

Step 2 : The end plates were centred using lines marked on them as well as on the reaction plate, so that the vertical centerline of the rock beam, when placed on the end supports, would coincide with the vertical centerline of the end plates.

Step 3 : The beam supports were placed on the base plate and separated from the end plates by two short hard-board packing pieces (3 mm thick). The latter were used to allow free rotation of the vertical supports as the rock beam deflected. The supports were placed on steel packing pieces so that the horizontal centerline of the rock beam, when placed on them, would coincide with the horizontal centerlines of the end plates.

Step 4 : The rock beam specimen was placed on the end supports and was centred using centerline marks on the supports as well as those on the end plates.

Step 5 : The end plates were adjusted to bring them into uniform contact with the ends of the rock beam. A slight prestress was applied in this process and the resulting forces recorded on the restraining bars were adjusted until equalized. This was necessary to ensure a uniform load distribution across the width of the rock beam during the experiment. In one of the tests a variation was used. In this case, an initial prestressing was added by tightening each restraining bar to a predetermined load, modelling the horizontal principal stress in the field. Owing to the interaction of the four bars, this process required a few trials to make sure that equal prestress was attained on all four bars.

Step 6 : Vertical loading of the beam commenced after recording the zero reading on all channels.

Initiation and propagation of cracks were marked with a pen during each test. For some specimens photographs were taken at different stages of the test. At the completion of a test, crack path tracing data were transferred on to a piece of paper before removing the specimen from the testing frame. This procedure was omitted if earlier tests had shown similar crack patterns.

Loading was continued well beyond the peak load when possible. In the majority of cases, however, the beam collapsed just after peak load.

Finally, the rock beam specimen was removed and examined in detail. This included checking the extent of cracking on beam extremities, nature of the crack surfaces, etc.

8.5 BEAM SPECIMENS

Fifteen longitudinally constrained beams of three different rock types were tested in this study. The rock types were : a) Saskatoon Potash, b) Lac Du Bonnet Granite, and c) Tyndall Stone.

Saskatoon Potash is composed of fine to medium grained sylvite with some halite. Saskatoon Potash is a weak rock with compressive and tensile strengths of 15 MPa and 2 MPa respectively. For short-term loading, its Young's modulus is 3.5 GPa, while Poisson's ratio is 0.3.

Lac Du Bonnet Granite is a homogeneous, fine to medium grained rock consisting of feldspar and quartz, with some mica and hornblende. The compressive and tensile strengths of this strong rock are 240 MPa and 14 MPa respectively. The Young's modulus for Lac Du Bonnet Granite is 70 GPa, while the Poisson's ratio is 0.25.

The rock of the majority of beams tested was Tyndall Stone. It is a building stone quarried in the Province of Manitoba, and is composed of calcite and dolomite with minor amounts of clay. This beige-grey rock is heterogenic in appearance due to the presence of mottling, i.e., the dark patches. These dark areas represent dolomite, while the light areas are predominantly calcite. This limestone appears granular under the microscope. It is a moderately strong rock with an average compressive strength of 50 MPa and tensile strength of 3.7 MPa.

Its Young's modulus and Poisson's ratio are 32 GPa and 0.21 respectively.

In this testing program thick beam specimens, i.e., span to depth ratio < 5 were used. The lengths varied from 20 to 30 cm, while the approximately square cross-sectional dimensions ranged from 4 to 11 cm. A complete record of beam geometries and materials is presented in Appendix — VI.

Specimens were cut from larger blocks of rock using a diamond saw. The rough surfaces of the specimens were then ground. Perpendicularity of surfaces was required in this process so that the beams would fit evenly in the testing frame.

There are various reasons for selecting these three rock types to prepare rock beams. Tyndall Stone is a strong limestone similar to that of Dawson Bay Limestone which forms the intermediate roof of the Saskatchewan Potash mines. In addition, this material was selected for most of the tests because of ease of preparation of beams, visibility of fracturing, and availability. Saskatoon Potash is the rock type which is being worked in the Saskatoon Potash mines. This rock type was used to simulate roof material in these mines. Also, since its stiffness is considerably less than that of the other two rock types used, the longer post-peak loading interval during the testing made it possible to observe the fracturing in that period.

Lac Du Bonnet Granite was used mainly for its homogeneity.

8.6 INDIVIDUAL BEAM TEST BEHAVIOUR

Data obtained during the tests provide a complete account of the behaviour of the model beam from the initiation of loading till ultimate failure. In this section, two typical tests will be described. Results from all fifteen tests are available in Appendix — VI.

To illustrate the typical behaviour of the rock beams, two tests will be discussed.

The first test, DL8, is representative of the general behaviour observed in all tests. The second one, GR3, illustrates the effect of prestressing.

The results of test DL8 are shown in Figs. 8.3, 8.4, and 8.5. In the early stages of vertical loading, the specimen behaved like a normal elastic beam with the load-deflection curve rising linearly. This stage abruptly ceased with the propagation of a tensile crack in the lower fibres at midspan (Figs. 8.6, stage I). This event marks the change from beam behaviour to that of a linear or flat arch. A linear or flat arch is a linear structure where vertical load is carried by horizontal thrust developed due to arching action (Fig. 5.1). The midspan crack destroys the specimen's ability to resist load by beam action. Consequently, resistance is derived by linear arching as the vertical load is increased further. The crack also causes redistribution of stresses. As there is no more shear flow (shear flow is defined as horizontal shear force per unit length of the beam.) between the tensile and compressional halves, the beam action ceases, and the specimen carries load as a linear arch. Since loading in this case was by constant-rate deflection, the midspan tensile crack causes an instantaneous drop in load (Fig. 8.3). This is because, with the cessation of shear flow, the equilibrium load of the newly formed linear arch is smaller than that of the beam just prior to mid-span cracking.

The vertical load is now being carried by linear arching and the load/deflection modulus begins to rise since the compression zone of the linear arch is now carrying more and more load. The compression zone of the linear arch is the zone of high horizontal compression at the centre and abutments (see Fig. 5.1).

The eccentricity of the thrust about the horizontal centre line of the beam was determined by resolution of the upper and lower bar loads. Appendix — VII presents the procedure for calculating the eccentricity. When the midspan crack occurred, the eccentricity of the thrust line jumped from zero to the highest value instantaneously, and then began to fall (Fig. 8.4). This phenomenon is evidence that crushing at the extreme fibres caused the compression

95
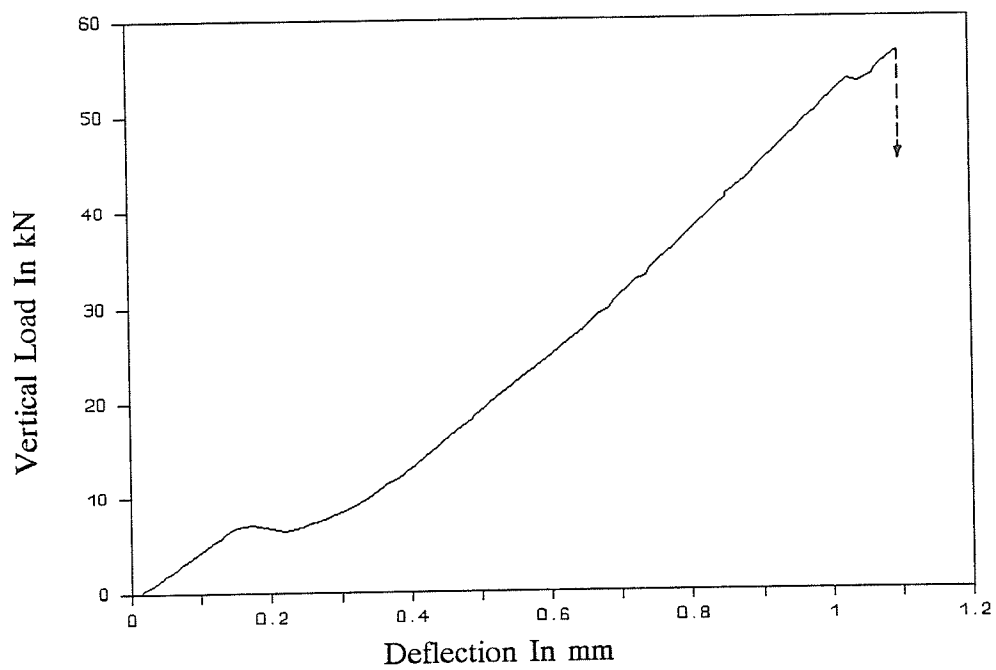
Fig. 8.3 Vertical load/deflection graph for test DL8.
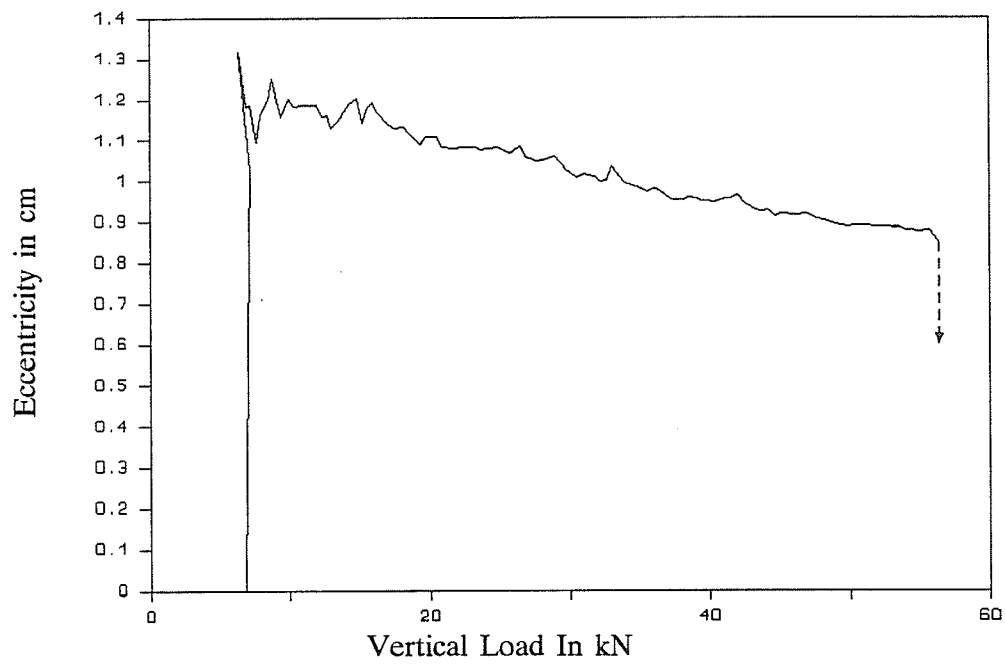
Fig. 8.4 Eccentricity/vertical load graph for test DL8.
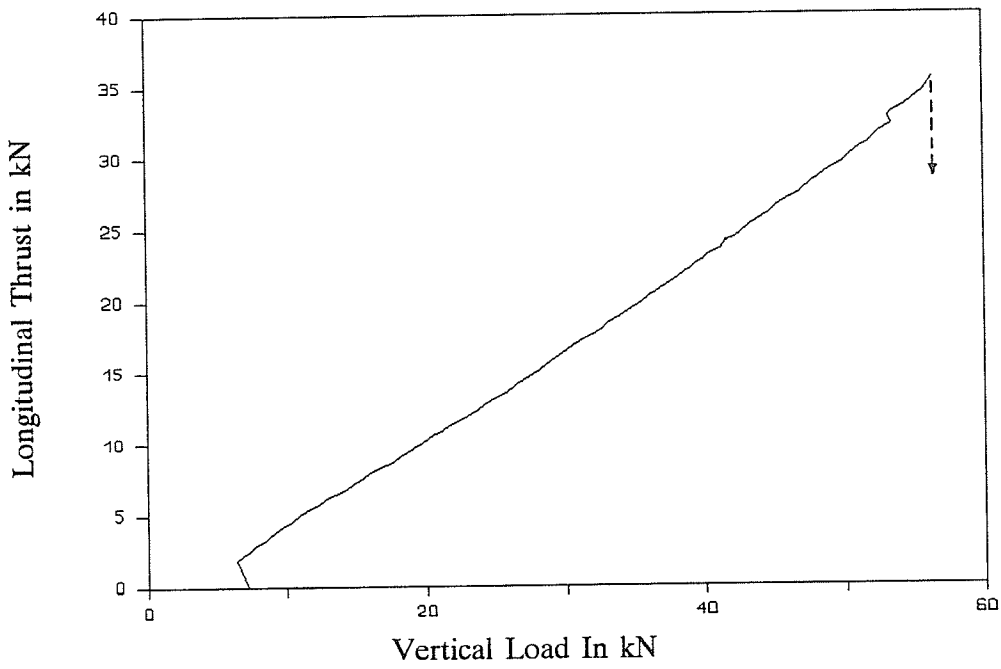
Fig. 8.5 Longitudinal thrust/vertical load graph for test DL8.

zone to spread , and hence eccentricity to fall. The widening of the compression zone entails shortening of the lever arm, which is the distance between the lines of action of the central and abutmental horizontal thrusts (Fig. 5.1). The effect of the shortening of the lever arm is not sufficient to stop the rise in the load/deflection modulus.

Before the midspan cracking, there is practically no measurable change in the longitudinal thrust from the initial zero value. With the creation of the midspan crack, the longitudinal thrust suddenly increases as the vertical load momentarily drops (Fig. 8.5). From this point, the longitudinal thrust increases at a faster rate relative to vertical load because it has to compensate for the shortening of the lever arm caused by the widening of the compressive zone.

With continued loading, at a point close to the peak load, two inclined cracks develop remotely from the midspan crack and propagate very rapidly towards the abutments of the beam. These are called diagonal cracks (Fig. 8.6, stage II).

As loading continues —— from this point to ultimate failure of the specimen —— the load/deflection modulus, eccentricity and longitudinal thrust relative to the vertical load remain similar to those in the previous stage , namely the linear arch without diagonal cracks (Figs. 8.3, 8.4, and 8.5).

The next test to be described in some detail is test GR3. This test was performed with a 125 kN prestress to simulate an in situ horizontal principal stress. Behaviour of this specimen is similar to specimen DL8 with a few exceptions (Figs. 8.7 and 8.8). The midspan crack initiates at a higher vertical load, as would be expected with a prevailing prestressing condition. There were no longitudinal load drops at midspan cracking or with diagonal cracking; only a momentary reduction in the rate of vertical loading was noticed. With regard to eccentricity, the specimen behaved somewhat differently. The highest eccentricity value was not attained immediately following midspan cracking. Rather, the initial increase was not rapid or large be-
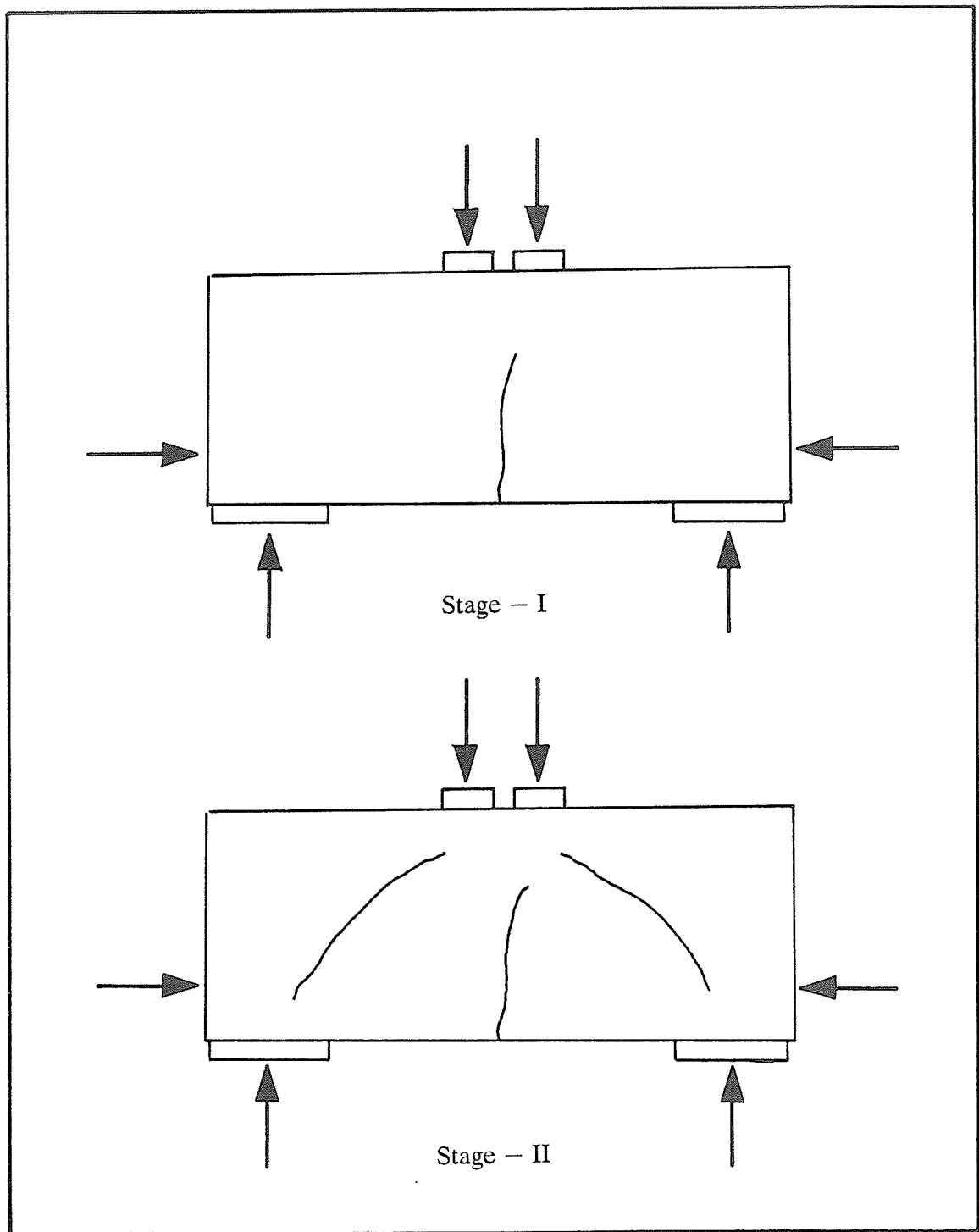
Fig. 8.6 Failure mechanisms at stages I and II in beam test.
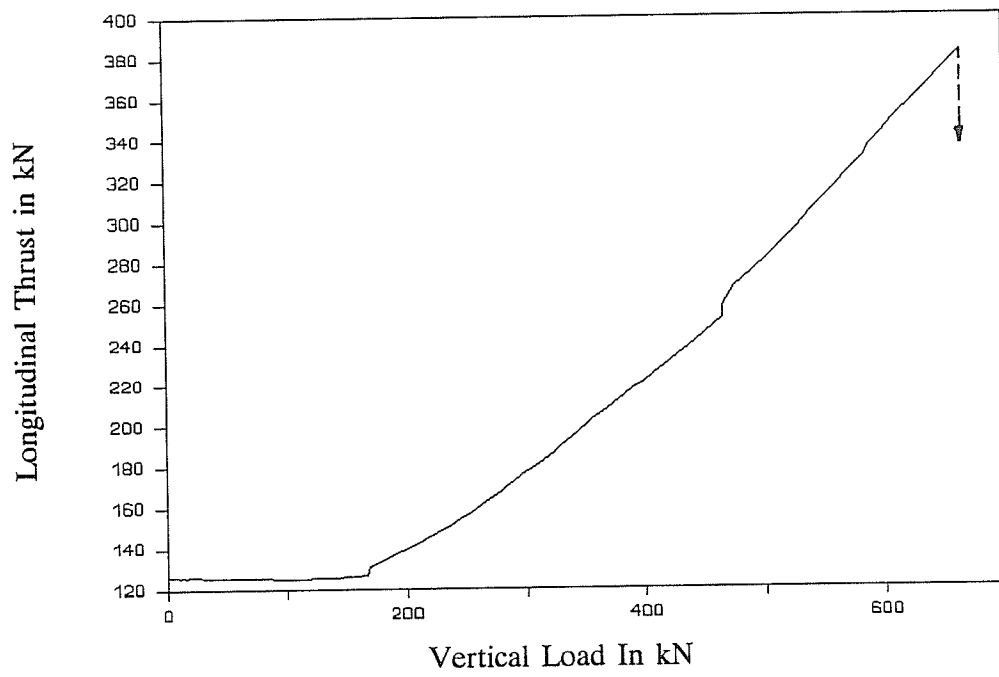
Fig. 8.7 Longitudinal thrust/vertical load graph for test GR3.
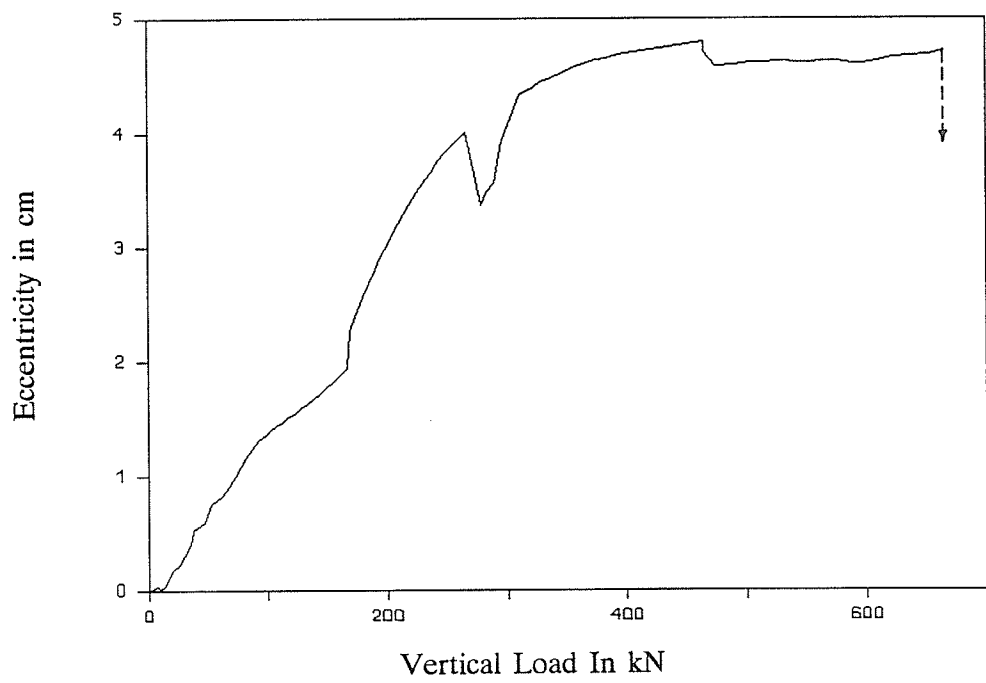
Fig. 8.8 Eccentricity/vertical load graph for test GR3.

cause the blocks in the beam did not have to suddenly rotate to develop longitudinal thrust as there was an initial prestress. Subsequently, the eccentricity declined, and then began to rise until the advent of diagonal cracking. Then, after declining momentarily, the value once again increased until ultimate failure of the arch at the peak vertical load (Fig. 8.8). The highest eccentricity occurred at the moment of diagonal cracking. The general increase in eccentricity after midspan cracking may be explained by the fact that the ends of the specimen remained almost free from crushing, allowing the eccentricity to rise as the increasing deflection caused a pivoting about the lower edge of the beam extremities.

8.7 FAILURE MECHANISMS

The present experimental work revealed a progressive failure mechanism, which presents a quite different concept of linear arch failure to that of the classical view. An illustration of classical linear arch is given in Brady and Brown (1985). Fig. 8.9 shows the geometry of a classical linear arch. Here, the linear arch of span, s and thickness, t supports its own weight, W, by vertical and induced lateral compression, T. Also, f_c is the maximum longitudinal compressive stress, and z is the lever arm measured between the lines of action of the central and abutment compression zones. According to the classical theory, the linear arch would fail if the maximum longitudinal compressive stress, f_c exceeds the uniaxial compressive strength, σ_c, of the material of linear arch. The failure would occur through crushing at the centre or the abutments of the arch.

In this study, however, from the commencement of loading to ultimate collapse , the progressive failure of the rock beam occurred in three distinct stages. Stage I, namely the initial beam stage, ends with the initiation of a tensile crack in the lower fibres at midspan (Fig.

103
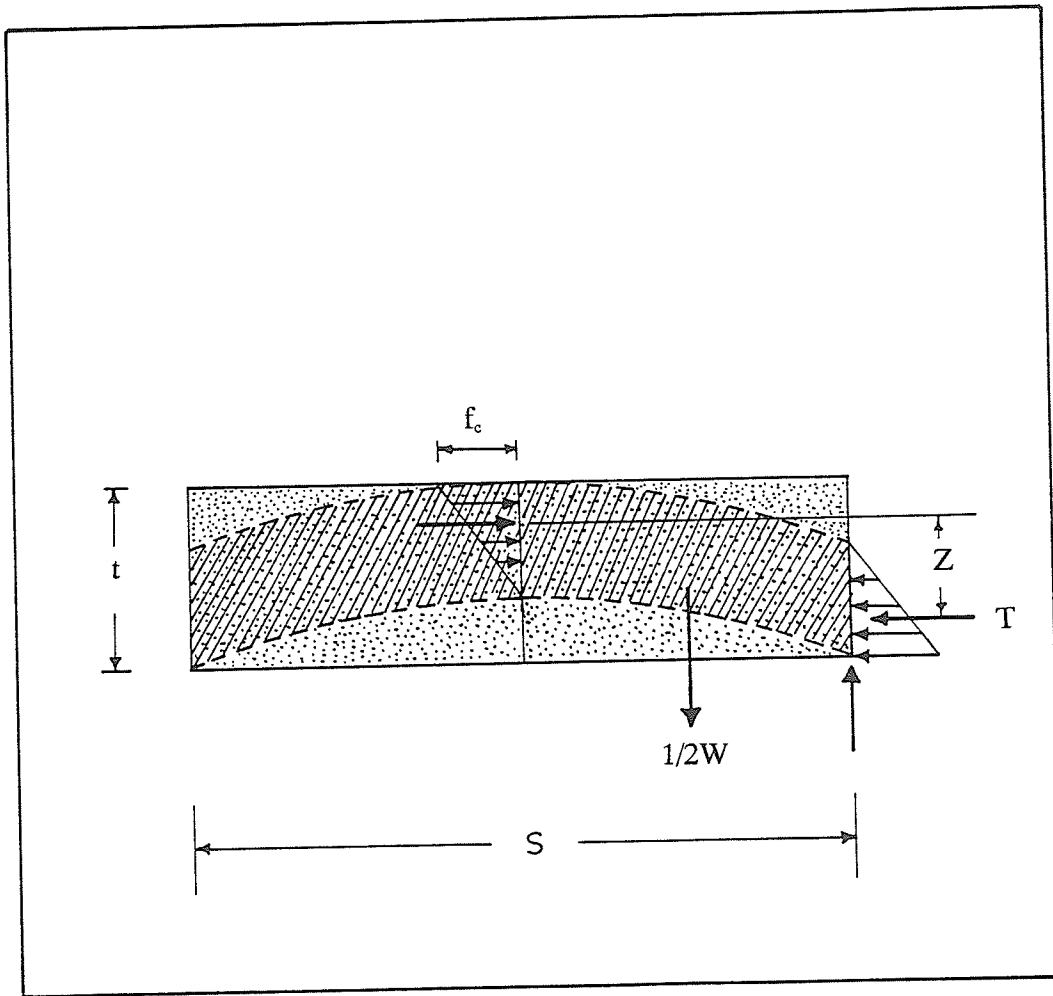
Fig. 8.9 Classical linear arch geometry (after Brady and Brown, 1985).

8.6, stage I), which also marks the development of the linear arch.

Strain gauges applied on the specimen show this transformation (Figs. 8.10, 8.11, and 8.12). As would be expected for a beam, in Fig. 8.10, at relatively small load strain gauge, R3, shows tensile stress. After bottom midspan cracking, the gauge indicates a gradual change to compressive stress, which subsequently increases steadily till ultimate failure. Fig. 8.11 depicts similar behaviourr for strain gauge R2. The strain gauge, R1 shown in Fig. 8.12, because of its position above the neutral axis, remains compressive throughout the loading history.

As loading continues following mid-span cracking, a pair of diagonal cracks initiates and propagates very rapidly towards each abutment of the rock beam. Their development marks the end of stage II of failure (Fig.8.6). Strain gauges placed on the specimen show that the diagonal cracks are tensile in origin (Fig. 8.13). The strain gauge depicted in this Figure indicates a compressive stress as the midspan crack initiates, followed by an increasing, tensile response. The tensile stress drops momentarily as the midspan crack passes by it vertically, but then steadily increases to approximately 3.3 MPa. Finally, the tensile stress increases indefinitely as the diagonal crack opens just beneath the strain gage. The average tensile strength of Tyndall Stone used to prepare the specimen is 3.7 MPa.

The diagonal cracking occurs when the tensile stress at some point in the specimen reaches the tensile strength of the rock. To verify this, the vertical shear stress corresponding to the limiting tensile stress can be computed (eqn. 8.1) and compared to the maximum vertical shear stress obtained from the measured vertical load at the instant of diagonal cracking. The computed vertical stress, v_{urc}, is be given as

$$v_{urc} = (\sigma_t^2 + \sigma_{ca}\sigma_t)^{1/2} \qquad (8.1)$$

where,

σ_{ca} = axial stress

105
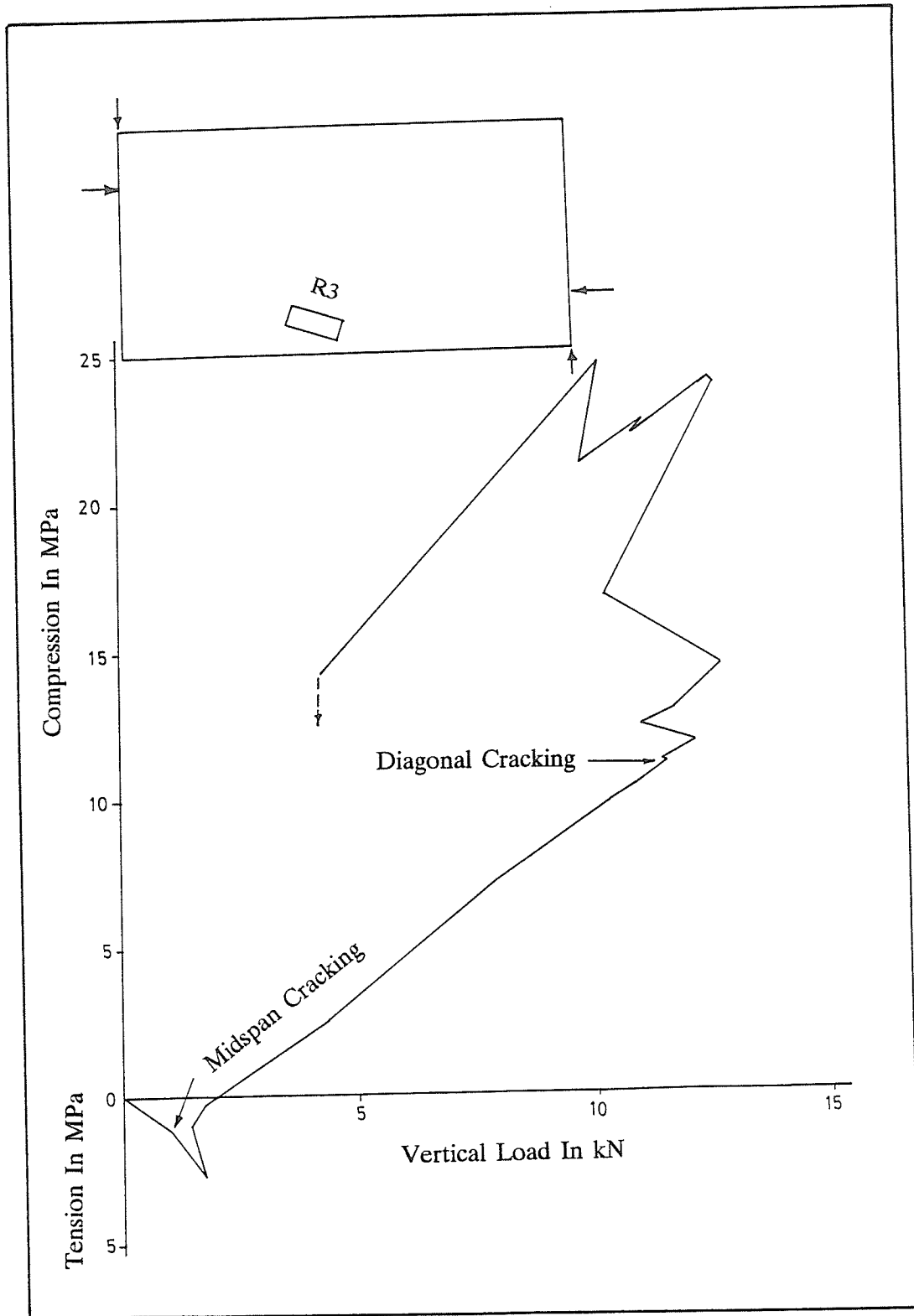
Fig. 8.10 Estimated stress from strain registered on the gage R3 vs. vertical load.
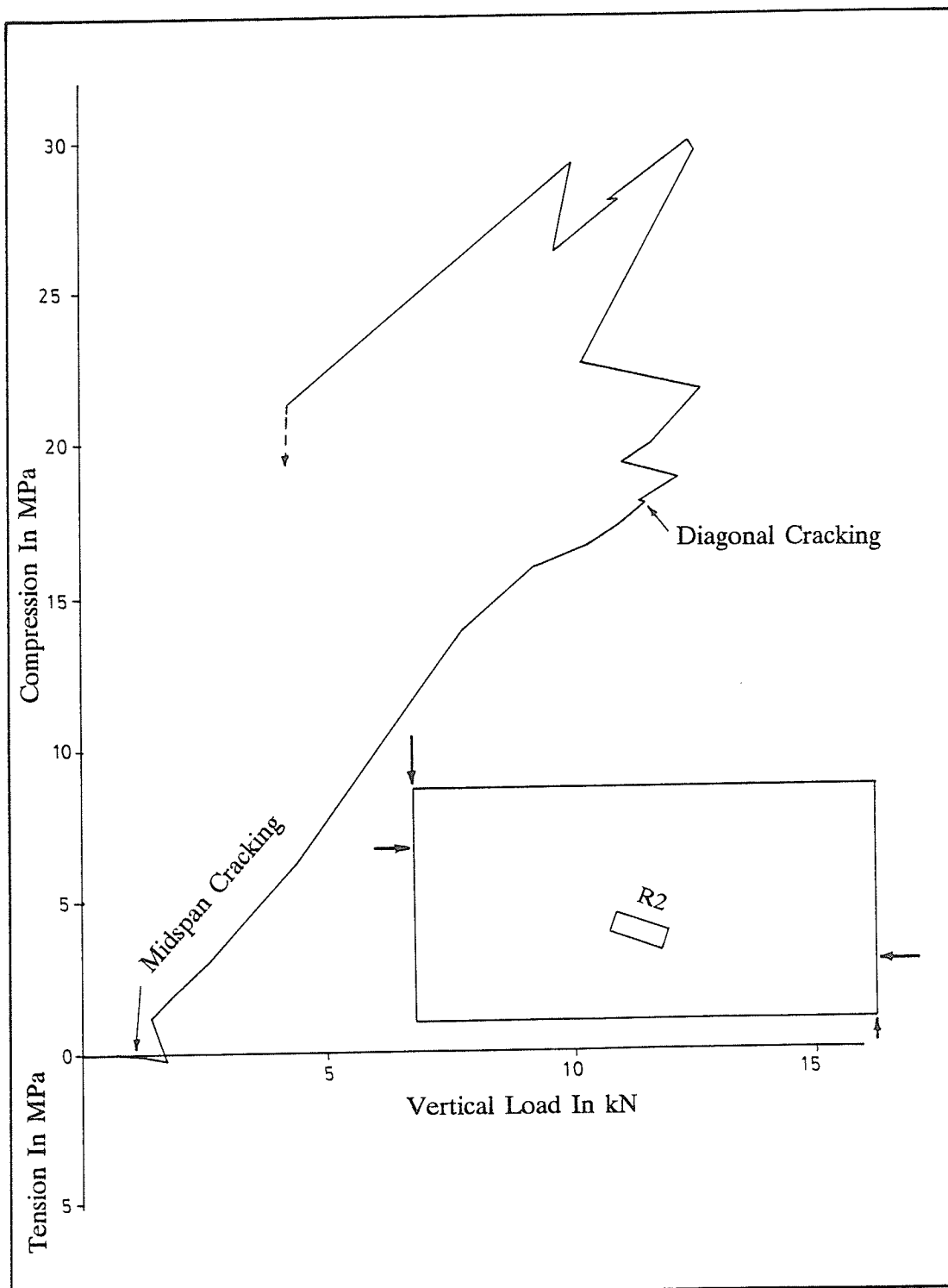
Fig. 8.11 Estimated stress from strain registered on the gage R2 vs. vertical load.
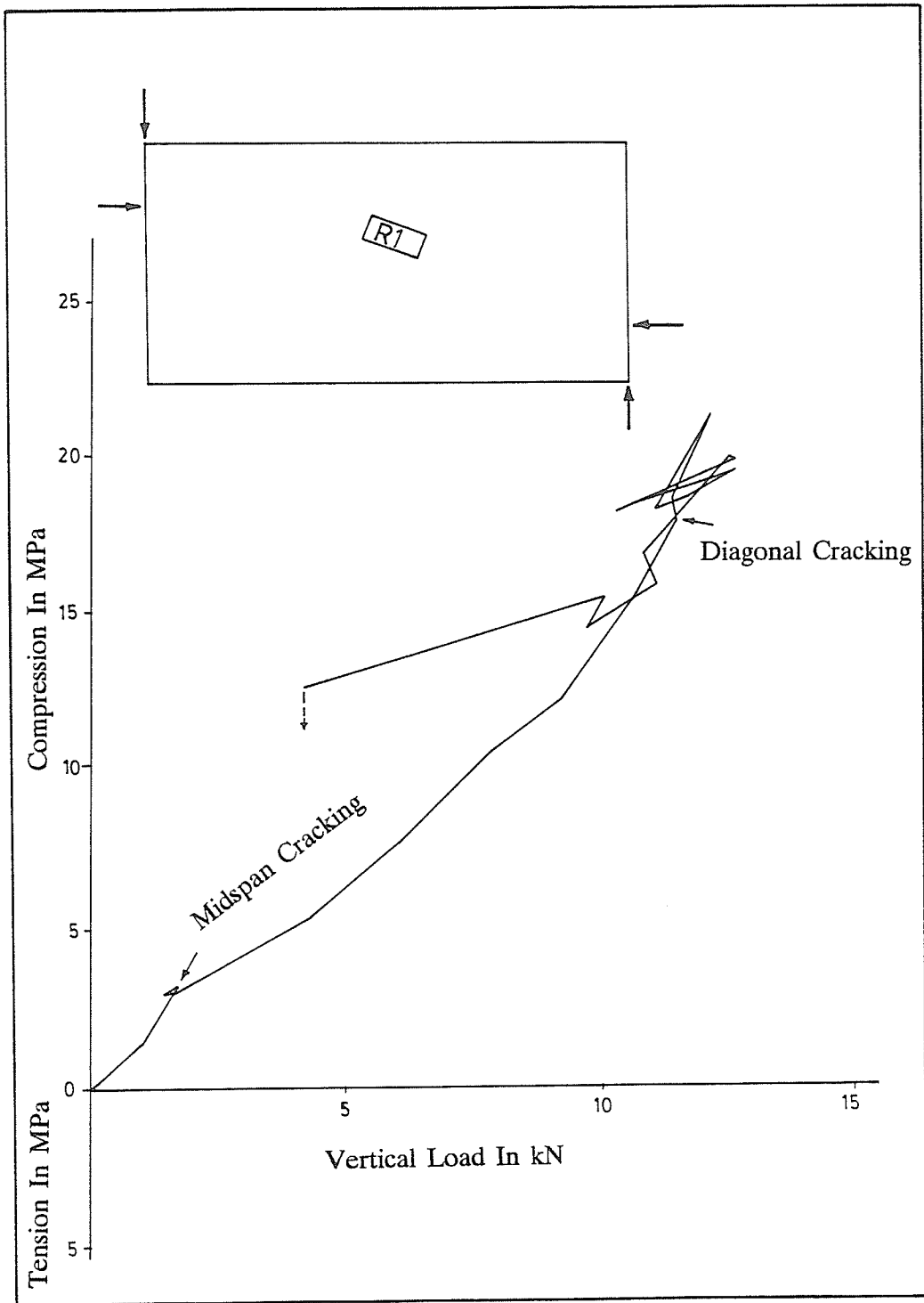
Fig. 8.12 Estimated stress from strain registered on the gage R1 vs. vertical load.
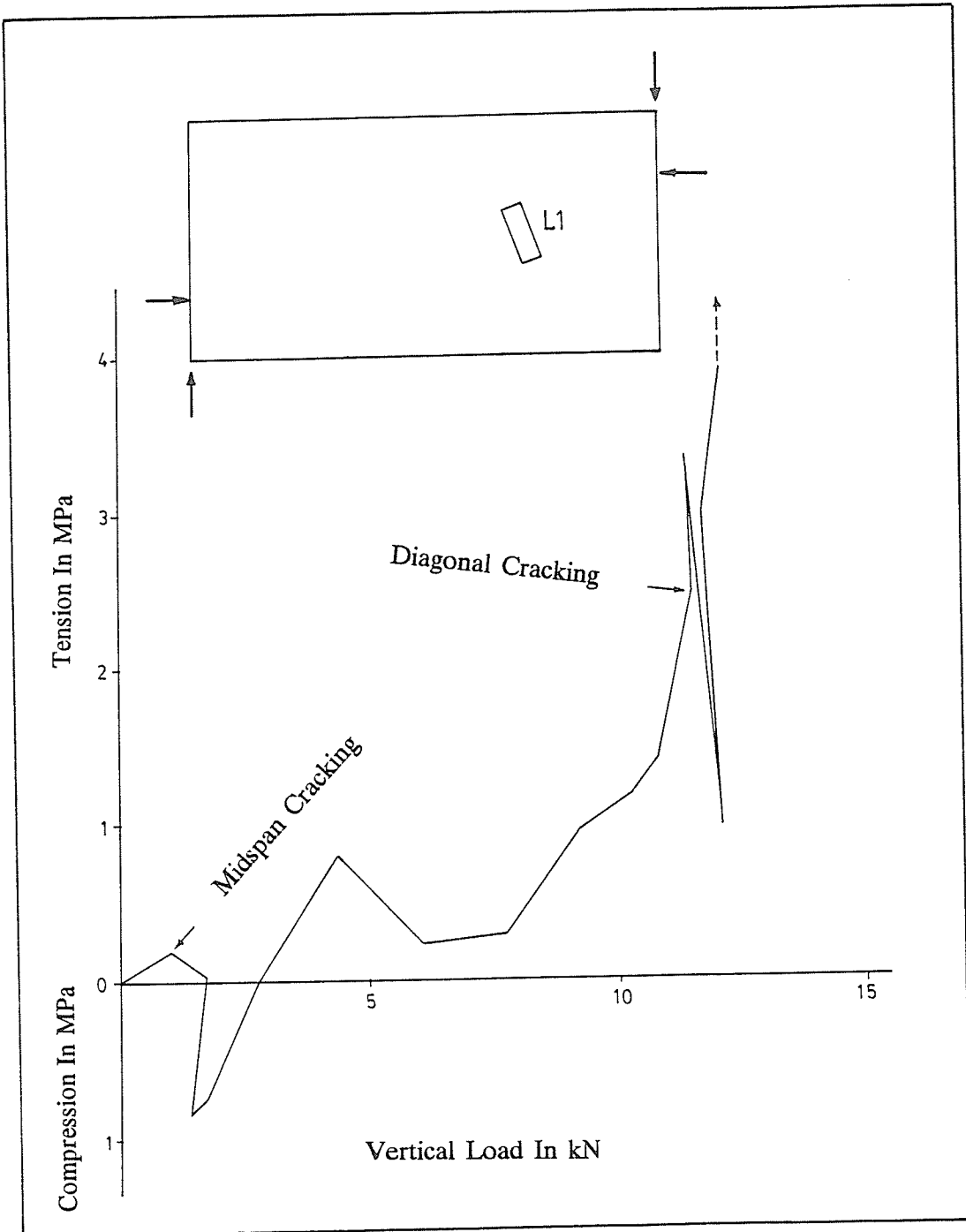
Fig. 8.13 Estimated stress from strain registered on the gage L1 vs. vertical load.

σ_t = tensile strength

Fig. 8.14 shows good agreement between the computed and measured values. A sample calculation of the data used in this plot is presented in Appendix — VIII.

With continued loading beyond the stage of diagonal cracking, ultimate, violent failure occurs either by (a) failure of intact rock above the diagonal crack and consequent shearing of the remnant intact rock below, or by (b) shearing along a plane that contains the diagonal crack (Fig. 8.15). It was found that the second mode of ultimate failure tends to occur in thinner beams. This observation was based on the examination of specimens recovered after ultimate failure in beam tests. Sketches of the recovered specimens, emphasizing the important features, are shown in Fig. 8.15. Here, ultimate failure modes (a) and (b) are depicted in the left and right schematics respectively.

The importance of these experimental findings is that the classical Voussoir arch theory, in which ultimate collapse is attributed to compressional crushing at the centre or the abutments, is not corroborated by these experiments (Fig.8.9). Rather, the rock beam is progressively weakened by tensile fracturing and ultimately fails by rupture through a remnant zone of intact rock or rock bridge (Fig.8.15).

8.8 STABLE VS. UNSTABLE FAILURE OF LINEAR ARCH

In a testing machine, stable or unstable failure of a specimen depends on the stiffness of the loading system relative to that of the rock at failure.

This topic has been discussed by Jaeger and Cook (1979). In Fig. 8.16, the load-displacement relationships for the machine and for a rock sample in uniaxial compression are shown. The stiffnesses of a soft and a stiff machine are expressed by lines, k_1 and k_2 respec-
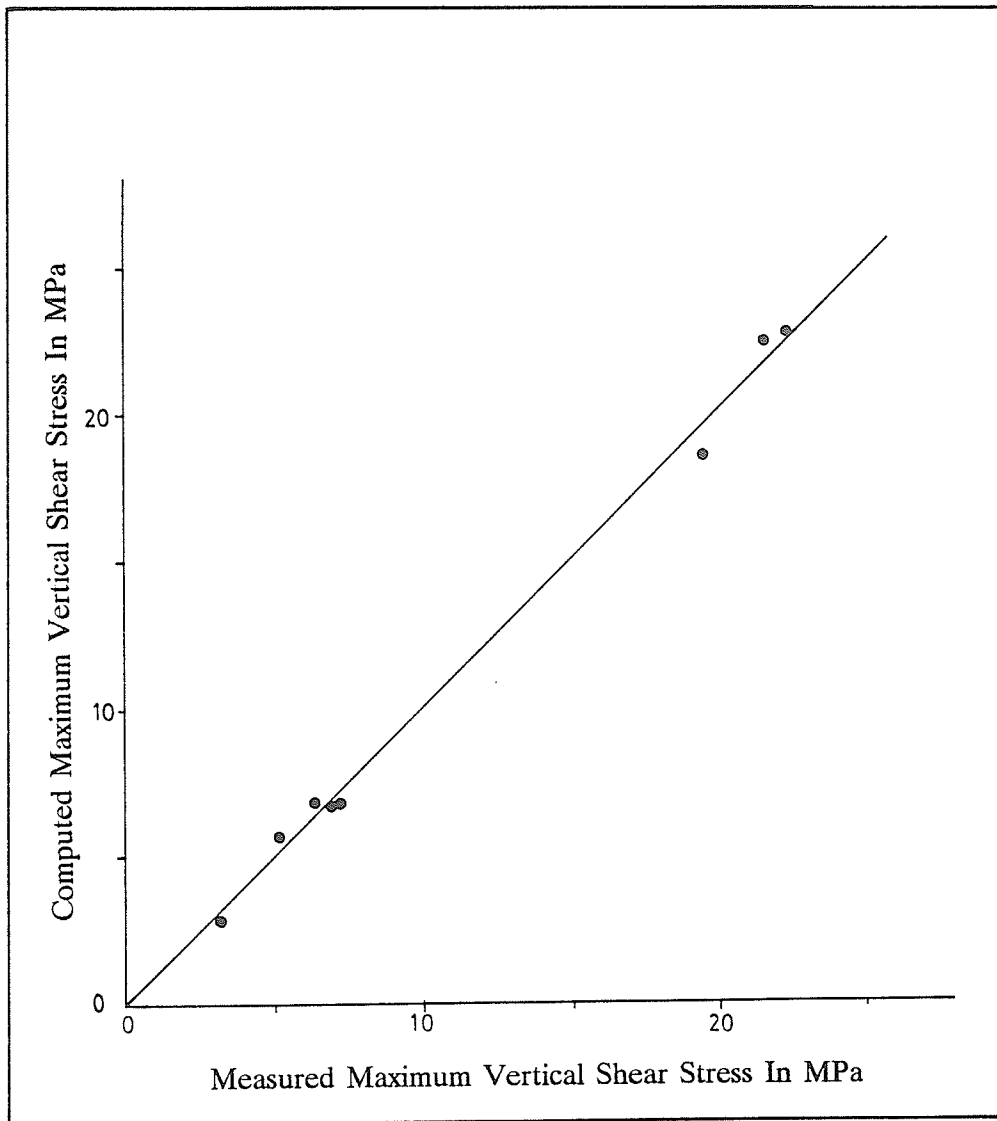
Fig. 8.14 Comparison of computed and measured maximum vertical shear stresses at diagonal cracking.
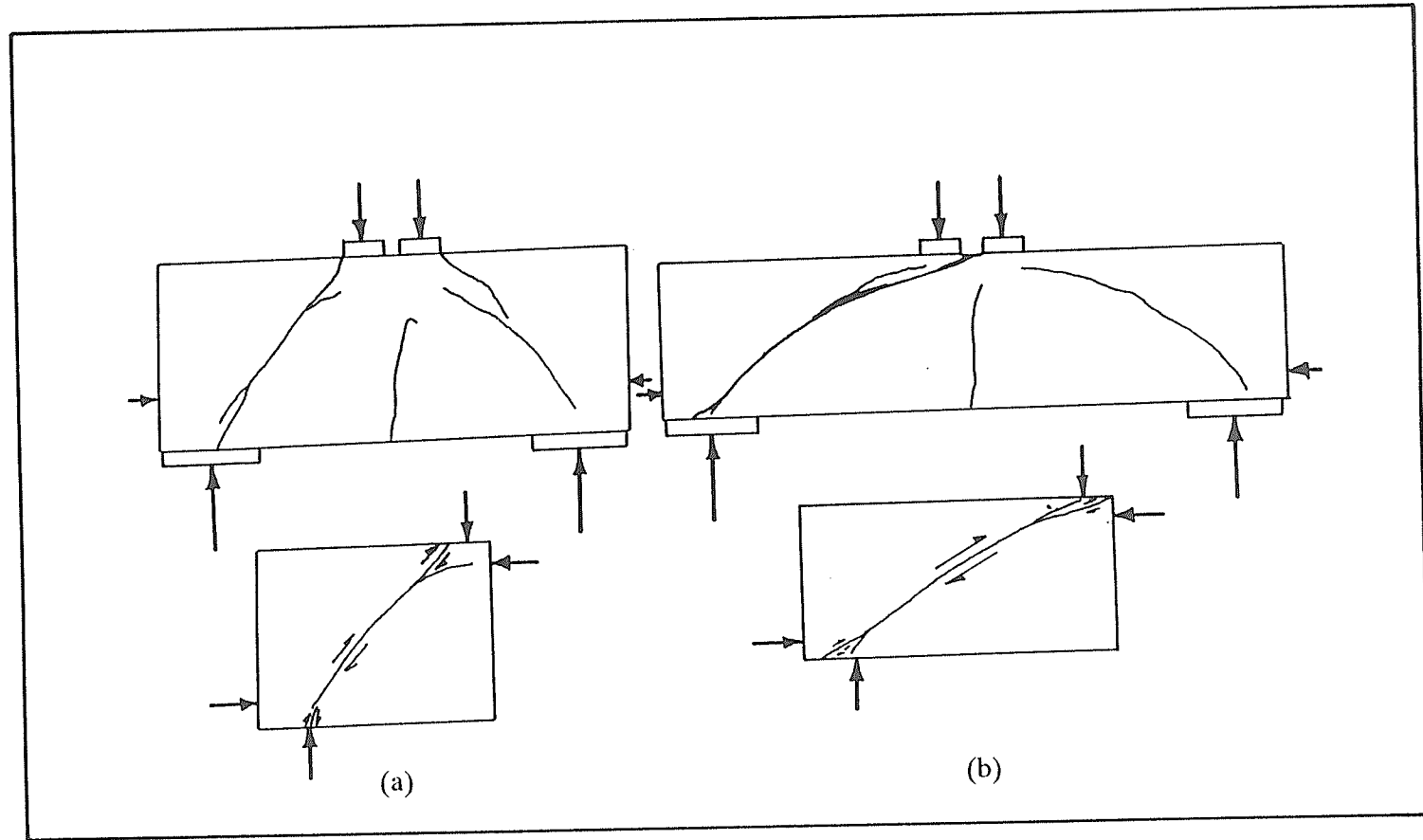
Fig. 8.15 Failure mechanisms at the stage III in beam test : (a) failure of intact rock above diagonal crack and consequent shearing of the intact rock below, and (b) slip along diagonal crack.
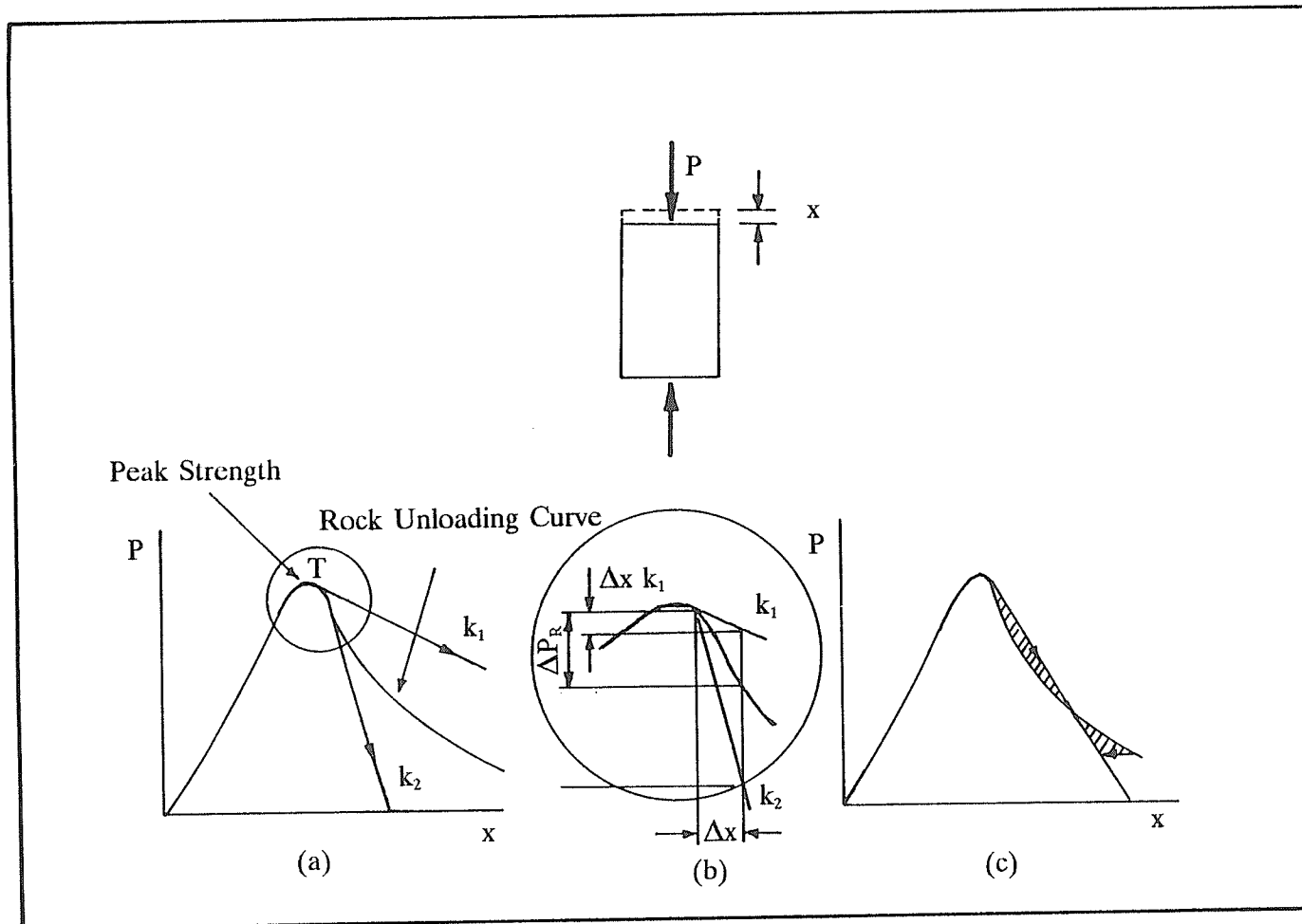
Fig. 8.16 (a) A complete load-displacement curve for a rock specimen with lines showing the behaviour of soft, k_1, and stiff, k_2, testing machines. (b) An enlargement of the peak of the load-displacement diagram. (c) Transient instability (after Jaeger and Cook, 1978).

tively.

In the event of a small additional compression, Δx, near the point of tangency, T (Fig. 8.16) the resistanceof the rock specmen decreases by an amount $\Delta P_R = (dP/dx)\Delta x$. Also, if energy is neither added to nor extracted from the system in this interval, the load applied by the machine decreases by $k\Delta x$. For k_1, $| dP/dx | > | k_1 |$, i.e., the specimen resistance is less than the load applied to it by the machine at $x + \Delta x$. Over this interval, the machine contains more energy (represented by the area beneath the line k_1) than the energy required to deform the specimen by Δx (represented by the area beneath the load-displacement curve). The excess must be released, and does so in the form of kinetic energy and heat energy. The rock sample, already fractured, accelerates and a violent and abrupt failure results, with rock fragments ejected from the testing machine.

In the case of a stiff machine, k_2, $| dP/dx | < | k_2 |$, the situation is stable, since the machine contains less energy (area beneath the line k_2) than the energy required for additional compression, Δx (area beneath the load-displacement curve of the specimen).

In Fig. 8.16(c), the non-linear nature of the post-peak load-displacement curve of the rock sample makes it possible for a transient instability to arise at a point where $| dP/dx | > | k |$ and the total energy stored in the testing machine is less than that required for complete compression of the specimen.

In testing rock beams with "soft" machines (i.e., the stiffness of the loading machine and testing frame is lower than that of the specimen unloading curve at failure) such as the one used in this study, the ultimate failure was sudden and violent.

8.9 IMPLICATION REGARDING SEISMICITY

8.9.1 THE MECHANISM OF EARTHQUAKE

In seismometry, the simplest and most conventional picture of an earthquake source —— a point source —— is used to locate the origin of seismic waves. Although the point source model is suitable for such a purpose, it is unrealistic for a more detailed analysis for a source mechanisms.

On physical grounds, it is evident that the energetic process at the source occupies a finite volume in the earth. Empirical formulae based on various data indicate that the source dimensions are related to the magnitude. The larger the earthquake magnitude, the greater the volume of the source.

The above statements lead to the dual view of source —— (a) as a point source in the seismometric sense, and (b) as a volume source in the energetic sense. This dual approach, however, causes little confusion (Kasahara, 1981). The source volume, actually, represents a space around a fault from which the strain energy is released. Also, the focus, i.e., the point source in the seismometric sense is the point in this volume where rupture begins and from which the earliest P-wave radiates. Therefore, the two views of a source are complementary, rather than contradictory to each other when describing physical processes at the source of an earthquake.

Much of our knowledge of the events that occur in the vicinity of the focus of an earthquake has come from the "elastic rebound theory" of Reid (1911). According to this theory, an earthquake occurs as a result of progressive accumulation of elastic strain energy in the rock, and the consequent release of the stored energy by faulting when the strength is

exceeded. The concept of shear-fracture (according to the Mohr-Coulomb rupture criterion) causing the earthquake is implied in the elastic rebound theory.

The nature of shear failure in brittle, elastic material is illustrated in Fig. 8.17. Here, relative movement of rock taking place on opposite side of the plane of maximum effective shear stress strains the rock to the point where fracture is produced. The rock "snaps" back to the unstrained condition upon fracturing. This action, which is called "elastic rebound", releases the elastic energy stored in the rock. It would have the same effect on rock as would an explosion or a blow with a hammer, and would produce elastic waves which correspond to the seismic waves of an earthquake (Woodruff, 1966).

It is easy to imagine that processes of fracture in the real Earth must be rather complicated. But, the above model of the mechanism of earthquake is a reasonable simplification which has been used by various researchers for the energy calculations of mining-induced seismicity (e.g., Woodruff, 1966; Cook, 1976; Ortlepp, 1983).

8.9.2 POSSIBLE EARTHQUAKE MECHANISMS IN SASKATCHEWAN POTASH MINES EXCLUDING RE-ACTIVATION OF EXISTING FAULT

Mine excavations disturb the virgin state of stress by creating stress concentrations in the rock. Rock mass, when stresses approach the value its strength, emits seismic pulses. Mining activity gives rise to seismicity ranging from microseismic events radiating 10^{-5} J (Richter magnitude : $M_L = -6$) to rockbursts radiating 10^9 J (Richter magnitude : $M_L = 5$) (Cook, 1976).

As discussed in the preceding section, seismicity occurs when a mass of brittle rock undergoes sudden failure along a shear plane. In the case of the Dawson Bay Formation

116

Tension Waves   Compressive Waves

(a)   (b)   (c)

(a) Element Subjected to Shear Stress   (b) Strain Produced by Shear Stress

(c) Shear Fracture and "Elastic Rebound"
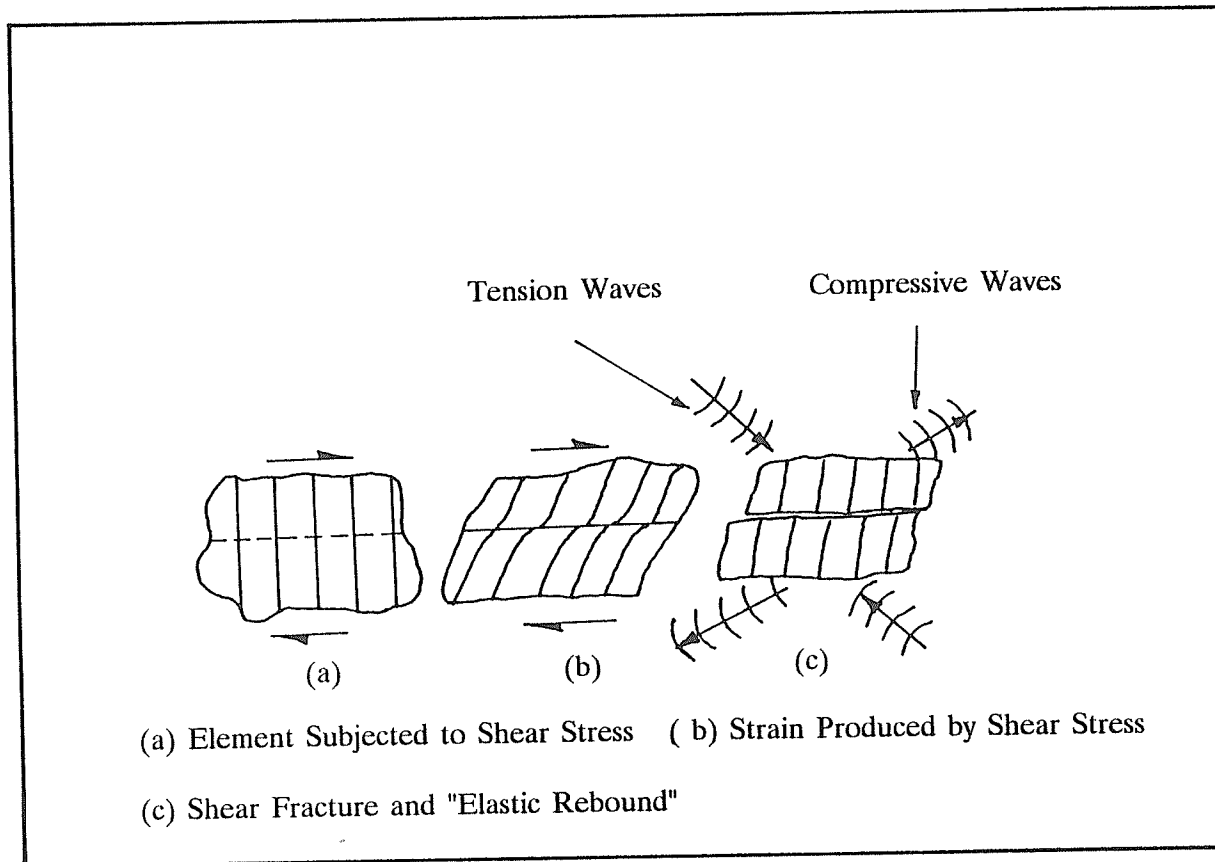
Fig. 8.17 (a) Rock element subjected to shear stress. (b) Strain produced by shear stress. (c) Shear fracture and elastic rebound (after Woodruff, 1966).

in the Saskatchewan potash mining area, this situation could arise in the following two events :

(a) slip (shear fracture) along the bedding plane of the Dawson Bay Beam, and

(b) ultimate rupture of Dawson Bay Linear Arch.

It had been shown in Chapter 7 that failure along the bedding plane of Dawson Bay Beam is capable of generating only microseismicity (Richter Scale : $M_L < 0$), not larger events. However, the ultimate rupture of a Dawson Bay Linear arch could generate larger seismic events.

In the physical simulation of a linear arch, the loading machine was "soft", and consequently, the ultimate failure was sudden and violent (see Section 8.8), releasing seismic energy instantaneously. In Saskatchewan Potash mines, when a panel is excavated, initially, the pillars support the overburden. Owing to the time-dependent mechanical properties of evaporites, the support pillars would progressively lose their strength. Consequently, the overburden would be increasingly carried by the brittle dolomites and limestones of the Dawson Bay Formation just above the salt and potash as it continuously undergoes increasing subsidence. Since the overlying strata which load upper surface of the Dawson Bay Linear Arch is of generally weaker material, should such pillars be of insufficient strength and begin to fail, the loading of the Dawson Bay Linear Arch would proceed inexorably under the weight of the overburden, as it does in the case of the rock specimen tested in a "soft" or "dead-weight" testing machine. In this case, a significant seismic event would result.

Tentative calculations (presented in Section 8.9.3) based on the mode of mechanism of earthquake discussed in Section 8.9.1, show that the magnitude of the seismic energy released in a full scale rupture of a Dawson Bay linear arch would be in the order that has been observed for the larger events.

In the calculations, shear of failure of an intact linear arch is considered. Obviously, the intact linear arch would be weakened beforehand by midspan cracking and diagonal cracking as predicted by the physical modelling of the linear arch (see Section 8.7). But

due to the absence of data on the interface shear transfer across the crack, these detail mechanisms could not be incorporated into the calculation scheme. Accordingly, calculations which are given in the next Section are, in fact, the upper bound of the estimate of seismic energy that would be released in a full scale rupture of the Dawson Bay linear arch.

8.9.3 ESTIMATE OF SEISMIC ENERGY RELEASE

For this calculations, the rupture of a 40 m (t) thick Dawson Bay linear arch is considered. The maximum shear stress in this linear arch would develop at an angle, $\alpha = 45^0 - \phi/2$ from the direction of the major principal stress, where, ϕ is the angle of internal friction and in this case, $\phi = 46^0$. Therefore, $\alpha = 22^0$.

Hence, in case of a failure, for the major principal stress parallel to the axial direction, the length of the fault plane l, is

$$l = t/Sin\alpha = 107 \text{ m}$$

The fault surface that would be created by the shear fracture of the Dawson Bay linear arch is taken to be circular as is generally assumed for a realistic model of faulting (Savage, 1966).

The physics of the situation when the traction on a circular fault having a diameter of 107 m in a shear field is suddenly lost will now be discussed.

For an average panel span (s) of 150 m the volume of the rock under induced stress v_i, is

$$v_i = \frac{1}{4} (\pi * l^2) * s = 1348804 \text{ m}^3 \qquad (8.2)$$

From the simple eqn. (8.3) one can calculate the energy release, U, per unit volume when the fault is suddenly created.

$$U = \left\{ \frac{(m+1)*(m-2)}{m*(m-1)} \right\} * \sigma_c^2/2*E \qquad (8.3)$$

where,

m = Poisson's constant = 4

σ_c = uniaxial compressive strength = 104 Mpa

E = Young's modulus = 35 GPa

Therefore, U = 0.14 MJ/m^3.

If the distribution of compressive stress in the rock prior to the rupture is linear, the distribution of energy release would be parabolic as the energy released per unit volume varies as the square of the stress. And therefore, the average unit energy release, U_a, is

$$U_a = U/3 = 0.047 \text{ MJ/m}^3 \qquad (8.4)$$

From eqns. (8.2) and (8.4) :

Total Energy Release, $E_r = v_i*U_a$

= 63264 MJ

Seismic efficiency, i.e., the percentage of seismic energy released has been found to be in the order of 1% (Cook, 1963). Accordingly, the seismic energy released E_s, is

$$E_s = 633 \text{ MJ}$$

From the relationship between local magnitude (i.e., the Richter Magnitude), M_L and seismically radiated energy (expressed in MJ) given by Richter (1958) :

$$\log(E_s) = 1.5 M_L - 1.2$$

Therefore, M_L = 2.7.

CHAPTER 9

NUMERICAL MODELLING

9.1 INTRODUCTION

The principal objective of the numerical analyses was to gain greater understanding of the failure mechanism which was observed in the previously described beam testing.

The numerical modelling of this study was performed using a finite difference program and a finite element program, with the model based on the mechanical properties of Tyndall Stone (Table 9.1).

9.2 FINITE DIFFERENCE ANALYSIS

The finite difference program used in this study is called FLAC (Fast Lagrangian Analysis of Continua). It is a commercial finite difference package for personal computer written by ITASCA Consulting Group Inc. (see the FLAC manual).

FLAC is an explicit finite difference code which simulates the behavior of structures built of geological materials which may undergo plastic flow when their yield limit is reached. Materials are represented by two-dimensional zones (elements) interconnected at their gridpoints (nodes), which form a meshwork that is adjusted by the user to fit the shape of the object to be modelled. In response to the applied forces and boundary restraints, each zone

Uniaxial copressive strength	50 MPa
Modulus of elasticity	32 Gpa
Poisson's ratio	0.21
Uniaxial tensile strength	3.7 MPa
Angle of internal friction	40°
Cohesion	10.5 MPa
Fracture toughness	1.25 MPa $\sqrt{m}$

Table 9.1 Average mechanical properties of Tyndall Stone.

follows a user prescribed linear or non-linear stress/strain law. The mesh actually deforms and moves with the material it represents in the event where stresses are high enough to cause the material to yield and flow. This calculation scheme is well suited to modelling large distortions and is called "Lagrangian".

FLAC uses the explicit finite difference method to solve the basic equations of motion. This method makes use of the idea that, for small timesteps, a disturbance at a given gridpoint is experienced only by the points in the immediate vicinity. For a short period of time, only the neighboring gridpoints would "realize" the disturbance. As time elapses, however, the effect of the disturbance will spread through the grid. The timestep, which must be less than the time of propagation of the phenomenon between two adjacent gridpoints, is automatically determined by FLAC to ensure numerical stability.

This program solves static problems by properly damping the dynamic solution. In this case, "timestep" refers to a computational timestep, not a physical timestep. Because matrices are never formed, the computational effort per timestep is small and hence the computer memory requirements are minimal. The explicit calculation cycle employed by FLAC is explained in Fig. 9.1. This calculation is repeated every timestep to reach equilibrium. The number of timesteps required in this regard depends on factors such as the user's prescribed numerical tolerence, the extent of yield in the material, the size of the problem, etc.

9.2.1 FLAC RESULTS

A typical beam test (span X depth : 30 cm X 7 cm) was simulated using the FLAC code. Fig. 9.2(a) shows the rock specimen and the restraining end plates with meshwork right of the symmetry line. Soon after loading commences, tensile stresses at the lower fibres

```
┌─────────────────────────────────────────────────┐
│                 LAW OF MOTION                    │
│                                                  │
│              For Each Gridpoint                  │
│                                                  │
│                                                  │
│   · determine out-of-balance forces at grid-    │
│     point from zone stresses                     │
│                                                  │
│                                                  │
│   · determine gridpoint velocity components     │
│     from out-of-balance forces                   │
│                                                  │
│                                                  │
│   · determine gridpoint displacements by in-    │
│     tegrating velocities                         │
│                                                  │
└─────────────────────────────────────────────────┘


┌─────────────────────────────────────────────────┐
│               STRESS-STRAIN LAW                  │
│                                                  │
│                For Each Zone                     │
│                                                  │
│                                                  │
│   · determine strain rates from gridpoint       │
│     velocities                                   │
│                                                  │
│                                                  │
│   · calculate stress increment from stress-     │
│     strain law                                   │
│                                                  │
└─────────────────────────────────────────────────┘
```

Fig. 9.1 Overview of FLAC code operations (FlAC manual, 1987).

Rock Specimen

(a)

End Plate

Mohr-Coulomb Safety Factor (Contour Interval = 0.5)
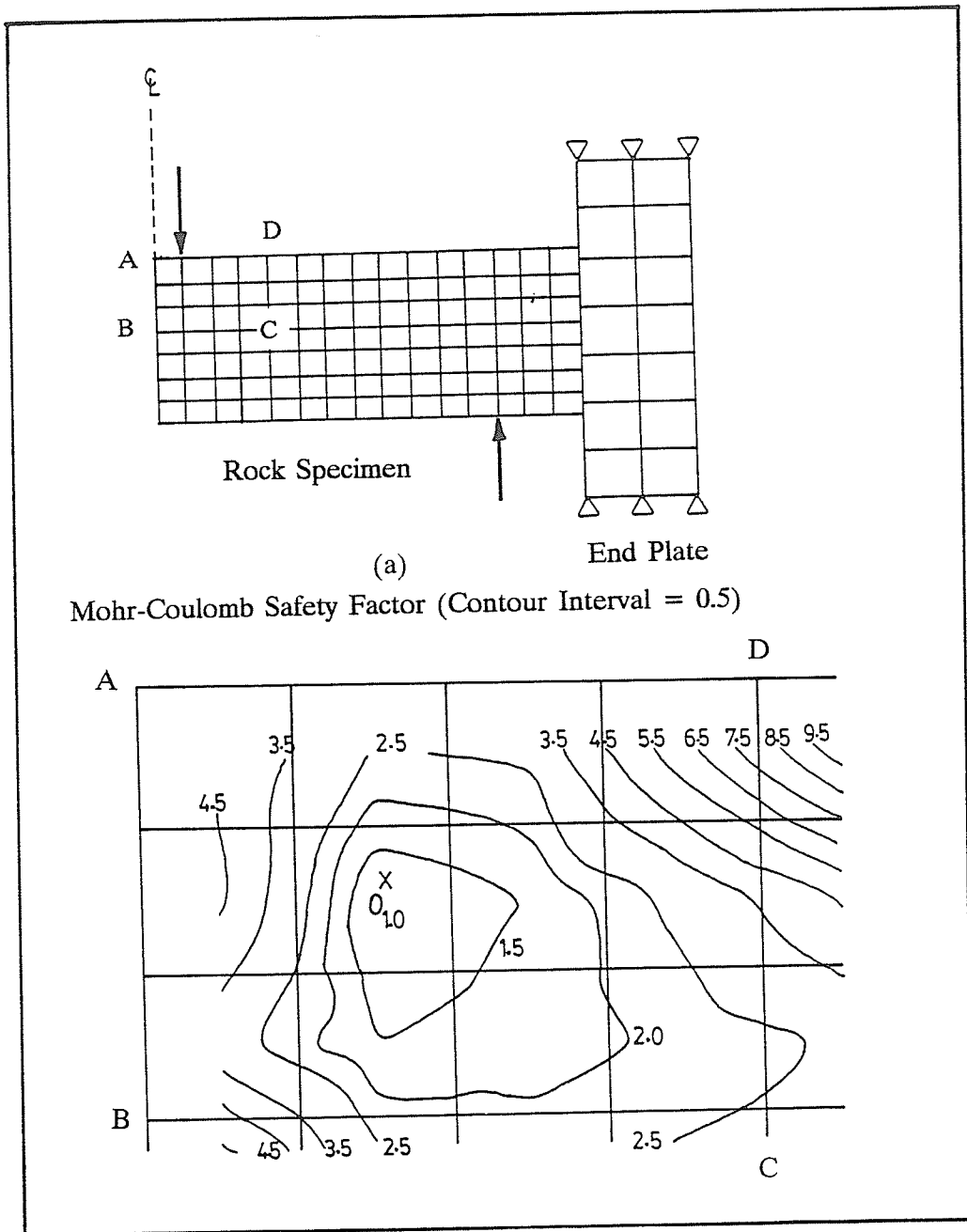
(b)

Fig. 9.2 Simulation of a typical beam test using FLAC code.

in the midspan exceed the tensile strength of the rock. At this point, the midspan crack was simulated by releasing selected grid points. As the loading continues, the change in the stress field (Fig. 9.3) due to the presence of this midspan crack and the development of a linear arch results in the initiation of the diagonal crack, principally under tensile stress.

In Fig. 9.3, at point marked "x", the maximum and minimum principal stresses are 21.7 MPa (compressive stress) and 2.9 MPa (tensile stress) respectively. This stress combination satisfies the condition of Mohr-Coulomb yield criterion at that point. Fig. 9.2(b) shows the contours of the Mohr-Coulomb Factor of Safety plotted in the ABCD region [Fig. 9.2(a)] of the specimen. Hence, at point x, where the Factor of Safety is 1, the diagonal crack initiates. The position at which diagonal cracking takes place is comparable to that from the beam testing results.

Additionally, a preliminary analysis to simulate a full scale mine excavation using FLAC was attempted by the writer. In this analysis, the various rock strata were modelled using Mohr-Coulomb elasto-plastic elements having strain-hardening/strain-softening capabilities. The Prairie Evaporite Formation and the Dawson Bay Formation along with the joints and bedding planes were modelled using the material properties data given in Table 2.1. A 150 m span single room was "excavated" within the rock mass of potash. This simulation represents the situation long after the excavation of the openings when the support pillars within the mine panel have completely lost their strength. Since the elasto-plastic model does not incorporate any time-dependent material behavior, this was how long-term simulation was carried out. The results show that the failure zone in the Dawson Bay Formation has an outline of the arch (Fig.9.4).
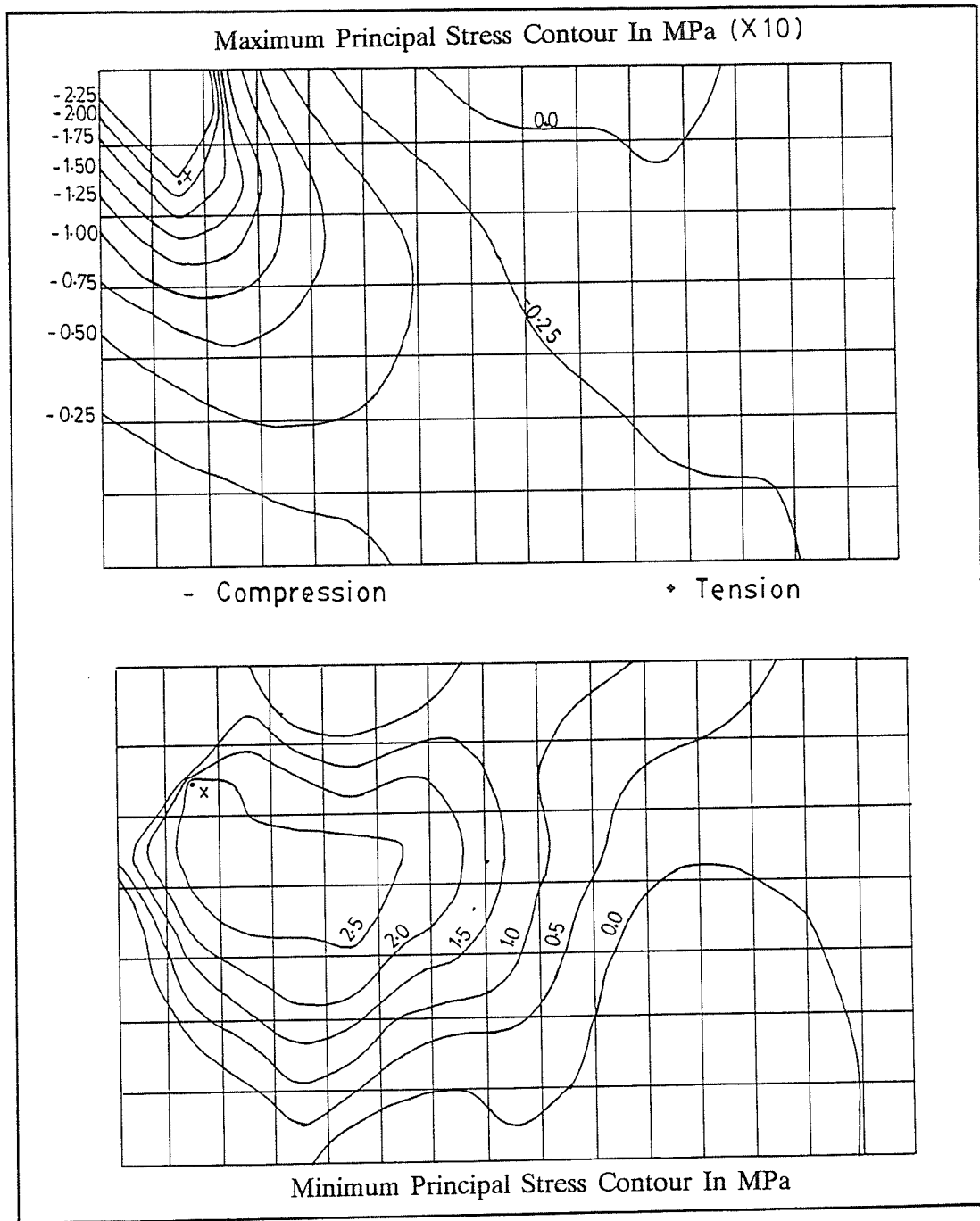
Fig. 9.3 Contour plots of major and minor principal stresses at diagonal cracking from the results of a typical beam test simulated by FLAC code.
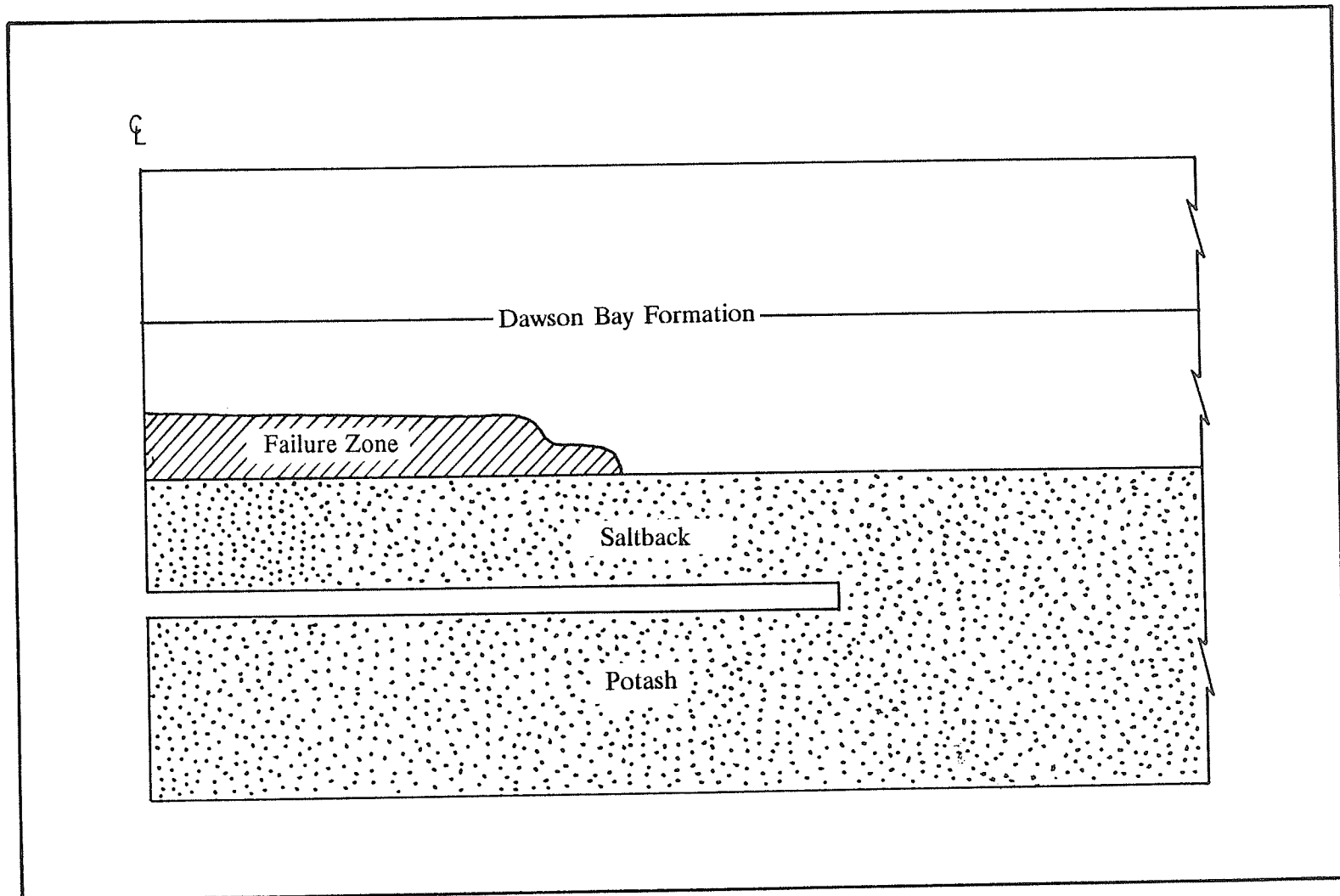
Fig. 9.4 Arch-like outline of the failure zone in the Dawson Bay Formation.

9.3 FEM MODELLING WITH CRACK PROPAGATION

9.3.1 INTRODUCTION

The finite element method (FEM), because of its ability to take into account conditions of equilibrium, compatibility and non-linear material behavior, is a valuable analytical tool which can be used to simulate structural response in the entire load range up to ultimate failure.

Representation of crack propagation is a more recent development in finite element analysis and can be carried out by one of the two following ways. The first is the crack band approach used in conjunction with a "smeared crack" model, in which the cracking is accounted for by changing the isotropic elastic matrix to an orthotropic one, reducing the material stiffness in the direction normal to the cracks in the band (ASCE, 1982). In contrast, the discrete crack models assume that the fracture zone consists of only a "tied" crack, i.e., a crack of varying width δ with ability to transfer stresses σ according to the σ - δ curve.

Since the latter approach models the reduction of stiffness during failure, not as that of an inherent material property, but rather as a structural property, wherein the proliferation of cracking leads to a reduction in the effective cross-sectional area, it is more realistic. Hence, the latter model, namely a discrete crack propagation model, written by Ayari el al. (1988), has been used in this study. In this model, the theory of linear elastic fracture mechanics (LEFM) under mixed mode loading in 2D was employed.

9.3.2 BASIC CONCEPTS OF LINEAR ELASTIC FRACTURE MECHANICS

9.3.2.1 THE STRESS INTENSITY FACTOR

The stress intensity factor of a crack in 2D can formally be defined as :

$$\left\{ \begin{matrix} K_I \\ K_{II} \end{matrix} \right\} = \lim_{r \to 0, \, \theta = 0} \sqrt{2\pi r} \left\{ \begin{matrix} \sigma_{22} \\ \sigma_{12} \end{matrix} \right\}$$

where σ_{ij} are the near crack tip stresses, and K_i are associated with two independent kinematic movements of the upper and lower crack surfaces with respect to each other in 2D, as shown in Fig. 9.5 :

Opening mode, I : in which two crack surfaces are pulled apart in the y direction, but where the deformations are symmetric about the x-z and x-y planes.

Shearing mode, II : in which the two crack surfaces slide over each other in the x-direction, but where the deformations are symmetric about the x-y plane and skew symmetric about the x-z plane.

9.3.2.2 MIXED MODE CRACK PROPAGATION

Having the stress intensity factors numerically (or analytically) computed and the material fracture toughness (K_{Ic}) experimentally determined, the next step is to formulate fracture initiation criteria encompassing these variables. These are : (a) determination of the angle of incipient crack propagation, with respect to the crack axis, and (b) determination of whether the stress intensity factors are in such a critical combination as to render the crack unstable and force it to propagate.
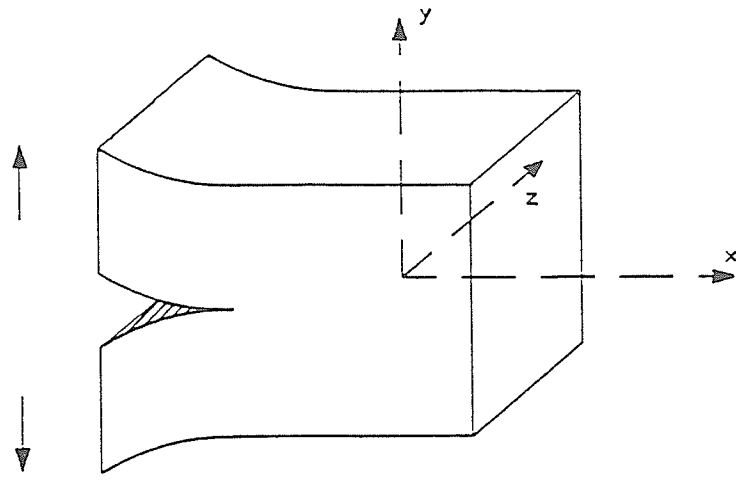
Fundamental mode of fracture

a) Opening Mode I
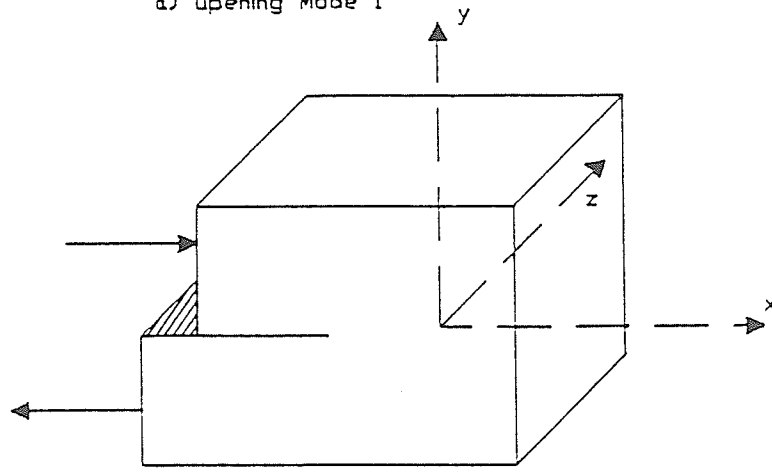
Fundamental mode of fracture

b) Shearing Mode II

Fig. 9.5 Independent modes of crack displacements in 2D.

In case of mode I problems, fracture extension occurs according to the inequality (9.2):

$$K_I \geq K_{Ic} \qquad (9.2)$$

In mixed mode (mode I and mode II) problems, fracture initiation criteria would, however, require a relationship between K_I, K_{II}, and K_{Ic} of the form shown in eqn. (9.3) :

$$F(K_I, K_{II}, K_{Ic}) = 0 , \qquad (9.3)$$

This relationship would be analogous to that between the two principal stresses and a yield stress, e.g., Von Mises criterion (eqn. 9.4) for planar problems.

$$F(\sigma_1, \sigma_2, \sigma_{yld}) = 0 , \qquad (9.4)$$

where,

σ_1 and σ_2 are principal stresses, and

σ_{yld} is the yield stress.

There is no single accepted criterion for mixed mode crack growth; three widely used criteria are discussed below.

9.3.2.2.1 MAXIMUM CIRCUMFERENTIAL TENSILE STRESS

The first mixed mode fracture initiation theory was put forward by Erdogen and Sih (1963). It is known as the Maximum Circumferential Stress Theory, and is based on the stress state near the crack tip, expressed in polar coordinates. According to this theory, crack extension starts : (a) at its tip in a radial direction, (b) in the plane perpendicular to the direction of greatest tension, and (c) when maximum tangential stress, $\sigma_{\theta max}$ reaches a critical material constant.

It can be shown that tangential stress, σ_θ, reaches its maximum value when the corresponding shear stress, $\tau_{r\theta} = 0$ (Ayari, 1988). Hence, if one expresses $\tau_{r\theta}$ as a function of K_I and

K_{II}, one obtains:

$$\tau_{r\theta} = 0 = \frac{\cos\theta_o}{2} \{ K_I \sin\theta_o + K_{II}(3\cos\theta_o - 1) \} = 0 \qquad (9.5)$$

Eqn.(9.5) has the following two solutions:

$$\theta_o = \pm\pi \quad \text{(trivial)} \qquad (9.6)$$

$$K_I \sin + K_{II}(3\cos\theta_o - 1) = 0 \qquad (9.7)$$

The angle of crack propagation can now be explicitly obtained from eqn. (9.8) :

$$\tan\theta_o = \frac{1}{4}\frac{K_I}{K_{II}} + \frac{1}{4}\left\{ \left(\frac{K_I}{K_{II}}\right)^2 + 8 \right\}^{1/2} \qquad (9.8)$$

Finally, equating the maximum circumferential tensile stress to a material dependent critical value, and expressing the equation in a normalized form, one obtains :

$$\frac{K_I}{K_{Ic}}\cos^3\frac{\theta_o}{2} - \frac{3}{2}\frac{K_{II}}{K_{Ic}}\cos\frac{\theta_o}{2} - \sin\theta_o = 1 \qquad (9.9)$$

9.3.2.2.2 MAXIMUM ENERGY RELEASE RATE

The maximum energy release rate theory states that the crack will grow in the direction along which the potential energy release per unit crack extension is maximum, and the crack would start to grow when this energy release rate reaches a critical value. It is based on the application of the Griffith-Irwin potential energy release rate criterion.

Hussain et al. (1974) proposed a solution to the above mathematical problem. According to them, the plane strain energy release rate associated with an infinitesimal extension of the

133

crack tip at an angle θ :

$$G(\theta) = \frac{4}{E} \left(\frac{1}{3 + Cos^2\theta}\right)^2 \left(\frac{1 - \theta/\pi}{1 + \theta/\pi}\right)^{\theta/\pi}$$

$$\{(1 + 3Cos^2\theta)K_I^2 + 8Sin\theta Cos\theta K_I K_{II} + (9 - 5Cos^2\theta)K_{II}^2\} \qquad (9.10)$$

The fracture locus predicted by this theory is given in the following normalized equation:

$$4\left(\frac{1}{3+Cos^2\theta_o}\right)^2 \left(\frac{1- \theta_o/\pi}{1+ \theta_o/\pi}\right)^{\theta_o/\pi} \{(1+3Cos^2\theta_o)\left(\frac{K_I}{K_{Ic}}\right)^2 + 8Sin\theta_o Cos\theta_o \frac{K_I K_{II}}{K_{Ic}^2}$$

$$+(9 - 5Cos^2\theta_o) \left(\frac{K_{II}}{K_{Ic}}\right)^2\} = 1 \qquad (9.11)$$

9.3.2.2.3. MINIMUM STRAIN ENERGY DENSITY

This theory, formulated by Sih (1974), states that the fracture initiates from the crack tip in a direction along which the strain energy density at a critical distance is a minimum and when this minimum reaches a critical value. The fracture locus predicted by minimum strain energy density theory is :

$$\frac{8T}{k - 1} \{a_{11}\left(\frac{K_I}{K_{Ic}}\right) + 2a_{12}\left(\frac{K_I K_{II}}{K_{Ic}^2}\right) + a_{22}\left(\frac{K_{II}}{K_{Ic}}\right)^2\} = 1 , \qquad (9.12)$$

where,

T = Shear Modulus

$k = 3 - \nu$ (plane stress) $\qquad\qquad\qquad (9.13)$

$k = \dfrac{3 - \nu}{1 + \nu}$ (plane strain) $\qquad\qquad\qquad (9.14)$

$a_{11} = \dfrac{1}{16T} \{(1 + Cos\theta)(k - Cos\theta)\} \qquad\qquad\qquad (9.15)$

$a_{12} = \dfrac{Sin\theta}{16T} [2Cos\theta - (k-1)] \qquad\qquad\qquad (9.16)$

134

$$a_{22} = \frac{1}{16T} \{(k + 1)(1 - Cos\theta) + (1 + Cos\theta)(3Cos\theta - 1)\} \qquad (9.17)$$

9.3.3 THE DISCRETE CRACK PROPAGATION MODEL

In the FEM Discrete Crack Propagation Model, cracks are nucleated, and then checked for local fracture stability. Linear elastic fracture mechanics governs the crack growth. Under mixed mode loading the cracks are propagated and failure tracing is readily performed. This is an interactive graphics finite element program for the simulation of crack growth in 2D and for the evaluation of a functional relationship between the normalized stess intensity factor and the crack length. Here, stress intensity factors are extracted numerically using quarter point singular elements around the crack tip (Fig. 9.9 (b)) (for detail on quarter element, see Saouma, 1987).

Algorithmically, the angle of crack propagation is first obtained. Next, the criteria for local stability are assessed. If the pair of stress intensity factors —— K_I and K_{II} —— is inside the fracture loci given in the previous sections, then, without sufficient increase in stress intensity factors, the crack cannot propagate. If outside, the crack is locally unstable. In that case, it will start to propagate. However, either of the following two situations could subsequently result : (a) an increase in the stress intensity factor (and hence, the energy release rate), resulting in a global instability —— failure of the structure (i.e., crack reaching a free surface) or (b) a decrease in the stress intensity factor (and hence, the energy release rate) due to stress redistribution, the pair of stress intensity factors returning to within the fracture loci.

In the discrete crack propagation FEM analysis the theory of maximum circumferential tensile stress, which is the most widely used criterion for mixed mode crack growth, was used.

It should be noted that a crack under mixed mode loading will tend to reorient itself so that the ratio K_{II}/K_I is minimized, i.e., K_{II} is minimized. Hence, a crack would often be, during its trajectory, in that portion of the normalized K_I/K_{Ic} -- K_{II}/K_{Ic} space where the above three theories of crack growth are in close agreements.

9.3.4 DISCRETE CRACK PROPAGATION FEM RESULTS

Using Discrete Crack Propagation FEM analysis, a typical beam test (beam dimensions : 30 cm X 6.25 cm) was replicated. The material properties used are given in Table 9.1. The geometry of the mesh, constraints and loadings are shown in Fig. 9.6. The constraints actually simulated the compressive interaction between the end plates and the rock beam in the beam testing (see Chapter 8). That was why, at each load step, the stresses at the higher constraining points were checked for the tension. Should tensile stress be found at any stage at some constraints during the loading history, the constraints were released before the "run". In the same way, the constraints shown in Fig. 9.6 represent the interaction of the end plates and the rock beam at a vertical load of 4.5 kN. In this simulation no initial longitudinal prestress was applied.

As loading commenced, an initially linear response characteristic of an elastic beam was obtained (upto (1) in Fig. 9.7). At a load of 4.5 kN, the stress at the midspan in the lowest fibre (Fig. 9.8) of the beam reached a value of 3.7 MPa, which is equal to the tensile strength of the rock.

At this point a midspan, vertical crack was nucleated at the bottom of the specimen. This midspan crack was extended (Fig. 9.10) with continued loading. A crack length of 1.6 cm was obtained under a load of 8.5 kN (Fig. 9.10 (a)). Due to the presence of the
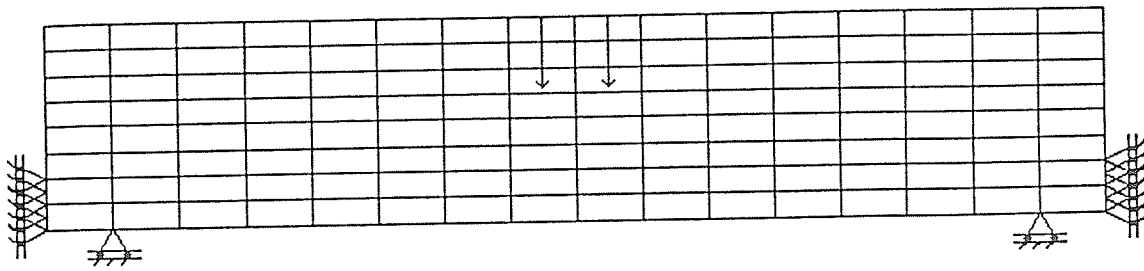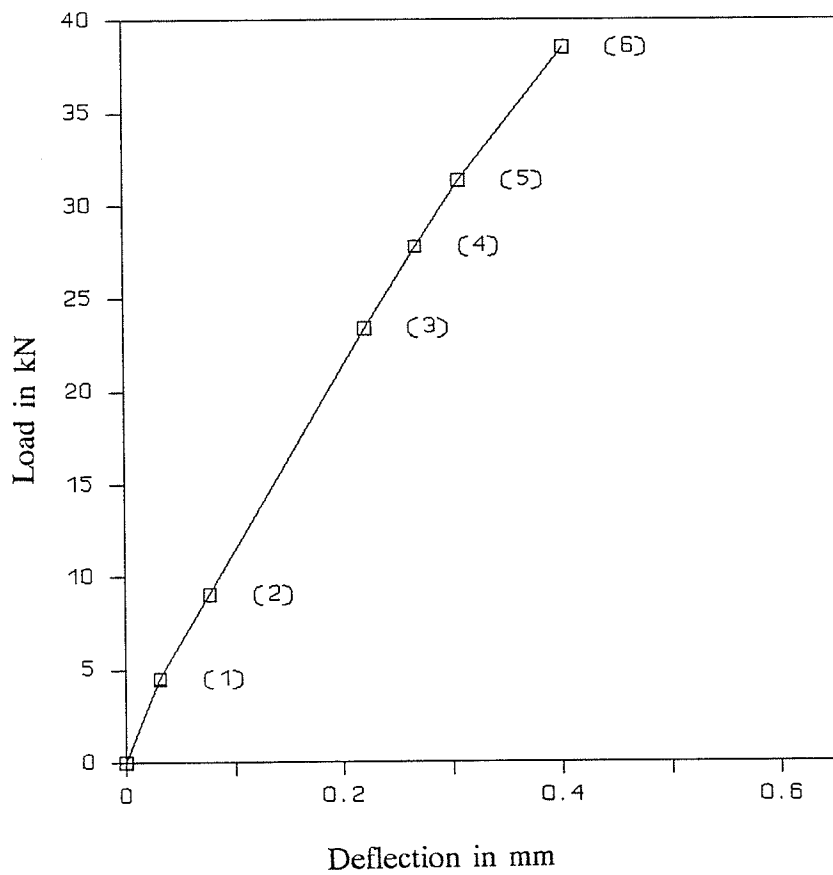
Load   Application

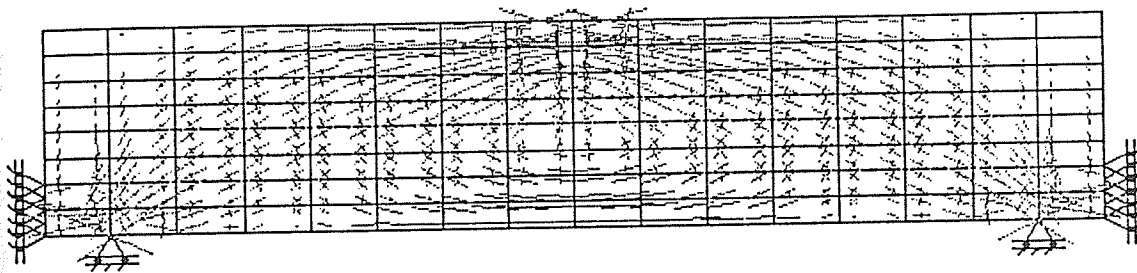

Fig. 9.6 The geometry of the mesh, constraints and loadings.

Deflection in mm

(1) Nucleation of axial crack.
(2) Axial crack (1.6 cm).
(3) Axial crack (3.9 cm).
(4) Axial crack (4.1 cm) and nucleation of diagonal cracks.
(5) Axial crack (4.1 cm) and diagonal cracks (Fig. 10.13).
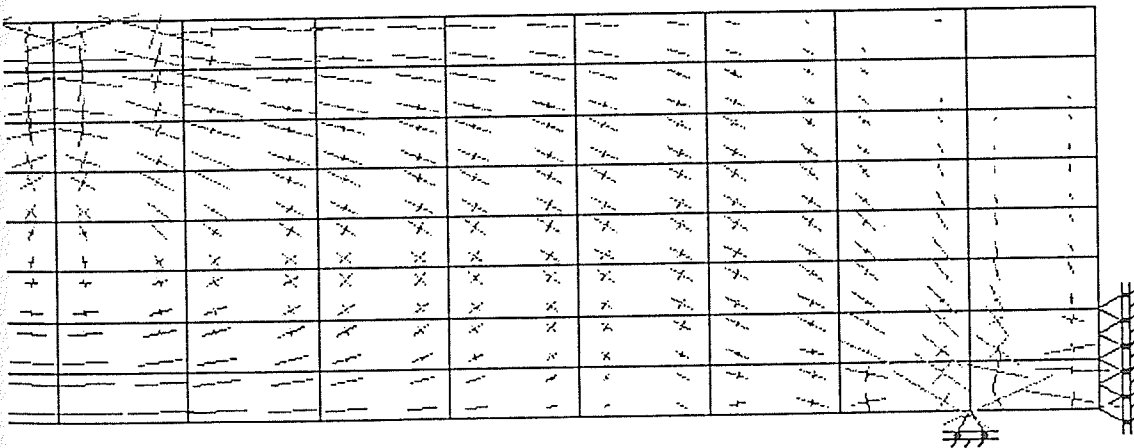(6) Collapse of the structure.

Fig. 9.7 Vertical load/deflection graph from the discrete crack propagation FEM results.
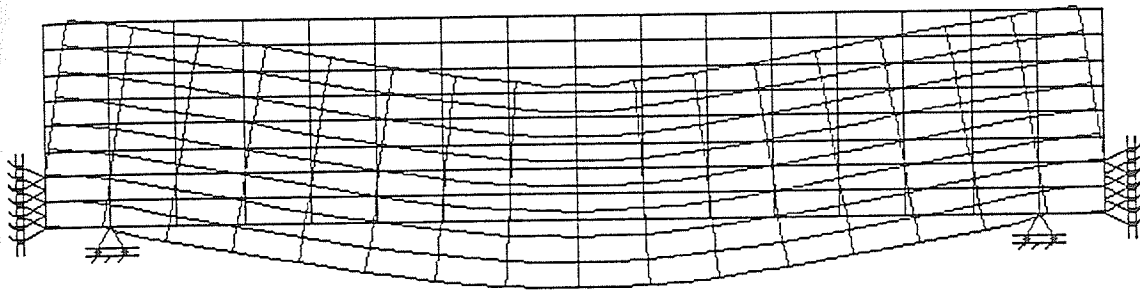
Fig. 9.8 (a) The deformed mesh (highly exaggerated) @ 4.5 kN, (b) plots of principal stresses, and (c) half of (b) right of the symmetry line.
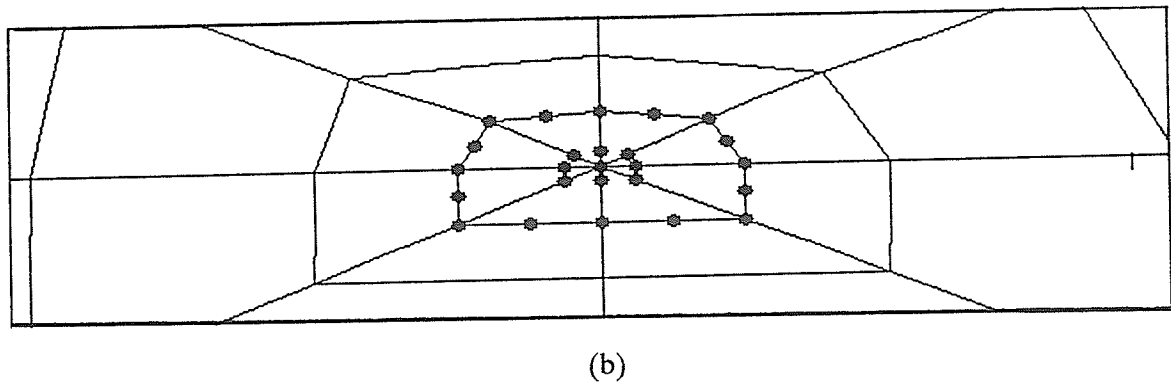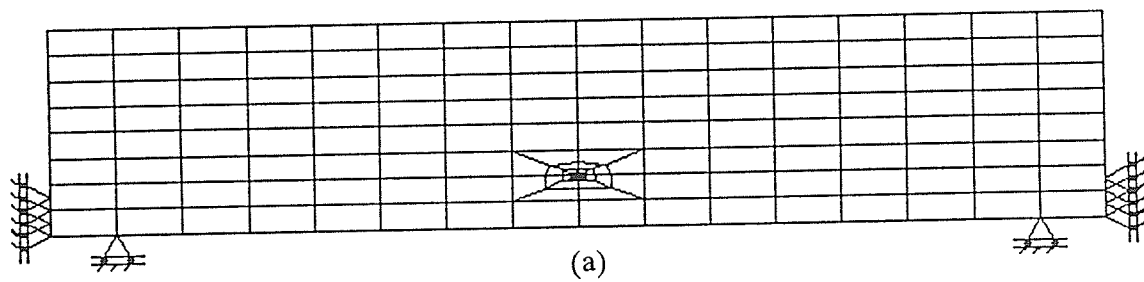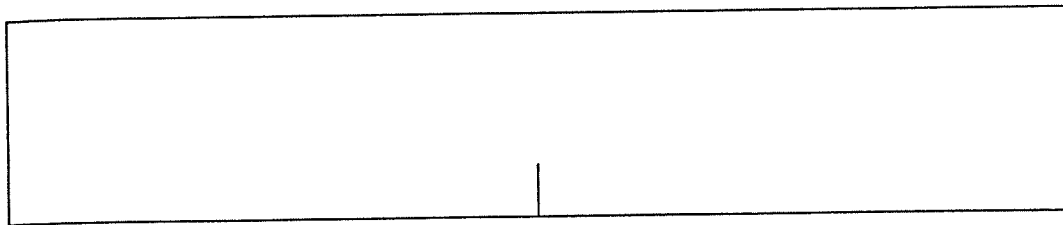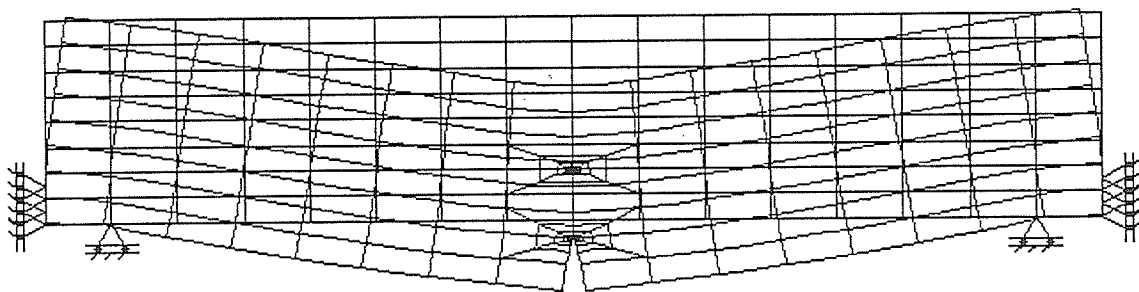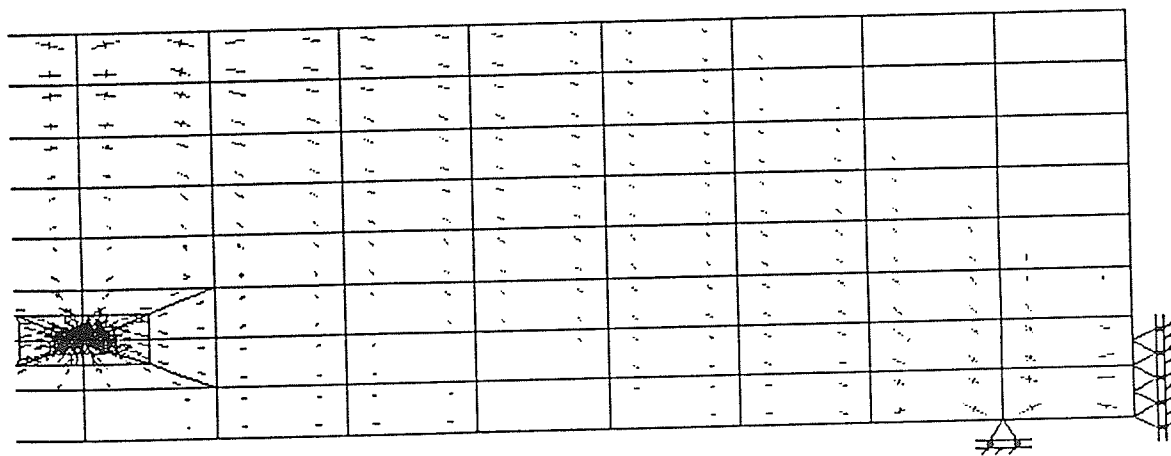
138

Fig. 9.9 (a) Generating a crack tip, (b) magnified crack tip showing quarter elements surrounding the crack tip which would create singularity at that point.

(a)

(b)

(c)

Fig. 9.10 (a) 1.6 cm axial crack @ 8.5 kN, (b) deformed mesh (highly exaggerated) @ 8.5 kN, and (c) principal stress plots @ 8.5 kN.

midspan crack, principal stresses plots show relative absence of tensile stresses at the bottom fibres (Fig. 9.10(c)).

This part of the vertical load/deflection graph depicts non-linearity (Fig. 9.7). This response is because of the physical introduction of a crack in the continuum. The midspan crack was then extended further to 3.9 cm and then to 4.1 cm under loads of 23.4 kN and 27.8 kN respectively (Figs. 9.11 and 9.12).

In Fig. 9.12(b), at point marked "x", the combination of the maximum and minimum principal stresses (compressive stress = 29.8 MPa and tensile stress = 2.9 MPa) reaches the Mohr-Coulomb yield criterion. Consequently, diagonal cracks were nucleated at points "x" following the compressive stress direction. The pair of diagonal cracks were extended (Fig. 9.13) under a load of 31.3 kN. This part of the vertical load/deflection graph shows even more non-linearity (Fig. 9.7). The principal stress plot shows concentrations of compressive stress at the upper tip of the diagonal cracks (Fig. 9.14).

It was noticed that the bottom end of the diagonal crack was predominantly under mode I, while the top end was mainly under mode II. Also, compared to the bottom end, the upper tip required less load increase to be extended. At this load the axial midspan crack could not be extended any further. Accordingly, the top end of the diagonal cracks were extended towards the top surface. The ultimate load needed to propagate the crack to the top surface (Fig. 9.14) was 38.5 kN. Fig. 14(c) shows the resulting stress relieved zone above the diagonal cracks. There was now also a concentration of compressive stress at the bottom ends of the diagonal cracks, which were predominantly under mode II. Therefore, the bottom ends of the diagonal cracks were next extended towards the bottom surface. It was found out that the load required to extend this crack (28.6 kN) was less than the previous load step of 38.5 kN. Hence, 38.5 kN —— the load required to extend the top diagonal cracks to the top surface —— was the collapse load of the structure. Collapse would follow instantaneously by shearing of the remnant
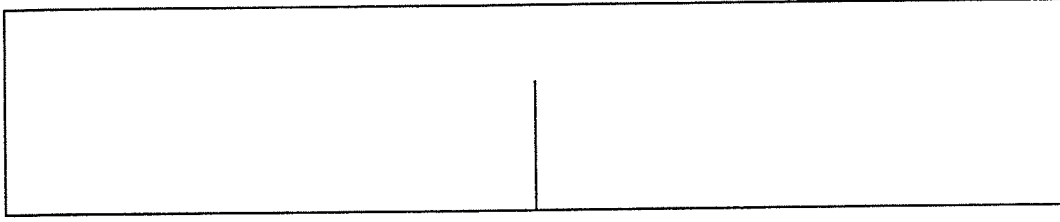
(a)
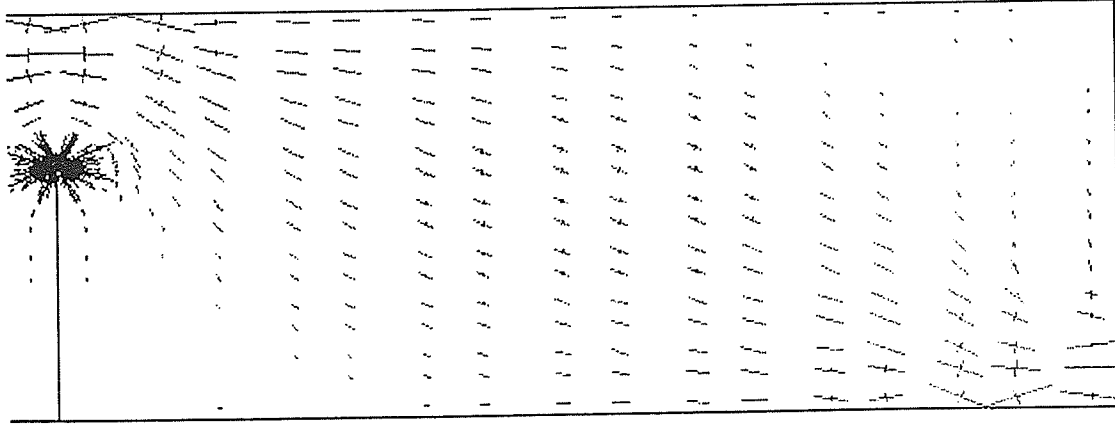
(b)

Fig. 9.11 (a) Axial crack extended to 3.9 cm @ 23.4 kN, and (b) principal stress plots @ 23.4 kN.
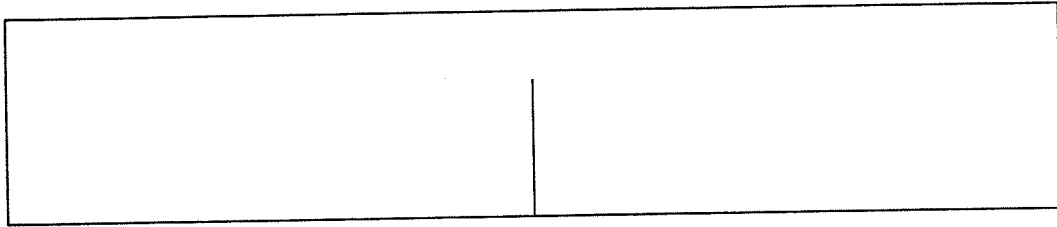
(a)
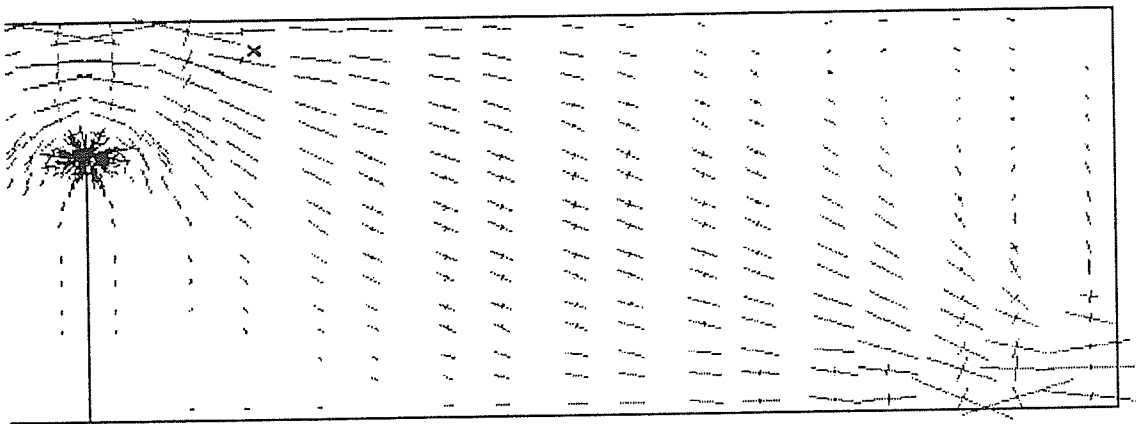
(b)

Fig. 9.12 (a) Axial crack extended to 4.1 cm @ 27.8 kN, and (b) principal stress plots @ 27.8 kN. At point "x" the principal stresses are : compression = 29.8 MPa and tension = 2.9 MPa.
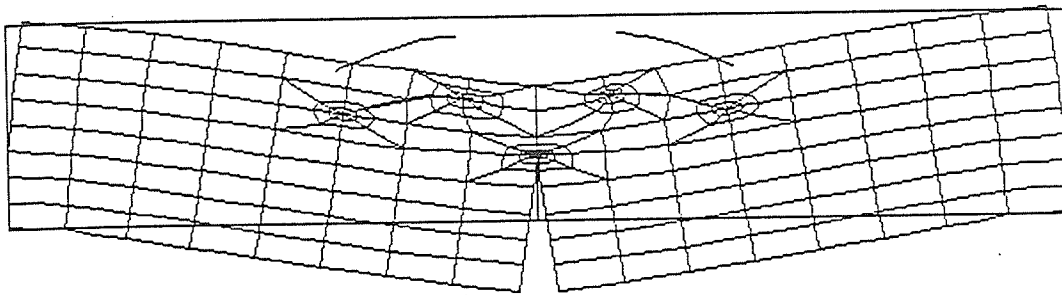
(a)
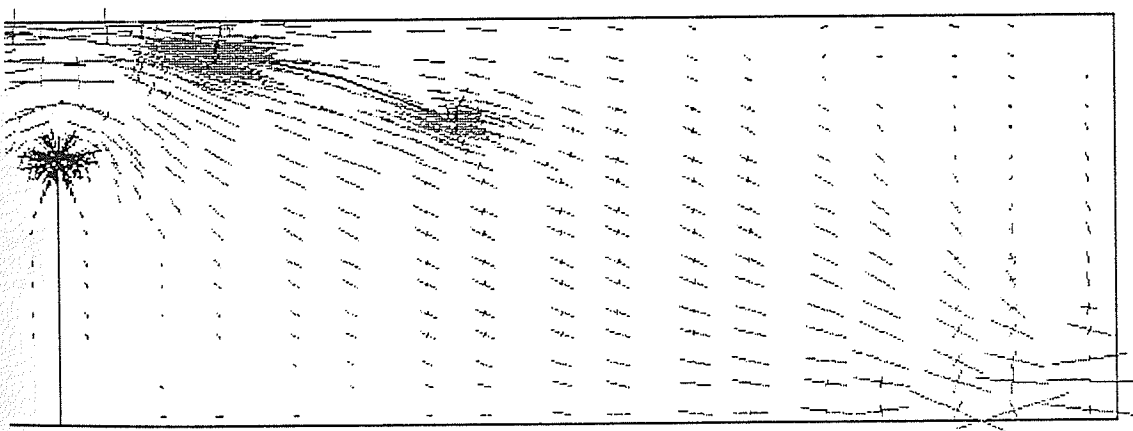
(b)

Fig. 9.13 (a) Deformed mesh (highly exaggerated) @ 31.3 kN and (b) principal stress
plots @ 31.3 kN, superimposed on the axial and diagonal crack geometries.
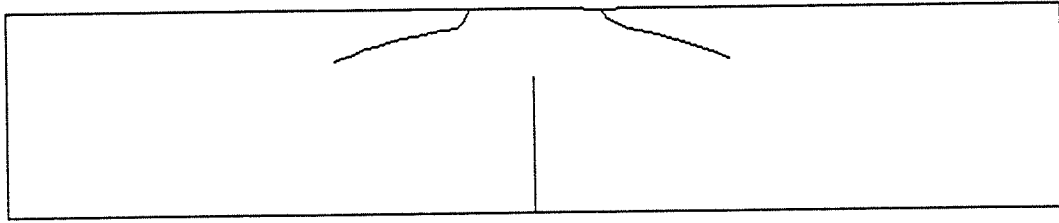
(a)
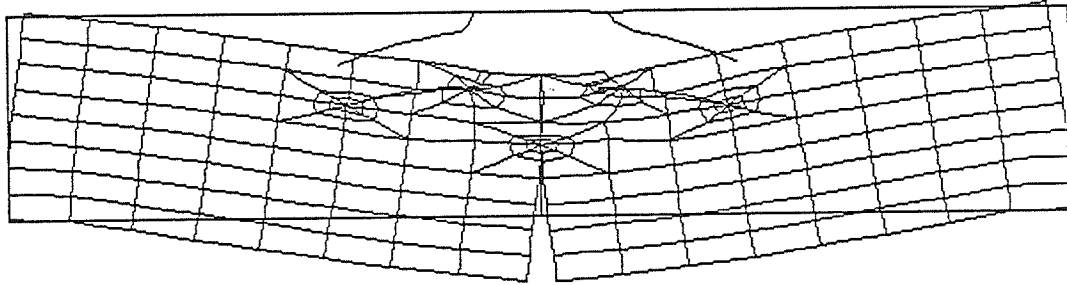
(b)
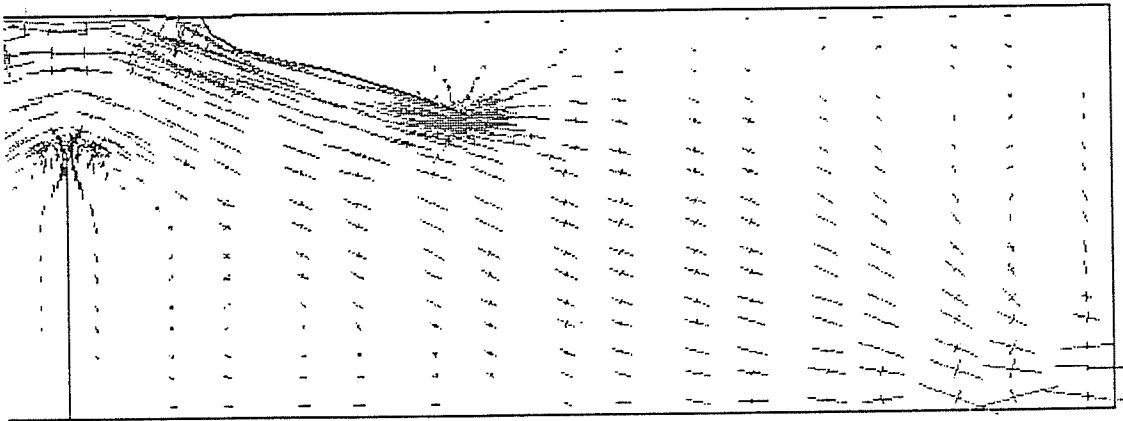
(c)

Fig. 9.14 (a) Axial and diagonal crack geometries @ 38.5 kN, and (b) deformed mesh (highly exaggerated) @ 38.5 kN, and (c) principal stress plots @ 38.5 kN.

145

rock bridge at the bottom of end of the diagonal cracks.

This simulation of a typical beam test by Discrete Crack Propagation FEM thus successfully validated the failure mechanisms (Section 8.7) observed in the beam testing.

CHAPTER 10

DISCUSSION

10.1 SUMMARY

The main purpose of this study was to investigate possible failure mechanism(s) inducing seismicity in the Saskatchewan potash mines. Although, researchers have established beyond reasonable doubt that seismicity recorded above potash mines is associated with the failure of the Dawson Bay Formation, no experimental or analytical rock mechanics has been carried out to investigate possible mechanisms in more detail.

According to the concept of critical energy release rate, rock has a capacity up to certain critical rate, beyond which violent failure is likely to occur. This study represents the first attempt to employ this concept to the problem of mining-induced seismicity in bedded deposits. The theoretical energy release rates were obtained using the same analytical model employed in the study of bedding plane failure (see Chapter 4). In order to predict seismicity from the calculated energy release rate, additionally, a knowledge of the corresponding critical value established for a given mining regime is required. This value, unfortunately, has not yet been determined for the Saskatchewan potash mines. However, from the estimates of energy release rate itself, it can be inferred that violent failure in Dawson Bay Formation will occur with limited warning, because of the very strong sensitivity of energy release rate to the increase in mine span. Also, one can check the seismic severity of a mining district by using the critical energy release rate established for some other mining area having comparable ground conditions.

In this study, the writer examined two possible causal explanations of seismicity in the Dawson Bay Formation.

Failure along bedding planes was examined using an analytical model based on beam theory (see Chapter 7). It was found that bedding plane failure in the rock beam over the abutments of the mine openings cannot be completely excluded as a possible mechanism (Figs.7.1 and 7.2). However, it was also noted that the zones of slip and horizontal shear stress are not extensive, i.e., they effect a small volume of the rock mass, and therefore it was considered unlikely that the larger events can be attributed to this mechanism, as was suggested by Gendzwill and Prugger (1987). It is, however, capable of generating microseismicity. Failure along bedding planes, as a result of initial beam action of Dawson Bay Formation, is consistent with the field observation that microseismic events cluster over the panels that are being actively mined (see Chapter 4).

In this study, rupture of the Dawson Bay linear arch under the "dead-weight" of the overburden was found to be a possible causal explanation of larger seismic events. The magnitude of the seismic energy released in a full scale rupture of the Dawson Bay linear arch was shown to be in the order that has been recorded for the larger events in the potash mines (see Section 8.9).

Physical modelling and numerical analyses have established that failure of a thick massive roof beam takes place in three stages : (a) vertical midspan cracking, (b) diagonal cracking, and (c) failure of remnant of rock bridges (Chapters 8 and 9). The first two events release small amount of energy, while the ultimate failure occurs violently.

Numerical simulation incorporating crack propagation has yet to be undertaken to simulate the full excavation sequence in Saskatchewan potash mines. However, a preliminary analysis to simulate the mine excavation using FLAC (time- independent) was attempted by the

writer (see Section 9.2). The results obtained show that the failure zone in the Dawson Bay Formation has the outline of an arch (Fig. 9.4). Time-dependent modelling using visco-elastic/visco-plastic material behaviour was undertaken by Sepehr (1988). In this model rooms were sequentially created towards the centre of the panel. The results thus obtained also show similar arch-like outline of the failure zone in the Dawson Bay Formation after a simulated period of 5 years from the creation of the mine openings (Fig. 10.1). These arch-like outline may be indicative of fully developed diagonal cracks in the linear arch; in both the cases the loads will now be carried by the materials above this feature.

10.2 FIELD EVIDENCE

Very recently, observations of layered salt roof failures from Cominco's Vanscoy Mine, Saskatchewan, provide some field evidence for the proposed mechanisms of failure of a thick linear arch. The opportunity arose to examine a drift excavated along the roof line of a series of openings originally cut 15-20 years ago. Fig. 10.2 shows a typical roof collapse which is bounded by rough tension cracks that may be interpreted as diagonal cracking of roof beam which eventually collapsed (see Chapter 8).

It should be noted that, since the Dawson Bay Formation is not accessible to direct inspection, direct evidence of failure of a Dawson Bay linear arch is still awaited. In the absence of this field data, however, these roof collapse features of the much weaker saltback, which forms the immediate roof lying just beneath the Dawson Bay Formation, provide some support for the concept.

Apart from the ultimate collapse of a Dawson Bay linear arch, which could cause large seismic events, the earlier diagonal cracking, could lead to mine flooding by providing

149
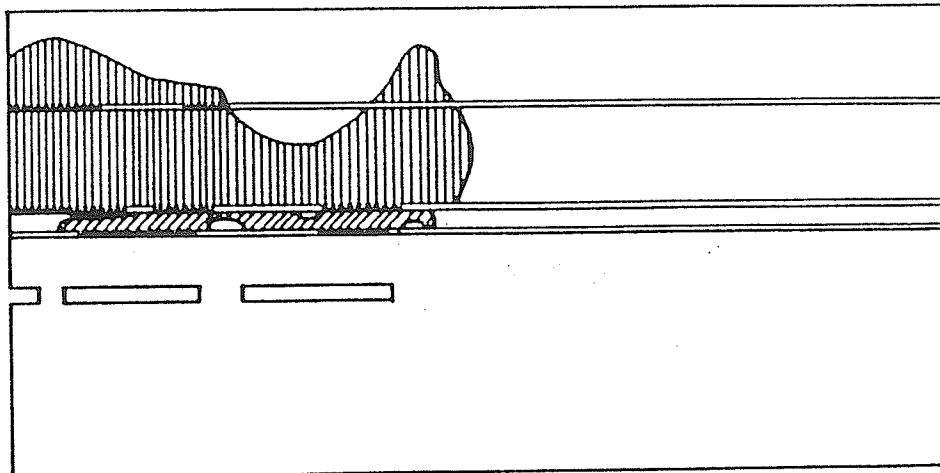
5 Years After

� Plastic Zone Dawson Bay Limestone

▨▨▨▨▨▨▨ Plastic Zone In Second Red Bed

Fig. 10.1 Failure zone in the Dawson Bay Formation (after Sepehr, 1988).
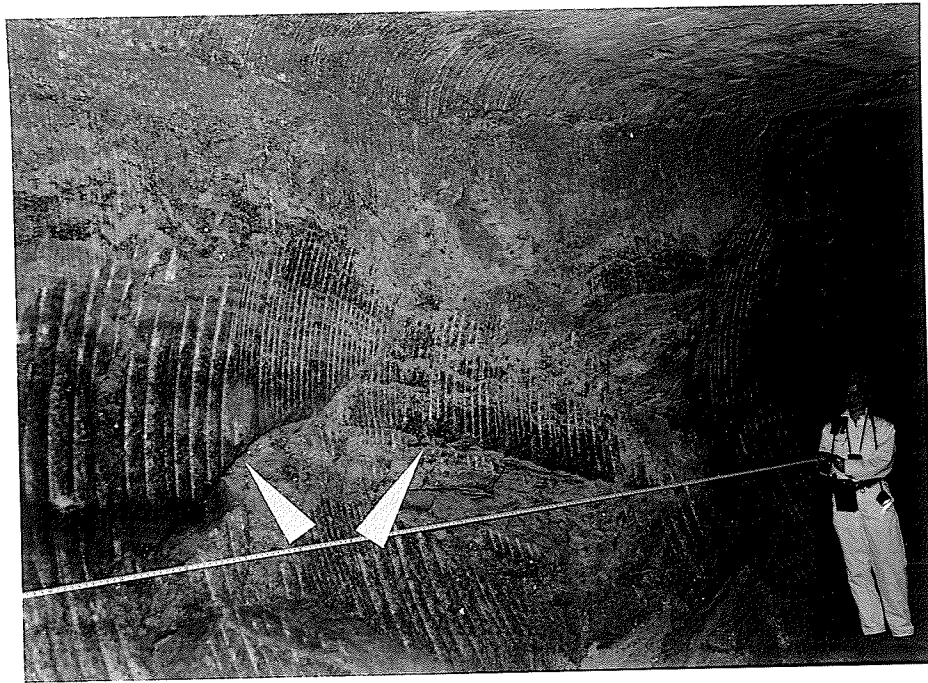
Fig. 10.2 (a) Photograph from Cominco's Vanscoy Mine showing diagonal cracks in the saltback.
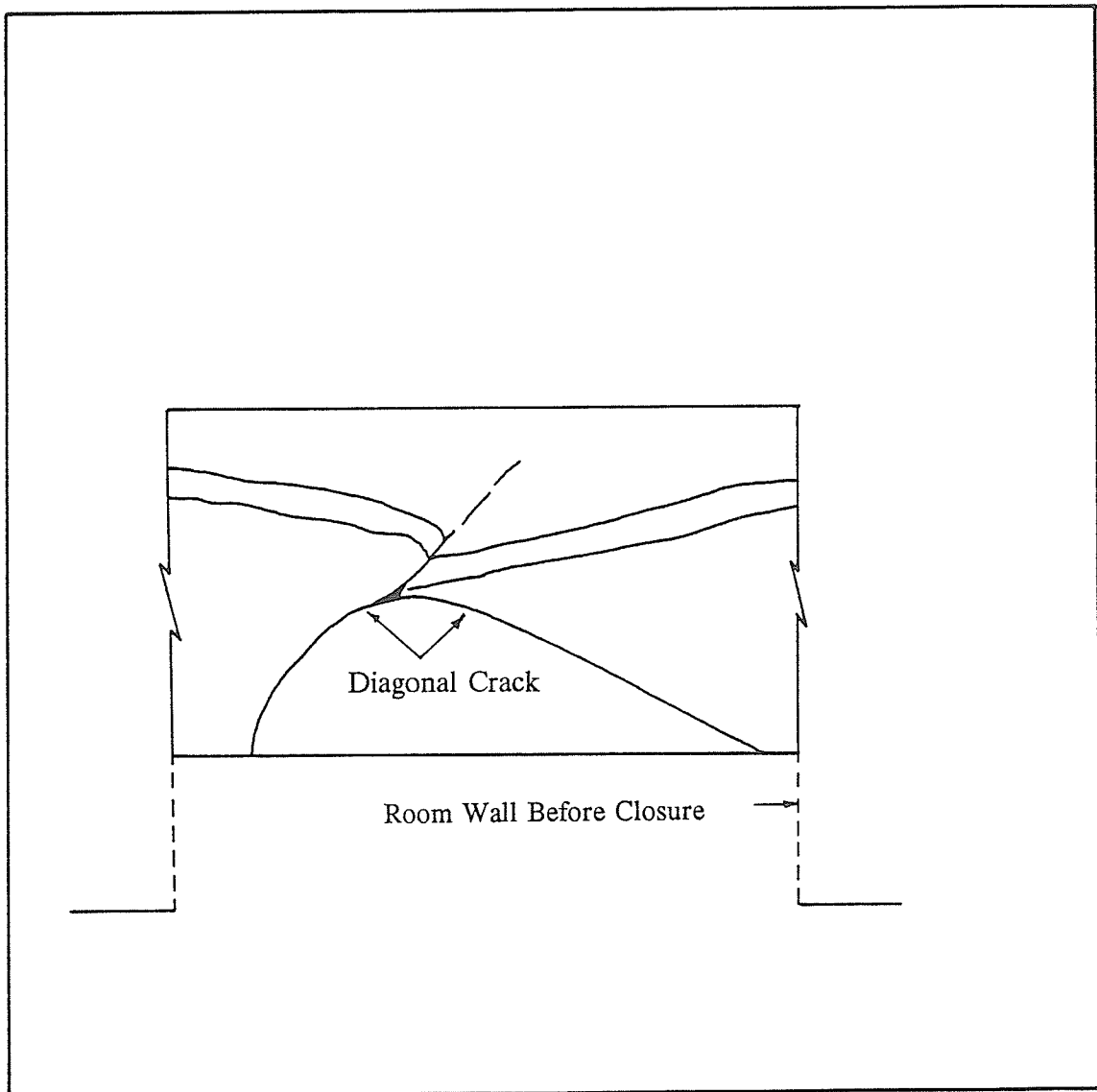
Fig. 10.2 (b) Schematic diagram of (a).

avenues for water. In fact, in one potash mine, following a major water ingress, arch-shaped

conduits were discovered in the saltback, resembling once again diagonal cracking [(Stimpson,

1989 (personal communication)].

10.3 FUTURE RESEARCH

Rock mechanics research on the seismicity problem of potash mines in

Saskatchewan is, in fact, just beginning. As mentioned earlier, this study is the first piece of

such work. It is believed that further research in the areas outlined below would be very

valuable.

1. A detailed testing program to examine the failure mechanisms of a rock beam as

function of shear span/depth ratio. This would enable one to formulate a generalized theory of

the failure of linear arch.

2. A study of the interface shear transfer across the cracks during the failure of a linear

arch.

3. A testing program to examine the failure mechanisms in a layered rock beam model

of the entire mine roof —— the Dawson Bay Formation along with the saltback.

4. Numerical analysis of the mining sequence in the Saskatchewan potash mines using

a model which is capable of simulating crack propagation, namely, the Discrete Crack

Propagation FEM.

CHAPTER 11

CONCLUSIONS

1. A theory for the elastic beam on elastic supports, based on differential equation of the elastic line was developed for a general variable load, and has been adopted as the analytical model for simulating the response of the Dawson Bay Formation to potash mining. Both thin beam and thick beam formulation were derived. Consideration of two different elastic moduli for the beam was also made.

2. The concept of critical energy release rate to the problem of seismicity in bedded deposits was employed. From the obtained energy release rate itself, it can be inferred that violent failure in Dawson Bay Formation will occur with limited warning, because of the very strong sensitivity of energy release rate to the increase in mine span.

3. It was found that the bedding plane failure cannot be completely excluded as a possible mechanism of mining-induced seismicity. The magnitude and extent of the bedding plane slip were not considered sufficiently large to attribute larger seismic events to this mechanism. It is, however, capable of generating microseismicity.

4. Physical modelling has established that failure of a thick massive rock beam involves three fracture events : (a) vertical midspan cracking, (b) diagonal cracking, and (c) failure of remnant rock bridges. The first two events release small amount of energy, while the ultimate failure occurs violently.

5. Numerical analysis validated the findings of the physical modelling. Results from the finite difference analysis simulated the initiation of the diagonal crack in a typical beam test. Moreover, the discrete crack propagation FEM was successfully used to replicate the failure mechanisms of a typical beam test.

6. It is proposed that the rupture of the Dawson Bay linear arch under the "dead weight" of the overburden is the causal explanation of larger seismic events. The magnitude of the seismic energy released in a full scale rupture of the Dawson Bay linear arch was shown to be in the order that has been recorded for the larger events in the Saskatchewan potash mines.

REFERENCES

Alder, L.,1961, Rib control of bedded roof stresses. In : Hartman, H. L. (editor), Proc. Symp. Rock Mech. 4th, Pennsylvania State Univ., Pa —— Bull. Miner Ind. Exp. Stn., Pennsylvania State Univ., pp. 205-209.

American Society of Civil Engineers, 1982, State of the art report on finite element analysis of reinforced concrete, Task Committee on finite element analysis of reinforced concrete structures of the Structural Division Committee on concrete and masonry structures, New York.

Ayari, M. L., 1988, Static and dynamic fracture mechanics of concrete gravity dams, Ph. D. Thesis, Department of Civil and Architectural Engineering, University of Colorado.

Ayari, M. L., B. Stimpson and E. Z. Lajtai, 1989, Modelling of mining induced fractures, Presented at the 42nd. Canadian Geotechnical Conference, Oct. 23-25, Winnipeg.

Baar, C. A., 1971, Creep measured in deep potash mines vs. theoretical predictions, Proc. 7th Canadian Rock Mech. Symp., pp. 23-77.

Bannatyne, B. B., 1975, High-calcium limestone deposits of Manitoba, Man. Dept.of Mines, Res. and Env. Management, Publ. 75-1, pp.103.

Barron, K.,1984, An analytical approach to the design of pillars in coal, Part I : The analytical method, Final report, Phase I, Canada Centre for Mineral and Energy Technology, Energy, Mines and Resources, Canada.

Brady, B. H. and E.T. Brown, 1985, Rock Mechanics, George Allen and Unwin.

Cook, N. G. W., 1963, The seismic location of rockbursts, Proc. 5th Symp. Rock Mech., Vergamon Press, pp. 493 - 516.

Cook, N. G. W., 1976, Seismicity associated with mining, Engineering Geology : 10, pp.99-122.

Cook, N. G. W., 1978, Rockbursts and rockfalls, Chamber of Mines of S. Afr. Publication No. 216.

Dunn, C. E., 1975, Saskatchewan potash in 1975 —— an update on our knowledge, Eleventh Industrial Mineral Forum, pp. 51-60.

Dunn, C. E., 1982, Geology of the Middle Devonian Dawson Bay Formation in the Saskatchewan potash mining district, Saskatchewan, Saskatchewan Energy and Mines, Report 194.

Erdogan, F. and G. C. Sih, 1963, On the crack extension in plates under plane loading and transverse shear, Journal of Basic Engineering, V. 85, pp. 519-527.

FLAC (Fast Lagrangian Analysis of Continua), 1987, Version 2.02, ITASCA Consulting Group Inc., Minneapolis, Minnesota.

Fuzesy, L. M., 1980, Geology of the Deadwood (Cambrian), Meadow Lake and Winnipegosis (Devonian) in west-central Saskatchewan. Sask. Dept. Min. Res. Report 210, pp.64.

Gendzwill, D. J., 1983, Elastic properties of carbonate rocks over the Cory Mine, Proc. Potash '83, Pergamon Press.

Gendzwill, D. J., 1984, Induced seismicity in Saskatchewan potash mines. In : Rockbursts and seismicity in mines, Gray, N. C. and E. H. Wainright (eds.), The South African Institute of Mining and Metallurgy.

Gendzwill, D. J. and A. F. Prugger, 1987, Seismic studies in Saskatchewam potash mines, presented to Workshop of mining induced seismicity, Montreal.

Gendzwill, D. J.,R. B. Horner and H. S. Hasegawa, 1982, Induced Earthquakes at a potash mine near Saskatoon, Canada, Can. J. Earth Sciences, vol. 19, pp. 466-475.

Graystone, L. D., D. F. sherwin, and J. R. Allan, 1964, Middle Devonian. In :Geological History of Western Canada (eds. R. G. McCrossan and R. P. Glaister), Alberta Soc. Petrol. Geol., Calgary, pp. 232.

Holter, M. E., 1969, The Middle Devonian Prairie Evaporite of Saskatchewan : Saskatchewan

Dept. Mineral Resources Rept. 123, 134 p.

Horner, R. B., 1983, Earthquakes in Saskatchewan : a potential Hazard to the Potash Industry,

Proc. Potash '83, Pergamon Press.

Hussain, M. A. and S. L. Pu and J. H. Underwood, 1974, Strain energy release rate for a

crack under combined mode I and mode II, Fracture Analysis, ASTM, STP 560, 22-28.

Jaeger, J. C. and N. G. W. Cook, 1976, Fundamentals of Rock Mechanics, Chapman and

Hall, 2nd Edition.

Kasahara, K.,1981, Earthquake Mechanics, Cambridge University Press, Cambridge.

Kilgour, J. D., 1984, Fracture Toughness of Tyndall Limestone, B. Sc. Thesis, Civil

Engineering, University of Manitoba.

Kroll, D. W., 1987, Basic geomechanical properties of the Dawson Bay Formation, M. Sc.

Thesis, Civil Engineering, University of Manotoba.

Lane, D. M., 1959, Dawson Bay Formation in the Quill Lakes —— Qu'Appelle area,

Saskatchewan Dept. Mineral Resources Rept. 28, 49 p.

Molavi, M. A., 1987, A study of potash mining methods related to ground control criteria, M.

Eng. Thesis, Dept. of Mining and Metallurgical Eng., McGill University, Quebec,

Canada.

Ortlepp, W. D., 1983, The mechanism and control of rockbursts, In : Rock Mechanics in

Mining Practice, S. Budavari (editor), The South African Institute of Mining and

Metallurgy.

Reid, H. F., 1911, The elastic-rebound theory of earthquakes, University of California Publ.

Geol. Sci., 6, pp. 413-444.

Richter, C. F., 1958, Elementary seismology, W. H. Freeman, San Francisco.

Saouma, V. E., 1987, AUTOCRACK-2D, FATLIF, SAMPLING, and CMPLMG, interactive

computer graphic simulation of crack propagation, User's Manual, Boulder, Co.

Savage, J. C., 1966, Radiation from a realistic model of faulting, Bull. Seis. Soc. Am., Vol. 56, No. 2, pp. 577-592.

Sepehr, K.,1988, Non-linear and time-dependent finite element modelling of underground excavations with special reference to induced seismicity in potash minging, Ph.D. Thesis, Civil Engineering, University of Manitoba.

Sepehr, K. and B. Stimpson, 1988, Roof deflection and sag in jointed, horizontally bedded strata —— a numerical study, Rock Mechanics and Rock Engineering 21, pp. 207-218.

Serata, S., 1968, Application of continuum mechanics to design of deep potash mines in Canada, Int. J. Rock Mech. Min. Sci., Vol. 5, pp. 293-314.

Serata, S., 1982, Stress control methods : quantitative approach to stabilizing mine opening in weak ground, First Intl. Conf. on stability in underground mining, Vancouber, B. C.

Sheorey, P. R., 1972, Stability of single openings in horizontally bedded rock : A discussion, Engineering Geology 6, pp. 313-314.

Sih, G. C., 1974, Strain energy factors applied to mixed mode crack problems, Int. J. Fracture, V. 10, p. 305.

Stephannson, O., 1971, Stability of single opening in horizontally bedded rock, Eng. Geol. 5, pp. 5-77.

Sterling, R. L., 1977, Roof design for underground openings in near-surface bedded rock formations, Ph. D. Thesis, Civil Eng., University of Minnesota.

Stimpson, B. and M. Ahmed, 1987, The ratio of the moduli of elasticity of the Dawson Bay Limestone in compression and tension and its influence on beam formulation, Internal Report, Dept. of Geol. Eng., Univ. of Manitoba.

Tincelin, E. and P. Sinou, 1960, Collapse of areas worked by the small pillar method, Int. Conf. on strata control, 3rd, Paris, pp. 571-589.

Woodruff, S. D., 1966, Methods of working coal and metal mines, Vol. 1, Pergamon Press, Oxford.

APPENDIX – I

BEAM FORMULATIONS

THIN BEAM

The differential equation of a thin beam over a deformable abutment (Fig. 6.6) for the defined clamping load (eqn. 6.16) :

$$K \frac{d^4y}{dx^4} + C_u y = S_v - Se^{\lambda_s x} + Ce^{\lambda_c x}$$

$$\text{or,} \quad \frac{d^4y}{dx^4} + \alpha^4 y = \frac{S_v}{C_u} - Se^{\lambda_s x} + Ce^{\lambda_c x} \tag{I1}$$

where,

$$K = \frac{EI}{1 - \nu^2}$$

$$I = \frac{D^3}{12}$$

D = thickness of beam

E = elastic modulus of beam

ν = poisson's ratio of beam

$$\alpha = \left(\frac{C_u}{4K}\right)^{1/4}$$

$$C_u = \frac{E_a}{D_a(1 - \nu_a^2)}$$

E_a = elastic modulus of abutment

D_a = thickness of abutment

160

ν_a = Poisson's ratio of abutment

From eqn. (I1) :

$$\text{Complementary function} = (A_1 \text{Sin}\alpha x + B_1 \text{Cos}\alpha x)e^{\alpha x} + C_1 \text{Sin}\alpha x$$

$$+ D_1 \text{Cos}\alpha x)e^{-\alpha x}$$

$$\text{Particular integral} = \frac{S_v}{C_u} + Ae^{\lambda_s x} + Be^{\lambda_c x}$$

where,

$$A = - \frac{S}{K\lambda_s^4 + C_u}$$

$$B = \frac{C}{K\lambda_c^4 + C_u}$$

$$\therefore y = (A_1 \text{Sin}\alpha x + B_1 \text{Cos}\alpha x)e_{\alpha x} + (C_1 \text{Sin}\alpha x + D_1 \text{Cos}\alpha x)e^{-\alpha x}$$

$$+ \frac{S_v}{C_u} + Ae^{\lambda_s x} + Be^{\lambda_c x} \tag{I2}$$

But, as $x \to \infty$, $y = \frac{S_v}{C_u}$

$$\text{Hence, } y = A_1 \text{Sin}\alpha x e^{\alpha x} + B_1 \text{Cos}\alpha x e^{\alpha x} + \frac{S_v}{C_u} + Ae^{\lambda_s x} + Be^{\lambda_c x} \tag{I3}$$

$$\therefore \frac{dy}{dx} = \alpha (A_1 + B_1)\text{Cos}\alpha x e^{\alpha x} + \alpha (A_1 - B_1)\text{Sin}\alpha e^{\alpha x}$$

$$+ \lambda_s Ae^{\lambda_s x} + \lambda_c Be^{\lambda_c x} \tag{I4}$$

$$\therefore \frac{d^2 y}{dx^2} = 2\alpha^2 A_1 \text{Cos}\alpha x e^{\alpha x} - 2\alpha^2 B_1 \text{Sin}\alpha e^{\alpha x}$$

$$+ \lambda_s^2 Ae^{\lambda_s x} + \lambda_c^2 Be^{\lambda_c x} \tag{I5}$$

$$\therefore \frac{d^3 y}{dx^3} = 2\alpha^3 (A_1 - B_1)\text{Cos}\alpha x e^{\alpha x} - \alpha (A_1 + B_1)\text{Sin}\alpha e^{\alpha x}$$

$$+ \lambda_s^3 Ae^{\lambda_s x} + \lambda_c^3 Be^{\lambda_c x} \tag{I6}$$

161

@ x = 0, from (I3) through (I6) :

$$y = B_1 + \frac{S_v}{C_u} + A + B \tag{I7}$$

$$\frac{dy}{dx} = \alpha A_1 + \alpha B_1 + \lambda_s A + \lambda_c B \tag{I8}$$

$$\frac{d^2y}{dx^2} = 2\alpha^2 A_1 + \lambda_{s2} A + \lambda_c^2 B \tag{I9}$$

$$\frac{dy^3}{dx^3} = 2\alpha^3 A_1 - 2\alpha^3 B_1 + \lambda_s^3 A + \lambda_c^3 B \tag{I10}$$

The differential equation for a thin beam over the opening is as follows :

$$K\frac{d^4y}{dx^4} = P \tag{I11}$$

$$\text{Let, } y = \frac{Px^4}{24K} + L_1 x^3 + N_1 x^2 + R + Q \tag{I12}$$

$$\frac{dy}{dx} = \frac{Px^3}{6K} + 3L_1 x^2 + N_1 x + R \tag{I13}$$

$$\frac{d^2y}{dx^2} = \frac{Px^2}{2K} + 6L_1 x + 2N_1 \tag{I14}$$

$$\frac{d^3y}{dx^3} = \frac{Px}{K} + 6L_1 \tag{I15}$$

@ x = 0, from (I11) through (I15) :

$$y = Q \tag{I16}$$

$$\frac{dy}{dx} = R \tag{I17}$$

$$\frac{d^2y}{dx^2} = 2N_1 \tag{I18}$$

$$\frac{d^3y}{dx^3} = 6L_1 \tag{I19}$$

From (I19) and (I10) :

$$L_1 = \frac{1}{6} \{2\alpha^3(A_1 - B_1) + \lambda_s^3 A + \lambda_c^3 B)\} \tag{20}$$

From (I18) and (I9) :

$$N_1 = \frac{1}{2} (2\alpha^2 A_1 + \lambda_s^2 A + \lambda_c^2 B) \tag{I21}$$

From (I17) and (I8) :

$$R = \alpha(A_1 + B_1) + \lambda_s A + \lambda_c B = \tan\phi_1 \quad \text{(say)} \tag{I22}$$

From (I16) and (I7) :

$$Q = B_1 + \frac{S_v}{C_u} + A + B = y_1 \quad \text{(say)} \tag{I23}$$

From (I23) :

$$B_1 = y_1 \frac{S_v}{C_u} - A - B \tag{I24}$$

From eqns. (I22) and (I24) :

$$A_1 = \frac{1}{\alpha} \{\tan\phi_1 - \alpha (y_1 - \frac{S_v}{C_u}) + A(\alpha - \lambda_s) + B(\alpha - \lambda_c)\} \tag{I25}$$

But, shearing force,

$$T = -K \frac{d^3y}{dx^3} \tag{I26}$$

@ x = 0, from (I26) an (I19) :

$$T = -6KL_1 \tag{I27}$$

Again, @ x = 0,

$$T = \frac{Pl}{2} + T_c \tag{I28}$$

163

where,

l = beam span

T_c = contribution by variable load over the abutment

Inspecting eqn. (I10) :

$$T_c = - K(\lambda_s^3 A + \lambda_c^3 B) \tag{I29}$$

Therefore, from eqns. (I28) and (I29) :

$$T = \frac{Pl}{2} - K\lambda_s^3 A - K\lambda_c^3 B \tag{I30}$$

From (I27), (I30) and (I20) :

$$\frac{Pl}{2} = - 2K\alpha^3 (A_1 - B_1) \tag{I31}$$

Substituting the values of A_1 and B_1 from eqns. (I24) and

(I25) in eqn. (I31) :

$$\tan\phi_1 = 2\alpha (y_1 - \frac{S_v}{C_u} - A - B) + \lambda_s A + \lambda_c B - \frac{Pl}{4K\alpha^2} \tag{I32}$$

From (I13), (I20), (I21) and (I22) :

$$\frac{dy}{dx} = \frac{Px^3}{6K} + \alpha^3 (A_1 - B_1)x^2 + \lambda_s^3 Ax^2/2 + \lambda_c^3 Bx^2/2 + 2\alpha^2 A_1 x$$

$$+ \lambda_s^2 Ax + \lambda_c^2 Bx + \tan\phi_1 \tag{I33}$$

From (I33), (I24) and (I25) :

$$\frac{dy}{dx} = \frac{Px^3}{6K} + \alpha^3 (\frac{\tan\phi_1}{\alpha} - \frac{\lambda_s A}{\alpha} - \frac{\lambda_c B}{\alpha} - 2y_1 + \frac{2S_v}{C_u} + 2A + 2B)x^2$$

$$+ \lambda_s^3 Ax^2/2 + \lambda_c^3 Bx^2/2$$

$$+ 2\alpha^2 (\frac{\tan\phi_1}{\alpha} - \frac{\lambda_s A}{\alpha} - \frac{\lambda_c B}{\alpha} - 2y_1 + \frac{S_v}{C_u} + 2A + 2B)x$$

$$+ \lambda_s^2 Ax + \lambda_c^2 Bx + \tan\phi_1 \tag{I34}$$

But, @ $x = 1/2$, $\frac{dx}{dy} = 0$ \tag{I35}

Hence, from (I34), @ x = 0 :

$$\frac{Pl^3}{48K} + \frac{\alpha^2 l^2 \tan\phi_1}{4} + \frac{\alpha^3 l^2 S_v}{2C_u} - \frac{\alpha^3 l^2 y_1}{2} + \alpha l \tan\phi_1$$

$$- \alpha^2 l y_1 + \frac{\alpha^2 l S_v}{C_u} + \tan\phi_1$$

$$- \frac{\alpha^2 l^2 \lambda_s A}{4} - \frac{\alpha^2 l^2 \lambda_c B}{4} + \frac{\alpha^3 l^2 A}{2} + \frac{\alpha^3 l^2 B}{2} + \frac{l^2 \lambda_s^3\, A}{8} + \frac{l^2 \lambda_c^3\, A}{8}$$

$$- \alpha l \lambda_s A - \alpha l \lambda_c B + \alpha^2 l A + \alpha^2 l B + l \lambda_s^2 A/2 + l \lambda_{c2} B/2 = 0 \qquad (I36)$$

From (I32) and (I36) :

$$y_1 = \frac{\dfrac{Pl^3}{24K} + \dfrac{Pl^2}{4K\alpha} + \dfrac{Pl}{4K\alpha^2}}{\alpha^2 l + 2\alpha} + \frac{\dfrac{S_v l \alpha^2}{C_u} + \dfrac{2S_v\alpha}{C_u}}{\alpha^2 l + 2\alpha} + \frac{A(\alpha^2 l + 2\alpha)}{\alpha^2 l + 2\alpha} + \frac{B(\alpha^2 l + 2\alpha)}{\alpha^2 l + 2\alpha}$$

$$- \frac{A(\lambda_s + l\lambda_s^2/2 + l^2\lambda_s^3/8)}{\alpha^2 l + 2\alpha} + \frac{B(\lambda_c + l\lambda_c^2/2 + l^2\lambda_c^3/8)}{\alpha^2 l + 2\alpha} \qquad (I37)$$

But, $K = \dfrac{C_u}{4\alpha^4}$ \qquad\qquad (I38)

$$y_1 = \frac{P}{C_u}\left(l\alpha^3 \frac{l^2/6 + l/\alpha + 1/\alpha^2}{\alpha l + 2}\right) - \frac{A(\lambda_s + l\lambda_s^2/2 + l^2\lambda_s^3/8)}{\alpha^2 l + 2\alpha}$$

$$- \frac{B(\lambda_c + l\lambda_c^2/2 + l^2\lambda_c^3/8)}{\alpha^2 l + 2\alpha} + \frac{S_v}{C_u} + A + B \qquad (I39)$$

Let,

$$\beta_1 = \frac{l^2/6 + l/\alpha + 1/\alpha^2}{\alpha l + 2} \qquad\qquad (I40)$$

$$\beta_2 = \frac{\lambda_s + l\lambda_s^2/2 + l^2\lambda_s^3/8}{\alpha^2 l + 2\alpha} \qquad\qquad (I41)$$

$$\beta_3 = \frac{\lambda_c + l\lambda_c^2/2 + l^2\lambda_c^3/8}{\alpha^2 l + 2\alpha} \qquad\qquad (I42)$$

Substituting the values from (I40), (I41) and (I42) in (I39):

$$y_1 = \frac{Pl\alpha_3\beta_1}{C_u} + \frac{S_v}{C_u} + A(1 - \beta_2) + B(1 - \beta_3) \qquad (I43)$$

Finally,

Over opening :

$$\text{Deflection} = \frac{Px^4}{24K} + L_1x^3 + N_1x^2 + \tan\phi_1 + y_1 - \frac{S_v}{C_u} \qquad (I44)$$

where,

L_1, N_1, $\tan\phi_1$ and y_1 can be obtained from (I20), (I21), (I22) and (I43).

$$\text{Maximum horizontal shear stress} = -\frac{3K}{2D}\left(\frac{Px}{K} + 6L_1\right) \qquad (I45)$$

$$\text{Outermost fibre stress} = \pm\frac{KD}{2I}\left(\frac{Px^2}{2K} + 6L_1x + 2N_1\right) \qquad (I46)$$

Over the abutment :

$$\text{Deflection} = A_1\text{Sin}\alpha x e^{\alpha x} + B_1\text{Cos}\alpha x e^{\alpha x} + Ae^{\lambda_s x} + Be^{\lambda_c x} \qquad (I47)$$

$$\text{Maximum horizontal shear stress} = -\frac{3K}{2D}[2\alpha^3(A_1 - B_1)\text{Cos}\alpha x e^{\alpha x}$$

$$-2\alpha^3(A_1 + B_1)\text{Sin}\alpha x e^{\alpha x} + \lambda_s^3 Ae^{\lambda_s x} + \lambda_c^3 Be^{\lambda_c x}] \qquad (I48)$$

$$\text{Outermost fibre stress} = \pm\frac{KD}{2I}(2\alpha^2 A_1\text{Cos}\alpha x e^{\alpha x} - 2\alpha^2 B_1\text{Sin}\alpha x e^{\alpha x}$$

$$+ \lambda_s^2 Ae^{\lambda_s x} + \lambda_c^2 Be^{\lambda_c x}) \qquad (I49)$$

THICK BEAM

For a small element of thick beam (Fig. 6.6),

$$\text{Shear stress, } \tau_{xy} = \frac{3T}{3D}\left(1 - \frac{d^2}{z^2}\right) \qquad (I50)$$

where,

d = distance from the neutral axis

z = distance between the neutral axis and outer boundary

$$\text{Shear modulus, } G = \frac{E}{2(1 + \nu)} \qquad (I51)$$

From Fig. 25 in Chapter 6, summation of vertical forces :

$$T - (T + dT) + C_u y_3 dx - (S_v - Se^{\lambda_s x} + Ce^{\lambda_c x})dx = 0$$

where,

y_3 = deflection of lowest fibre of thick beam over abutment

= deflection of thin beam over abutment

$$= A_1 \text{Sin}\alpha x e^{\alpha x} + B_1 \text{Cos}\alpha x e^{\alpha x} + \frac{S_v}{C_u} + Ae^{\lambda_s x} + Be^{\lambda_c x} \qquad (I52)$$

$$\text{Therefore, } \frac{dT}{dx} = C_u y_3 - (S_v - Se^{\lambda_s x} - Ce^{\lambda_c x}) \qquad (I53)$$

From eqns. (50) and (51), the shearing strain γ, is

$$\gamma = \frac{3T(1 + \nu)}{2DE} (1 - \frac{d^2}{z^2}) \qquad (I54)$$

Therefore, the slope of the deflection curve due to shear :

$$\frac{dy_4}{dx} = \frac{3T(1 + \nu)}{2DE} (1 - \frac{d_2}{z^2}) \qquad (I55)$$

where,

y_4 = deflection due to shear

Hence, the curvature produce by shear is

$$\frac{d^2 y_4}{dx^2} = \frac{3(1 + \nu)}{2DE} (1 - \frac{d^2}{z^2})\{C_u y_3 - (S_v - Se^{\lambda_s x} + Ce^{\lambda_c x})\} \qquad (I56)$$

If y is the total deflection, then the total curvature is

$$\frac{d^2 y}{dx^2} = \frac{d^2 y_3}{dx^2} + \frac{d^2 y_4}{dx^2} \qquad (I57)$$

167

Integrating (I56) :

$$y_4 = aC_u \left(\frac{B_1}{2\alpha^2} \sin\alpha e^{\alpha x} - \frac{A_1}{2\alpha^2} \cos\alpha x e^{\alpha x} + \frac{A}{\lambda_s^2} e^{\lambda_s} + \frac{B}{\lambda_c^2} e^{\lambda_c}\right)$$

$$+ \frac{aSS_v}{\lambda_s^2} e^{\lambda_s} - \frac{aCS_v}{\lambda_c^2} e^{\lambda_c} + C_1 x + C_2 \tag{I58}$$

But, as $x \to \infty$, $y = \frac{S_v}{C_u}$

$\therefore C_1 = C_2 = 0$

$$y_4 = aC_u \left(\frac{B_1}{2\alpha^2} \sin\alpha e^{\alpha x} - \frac{A_1}{2\alpha^2} \cos\alpha x e^{\alpha x} + \frac{A}{\lambda_s^2} e^{\lambda_s} + \frac{B}{\lambda_c^2} e^{\lambda_c}\right)$$

$$+ \frac{aSS_v}{\lambda_s^2} e^{\lambda_s} - \frac{aCS_v}{\lambda_c^2} e^{\lambda_c} \tag{I59}$$

where,

$$a = \frac{3(1 + \nu)}{2DE} \left(1 - \frac{d^2}{z^2}\right)$$

From (I59) and (I52) :

$$y = y_3 + y_4$$

$$= \left(A_1 + \frac{aC_u B_1}{2\alpha^2}\right)\sin\alpha x e^{\alpha x} + \left(B_1 - \frac{aC_u A_1}{2\alpha^2}\right)\cos\alpha x e^{\alpha x}$$

$$+ \left(A_1 + \frac{aC_u A}{\lambda_s^2} + \frac{aS}{\lambda_s^2}\right)e^{\lambda_s x} + \left(B + \frac{aC_u B}{\lambda_c^2} - \frac{aC}{\lambda_c^2}\right)e^{\lambda_c x}$$

$$+ \frac{S_v}{C_u} \tag{I60}$$

$$\therefore \frac{dy}{dx} = \left\{\alpha (A_1 - B_1) + \frac{aC_u (A_1 + B_1)}{2\alpha}\right\}\sin\alpha x e^{\alpha x}$$

$$+ \left\{\alpha (A_1 + B_1) - \frac{aC_u (A_1 - B_1)}{2\alpha}\right\}\cos\alpha x e^{\alpha x}$$

$$+ \left(\lambda_s A + \frac{aC_u A}{\lambda_s} + \frac{aS}{\lambda_s}\right)e^{\lambda_s x}$$

$$+ \left(\lambda_s B + \frac{aC_u B}{\lambda_c} + \frac{aC}{\lambda_c}\right)e^{\lambda_c x} \tag{I61}$$

168

$$\frac{d^2y}{dx^2} = (aC_uA_1 - 2\alpha^2B_1)Sin\alpha xe^{\alpha x} + (aC_uB_1 + 2\alpha^2A_1)Cos\alpha xe^{\alpha x}$$

$$+ (\lambda_s^2A + aC_uA + aS)e^{\lambda_s x}$$

$$+ (\lambda_c^2B + aC_uB + aC)e^{\lambda_c x} \tag{I62}$$

Let, the differential equation for a thick beam over the opening is :

$$y = \frac{Px^4}{24K} + L_2x^3 + N_2x^2 + R_2 + Q_2 \tag{I63}$$

$$\frac{dy}{dx} = \frac{Px^3}{6K} + 3L_2x^2 + N_2x + R_2 \tag{I64}$$

$$\frac{d^2y}{dx^2} = \frac{Px^2}{2K} + 6L^2x + 2N_2 \tag{I65}$$

Equating (I60), (I61) and (I62) with (I63), (I64) and (I65)

respectively @ x = 0 :

$$Q_2 = B_1 - \frac{aC_uA_1}{2\alpha^2} + A + \frac{aC_uA}{\lambda s^2} + \frac{aS}{\lambda s^2}$$

$$+ B + \frac{aC_uB}{\lambda_c^2}A + \frac{aC}{\lambda_c^2} + \frac{S_v}{C_u} \tag{I66}$$

$$R_2 = \alpha (A_1 + B_1) - \frac{aC_u(A_1 - B_1)}{2\alpha} + \lambda_s A + \frac{aC_uA}{\lambda_c} + \frac{aS}{\lambda_c}$$

$$+ \lambda_cB + \frac{aC_uB}{\lambda_c} - \frac{aC}{\lambda_c} \tag{I67}$$

$$N_2 = (aC_uB_1 + 2\alpha^2A_1 + \lambda_s^2A + aC_uA + aS + \lambda_c^2B$$

$$+ aC_uB - aC)/2 \tag{I68}$$

But, @ $x = 1/2$, $\frac{dy}{dx} = 0$

$\therefore$ @ $x = 1/2$, from (I64) :

$$L_2 = -\frac{4}{3l^2} \left(\frac{Pl^3}{48K} + N_2l + R_2 \right) \tag{I69}$$

169

Finally,

Over opening :

$$\text{Deflection} = \frac{Px^4}{24K} + L_2x^3 + N_2x^2 + R_2 + Q_2 - \frac{S_v}{C_u} \qquad (I70)$$

where,

Q_2, R_2, N_2 and L_2 can be obtained from (I66), (I67), (I68) and (I69).

Over the abutment :

$$\text{Deflection} = (A_1 + \frac{aC_uB_1}{2\alpha^2})Sin\alpha xe^{\alpha x} + (B_1 - \frac{aC_uA_1}{2\alpha^2})Cos\alpha xe^{\alpha x}$$

$$+ (A_1 + \frac{aC_uA}{\lambda_s^2} + \frac{aS}{\lambda_s^2})e^{\lambda_s x} + (B + \frac{aC_uB}{\lambda_c^2} - \frac{aC}{\lambda_c^2})e^{\lambda_c x} \qquad (I71)$$

170

COMPUTER PROGRAMS USED FOR OBTAINING RESULTS

FROM BEAM FORMULATION

PROGRAM I :

```
10 REM THE NAME OF THIS PROGRAM IS "NEWTN"
20 REM THIS PROGRAM CALCULATES FROM THIN BEAM FORMULATION
30 SHORT X,Y,Y3,Y4,Z5,Y7
40 INTEGER N7
50 S1$='1000'
60 P$='68.895'
70 INPUT 'OVERBURDEN (DEPTH) = ',S1$;S1
80 S1=27000*S1
90 K1=.33
100 L2=5
110 M2=.95
120 L=50
130 L5=L/2
140 D=40
150 W=12.5
160 B2=6.25
170 H=3
180 D1=100
190 E3=35000000000
200 E4=E3/1.9
210 E=4*E3*E4/(E3^.5+E4^.5)^2
220 N=.25
230 E1=2500000000
240 N1=.3
250 Y8=(W+B2)/B2
260 Y2=2.048-.919*K1+.572*LOG(W/H)+.09*((W/B2)^2-1)
270 P0$='100'
280 INPUT 'LOAD OVER OPENING (DEPTH)=',P$;P
290 P=27000*P
300 INPUT 'LOAD AT X=0(DEPTH)=',P0;P0
310 P0=27000*P0
320 IF Y8>Y2 THEN 350
330 Y9=Y2
340 GOTO 360
```

```
350 Y9=Y8
360 C=P*(Y9-1)
370 S=S1*P*Y9-P-P0
380 L4=LOG(S/(S+P0-M2*S1))/L2
390 L3=L4*C/(5*P*Y9*R*L4+P*R*L4-5*P0*R*L4+S)
400 I=D^3/12
410 K=E*I/(1-N^2)
420 C1=E1/(D1*(1-N1^2)
430 M9=S1/C1
440 A2=(C1/(4*K))^.25
450 A=S/(K*L4^4+C1)
460 B=C/(K*L3^4+C1)
470 B3=(L^2/6+L/A2+1/A2^2)/(A2*L+2)
480 B7=(L4+L*L4^2/2+L^2*L4^3/8)/(A2^2*L+2*A2)
490 B8=(L3+L*L3^2/2+L^2*L3^3/8)/(A2^2*L+2*A2)
500 Y1=P*L*A2^3*B3/C1+S1/C1+A*(1-B7)+B*(1-B8)
510 F4=2*A2*(Y1-S1/C1-A-B)+L4*A+L3*B-P*L/(4*K*A2^2)
520 B1=Y1-S1/C1-A-B
530 A1=1/A2*(F4-A2*(Y1-S1/C1)+A*(A2-L4)+B*(A2-L3)
540 L9=(2*A2^3*(A1-B1)+L4^3*A+L3^3*B)/6
550 N9=(2*A2^2*A1+L4^2*A+L3^2*B)/2
560 N7=1
570 FOR X=L5 TO 0 STEP -.9
580 Y=(P*X^4/(24*K)+L9*X^3+N9*X^2+F4*X+Y1-M9)*1000
590 Y3=D*(P*X^3/(6*K)+3*L9*X^2+N9*X+F4)
600 Y3=Y3*1000
610 Y4=-1.5*K*(P*X*/K+6*L9)/D
620 Y4=Y4/1000000
630 Z5=-.5*K*D*(P*X^2/(2*K)+6*L9*X+2*N()/I
640 IF Z5>=0 THEN 670
650 Z5=E3^.5/(E3^.5+E4^.5)*Z5/(1000000*.5)
660 GOTO 680
670 Z5=.5*Z5/(E3^.5/(E3^.5+E4^.5))/1000000
680 Y7=0
690 ASSIGN # 1 TO 'DATA'
700 PRINT # 1,N7 ; X,Y,Y3,Y4,Z5,Y7
710 N7=N7+1
720 NEXT X
730 FOR X=0 TO -300 STEP -.3
740 IF N7<=58 THEN 760
750 FOR X=-9 TO -300 STEP -1.8
760 Y=A1*SIN(A2*X)*EXP(A2*X)+B1*COS(A2*X)*EXP(A2*X)+S1/C1
    +A*EXP(L4*X)+B*EXP(L3*X)-M9
770 Y=Y*1000
780 O=A2*EXP(A2*X)*(COS(A2*X)*(A1+B1)+SIN(A2*X)*(A1-B1))
790 T=A*L4*EXP(L4*X)+B*L3*EXP(L3*X)
800 Y3=D*(O+T)
810 Y3=Y3*1000
820 F1=2*(A1B1)*A2^3*EXP(A2*X)*COS(A2*X)
```

```
        -2*(A1+B1)*A2^3*EXP(A2*X)*SIN(A2*X)
830 Z=A*L4^3*EXP(L4*X)+B*L3^3*EXP(L3*X)
840 Y4=-1.5/D*K*(F1+Z)
850 Y4=Y4/1000000
860 Z5=2*A2^2*A1*COS(A2*X)*EXp(A2*X)
        -2*A2^2*B1*SIN(A2*X)*EXp(A2*X)+L4^2*A*EXP(L4*X)
870 Z5=Z5+L3^2*B*EXP(L3*X)
880 Z5=-.5*K*D*Z5/I
890 Z5=.5*Z5/(E3^.5/(E3^.5+E4^.5))/1000000
900 Y5=P+C*EXP(L3*X)
910 Y6=S1-P-S*EXP(L4*X)
920 Y7=Y5+Y6
930 PRINT # 1,N7 ; X,Y,Y3,Y4,Z5,Y7
940 N7=N7+1
950 NEXT X
960 END
```

PROGRAM II :

```
10 REM THE NAME OF THIS PROGRAM IS "NEWTKH"
20 REM THIS PROGRAM CALCULATES FROM THICK BEAM FORMULATION
30 INTEGER N7
40 S1$='1000'
50 P$='68.895'
60 INPUT 'OVERBURDEN (DEPTH) = ',S1$;S1
70 S1=27000*S1
80 K1=.33
90 L2=5
100 M2=.95
110 L=50
120 L5=L/2
130 D=40
140 W=12.5
150 B2=6.25
160 H=3
170 D1=100
180 E3=35000000000
190 E4=E3/1.9
200 E=4*E3*E4/(E3^.5+E4^.5)^2
210 N=.25
220 E1=2500000000
230 N1=.3
240 Y8=(W+B2)/B2
250 Y2=2.048-.919*K1+.572*LOG(W/H)+.09*((W/B2)^2-1)
260 P0$='100'
```

```
270 INPUT 'LOAD OVER OPENING (DEPTH)=',P$;P
280 P=27000*P
290 INPUT 'LOAD AT X=0(DEPTH)=',P0;P0
300 P0=27000*P0
310 IF Y8>Y2 THEN 340
320 Y9=Y2
330 GOTO 350
340 Y9=Y8
350 C=P*(Y9-1)
360 S=S1*P*Y9-P-P0
370 L4=LOG(S/(S+P0-M2*S1))/L2
380 L3=L4*C/(5*P*Y9*R*L4+P*R*L4-5*P0*R*L4+S)
390 I=D^3/12
400 K=E*I/(1-N^2)
410 C1=E1/(D1*(1-N1^2)
420 M9=S1/C1
430 A2=(C1/(4*K))^.25
440 A3=3*(1+N)/(2*D*E)
450 A=S/(K*L4^4+C1)
460 B=C/(K*L3^4+C1)
470 B3=(L^2/6+L/A2+1/A2^2)/(A2*L+2)
480 B7=(L4+L*L4^2/2+L^2*L4^3/8)/(A2^2*L+2*A2)
490 B8=(L3+L*L3^2/2+L^2*L3^3/8)/(A2^2*L+2*A2)
500 Y1=P*L*A2^3*B3/C1+S1/C1+A*(1-B7)+B*(1-B8)
510 F4=2*A2*(Y1-S1/C1-A-B)+L4*A+L3*B-P*L/(4*K*A2^2)
520 B1=Y1-S1/C1-A-B
530 A1=1/A2*(F4-A2*(Y1-S1/C1)+A*(A2-L4)+B*(A2-L3))
540 Y1=B1-A3*C1*A1/(2*A2^2)+A+A3*C1*A/L4^2+A3*S/L4^2+B
        +A3*C1*B/L3^2-A3*C/L3^2+S1/C1
550 F4=A2*(A1+B1)-A3*C1*(A1-B1)/(2*A2)+L4*A+A3*C1*A/L4
        +A3*S/L4+L3*B+A3*C1*B/L3-A3*C/L3
560 N9=(A3*C1*B1+2*A2^2*A1+L4^2*A+A3*C1*A+A3*S+L3^2*B
        +A3*C1*B-A3*C)/L3
570 L9=4*(-P*L^3/(48*K)-N9*L-F4)/(3*L^2)
580 N7=1
590 FOR X=L5 TO 0 STEP -.9
600 Y=(P*X^4/(24*K)+L9*X^3+N9*X^2+F4*X+Y1-M9)*1000
610 Y3=D*(P*X^3/(6*K)+3*L9*X^2+N9*X+F4)
620 Y3=Y3*1000
630 Y7=0
640 ASSIGN # 1 TO 'DATA'
650 PRINT # 1,N7 ; X,Y,Y3,Y4,Z5,Y7
660 N7=N7+1
670 NEXT X
680 FOR X=0 TO -300 STEP -.3
690 IF N7<=58 THEN 710
700 FOR X=-9 TO -300 STEP -1.8
710 Y=(A1+A3*C1*B1/(2*A2^2))*SIN(A2*X)*EXP(A2*X)
        +(B1-A3*C1*A1/(2*A2^2))*COS(A2*X)*EXP(A2*X)
```

```
720 Y=Y+(A+A3*C1*A/L4^2+A3*S/L4^2)*EXP(L4*X)
    +(B+A3*C1*B/L3^2-A3*C/L3^2)*EXP(L3*X)+S1/C1
730 Y=(Y-M9)*1000
740 Y3=(A2*(A1-B1)+A3*C1*(A1+B1)/(2*A2))*SIN(A2*X)*EXP(A2*X)
750 Y3=Y3+(A2*(A1+B1)-A3*C1*(A1-B1)/(2*A2))*COS(A2*X)
    *EXP(A2*X)
760 Y3=Y3+(L4*A+A3*C1*A/L4+A3*S/L4)*EXP(L4*X)
    +(L3*B+A3*C1*B/L3+A3*C/L3)*EXP(L3*X)
770 Y3=D*Y3*1000
780 Y5=P+C*EXP(L3*X)
790 Y6=S1-P-S*EXP(L4*X)
800 Y7=Y5+Y6
810 PRINT # 1,N7 ; X,Y,Y3,Y7
820 N7=N7+1
830 NEXT X
840 END




PROGRAM III :

10 REM THE NAME OF THIS PROGRAM IS "NEWTKE"
20 REM THIS PROGRAM CALCULATES STRAIN ENERGY RELEASE RATE
   USING THICK BEAM FORMULATION
30 INTEGER N7
40 S1=1000
50 S1=27000*S1
60 K1=.33
70 L2=5
80 M2=.95
90 N8=1
100 FOR L=1 TO 350 STEP1
110 L5=L/2
120 D=40
130 W=12.5
140 B2=6.25
150 H=3
160 D1=100
170 E3=35000000000
180 E4=E3/1.9
190 E=4*E3*E4/(E3^.5+E4^.5)^2
200 N=.25
210 E1=2500000000
220 N1=.3
230 P=1000
240 P=27000*P
250 P0=100
```

```
260 P0=27000*P0
270 Y9=1+L/30
280 C=P*(Y9-1)
290 S=S1*P*Y9-P-P0
300 L4=LOG(S/(S+P0-M2*S1))/L2
310 L3=L4*C/(5*P*Y9*R*L4+P*R*L4-5*P0*R*L4+S)
320 I=D^3/12
330 K=E*I/(1-N^2)
340 C1=E1/(D1*(1-N1^2)
350 M9=S1/C1
360 A2=(C1/(4*K))^.25
370 A3=3*(1+N)/(2*D*E)
380 A=S/(K*L4^4+C1)
390 B=C/(K*L3^4+C1)
400 B3=(L^2/6+L/A2+1/A2^2)/(A2*L+2)
410 B7=(L4+L*L4^2/2+L^2*L4^3/8)/(A2^2*L+2*A2)
420 B8=(L3+L*L3^2/2+L^2*L3^3/8)/(A2^2*L+2*A2)
430 Y1=P*L*A2^3*B3/C1+S1/C1+A*(1-B7)+B*(1-B8)
440 F4=2*A2*(Y1-S1/C1-A-B)+L4*A+L3*B-P*L/(4*K*A2^2)
450 B1=Y1-S1/C1-A-B
460 A1=1/A2*(F4-A2*(Y1-S1/C1)+A*(A2-L4)+B*(A2-L3))
470 Y1=B1-A3*C1*A1/(2*A2^2)+A+A3*C1*A/L4^2+A3*S/L4^2+B
      +A3*C1*B/L3^2-A3*C/L3^2+S1/C1
480 F4=A2*(A1+B1)-A3*C1*(A1-B1)/(2*A2)+L4*A+A3*C1*A/L4
      +A3*S/L4+L3*B+A3*C1*B/L3-A3*C/L3
490 N9=(A3*C1*B1+2*A2^2*A1+L4^2*A+A3*C1*A+A3*S+L3^2*B
      +A3*C1*B-A3*C)/L3
500 L9=4*(-P*L^3/(48*K)-N9*L-F4)/(3*L^2)
510 Z6=(P^2*L^5/(3840*K)+P*L9*L^4/64+P*N9*L^3/24+P*F4*L^2/8
      +P*Y1*L/2-P*M9*L/2)/1000000
520 Z7=(P^2*L^4/(768*K)+P*L9*L^3/16+P*N9*L^2/8+P*F4*L/4
      +P*Y1/2-P*M9/2)/1000000
530 ASSIGN # 1 TO 'DATA'
540 PRINT # 1,N8 ; N8,L,Z7
550 N8=N8+1
560 NEXT L
570 END
```

APPENDIX – III

ESTIMATE FOR MAXIMUM STRESS CONCENTRATION

For a row of rectangular openings, characteristic of the Saskatchewan potash mine panels, the maximum stress concentration Y_m, is

$$Y_m = (2.04 - 0.919K_o) + 0.572\ln(\frac{W}{H})$$

$$- 0.09\{(\frac{W}{B} + 1)^2 - 1\} \qquad\qquad (III1)$$

or, $Y_m = \dfrac{W + B}{B}$ (III2), whichever is greater(Barron,1984).

where,

    K_o = horizontal stress/vertical stress

    W = room width

    B = pillar width

    H = height of opening

APPENDIX – IV

ENERGY RELEASE FOR AN UNDERMINED ROOF ACTING AS A BEAM

The bending behavior of a roof beam having a thickness t, span l, and breadth b, exposed by excavation, can be described by elastic beam theory (Fig. 8.3).

When the span is undermined the beam will do work against any support force along the lower surface. If the support force reduces linearly from the virgin state to zero on the final free surface then, for a small strip, dx (Fig. 8.4), the work done by the beam is given by :

$$W_1 = \frac{1}{2} P * b * \delta * dx$$

where,

P = initial normal stress before mining

δ = beam deflection for the strip dx

Along the upper surface of the beam external loads applied by the rock strata above the beam do work on the beam. For a constant loading the work done at the completion of beam deflection is given by :

$$W_2 = P * b * \delta * dx$$

The difference between the work done by the beam and the work done on the beam is the strain energy stored in the beam, W_3,

$$W_3 = \frac{1}{2} P * b * \delta * dx \qquad\qquad (IV1)$$

If the excavation is made instantaneously, i.e., no gradual reduction of support forces, no work is done by the beam against the support forces and the excess energy causes oscillation

of the beam. Eventually the beam comes to rest and the stored strain energy is still given by eqn. (IV1). The excess energy, W_r, or released energy, must therefore be given by the difference between W_2 and W_s, i.e.,

$$W_r = \frac{1}{2} P * b * \delta * dx \tag{IV2}$$

Therefore, $W_s = W_r$

To obtain W_s and W_r for the whole beam these equations must be integrated over the total span.

The released energy, W_r due to the excavation of opening can now be obtained as follows :

$$W_r = 2 \int_0^{l/2} \frac{1}{2} P * b * \delta * dx \tag{IV2}$$

where,

$$\delta = \text{deflection of beam}$$

Substituting the value of δ from eqn. (I63), taking $b = 1$, and integrating :

$$W_r = \frac{P^2 l^5}{3840K} + \frac{PL_2 l^4}{64} + \frac{PN_2 l^3}{24} + \frac{PR_2 l^2}{8} + \frac{PQ_2 l}{2}$$

$$- \frac{S_v P l}{2C_u} \tag{IV3}$$

Finally, the rate of energy release for the next increament in span, can be derived by differentiating eqn. (IV4) with respect to the span l :

$$\frac{dW_r}{dl} = \frac{P^2 l^2}{768K} + \frac{PL_2 l^4}{16} + \frac{PN_2 l^3}{8} + \frac{PR_2}{4} + \frac{PQ_2 l}{2}$$

$$- \frac{S_v P}{2C_u} \tag{IV4}$$

179

APPENDIX – V

CALIBRATION CURVES FOR RESTRAINING BARS

The restraining bars were calibrated for load/microstrain output of the strain gauges using a Universal Testing System. The calibration was done for a range of load from 0 to 18 kN. The following Figs. V1, V2, V3 and V4 show the calibration curves for the larger restraining bars LI, LII, LIII and LIV respectivey, which were mosty used in the beam testing.
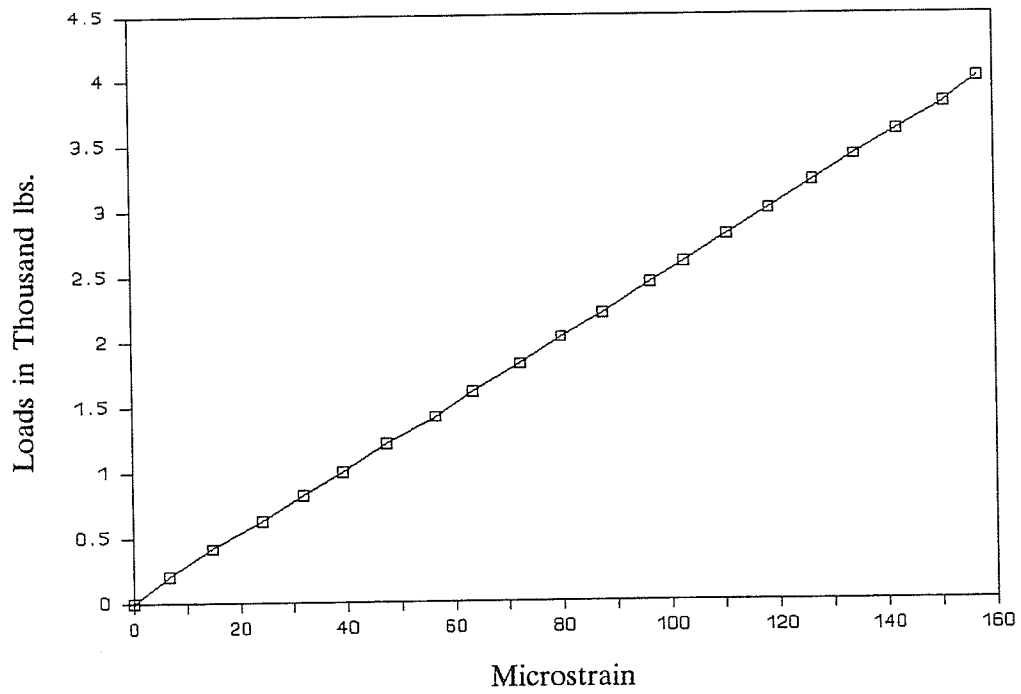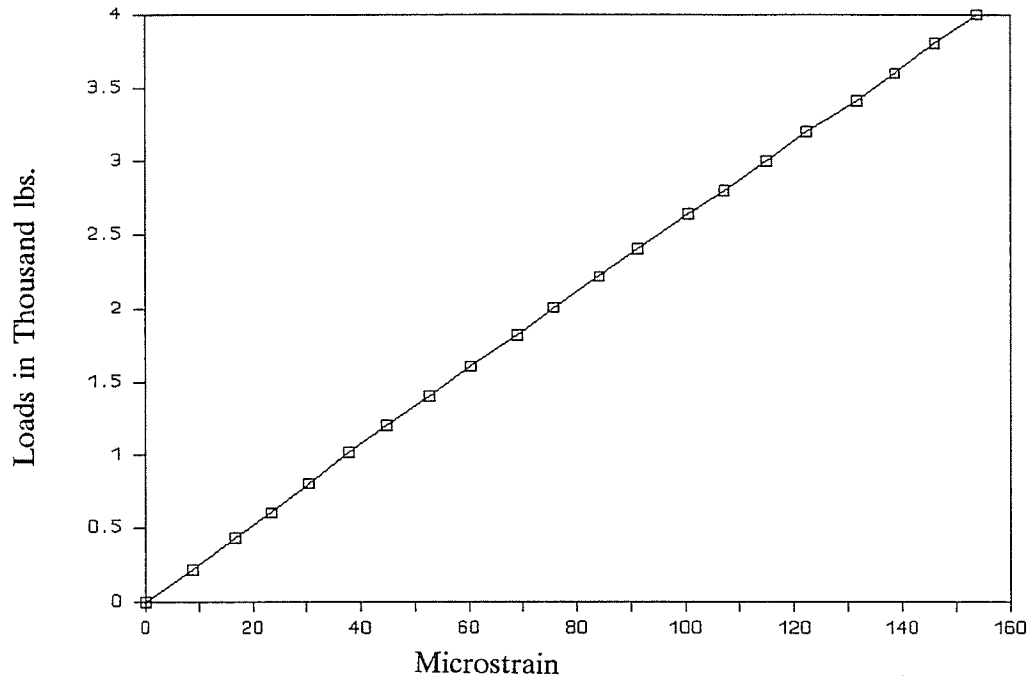
Fig. V1 Calibration curve for restraining bar LI.

Fig. V2 Calibration curve for restraining bar LII.
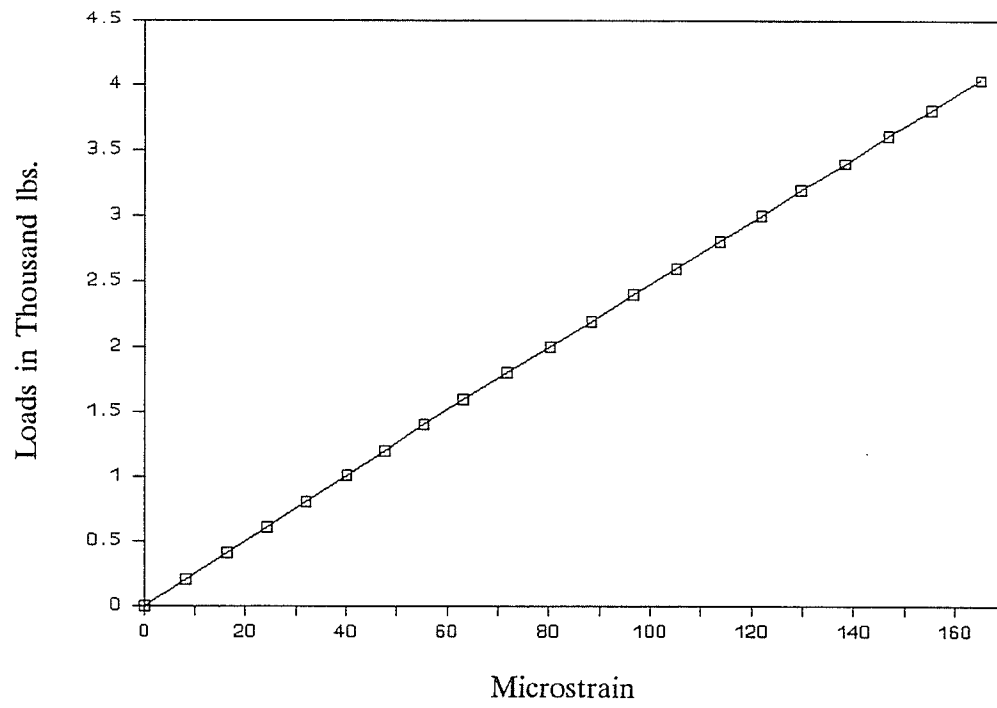
Fig. V3 Calibration curve for restraining bar LIII.
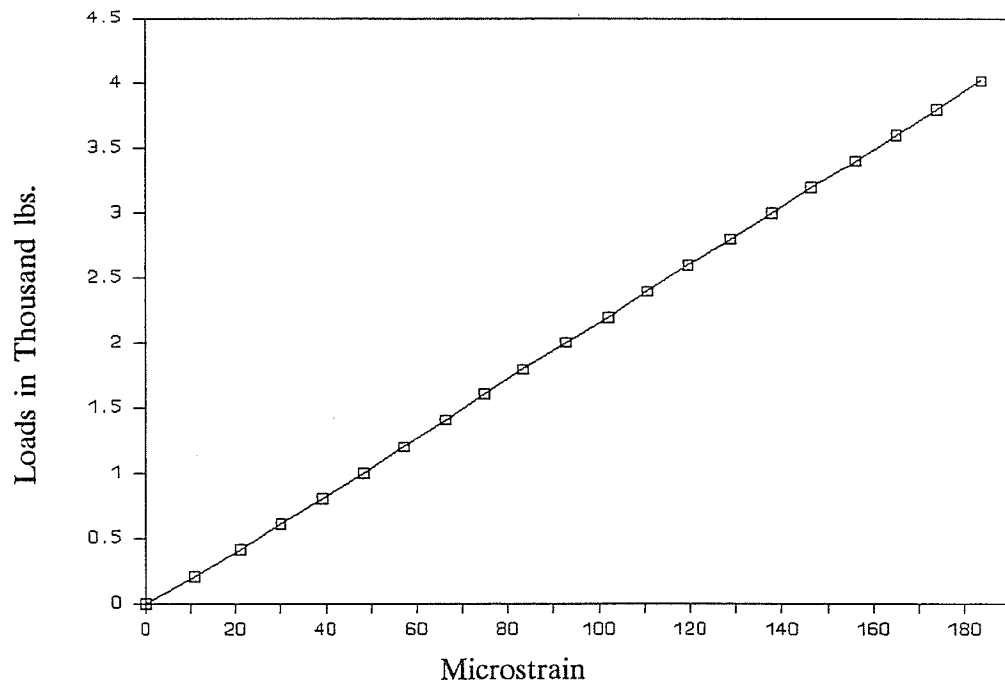
Fig. V4 Calibration curve for restraining bar LIV.

INDIVIDUAL BEAM TEST RESULTS

TEST SP0

Purpose : Trial test

Material : Saskatoon Potash

Dimensions of Beam : Depth   Breadth   Length

                          2.3 cm   2.3 cm   12.5 cm

Separation of Vertical supports : 10 cm

Loading Conditions : 1 point loading.

Notes :

(a) Midspan cracking commenced @ 0.27 kN.

(b) Diagonal cracking occurred @ 2.7 kN, which is just below the peak

    load.

TEST SP1

Purpose : Standard test

Material : Saskatoon Potash

Dimensions of Beam : Depth   Breadth   Length

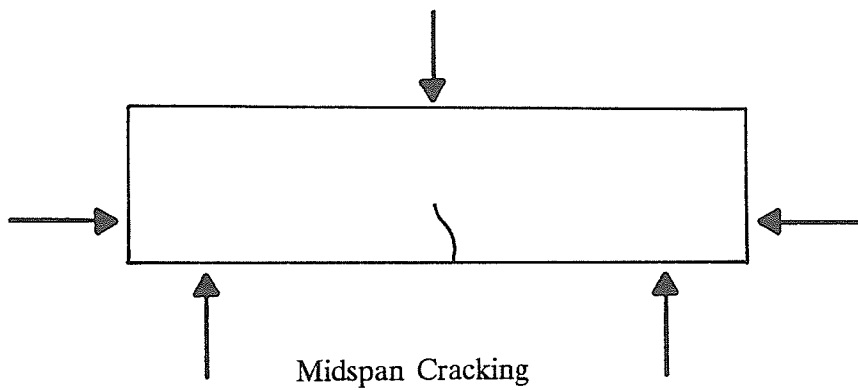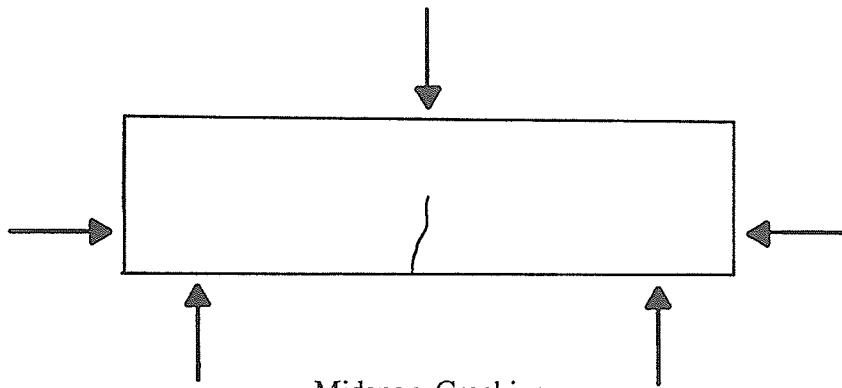   5.3 cm   4.8 cm   29.8 cm

Separation of Vertical supports : 18.9 cm

Loading Conditions : 1 point loading.
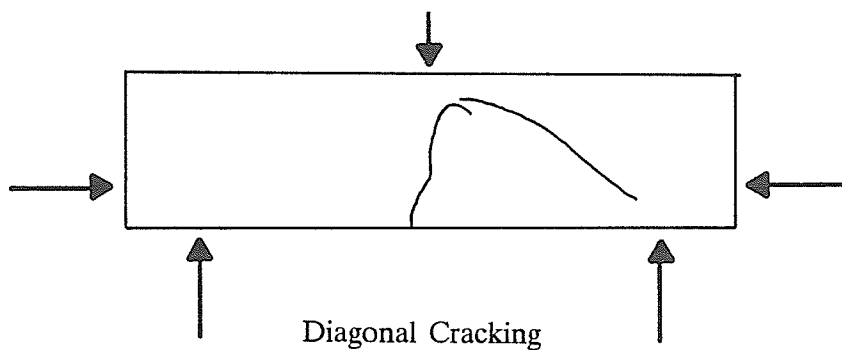

Notes :

(a) Slight Prestress used to even restraining bars outputs.

(b) No additional load noticed on restraining bars until after 1st crack

    i.e., midspan crack @ 2 kN; then immediate jump.

(c) Midspan extended upto about 4/5 of the beam depth.

(d) Diagonal cracking occurred @ 12.1 kN, which is just below the peak

    load.

SP1 Crack Patterns :

Midspan Cracking

Diagonal Cracking
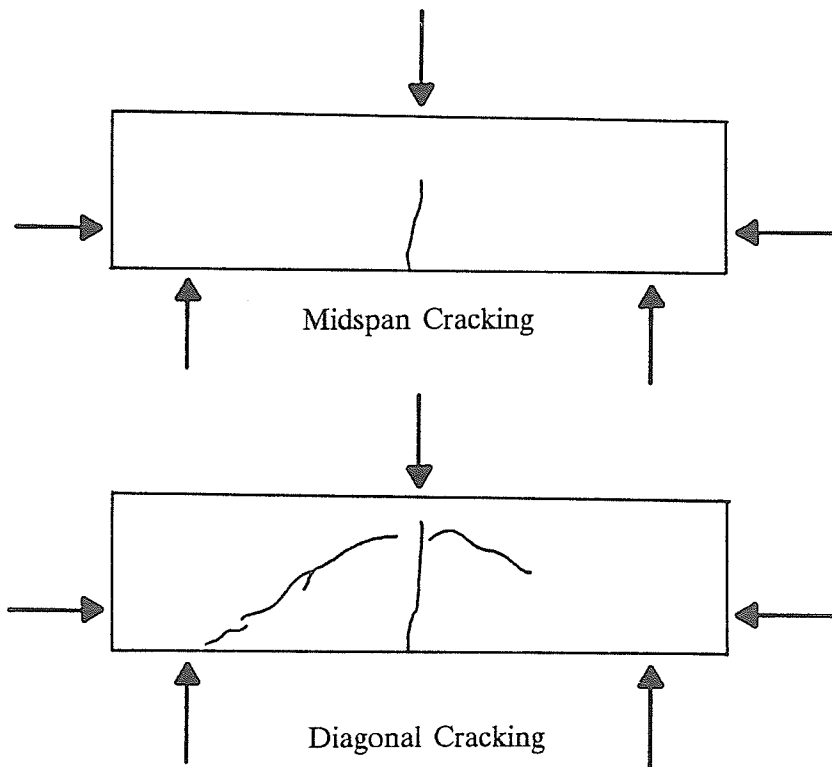
TEST SP2

Purpose : Standard test

Material : Saskatoon Potash

Dimensions of Beam : Depth   Breadth   Length

                    4.9 cm   3.7 cm   26.9 cm

Separation of Vertical supports : 16 cm

Loading Conditions : 1 point loading.

Notes :

(a) Slight Prestress used to even restraining bars outputs.

(b) No additional load noticed on restraining bars until after 1st crack i.e., midspan

crack @ 1.5 kN; then immediate jump.

(c) Midspan extended beyond about 4/5 of the beam depth.

(d) Diagonal cracking occurred @ 8.5 kN, which is just below the peak load.

SP2 Crack Patterns :

Midspan Cracking

Diagonal Cracking
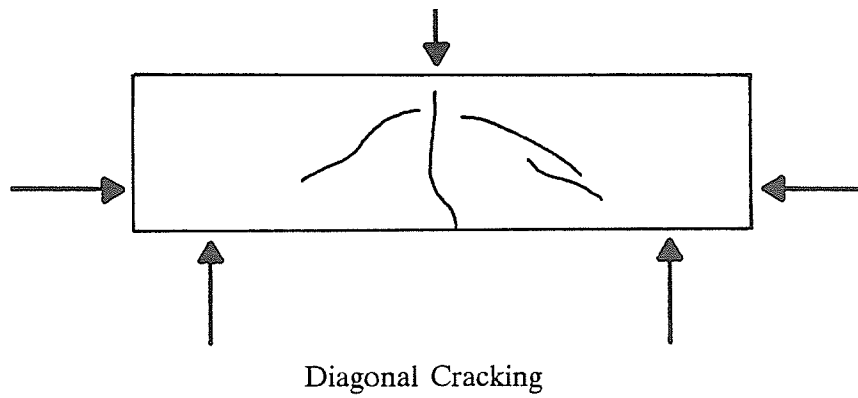
TEST DL1

Purpose : Standard test

Material : Tyndall Stone

Dimensions of Beam : Depth   Breadth   Length

                            4.7 cm   5.0 cm   26.3 cm

Separation of Vertical supports : 15.4 cm

Loading Conditions : 1 point loading.

Notes :

(a) Slight Prestress used to even restraining bars outputs.

(b) No additional load noticed on restraining bars until after 1st crack i.e., midspan crack @ 1.7 kN; then immediate jump.

(c) Midspan extended beyond about 4/5 of the beam depth.

(d) Diagonal cracking occurred @ 5.7 kN.

(e) Peak load of 7 kN reached after diagonal cracking.

(f) Ultimate collapse appears to have occrred as a result of failure along the diagonal crack.

DL1 Crack Patterns :

Midspan Cracking

Diagonal Cracking
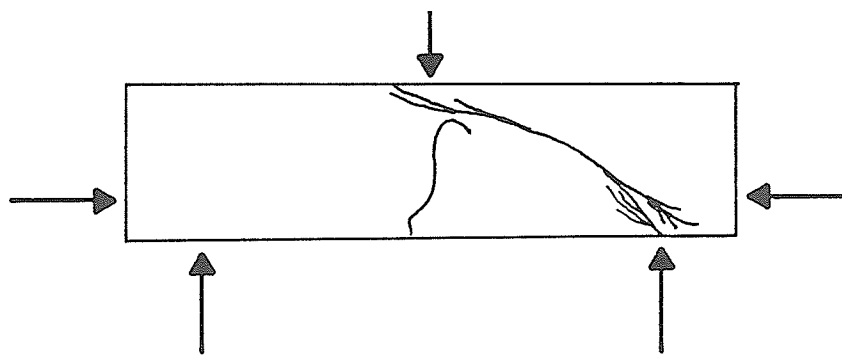
Ultimate Failure

TEST DL2

Purpose : Standard test

Material : Tyndall Stone

Dimensions of Beam : Depth   Breadth   Length

   4.8 cm   4.8 cm   29.9 cm

Separation of Vertical supports : 19 cm

Loading Conditions : 1 point loading.

Notes :

(a) Slight Prestress used to even restraining

     bars outputs.

(b) No additional load noticed on restraining bars until after 1st crack i.e., midspan

     crack @ 1.7 kN; then immediate jump.

(c) Midspan extended beyond about 4/5 of the beam depth.

(d) Diagonal cracking occurred @ 11.5 kN.

(e) Peak load of 12.2 kN reached after diagonal cracking.

(f) Ultimate collapse appears to have occrred as a result of failure along the

     diagonal crack.

DL2 Crack Patterns :

Midspan Cracking

Diagonal Cracking

Ultimate Failure
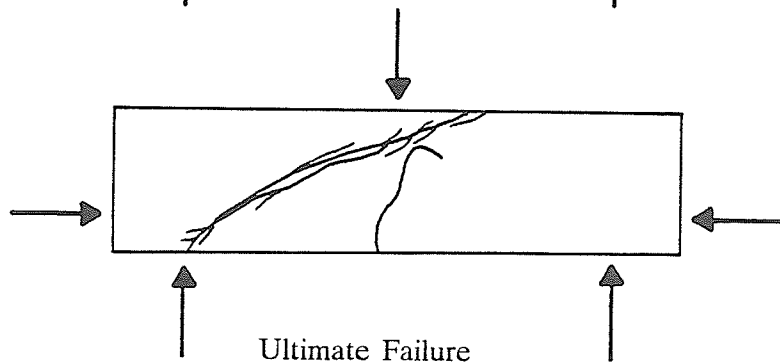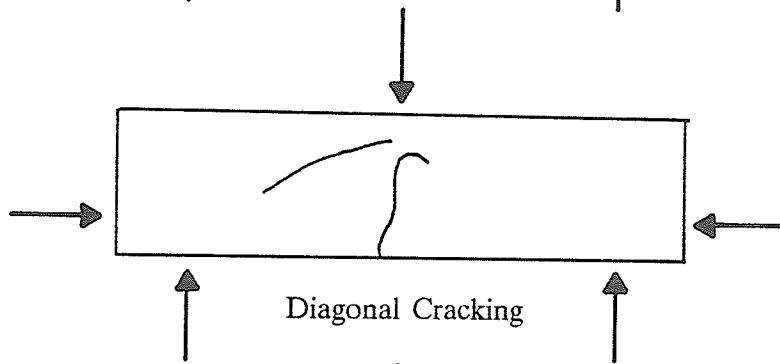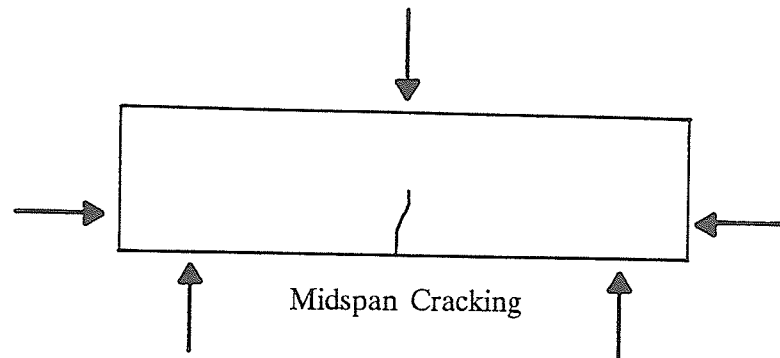
TEST DL3

Purpose : Standard test

Material : Tyndall Stone

Dimensions of Beam : Depth   Breadth   Length

                     6.3 cm   6.2 cm   29.8 cm

Separation of Vertical supports : 18.9 cm

Loading Conditions : 1 point loading.

Notes :

Premature split vertically along the length of the beam due to weak zone
under the point load.

TEST DL4

Purpose : Standard test

Material : Tyndall Stone

Dimensions of Beam : Depth   Breadth   Length

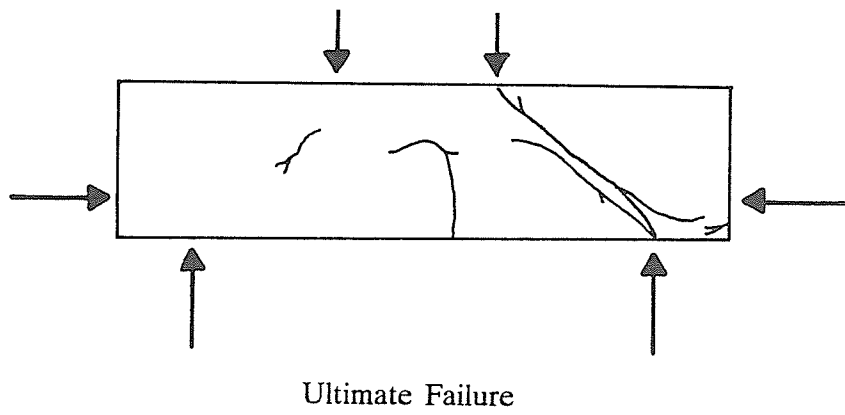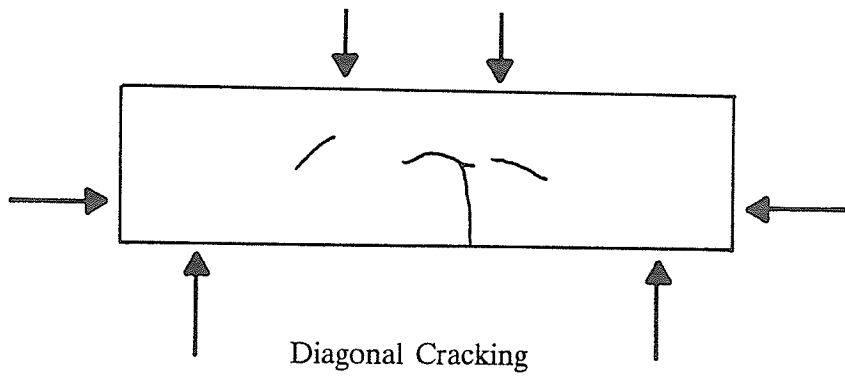   6.3 cm   6.3 cm   29.8 cm

Separation of Vertical supports : 18.9 cm

Loading Conditions : Two symmetric line loadings @ 4.7 cm

                     from the centre line of the beam.

Notes :

(a) Slight Prestress used to even restraining bars outputs.

(b) No additional load noticed on restraining bars until after 1st crack i.e., midspan crack @ 4.2 kN; then immediate jump.

(c) Midspan extended upto about 2/3 of the beam depth.

(d) Diagonal cracking occurred @ 63.4 kN.

(e) Ultimate collapse happened @ 70.5 kN, which is the peak load.

(f) Ultimate failure appears to have occrred as a result of failure of the intact rock above the diagonal crack.

DL4 Crack Patterns :

Midspan Cracking

Diagonal Cracking

Ultimate Failure
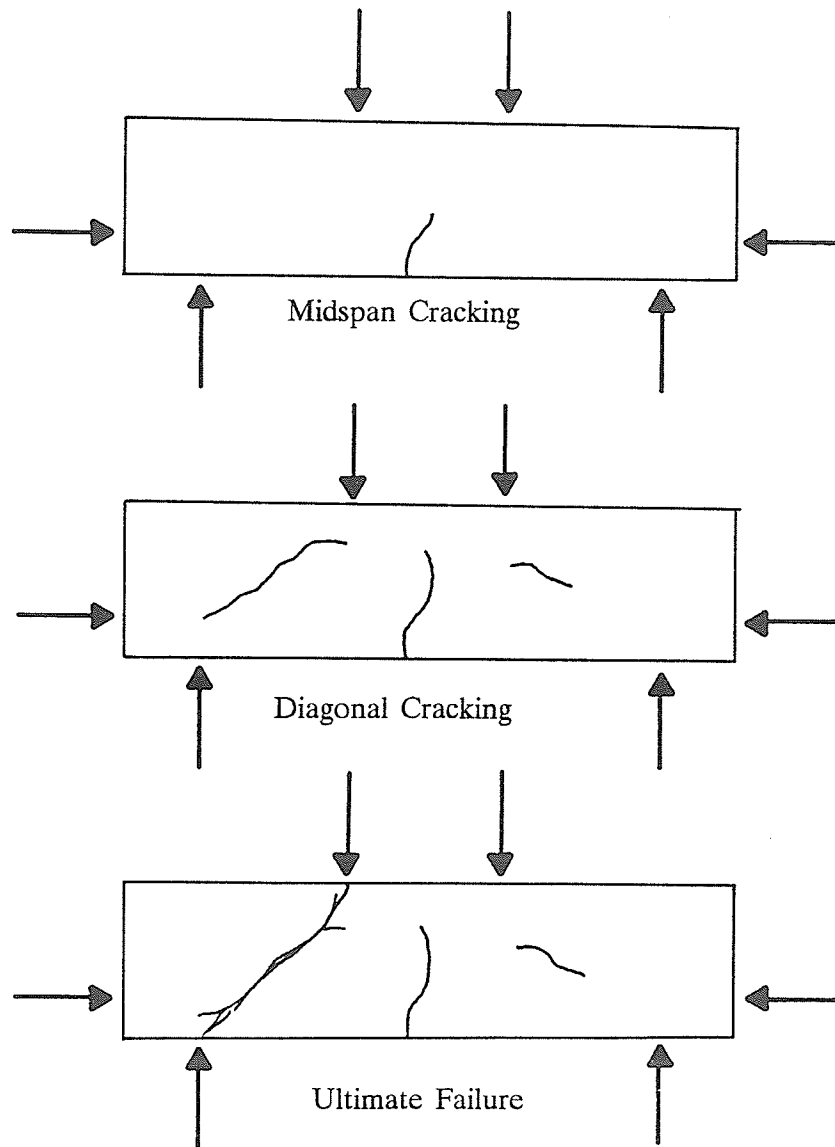
TEST DL5

Purpose : Standard test

Material : Tyndall Stone

Dimensions of Beam : Depth   Breadth   Length

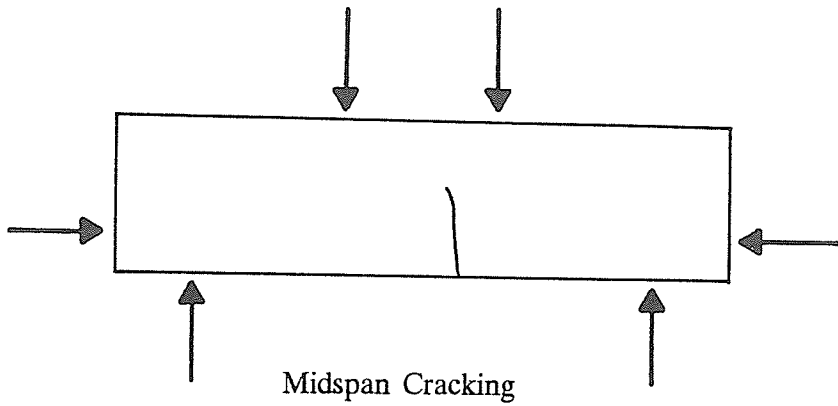   7.1 cm   6.8 cm   29.3 cm

Separation of Vertical supports : 23.5 cm

Loading Conditions : Two symmetric line loadings @ 7.8 cm

                       from the centre line of the beam.

Notes :

(a) Slight Prestress used to even restraining bars outputs.

(b) No additional load noticed on restraining bars until after 1st crack i.e., midspan crack @ 7.6 kN; then immediate jump.

(c) Midspan extended up to about 2/3 of the beam depth.

(d) Diagonal cracking occurred @ 81.1 kN.

(e) Ultimate collapse happened @ 100 kN, which is the peak load.

(f) Ultimate failure appears to have occurred as a result of failure of the intact rock above the diagonal crack.

DL5 Crack Patterns :

Midspan Cracking

Diagonal Cracking

Ultimate Failure

TEST DL6

Purpose : Standard test

Material : Tyndall Stone

Dimensions of Beam : Depth   Breadth   Length
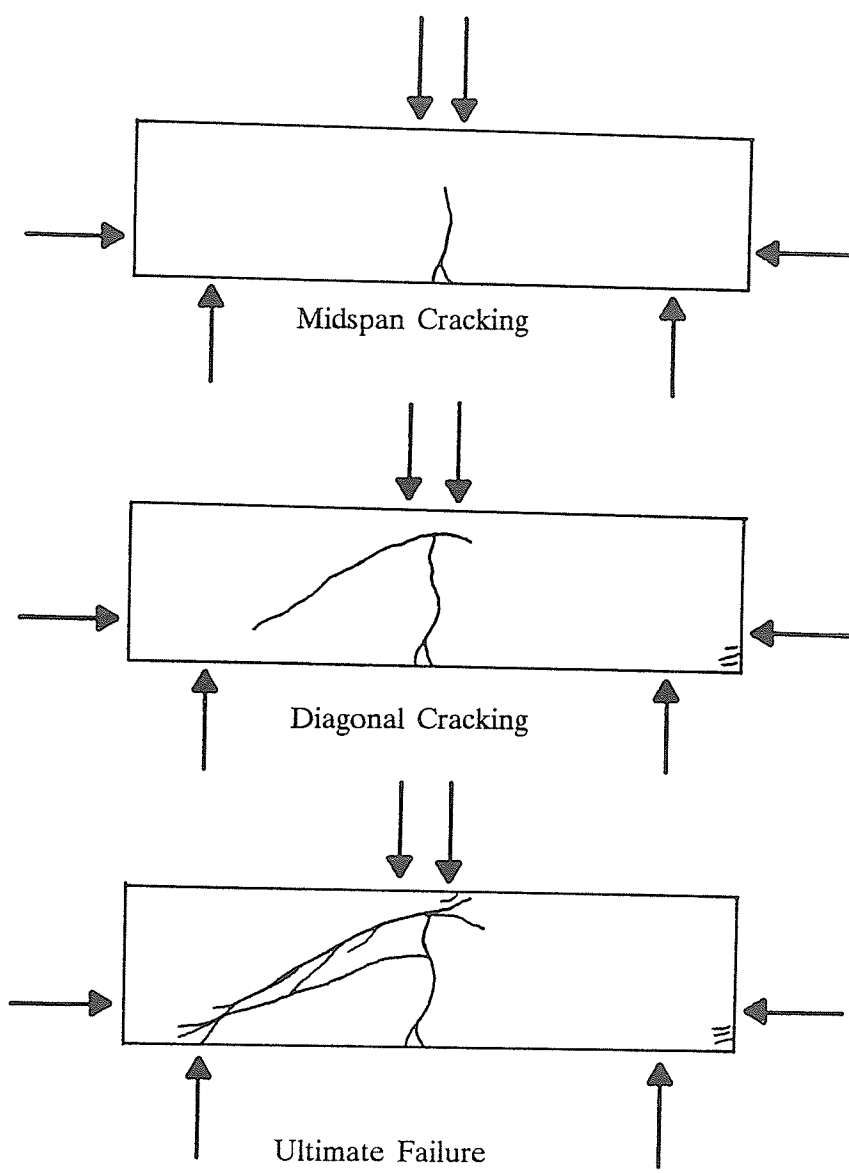
          5.95 cm   6.35 cm   29.7 cm

Separation of Vertical supports : 19.7 cm

Loading Conditions : Two symmetric line loadings @ 1.2 cm from the centre line of the beam.

Notes :

(a) Slight Prestress used to even restraining bars outputs.

(b) No additional load noticed on restraining bars until after 1st crack i.e., midspan crack @ 3.7 kN; then immediate jump.

(c) Midspan extended upto about 4/5 of the beam depth.

(d) Diagonal cracking occurred @ 41.4 kN.

(e) Peak load of 44.7 kN reached after diagonal cracking.

(f) Ultimate collapse appears to have occurred as a result of failure along the diagonal crack.

DL6 Crack Patterns :

Midspan Cracking

Diagonal Cracking

Ultimate Failure

TEST DL7

Purpose : Standard test

Material : Tyndall Stone

Dimensions of Beam : Depth   Breadth   Length

        6.7 cm   6.6 cm   23.9 cm

Separation of Vertical supports : 18.9 cm

Loading Conditions : Two symmetric line loadings @ 1.3 cm

from the cenrte line of the beam.

Notes :

Midspan crack occurred @ 8.9 kN; then accidentally the setup was

disturbed and consequently, the beam was sheared along the midspan crack.

TEST DL8

Purpose : Standard test

Material : Tyndall Stone

Dimensions of Beam : Depth   Breadth   Length
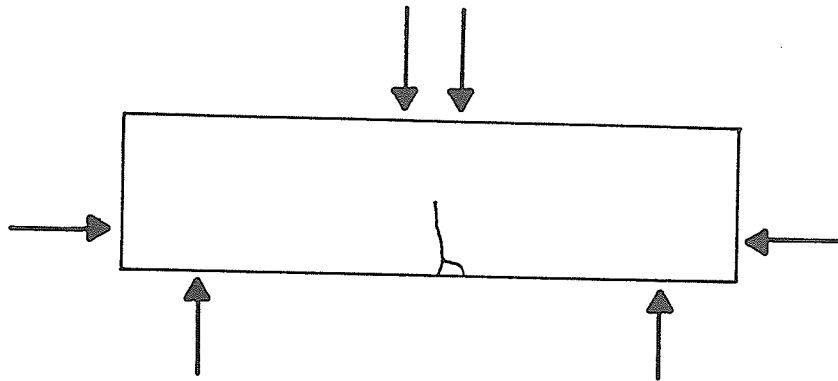
               6.3 cm   6.3 cm   29.6 cm

Separation of Vertical supports : 23.8 cm

Loading Conditions : Two symmetric line loadings @ 1 cm from the centre line
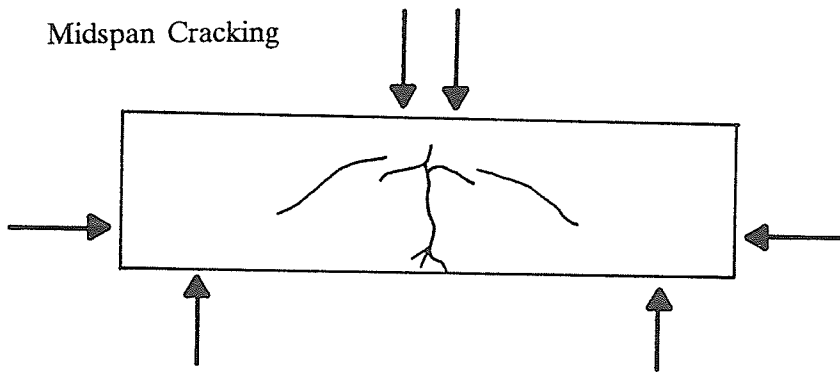
         of the beam.

Notes :

(a) Slight Prestress used to even restraining bars outputs.

(b) No additional load noticed on restraining bars until after 1st crack i.e., midspan

    crack @ 7.1 kN; then immediate jump.

(c) Midspan extended beyond about 3/4 of the beam depth.

(d) Diagonal cracking occurred @ 53.4 kN.

(e) Ultimate collapse happened @ 56.4 kN, which is the peak load.

(f) Ultimate failure appears to have occurred as a result of failure of the intact rock
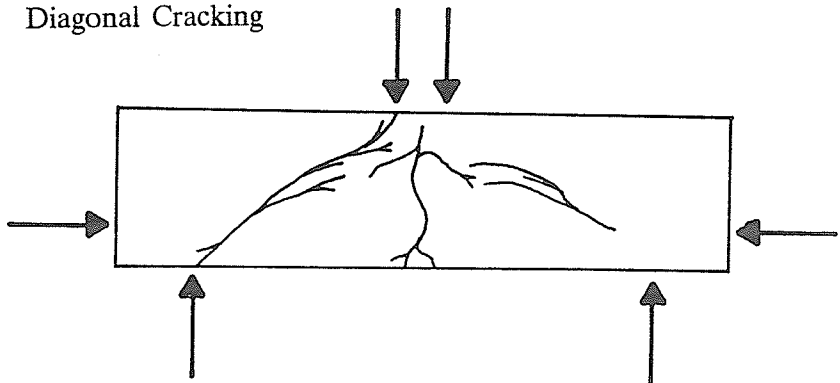
    above the diagonal crack.

DL8 Crack Patterns :

Midspan Cracking

Diagonal Cracking

Ultimate Failure

TEST DL9

Purpose : Standard test

Material : Tyndall Stone

Dimensions of Beam : Depth   Breadth   Length

                            10.1 cm   9.9 cm   24 cm

Separation of Vertical supports : 18.2 cm

Loading Conditions : Two symmetric line loadings @ 1 cm from the centre line

               of the beam.

Notes :

(a) Slight Prestress used to even restraining bars outputs.

(b) No additional load noticed on restraining bars until after 1st crack i.e., midspan

     crack @ 27.7 kN; then immediate jump.

(c) Midspan extended up to about 2/3 of the beam depth.

(d) Diagonal cracking occurred @ 150.9 kN.

(e) Ultimate collapse happened @ 189.7 kN, which is the peak load.

(f) Ultimate failure appears to have occurred as a result of failure of the intact

     rock above the diagonal crack.

DL9 Crack Patterns :

Midspan Cracking

Diagonal Cracking

Ultimate Failure
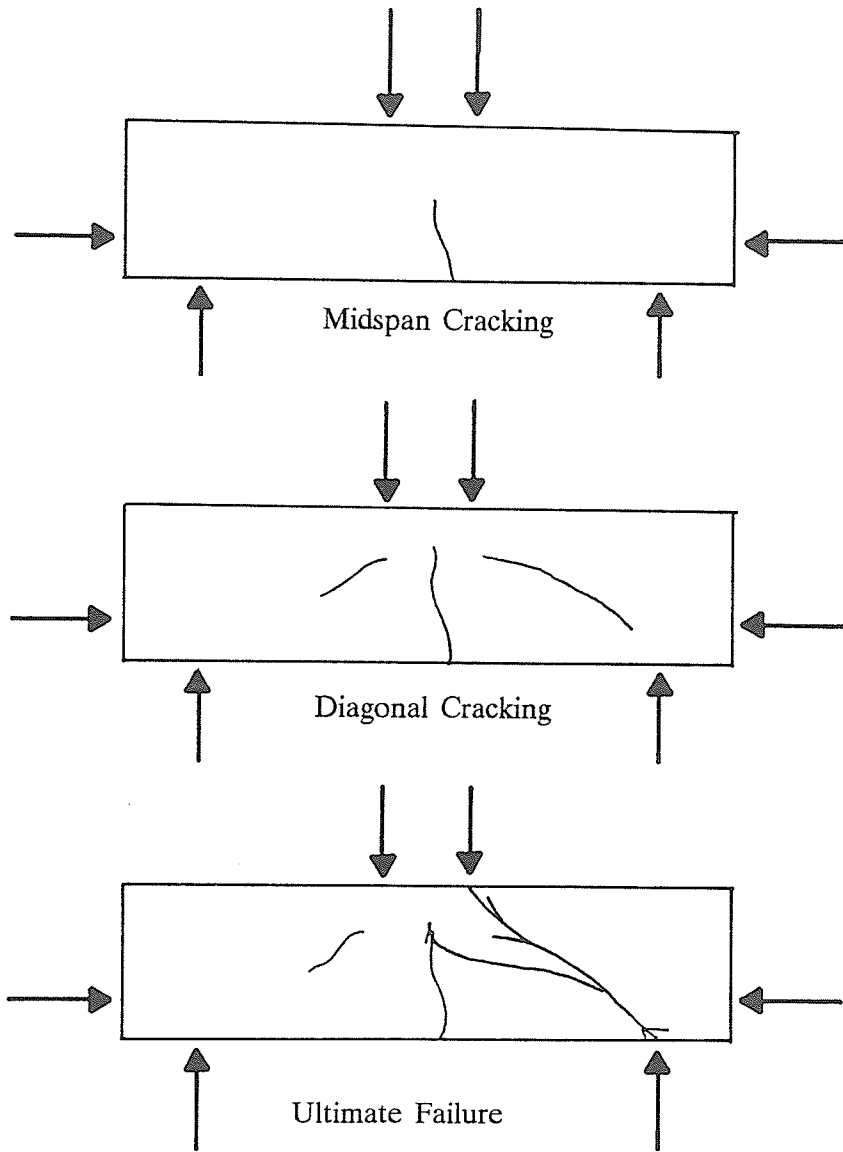
TEST GR1

Purpose : Four Line-load test

Material : Lac Du Bonnet Granite
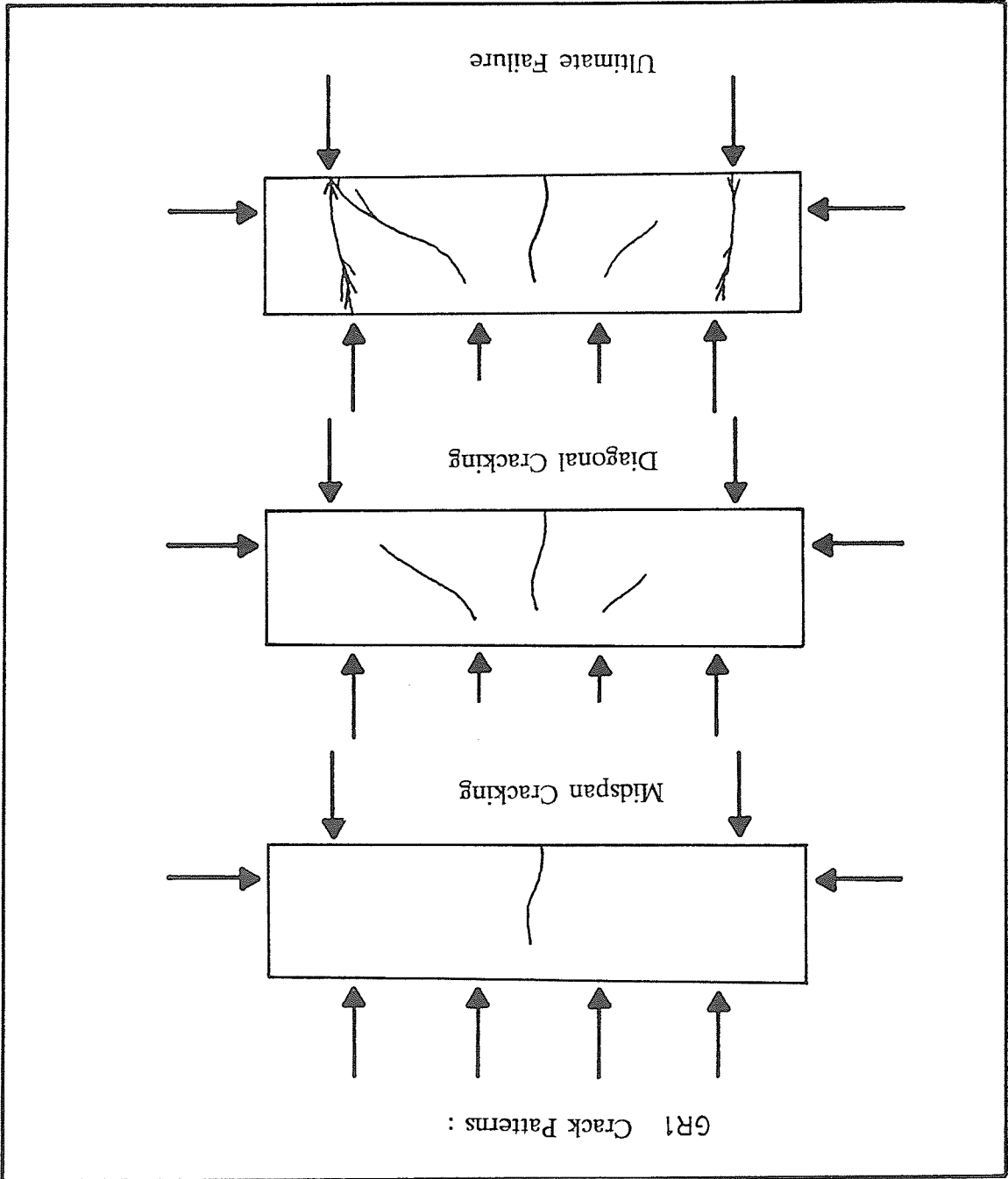
Dimensions of Beam : Depth   Breadth   Length

                     10.8 cm   9.5 cm   23.6 cm

Separation of Vertical supports : 17.8 cm

Loading Conditions : Four line loadings 2.7 cm apart

Notes :

(a) Slight Prestress used to even restraining bars outputs.

(b) No additional load noticed on restraining bars until after 1st crack i.e., midspan

crack @200.7 kN; then immediate jump.

(c) Midspan extended up to about 3/4 of the beam depth.

(d) Diagonal cracking occurred @ 891.2 kN.

(e) Peak load of 1200 kN reached after the diagonal cracking.

(f) The specimen was preserved just before the ultimate collapse.

TEST GR2

Purpose : Standard test

Material : Lac Du Bonner Granite

Dimensions of Beam : Depth   Breadth   Length

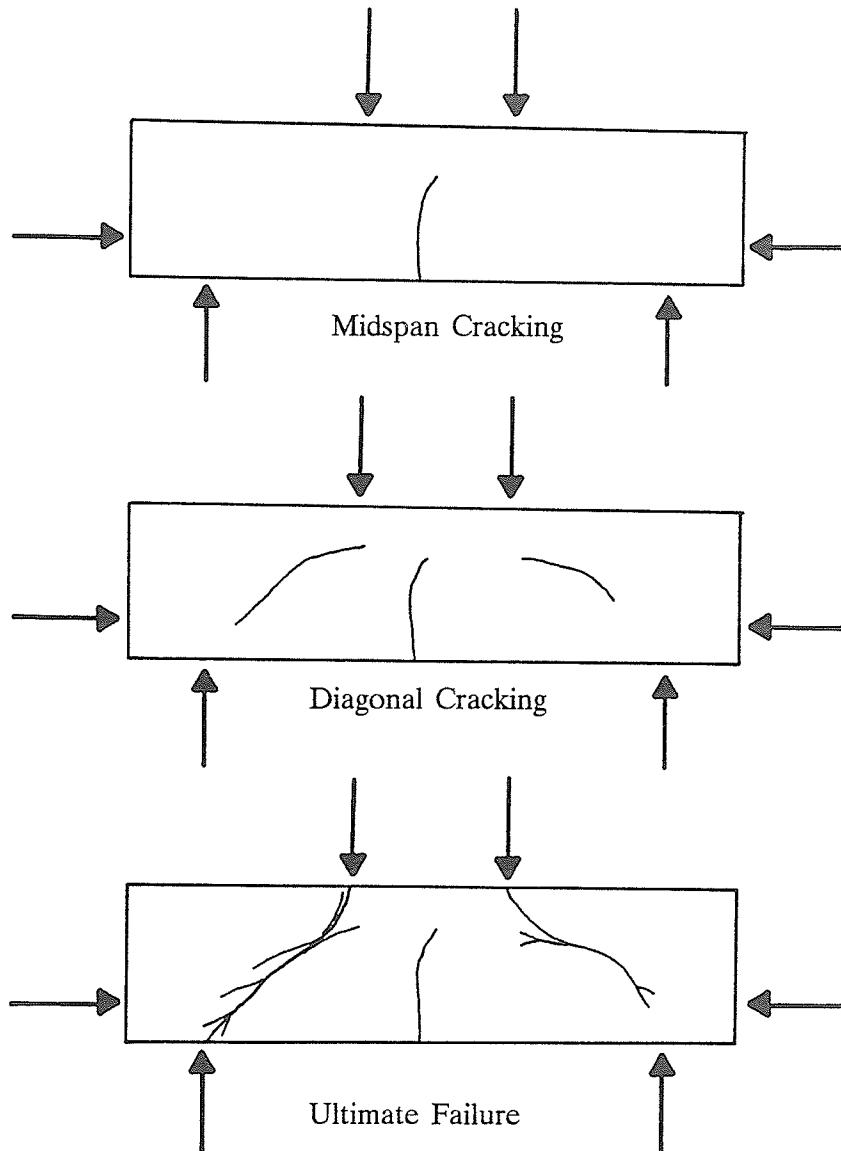   10.8 cm   9.7 cm   27.2 cm

Separation of Vertical supports : 21.4 cm

Loading Conditions : Two symmetric line loadings @ 0.5 cm from the centre line

of the beam.

Notes :

(a) Slight Prestress used to even restraining bars outputs.

(b) No additional load noticed on restraining bars until after 1st crack i.e., midspan

crack @ 73.2 kN; then immediate jump.

(c) Midspan extended upto about 2/3 of the beam depth.

(d) Diagonal cracking occurred @ 429 kN.

(e) Ultimate collapse happened @ 552.9 kN, which is the peak load.

(f) Ultimate failure appears to have occurred as a result of failure of the intact rock

above the diagonal crack.

GR2 Crack Patterns :

Midspan Cracking

Diagonal Cracking

Ultimate Failure

TEST GR3

Purpose : Test with prestress.

Material : Lac Du Bonner Granite

Dimensions of Beam : Depth   Breadth   Length

            10.7 cm   9.7 cm   29.3 cm

Separation of Vertical supports : 23.5 cm

Loading Conditions : Two symmetric line loadings @ 0.5 cm from the centre line of the beam.

Notes :

(a) A prestress of 125 kN was used to simulate the field condition.

(b) No additional load noticed on restraining bars until after 1st crack i.e., midspan crack @ 166.6 kN; but, then the increase in the longitudinal thrust was relatively low compared to the condition where there was no prestress.

(c) Midspan extended up to about 2/3 of the beam depth.

(d) Diagonal cracking occurred @ 465.3 kN.

(e) Ultimate collapse happened @ 665.5 kN, which is the peakload.

(f) Ultimate failure appears to have occurred as a result of failure of the intact rock above the diagonal crack.

GR3   Crack Patterns :

Midspan Cracking

Diagonal Cracking

Ultimate Failure
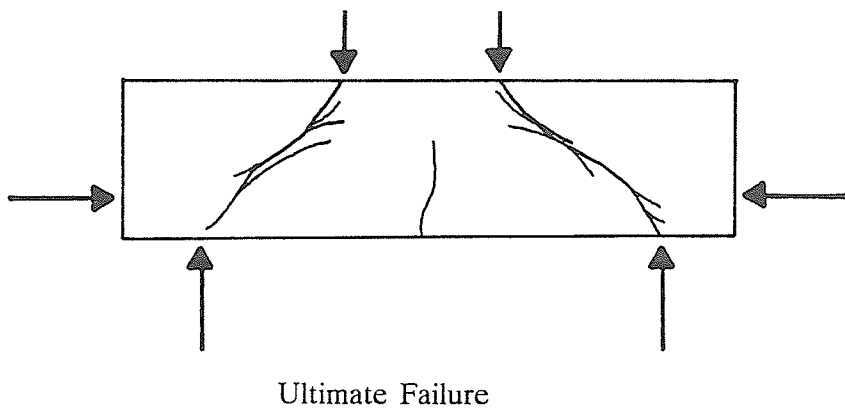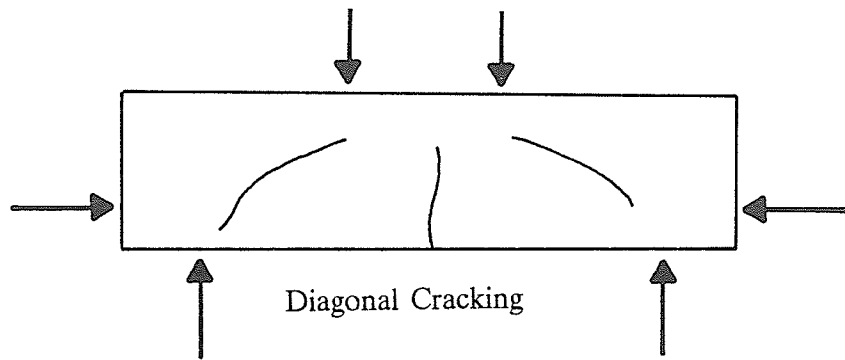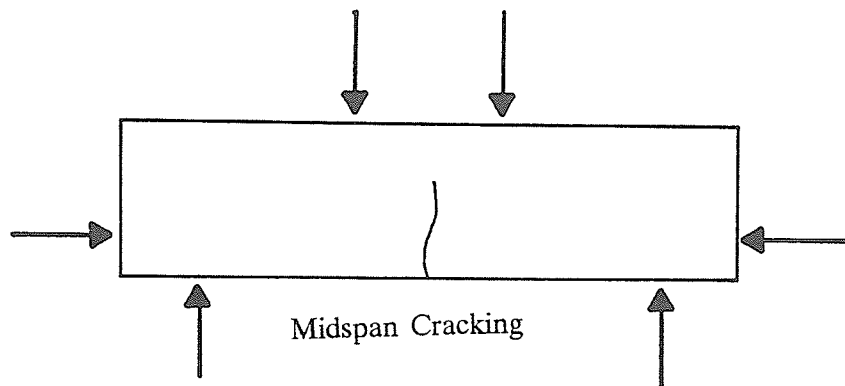
SCHEME FOR CALCULATING ECCENTRICITY

In Fig. VII1, H_t and H_b are the horizontal thrusts in the top and bottom restraining bars respectively. Here, d_t is the distance between the top and bottom restraining bars. The position of the actual horizontal thrust line is define by the distance d_a from the bottom restraining bars. Eccentricity, e is calculated by the following eqn. (VII1) :

$$e = d_t/2 - d_a \qquad\qquad\qquad (VII1)$$

The value of d_a can be obtained using eqn. (VII2) :

$$d_a = \frac{d_t}{3} \left(\frac{H_b + 2H_t}{H_b + H_t}\right) \qquad\qquad\qquad (VII2)$$

Now, from eqns. (VII1) and (VII2), eccentricity e, is

$$e = d_t\left\{\frac{1}{2} - \frac{1}{3}\left(\frac{H_b + 2H_t}{H}\right)\right\} \qquad\qquad\qquad (VII3)$$

where,

$$H = H_b + H_t$$

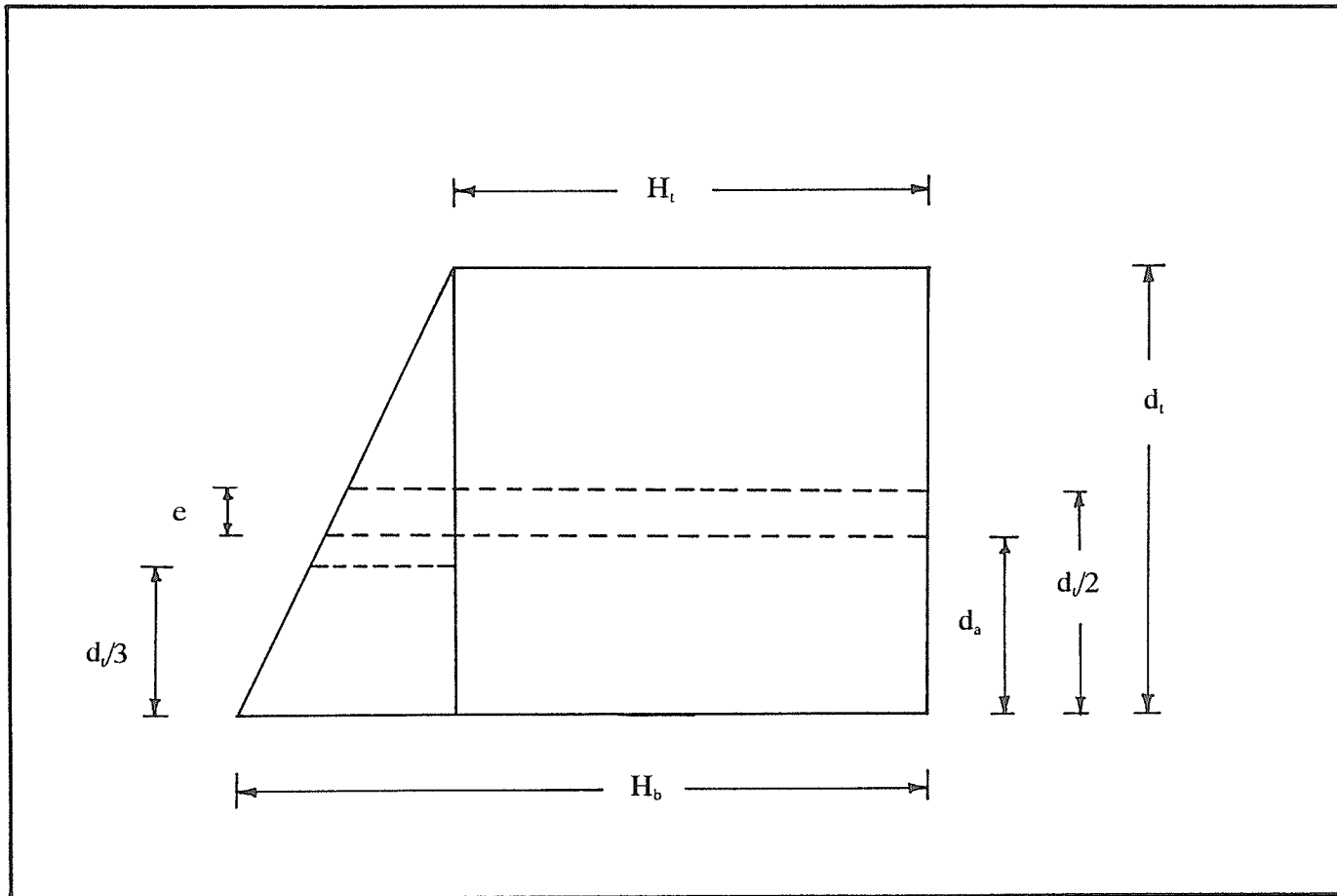$$= \text{total horizontal thurst}$$

Fig.VII1   Diagram showing the longitudinal thurst.

APPENDIX — VIII

SAMPLE CALCULATION FOR COMPARING MEASURED AND

COMPUTED VERTICAL SHEAR STRESSES AT DIAGONAL CRACKING

Fig. VIII1 shows the geometry of a rock beam under loading condition. The following is a sample calculation for the beam test DL6. Here :

Total horizontal thrust, H = 42.18 kN

Horizontal thrust in bottom restraining bars, H_b = 26.89 kN

Horizontal thrust in top restraining bars, H_t = 15.29 kN

Thickness of rock beam, t = 5.95 cm

Shear span, a = 8.65 cm

Distance between bottom and top restraining bars, d_t = 20 cm

Now, from eqn. (VII3), eccentricity e, is

$$ e = d_t \left\{ \frac{1}{2} - \frac{1}{3} \left(\frac{H_b + 2H_t}{H} \right) \right\} $$

$$ = 0.92 \text{ cm} $$

∴ Lever arm of horizontal thrust, d = 2 * e

$$ = 1.84 \text{ cm} $$

Assuming a rectangular distribution of horizontal thrust, which is a good approximation for the rock beam tests, the depth of the horizontal thrust nt (Fig. VIII1), is
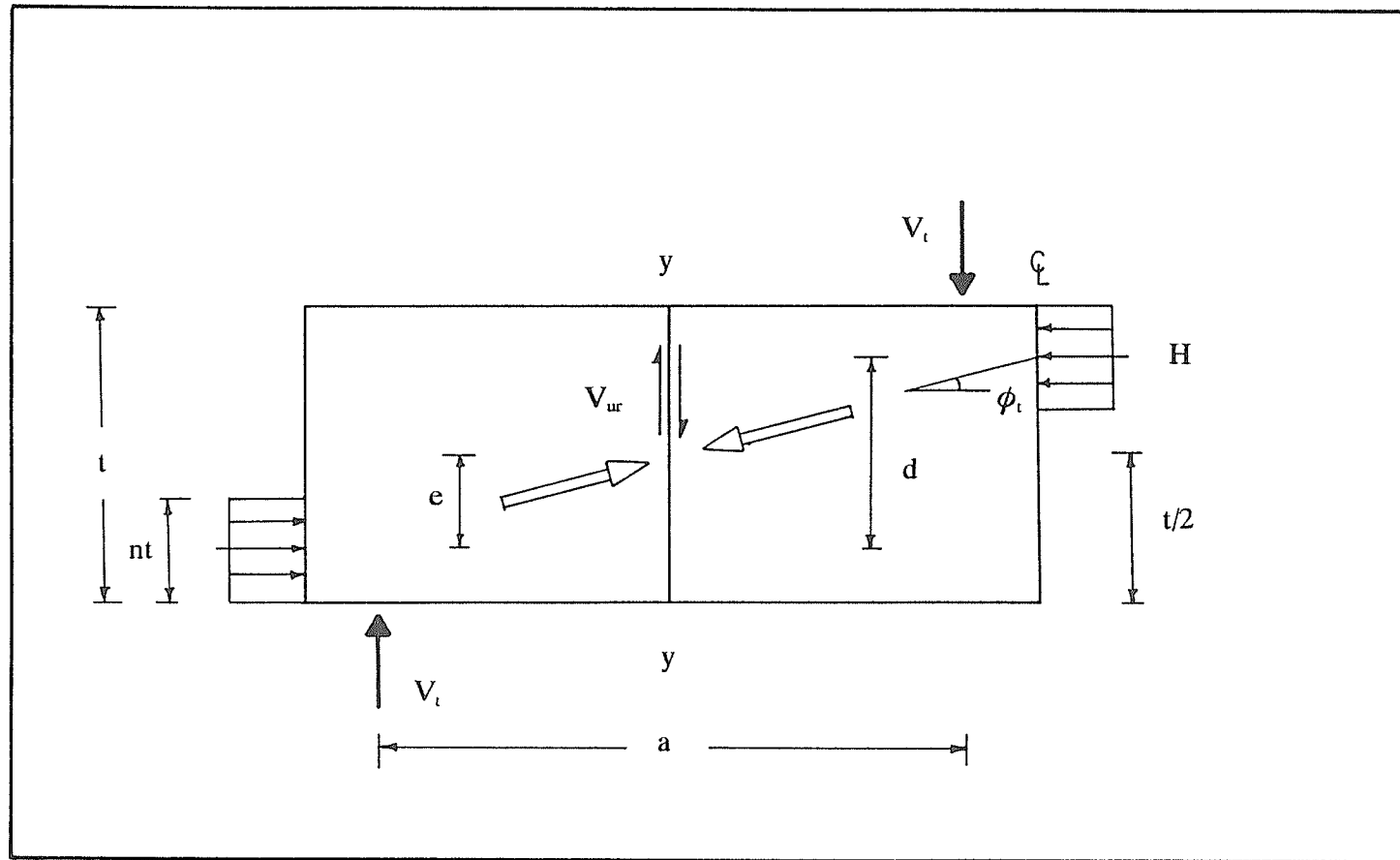
$$ nt = 2*(t/2 - e) $$

214

Fig.VIII1   Geometry of a test beam under loading Conditions.

$$= 4.117 \text{ cm}$$

The average angle of the thrust line ϕ_t, is

$$\phi_t = \tan^{-1}(d/a)$$

$$= 12^\circ$$

The measured total vertical shear force, V_t is

$$V_t = 20.7 \text{ kN}$$

Therefore, from Fig. VIII1, shear force carried by the rock V_{ur}, is

$$V_{ur} = V_t(1 - \text{Sin}\phi_t)$$

$$= 16.41 \text{ kN}$$

The width of the rock beam, $w = 6.35$ cm.

Therefore, the measured shear stress carried by the rock v_{urm} is

$$v_{urm} = V_{ur}/(w * nt)$$

$$= 6.3 \text{ MPa}$$

The computed vertical shear stress v_{urc}, is

$$v_{urc} = (\sigma_t^2 + \sigma_{ca}\sigma_t^2)^{\frac{1}{2}} \tag{VIII1}$$

where,

$$\sigma_{ca} = \text{axial stress}$$

$$\sigma_t = \text{tensile strength of rock}$$

In eqn. (VIII1), the effect of the major principal stress (in this case, axial stress, σ_{ca}) on the tensile strength, σ_t has not been taken into account. Assuming a simple linear dependence of σ_t on σ_{ca}, which is a reasonable approximation, the corrected tensile strength σ_{te}, is

$$\sigma_{tc} = \sigma_t (1 - \sigma_{ca}/\sigma_c)$$

where,

$$\sigma_c = \text{uniaxial compressive strength of rock}$$

Substituting this corrected value in eqn.(VIII1) yields :

$$v_{urc} = \left\{\sigma_t^2 \left(1 - \frac{\sigma_{ca}}{\sigma_c}\right)^2 + \sigma_{ca}\sigma_t \left(1 - \frac{\sigma_{ca}}{\sigma_c}\right)\right\}^{1/2}$$ (VIII2)

In this case,

Axial stress, σ_{ca} = H/(w * nt)

$\qquad$ = 16.13 MPa

Tensile strength of rock, σ_t = 3.7 MPa

Uniaxial compressive strength of rock, σ_c = 50 MPa

Finally, from eqn. (VIII2), the computed vertical shear stress v_{urc}, is

$\qquad v_{urc}$ = 6.8 MPa.